U.PORTO
FEUP FACULDADE DE ENGENHARIA
UNIVERSIDADE DO PORTO

Numerical study of the effect of lightning parameters and paint thickness on the damage induced by simulated lightning strikes in composite plates

João Nuno Moreira dos Santos Pedro

Thesis submitted to Universidade do Porto – Faculdade de Engenharia
in partial fulfillment of the requirements for the degree of
Master in Mechanical Engineering

Supervisor
Professor Albertino Arteiro

Mestrado em Engenharia Mecânica (M.EM)
Departamento de Engenharia Mecânica (DEMec)
Faculdade de Engenharia (FEUP)
Universidade do Porto (UP)

© Porto, 2022

Abstract

Aircraft design is increasingly based on Carbon Fibre Reinforced Plastic (CFRP) composite structures. The introduction of composites has a strong impact on the lightning certification strategy for aircraft programs. Despite their excellent mechanical properties, composites have low electrical and thermal conductivities, leading to the initiation and growth of structural damage.

Since lightning tests are expensive and time-consuming, a progressive need for reliable computational models to increase the knowledge and predict the effects of lightning arcs is needed. The main goal of this research is the development of reliable models that accurately predict the direct effects of lightning strikes on the mechanical damage caused in composite laminates. First, the definition of mechanical lightning loads and of a 3D modelling strategy is validated by comparing the numerical predictions with experimental results for the mechanical behaviour of composite laminates subjected to simulated lightning strikes. Because the mechanical lightning loads are obtained using semi-analytical approaches, the strong shock wave approximation used to determine the contribution of the plasma expansion is replaced by computational fluid dynamics (CFD) calculations. It is demonstrated that the effects predicted by the semi-analytical approach are similar to those relying on CFD calculations. Then, the previously validated models are used to study the effect of paint thickness on mechanical damage induced by lightning strikes. It is demonstrated that the thickness of the paint layer has a direct and significant impact on the damage generated by a lightning strike event. The higher the value of the thickness layer, the more damage will be generated. Finally, the effects of the lightning parameters are studied by means of a parametric analysis, showing that an increase of the peak current and of the action integral lead to more severe damage in composite laminates.

The previous studies are complemented by a case study, covering the application domain of the standard guidelines for simulated lightning strike testing of composite structures. It is shown that varying the peak current and action integral of a D-current waveform within the range specified by the SAE ARP-5412 standard leads to negligible differences in the extent of mechanical damage, confirming the suitability of the SAE standard.

The findings presented in this work demonstrate that the progress and development of reliable models that accurately predict the main effects of lightning strikes is key to a better understanding of this phenomenon in the context of virtual design and virtual certification of composite structures. Future work should rely, among other contributions, on the extension of this approach to coupled thermal-electrical-mechanical damage models.

Keywords: Lightning strike; Finite element method; Damage; Composite materials; Aircraft structures

Resumo

A conceção de aeronaves baseia-se cada vez mais em estruturas compósitas de plástico reforçado com fibra de carbono (CFRP). A introdução de compósitos tem um forte impacto sobre a estratégia de certificação de impacto de raios em conceção aeronáutica. Apesar das suas excelentes propriedades mecânicas, os compósitos têm baixa condutividade elétrica e térmica, tornando o impacto de raios uma fonte de severos danos estruturais.

Uma vez que os testes de impacto de raio são caros e demorados, existe uma necessidade progressiva de modelos computacionais fiáveis para aumentar o conhecimento e prever o comportamento de estruturas compósitas sujeitas a estes fenómenos.

O principal objetivo deste trabalho é o desenvolvimento de modelos fiáveis que prevejam com precisão os efeitos diretos de descargas elétricas no dano induzido em materiais compósitos. Em primeiro lugar, os modelos semianalíticos, usados nos cálculos das distribuições de pressão causadas por impacto de raio, e os modelos de análise de dano são validados comparando as previsões com resultados da resposta mecânica obtidos experimentalmente. De modo a testar a precisão da solução semianalítica usada para o cálculo das ondas de pressão causadas pela expansão do canal de plasma, esta é comparada com soluções de dinâmica dos fluidos computacional (CFD), demonstrando-se que a diferença entre os efeitos captados pela solução semianalítica e pela solução de CFD é deprezável. Utilizando os modelos validados previamente, estudou-se numericamente o efeito da espessura da camada de tinta no dano induzido por impacto de raio. Os resultados obtidos comprovam que à medida que a espessura da camada de tinta aumenta, aumenta também o dano gerado por estes eventos. Finalmente, estudou-se a influência dos parâmetros que definem a forma da descarga elétrica através de uma análise paramétrica, demonstrando-se que o aumento da corrente máxima e da ação integral traduz-se num aumento do dano mecânico gerado por impacto de raio.

Os estudos anteriores são complementados por um caso de estudo, cobrindo o domínio de aplicação das normas de boas práticas para o teste de compósitos laminados sujeitos a impacto de raio. Demonstra-se que variando a corrente máxima e a ação integral de um perfil de corrente do tipo D na gama especificada pela norma SAE ARP-5412 tem um impacto desprezável no dano mecânico induzido. Confirma-se assim, numericamente, a adequação da gama prevista para o perfil de corrente recomendado pela norma SAE.

Os resultados deste trabalho demonstram que o progresso e o desenvolvimento de modelos fiáveis capazes de prever com precisão os principais efeitos de impacto de raio no dano induzido em estruturas compósitas é chave para uma melhor compreensão deste fenómeno no contexto da conceção e certificação virtuais de estruturas compósitas. Trabalhos futuros passarão, entre outros, pela extensão desta abordagem a modelos acoplados de dano termo-eletro-mecânico.

Palavras-chave: Relâmpago; Método dos elementos finitos; Dano; Materiais compósitos; Estruturas aeronáuticas

‘We are what we repeatedly do.
Excellence then, is not an act, but a habit.’

Aristotle

Acknowledgements

I take this opportunity to express my sincere gratitude to Prof. Dr. Albertino Arteiro, my advisor, for the opportunity to participate in this project, and for the support and availability during this thesis and master's course. It was a gratification the collaboration in this work, all the meetings, advice, and sharing of expertise were very important for my development and honestly believed that will be very helpful for the rest of my professional career. It is a great pleasure to have had this opportunity with someone who has always been a reference for me.

I gratefully acknowledge the financial support provided by the European Commission for the scholarship in the scope of the project FibreGy. The financial support provided by AIRBUS (Germany) is also gratefully acknowledged. In particular, I am thankful to Dr. Christian Karch (AIRBUS, Germany), for all his assistance, for interest in this topic, and for helpful discussions.

I also acknowledge the INEGI for welcoming me to the Composites Materials and Structures Unity. Sincerely thanks for the opportunity for personal and professional development, in a stimulating and innovative environment. Especially, I acknowledge Paulo Reiner Gonçalves for the aids integration and all the technical support and helpful conversations.

I would like to express my gratitude to Prof. Dr. Carlos Fernandes for the opportunity in collaborating on a grant for research, the helpful advice, and for opening the possibility of working in the CETRIB - Tribology, Vibrations and Industrial Maintenance Unity of INEGI. I sincerely thanks to Prof. Dr. Jorge Seabra, Prof. Dr. Pedro Marques, Prof. Dr. David Gonçalves, Prof[a]. Dra. Beatriz Graça and João Marafona, PhD candidate, for all the support and easy adaptation in the CETRIB and my academic development.

Also, I acknowledge Pedro Romio and Justino Cruz, PhD candidates working at CETRIB, for all the guidance and encouragement. I would like to emphasize the friendship developed, all the hours of discussions and sharing of ideas. Undoubtedly, they are very important during my MSc course.

A special thanks to Prof. Dr. João Francisco Silva for all the advice, guidance, and encouragement in my initiation into the scientific research area, and for always expecting the best of me. All the conversations and time sharing in the Composite Materials Laboratory from ISEP – Instituto Superior de Engenharia do Porto unquestionably impacted my future.

I would also like to express my gratitude to Prof. Dr. José Dias Rodrigues for taking

the time to share his knowledge and all the debates during this thesis and the MSc course.

I would also like to specially thank my parents for their unconditional support and for always believing in me and my ambition for looking at new challenges and following my aspirations. A sincere thanks you for your patience and care during my university career, I am eternally grateful.

Since this thesis marks the end of a five years path for my graduation in Mechanical Engineering, I would like to express my heartfelt gratitude to my Professors and colleagues, and all those that, somehow, contributed to my professional and personal growth. I do not forget all the teachings and personal development that I have in my licentiate's degree at ISEP – Instituto Superior de Engenharia do Porto, and I am very glad to join FEUP – Faculdade de Engenharia da Universidade do Porto for my master's degree. Truthfully, my biggest and crucial change that I will never regret.

Contents

I Introduction **1**

1 Introduction **3**
1.1 Problem statement . . . 3
1.2 Background . . . 4
1.3 Objectives . . . 4
1.4 Thesis layout . . . 5

II State-of-art and literature review **7**

2 State of art **9**
2.1 Lightning phenomenon . . . 11
2.2 Aircraft lightning certification . . . 12
2.2.1 Current waveforms . . . 14
2.2.2 Zoning . . . 15
2.3 Induced damage . . . 17
2.3.1 Direct effects . . . 19
2.3.2 Indirect effects . . . 20
2.4 Laboratory tests . . . 21
2.5 Lightning strike damage to composite materials . . . 22
2.6 Modelling strategies . . . 25
2.7 Conclusion . . . 28

III Numerical model **29**

3 Lightning loads **31**
3.1 Lightning strike phenomena . . . 33
3.2 Lightning current . . . 33
3.3 Root radius . . . 35
3.4 Near-surface explosion of the lightning protection layer . . . 37
3.5 Supersonic plasma expansion . . . 40
3.6 Magnetic forces . . . 46

4 Finite element analysis and validation **51**
4.1 Finite element model . . . 53
4.2 Continuum damage mechanics model . . . 53
4.2.1 Constitutive model . . . 54
4.2.2 Damage activation functions . . . 56
4.2.3 Damage laws . . . 56

4.2.4 Delamination . . . 57
4.3 Experimental setup . . . 58
4.4 Mass scaling . . . 59
4.4.1 Reference model verification . . . 60
4.5 Model validation . . . 64
4.5.1 Conclusion . . . 71

IV Numerical study **73**

5 CFD analysis **75**
5.1 Introduction . . . 77
5.2 CFD approach . . . 77
5.3 Finite element calculations . . . 78
5.3.1 Pressure profile . . . 78
5.4 Numerical results . . . 80
5.4.1 Expanded copper foil 73 . . . 82
5.4.1.1 CFD - Ideal gas assumptions . . . 82
5.4.1.2 CFD - Doan Nickel . . . 84
5.4.1.3 CFD - Plooster . . . 86
5.4.2 Damage maps . . . 88
5.4.3 Expanded copper foil 195 . . . 92
5.4.3.1 CFD - Ideal gas assumption . . . 92
5.4.3.2 CFD - Doan Nickel . . . 94
5.4.3.3 CFD - Plooster . . . 96
5.4.4 Damage maps . . . 98
5.5 Discussion . . . 102
5.6 Conclusion . . . 102

6 Effect of paint thickness **103**
6.1 Introduction . . . 105
6.2 Surface explosion theory . . . 105
6.3 Literature background . . . 106
6.4 Numerical results . . . 107
6.4.1 Expanded copper foil 73 . . . 108
6.4.1.1 No paint . . . 108
6.4.1.2 200 µm paint thickness . . . 111
6.4.1.3 300 µm paint thickness . . . 114
6.4.1.4 400 µm paint thickness . . . 117
6.4.1.5 Damage maps . . . 120
6.4.2 Expanded copper foil 195 . . . 124
6.4.2.1 No paint . . . 124
6.4.2.2 200 µm paint thickness . . . 127
6.4.2.3 300 µm paint thickness . . . 130
6.4.2.4 400 µm paint thickness . . . 133
6.4.2.5 Damage maps . . . 136
6.5 Discussion . . . 140
6.6 Conclusion . . . 140

7 Waveform parameters 141
7.1 Introduction . . . 143
7.2 Parametric study . . . 143
7.3 Peak current variation . . . 144
7.3.1 Expanded copper foil 73 . . . 145
7.3.1.1 Root radius . . . 145
7.3.1.2 Near-surface explosion . . . 147
7.3.1.3 Supersonic plasma expansion . . . 149
7.3.1.4 Magnetic forces . . . 151
7.3.1.5 Finite element predictions . . . 153
7.3.1.6 Damage maps . . . 155
7.3.2 Expanded copper foil 195 . . . 159
7.3.2.1 Root radius . . . 159
7.3.2.2 Near-surface explosion . . . 160
7.3.2.3 Supersonic plasma expansion . . . 162
7.3.2.4 Magnetic forces . . . 164
7.3.2.5 Finite element predictions . . . 166
7.3.2.6 Damage maps . . . 168
7.4 Action integral variation . . . 172
7.4.1 Expanded copper foil 73 . . . 173
7.4.1.1 Root radius . . . 173
7.4.1.2 Near-surface explosion . . . 174
7.4.1.3 Supersonic plasma expansion . . . 176
7.4.1.4 Magnetic forces . . . 179
7.4.1.5 Finite element predictions . . . 181
7.4.1.6 Damage maps . . . 183
7.4.2 Expanded copper foil 195 . . . 187
7.4.2.1 Root radius . . . 187
7.4.2.2 Near-surface explosion . . . 188
7.4.2.3 Supersonic plasma expansion . . . 190
7.4.2.4 Magnetic forces . . . 192
7.4.2.5 Finite element predictions . . . 194
7.4.2.6 Damage maps . . . 196
7.5 Discussion and conclusions . . . 200

V Case study 201

8 SAE ARP 5412 recommended lightning current waveform: sensitivity analysis 203
8.1 Introduction . . . 205
8.2 Mechanical loads . . . 206
8.3 Waveform 1.42/44.3 µs, 96.4 kA . . . 208
8.4 Waveform 3.18/34.5 µs, 100 kA . . . 218
8.5 Waveform 4/34 µs, 110 kA . . . 228
8.6 Waveform 5/23.6 µs, 110 kA . . . 238
8.7 Waveform 6/51 µs, 90 kA . . . 248
8.8 Waveform 7/35 µs, 90 kA . . . 258
8.9 Damage maps . . . 268
8.10 Discussion . . . 281

8.11 Conclusion 281

VI Conclusions and future work **283**

9 Conclusions and future work **285**
9.1 Conclusions 285
9.2 Future Work 286

References **287**

List of Figures

2.1 Different types of lightning flashes . . . 11
2.2 Building-block approach in composite certification . . . 13
2.3 Scheme of the waveform for return current . . . 15
2.4 Airplane lightning zones . . . 18
2.5 Damage mechanisms induced by a lightning strike . . . 19
2.6 Illustration of the various direct effects at the attachment point . . . 21
2.7 Damage due to lightning strikes on aircraft composite structure . . . 23
2.8 Current intensity effect . . . 24

3.1 Double exponential waveform fittings for the waveform 26.8 µs/48.5 µs, 96.4 kA 34
3.2 Action integral for the waveform 26.8 µs/48.5 µs, 96.4 kA . . . 35
3.3 Arc expansion theory . . . 36
3.4 Fitted root radii as a function of time for the waveform 26.8 µs/48.5 µs, 96.4 kA . . . 37
3.5 Overpressure caused by explosion of lightning protection layers as a function of time for the waveform 26.8 µs/48.5 µs, 96.4 kA . . . 38
3.6 Force magnitude caused by explosion of lightning protection layers as a function of time for the waveform 26.8 µs/48.5 µs, 96.4 kA . . . 39
3.7 Impulse magnitude caused by explosion of lightning protection layers as a function of time for the waveform 26.8 µs/48.5 µs, 96.4 kA . . . 40
3.8 Dimensionless pressure function . . . 41
3.9 Shock wave overpressure over the radius for different times for the waveform 26.8 µs/48.5 µs, 96.4 kA . . . 42
3.10 Computed shock wave radius for the waveform 26.8 µs/48.5 µs, 96.4 kA . . . 43
3.11 Mean cylindrical shock wave pressure due to supersonic plasma expansion for the waveform 26.8 µs/48.5 µs, 96.4 kA . . . 44
3.12 Force magnitude caused by supersonic plasma expansion as a function of time for the waveform 26.8 µs/48.5 µs, 96.4 kA . . . 45
3.13 Impulse magnitude caused by supersonic expansion as a function of time for the waveform 26.8 µs/48.5 µs, 96.4 kA . . . 46
3.14 Scheme of the sample: two regions of the protection layer . . . 47
3.15 Maximum magnetic pressure evolution with time for the waveform 26.8 µs/48.5 µs, 96.4 kA . . . 47
3.16 Force magnitude caused by magnetic forces as a function of time for the waveform 26.8 µs/48.5 µs, 96.4 kA . . . 48
3.17 Impulse magnitude caused by magnetic forces as a function of time for the waveform 26.8 µs/48.5 µs, 96.4 kA . . . 49

4.1 Uniaxial response . . . 57

4.2 Configuration of the lightning strike test support and sample 59
4.3 Comparison of the kinetic energy between reference model and mass scaling model 61
4.4 Comparison of the internal energy between reference model and mass scaling model 61
4.5 Finite element predictions comparison between reference model and mass scaling model 62
4.6 Composite plate finite element mesh 65
4.7 Finite element predictions and VISAR measurements for ECF 73 69
4.8 Finite element predictions and VISAR measurements for ECF 195 70

5.1 Pressure profile of the EOS *Ideal gas assumption*, and comparison with the strong shock wave approximation 79
5.2 Pressure profile of the EOS *Doan-Nickel*, and comparison with the strong shock wave approximation 79
5.3 Pressure profile of the EOS *Plooster*, and comparison with the strong shock wave approximation 80
5.4 Bilinear interpolation foundation 81
5.5 Displacement map for ECF 73 within a time $t \leq 500\,\mu s$ (colour bar) of the EOS *Ideal gas assumption* 82
5.6 Finite element predictions with analytical approximation (solid lines) and CFD calculations of the EOS *Ideal gas assumption* (dashed lines) for ECF 73 83
5.7 Displacement map for ECF 73 within a time $t \leq 500\,\mu s$ (colour bar) of the EOS *Doan-Nickel* 84
5.8 Finite element predictions with analytical approximation (solid lines) and CFD calculations of EOS *Doan-Nickel* (dashed lines) for ECF 73 85
5.9 Displacement map for ECF 73 within a time $t \leq 500\,\mu s$ of the EOS *Plooster* 86
5.10 Finite element predictions with analytical approximation (solid lines) and CFD calculations of the EOS *Plooster* (dashed lines) for ECF 73 87
5.11 Displacement map for ECF 195 within a time $t \leq 500\,\mu s$ (colour bar) of the EOS *Ideal gas* 92
5.12 Finite element predictions with analytical approximation (solid lines) and CFD calculations of the EOS *Ideal gas* (dashed lines) for ECF 195 93
5.13 Displacement map for ECF 195 within a time $t \leq 500\,\mu s$ (colour bar) of the EOS *Doan-Nickel* 94
5.14 Finite element predictions with analytical approximation (solid lines) and CFD calculations of the EOS *Doan-Nickel* (dashed lines) for ECF 195 . . . 95
5.15 Displacement map for ECF 195 within time $\leq 500\,\mu s$ of the EOS *Plooster* . 96
5.16 Finite element predictions with analytical approximation (solid lines) and CFD calculations of the EOS *Plooster* (dashed lines) for ECF 195 97

6.1 Mechanical contributions for the unpainted sample of ECF 73 109
6.2 Finite element predictions for the unpainted sample of ECF 73 110
6.3 Mechanical contributions for the sample with 200 µm paint thickness of ECF 73 112
6.4 Finite element predictions for the sample with 200 µm paint thickness of ECF 73 113
6.5 Mechanical contributions for the sample with 300 µm paint thickness of ECF 73 115

6.6 Finite element predictions for the sample with 300 µm paint thickness of ECF 73 . . . 116
6.7 Mechanical contributions for the sample with 400 µm paint thickness of ECF 73 . . . 118
6.8 Finite element predictions for the sample with 400 µm paint thickness of ECF 73 . . . 119
6.9 Mechanical contributions for unpainted sample of ECF 195 . . . 125
6.10 Finite element predictions for unpainted sample of ECF 195 . . . 126
6.11 Mechanical contributions for the sample with 200 µm paint thickness of ECF 195 . . . 128
6.12 Finite element predictions for the sample with 200 µm paint thickness of ECF 195 . . . 129
6.13 Mechanical contributions for the sample with 300 µm paint thickness of ECF 195 . . . 131
6.14 Finite element predictions for the sample with 300 µm paint thickness of ECF 195 . . . 132
6.15 Mechanical contributions for the sample with 400 µm paint thickness of ECF 195 . . . 134
6.16 Finite element predictions for the sample with 400 µm paint thickness of ECF 195 . . . 135

7.1 Waveforms considering different currents . . . 144
7.2 Root radius for waveform alternatives to assess peak current influence for ECF 73 . . . 146
7.3 Overpressure caused by explosion of lightning protection layers as a function of time for waveform alternatives to assess peak current influence for ECF 73 147
7.4 Force magnitude caused by explosion of lightning protection layers as a function of time for waveform alternatives to assess peak current influence for ECF 73 . . . 148
7.5 Impulse magnitude caused by explosion of lightning protection layers as a function of time for waveform alternatives to assess peak current influence for ECF 73 . . . 148
7.6 Computed shock radius for waveform alternatives to assess peak current influence for ECF 73 . . . 149
7.7 Mean cylindrical shock wave pressure as a function of time due to supersonic plasma expansion for waveform alternatives to assess peak current influence for ECF 73 . . . 150
7.8 Force magnitude caused by supersonic plasma expansion as a function of time for waveform alternatives to assess peak current influence for ECF 73 . 150
7.9 Impulse magnitude caused by supersonic plasma expansion as a function of time for waveform alternatives to assess peak current influence for ECF 73 . 151
7.10 Maximum magnetic pressure evolution with time for waveform alternatives to assess peak current influence for ECF 73 . . . 152
7.11 Force magnitude caused by magnetic forces as a function of time for for waveform alternatives to assess peak current influence for ECF 73 . . . 152
7.12 Impulse magnitude caused by magnetic forces as a function of time for waveform alternatives to assess peak current influence for ECF 73 . . . 153

7.13 Finite element predictions for waveform alternatives to assess peak current influence, where solid lines represents the waveform 26.8/48.5 µs, 96.4 kA, dashed lines the waveform 26.8/41 µs, 106.04 kA and dashed dotted lines the waveform 26.8/58.6 µs, 86.76 kA for ECF 73 154
7.14 Root radius for waveform alternatives to assess peak current influence for ECF 195 159
7.15 Overpressure caused by explosion of lightning protection layers as a function of time for waveform alternatives to assess peak current influence for ECF 195 160
7.16 Force magnitude caused by explosion of lightning protection layers as a function of time for waveform alternatives to assess peak current influence for ECF 195 161
7.17 Impulse magnitude caused by explosion of lightning protection layers as a function of time for waveform alternatives to assess peak current influence for ECF 195 161
7.18 Computed shock radius for waveform alternatives to assess peak current influence for ECF 195 162
7.19 Mean cylindrical shock wave pressure as a function of time due to supersonic plasma expansion for waveform alternatives to assess peak current influence for ECF 195 163
7.20 Force magnitude caused by supersonic plasma expansion as a function of time for waveform alternatives to assess peak current influence for ECF 195 163
7.21 Impulse magnitude caused by supersonic plasma expansion as a function of time for waveform alternatives to assess peak current influence for ECF 195 164
7.22 Maximum magnetic pressure evolution with time for waveform alternatives to assess peak current influence for ECF 195 165
7.23 Force magnitude caused by magnetic forces as a function of time for for waveform alternatives to assess peak current influence for ECF 195 165
7.24 Impulse magnitude caused by magnetic forces as a function of time for waveform alternatives to assess peak current influence for ECF 195 166
7.25 Finite element predictions for waveform alternatives to assess peak current influence, where solid lines represents the waveform 26.8/48.5 µs, 96.4 kA, dashed lines the waveform 26.8/41 µs, 106.04 kA and dashed dotted lines the waveform 26.8/58.6 µs, 86.76 kA for ECF 195 167
7.26 Waveforms considering different action integrals 172
7.27 Root radius for waveform alternatives to assess action integral influence for ECF 73 173
7.28 Overpressure caused by explosion of lightning protection layers as a function of time for waveform alternatives to assess action integral influence for ECF 73 175
7.29 Force magnitude caused by explosion of lightning protection layers as a function of time for waveform alternatives to assess action integral influence for ECF 73 175
7.30 Impulse magnitude caused by explosion of lightning protection layers as a function of time for waveform alternatives to assess action integral influence for ECF 73 176
7.31 Computed shock radius for waveform alternatives to assess action integral influence for ECF 73 177

7.32 Mean cylindrical shock wave pressure as a function of time due to supersonic plasma expansion for waveform alternatives to assess action integral influence for ECF 73 . . . 177
7.33 Force magnitude caused by supersonic plasma expansion as a function of time for waveform alternatives to assess action integral influence for ECF 73 178
7.34 Impulse magnitude caused by supersonic plasma expansion as a function of time for waveform alternatives to assess action integral influence for ECF 73 179
7.35 Maximum magnetic pressure evolution with time for waveform alternatives to assess action integral influence for ECF 73 . . . 180
7.36 Force magnitude caused by magnetic forces as a function of time for for waveform alternatives to assess action integral influence for ECF 73 . . . 180
7.37 Impulse magnitude caused by magnetic forces as a function of time for waveform alternatives to assess action integral influence for ECF 73 . . . 181
7.38 Finite element predictions for waveform alternatives to assess action integral influence, where solid lines represents the waveform 26.8/48.5 µs, 96.4 kA, dashed lines the waveform 26.8/57.1 µs, 96.4 kA and dashed dotted lines the waveform 26.8/39.9 µs, 96.4 kA for ECF 73 . . . 182
7.39 Root radius for waveform alternatives to assess action integral influence for ECF 195 . . . 187
7.40 Overpressure caused by explosion of lightning protection layers as a function of time for waveform alternatives to assess action integral influence for ECF 195 . . . 188
7.41 Force magnitude caused by explosion of lightning protection layers as a function of time for waveform alternatives to assess action integral influence for ECF 195 . . . 189
7.42 Impulse magnitude caused by explosion of lightning protection layers as a function of time for waveform alternatives to assess action integral influence for ECF 195 . . . 189
7.43 Computed shock radius for waveform alternatives to assess action integral influence for ECF 195 . . . 190
7.44 Mean cylindrical shock wave pressure as a function of time due to supersonic plasma expansion for waveform alternatives to assess action integral influence for ECF 195 . . . 191
7.45 Force magnitude caused by supersonic plasma expansion as a function of time for waveform alternatives to assess action integral influence for ECF 195 191
7.46 Impulse magnitude caused by supersonic plasma expansion as a function of time for waveform alternatives to assess action integral influence for ECF 195 192
7.47 Maximum magnetic pressure evolution with time for waveform alternatives to assess action integral influence for ECF 195 . . . 193
7.48 Force magnitude caused by magnetic forces as a function of time for for waveform alternatives to assess action integral influence for ECF 195 . . . 193
7.49 Impulse magnitude caused by magnetic forces as a function of time for waveform alternatives to assess action integral influence for ECF 195 . . . 194
7.50 Finite element predictions for waveform alternatives to assess action integral influence, where solid lines represents the waveform 26.8/48.5 µs, 96.4 kA, dashed lines the waveform 26.8/57.1 µs, 96.4 kA and dashed dotted lines the waveform 26.8/39.9 µs, 96.4 kA for ECF 195 . . . 195

8.1 Root radius fitting comparison between new proposed equation and standard equation . . . 206

8.2 Double exponential for the waveform 1.42/44.3 µs, 96.4 kA 208
8.3 Root radius for the waveform 1.42/44.3 µs, 96.4 kA 209
8.4 Overpressure caused by explosion of lightning protection layers as a function of time for the waveform 1.42/44.3 µs, 96.4 kA 210
8.5 Force magnitude caused by explosion of lightning protection layers as a function of time for the waveform 1.42/44.3 µs, 96.4 kA 210
8.6 Impulse magnitude caused by explosion of lightning protection layers as a function of time for the waveform 1.42/44.3 µs, 96.4 kA 211
8.7 Computed shock for the waveform 1.42/44.3 µs, 96.4 kA 212
8.8 Mean cylindrical shock wave pressure as a function of time due to supersonic plasma expansion for the waveform 1.42/44.3 µs, 96.4 kA 212
8.9 Force magnitude caused by supersonic plasma expansion as a function of time for the waveform 1.42/44.3 µs, 96.4 kA 213
8.10 Impulse magnitude caused by supersonic plasma expansion as a function of time for the waveform 1.42/44.3 µs, 96.4 kA 214
8.11 Maximum magnetic pressure evolution with time for the waveform 1.42/44.3 µs, 96.4 kA 214
8.12 Force magnitude caused by magnetic forces as a function of time for the waveform 1.42/44.3 µs, 96.4 kA 215
8.13 Impulse magnitude caused by magnetic forces as a function of time for the waveform 1.42/44.3 µs, 96.4 kA 216
8.14 Finite element predictions for the waveform 1.42/44.3 µs, 96.4 kA 217
8.15 Double exponential for 3.18/34.5 µs, 100 kA 218
8.16 Root radius for 3.18/34.5 µs, 100 kA 219
8.17 Overpressure caused by explosion of lightning protection layers as a function of time for 3.18/34.5 µs, 100 kA 220
8.18 Force magnitude caused by explosion of lightning protection layers as a function of time for 3.18/34.5 µs, 100 kA 220
8.19 Impulse magnitude caused by explosion of lightning protection layers as a function of time for 3.18/34.5 µs, 100 kA 221
8.20 Computed shock radius for 3.18/34.5 µs, 100 kA 222
8.21 Mean cylindrical shock wave pressure as a function of time due to supersonic plasma expansion for 3.18/34.5 µs, 100 kA 222
8.22 Force magnitude caused by supersonic plasma expansion as a function of time for 3.18/34.5 µs, 100 kA 223
8.23 Impulse magnitude caused by supersonic plasma expansion as a function of time for 3.18/34.5 µs, 100 kA 224
8.24 Maximum magnetic pressure evolution with time for 3.18/34.5 µs, 100 kA . 224
8.25 Force magnitude caused by magnetic forces as a function of time for 3.18/34.5 µs, 100 kA 225
8.26 Impulse magnitude caused by magnetic forces as a function of time for 3.18/34.5 µs, 100 kA 226
8.27 Finite element predictions for 3.18/34.5 µs, 100 kA 227
8.28 Double exponential for 4/34 µs, 110 kA 228
8.29 Root radius for 4/34 µs, 110 kA 229
8.30 Overpressure caused by explosion of lightning protection layers as a function of time for 4/34 µs, 110 kA 230
8.31 Force magnitude caused by explosion of lightning protection layers as a function of time for 4/34 µs, 110 kA 230

8.32 Impulse magnitude caused by explosion of lightning protection layers as a function of time for 4/34 µs, 110 kA 231
8.33 Computed shock radius for 4/34 µs, 110 kA 232
8.34 Mean cylindrical shock wave pressure as a function of time due to supersonic plasma expansion for 4/34 µs, 110 kA 232
8.35 Force magnitude caused by supersonic plasma expansion as a function of time for 4/34 µs, 110 kA 233
8.36 Impulse magnitude caused by supersonic plasma expansion as a function of time for 4/34 µs, 110 kA 234
8.37 Maximum magnetic pressure evolution with time for 4/34 µs, 110 kA 234
8.38 Force magnitude caused by magnetic forces as a function of time for 4/34 µs, 110 kA 235
8.39 Impulse magnitude caused by magnetic forces as a function of time for 4/34 µs, 110 kA 236
8.40 Finite element predictions for 4/34 µs, 110 kA 237
8.41 Double exponential for 5/23.6 µs, 110 kA 238
8.42 Root radius for 5/23.6 µs, 110 kA 239
8.43 Overpressure caused by explosion of lightning protection layers as a function of time for 5/23.6 µs, 110 kA 240
8.44 Force magnitude caused by explosion of lightning protection layers as a function of time for 5/23.6 µs, 110 kA 240
8.45 Impulse magnitude caused by explosion of lightning protection layers as a function of time for 5/23.6 µs, 110 kA 241
8.46 Computed shock radius for 5/23.6 µs, 110 kA 242
8.47 Mean cylindrical shock wave pressure as a function of time due to supersonic plasma expansion for 5/23.6 µs, 110 kA 242
8.48 Force magnitude caused by supersonic plasma expansion as a function of time for 5/23.6 µs, 110 kA 243
8.49 Impulse magnitude caused by supersonic plasma expansion as a function of time for 5/23.6 µs, 110 kA 244
8.50 Maximum magnetic pressure evolution with time for 5/23.6 µs, 110 kA . . . 244
8.51 Force magnitude caused by magnetic forces as a function of time for 5/23.6 µs, 110 kA 245
8.52 Impulse magnitude caused by magnetic forces as a function of time for 5/23.6 µs, 110 kA 246
8.53 Finite element predictions for 5/23.6 µs, 110 kA 247
8.54 Double exponential for 6/51 µs, 90 kA 248
8.55 Root radius for 6/51 µs, 90 kA 249
8.56 Overpressure caused by explosion of lightning protection layers as a function of time for 6/51 µs, 90 kA 250
8.57 Force magnitude caused by explosion of lightning protection layers as a function of time for 6/51 µs, 90 kA 250
8.58 Impulse magnitude caused by explosion of lightning protection layers as a function of time for 6/51 µs, 90 kA 251
8.59 Computed shock radius for 6/51 µs, 90 kA 252
8.60 Mean cylindrical shock wave pressure as a function of time due to supersonic plasma expansion for 6/51 µs, 90 kA 252
8.61 Force magnitude caused by supersonic plasma expansion as a function of time for 6/51 µs, 90 kA 253

8.62 Impulse magnitude caused by supersonic plasma expansion as a function of time for 6/51 µs, 90 kA . . . 254
8.63 Maximum magnetic pressure evolution with time for 6/51 µs, 90 kA . . . 254
8.64 Force magnitude caused by magnetic forces as a function of time for 6/51 µs, 90 kA . . . 255
8.65 Impulse magnitude caused by magnetic forces as a function of time for 6/51 µs, 90 kA . . . 256
8.66 Finite element predictions for 6/51 µs, 90 kA . . . 257
8.67 Double exponential for 7/35 µs, 90 kA . . . 258
8.68 Root radius for 7/35 µs, 90 kA . . . 259
8.69 Overpressure caused by explosion of lightning protection layers as a function of time for 7/35 µs, 90 kA . . . 260
8.70 Force magnitude caused by explosion of lightning protection layers as a function of time for 7/35 µs, 90 kA . . . 260
8.71 Impulse magnitude caused by explosion of lightning protection layers as a function of time for 7/35 µs, 90 kA . . . 261
8.72 Computed shock radius for 7/35 µs, 90 kA . . . 262
8.73 Mean cylindrical shock wave pressure as a function of time due to supersonic plasma expansion for 7/35 µs, 90 kA . . . 262
8.74 Force magnitude caused by supersonic plasma expansion as a function of time for 7/35 µs, 90 kA . . . 263
8.75 Impulse magnitude caused by supersonic plasma expansion as a function of time for 7/35 µs, 90 kA . . . 264
8.76 Maximum magnetic pressure evolution with time for 7/35 µs, 90 kA . . . 264
8.77 Force magnitude caused by magnetic forces as a function of time for 7/35 µs, 90 kA . . . 265
8.78 Impulse magnitude caused by magnetic forces as a function of time for 7/35 µs, 90 kA . . . 266
8.79 Finite element predictions for 7/35 µs, 90 kA . . . 267

List of Tables

3.1 Waveform parameters for the waveform 26.8 µs/48.5 µs, 96.4 kA 35
3.2 Parameters for root radius fit for the waveform 26.8 µs/48.5 µs, 96.4 kA . . . 37

4.1 Time duration of the FE model 53
4.2 Damage map assessment for the four damage variables comparing the reference model (first row) and the model with mass scaling (second row) for ECF 73 64
4.3 T700/M21 UD ply density, Young's moduli, shear modulus and Poisson's ratios 66
4.4 T700/M21 strengths and material degradation properties used in the modified continuum damage mechanics model 66
4.5 T700/M21 interlaminar properties 67
4.6 Effective properties of ECF 73 and ECF 195 filled with epoxy resin M21 . . 67
4.7 Offset coordinates for ECF 73 and ECF 195 68

5.1 Damage map assessment of the damage variable in the longitudinal direction (d_1) for the strong shock wave approximation and CFD calculations for ECF 73 88
5.2 Damage map assessment of the damage variable in the transverse direction (d_2) for the strong shock wave approximation and CFD calculations for ECF 73 89
5.3 Damage map assessment of the shear damage variable (d_6) for the strong shock wave approximation and CFD calculations for ECF 73 90
5.4 Damage map assessment of the damage variable for cohesive surfaces (d) for the strong shock wave approximation and CFD calculations for ECF 73 91
5.5 Damage map assessment of the damage variable in the longitudinal direction (d_1) for the strong shock wave approximation and CFD calculations for ECF 195 98
5.6 Damage map assessment of the damage variable in the transverse direction (d_2) for the strong shock wave approximation and CFD calculations for ECF 195 99
5.7 Damage map assessment of the shear damage variable (d_6) for the strong shock wave approximation and CFD calculations for ECF 195 100
5.8 Damage map assessment of the damage variable for cohesive surfaces (d) for the strong shock wave approximation and CFD calculations for ECF 195 101

6.1 Damage map assessment considering the effect of paint thickness for the damage variable in the longitudinal direction (d_1) for ECF 73 120
6.2 Damage map assessment considering the effect of paint thickness for the damage variable in the transverse direction (d_2) for ECF 73 121

6.3 Damage map assessment considering the effect of paint thickness for the shear damage variable (d_6) for ECF 73 . . . 122
6.4 Damage map assessment considering the effect of paint thickness on delamination (d) for ECF 73 . . . 123
6.5 Damage map assessment considering the effect of paint thickness for the damage variable in the longitudinal direction (d_1) for ECF 195 . . . 136
6.6 Damage map assessment considering the effect of paint thickness for the damage variable in the transverse direction (d_2) for ECF 195 . . . 137
6.7 Damage map assessment considering the effect of paint thickness for the shear damage variable (d_6) for ECF 195 . . . 138
6.8 Damage map assessment considering the effect of paint thickness on delamination (d) for ECF 195 . . . 139

7.1 Waveform parameters for 26.8/48.5 µs, 96.4 kA . . . 144
7.2 Waveforms parameters for peak current variation cases . . . 145
7.2 Waveforms parameters for peak current variation cases . . . 145
7.3 Root radius parameters for waveform alternatives to assess peak current influence for ECF 73 . . . 146
7.3 Root radius parameters for waveform alternatives to assess peak current influence for ECF 73 . . . 147
7.4 Cylindrical shock wave parameters for waveform alternatives to assess peak current influence for ECF 73 . . . 149
7.5 Damage map assessment for damage variable in the longitudinal direction (d_1) for waveform alternatives to assess peak current influence for ECF 73 . 155
7.6 Damage map assessment for damage variable in the transverse direction (d_2) for waveform alternatives to assess peak current influence for ECF 73 156
7.7 Damage map assessment for shear damage variable (d_6) for waveform alternatives to assess peak current influence for ECF 73 . . . 157
7.8 Damage map assessment for delamination (d) for waveform alternatives to assess peak current influence for ECF 73 . . . 158
7.9 Root radius parameters for waveform alternatives to assess peak current influence for ECF 195 . . . 159
7.9 Root radius parameters for waveform alternatives to assess peak current influence for ECF 195 . . . 160
7.10 Cylindrical shock wave parameters for waveform alternatives to assess peak current influence for ECF 195 . . . 162
7.11 Damage map assessment for damage variable in the longitudinal direction (d_1) for waveform alternatives to assess peak current influence for ECF 195 168
7.12 Damage map assessment for damage variable in the transverse direction (d_2) for waveform alternatives to assess peak current influence for ECF 195 169
7.13 Damage map assessment for shear damage variable (d_6) for waveform alternatives to assess peak current influence for ECF 195 . . . 170
7.14 Damage map assessment for delamination (d) for waveform alternatives to assess peak current influence for ECF 195 . . . 171
7.15 Waveform parameters for for different action integrals . . . 172
7.15 Waveform parameters for for different action integrals . . . 173
7.16 Root radius parameters for waveform alternatives to assess action integral influence for ECF 73 . . . 174
7.16 Root radius parameters for waveform alternatives to assess action integral influence for ECF 73 . . . 174

7.17 Cylindrical shock wave parameters for waveform alternatives to assess action integral influence for ECF 73 . . . 176
7.18 Damage map assessment for damage variable in the longitudinal direction (d_1) for waveform alternatives to assess action integral influence for ECF 73 183
7.19 Damage map assessment for damage variable in the transverse direction (d_2) for waveform alternatives to assess action integral influence for ECF 73 184
7.20 Damage map assessment for shear damage variable (d_6) for waveform alternatives to assess action integral influence for ECF 73 . . . 185
7.21 Damage map assessment for delamination (d) for waveform alternatives to assess action integral influence for ECF 73 . . . 186
7.22 Root radius parameters for waveform alternatives to assess action integral influence for ECF 195 . . . 187
7.23 Root radius parameters for waveform alternatives to assess action integral influence for ECF 195 . . . 188
7.24 Cylindrical shock wave parameters for waveform alternatives to assess action integral influence for ECF 195 . . . 190
7.25 Damage map assessment for damage variable in the longitudinal direction (d_1) for waveform alternatives to assess action integral influence for ECF 195 196
7.26 Damage map assessment for damage variable in the transverse direction (d_2) for waveform alternatives to assess action integral influence for ECF 195197
7.27 Damage map assessment for shear damage variable (d_6) for waveform alternatives to assess action integral influence for ECF 195 . . . 198
7.28 Damage map assessment for delamination (d) for waveform alternatives to assess action integral influence for ECF 195 . . . 199

8.1 Waveform parameters for the waveform 1.42/44.3 µs, 96.4 kA . . . 208
8.2 Root radius parameters for the waveform 1.42/44.3 µs, 96.4 kA . . . 209
8.3 Cylindrical shock wave parameters for the waveform 1.42/44.3 µs, 96.4 kA . 211
8.4 Waveform parameters for 3.18/34.5 µs, 100 kA . . . 218
8.5 Root radius parameters for 3.18/34.5 µs, 100 kA . . . 219
8.6 Cylindrical shock wave parameters for 3.18/34.5 µs, 100 kA . . . 221
8.7 Waveform parameters for 4/34 µs, 110 kA . . . 228
8.8 Root radius parameters for 4/34 µs, 110 kA . . . 229
8.9 Cylindrical shock wave parameters for 4/34 µs, 110 kA . . . 231
8.10 Waveform parameters for 5/23.6 µs, 110 kA . . . 238
8.11 Root radius parameters for 5/23.6 µs, 110 kA . . . 239
8.12 Cylindrical shock wave parameters for 5/23.6 µs, 110 kA . . . 241
8.13 Waveform parameters for 6/51 µs, 90 kA . . . 248
8.14 Root radius parameters for 6/51 µs, 90 kA . . . 249
8.15 Cylindrical shock wave parameters for 6/51 µs, 90 kA . . . 251
8.16 Waveform parameters for 7/35 µs, 90 kA . . . 258
8.17 Root radius parameters for 7/35 µs, 90 kA . . . 259
8.18 Cylindrical shock wave parameters for 7/35 µs, 90 kA . . . 261
8.19 Longitudinal damage induced by alternative waveforms within the range specified by the SAE ARP 5412 standard . . . 269
8.19 Longitudinal damage induced by alternative waveforms within the range specified by the SAE ARP 5412 standard . . . 270
8.19 Longitudinal damage induced by alternative waveforms within the range specified by the SAE ARP 5412 standard . . . 271

8.20 Transverse damage induced by alternative waveforms within the range specified by the SAE ARP 5412 standard 272
8.20 Transverse damage induced by alternative waveforms within the range specified by the SAE ARP 5412 standard 273
8.20 Transverse damage induced by alternative waveforms within the range specified by the SAE ARP 5412 standard 274
8.21 Shear damage induced by alternative waveforms within the range specified by the SAE ARP 5412 standard 275
8.21 Shear damage induced by alternative waveforms within the range specified by the SAE ARP 5412 standard 276
8.21 Shear damage induced by alternative waveforms within the range specified by the SAE ARP 5412 standard 277
8.22 Delamination induced by alternative waveforms within the range specified by the SAE ARP 5412 standard 278
8.22 Delamination damage induced by alternative waveforms within the range specified by the SAE ARP 5412 standard 279
8.22 Delamination damage induced by alternative waveforms within the range specified by the SAE ARP 5412 standard 280

Part I

Introduction

Chapter 1

Introduction

1.1 Problem statement

Lightning is a natural phenomenon as a consequence of the electrical activity of thunderclouds. In particular, aeronautics is affected with this phenomenon, leading to a safety hazard for aircraft structures.

In recent years, replacing metallic materials with composite materials in aeronautics is increasing. Examples such as Boing 787 or Airbus A350 make use of composite materials in around 50% of the aircraft weight, being intensively employed, for example, in the the fuselage, wings, and fuel tanks. This transition comes from unique features of composite materials, beneficial in comparison with traditional metallic materials. The high strength- and stiffness-to-weight ratios allowed a reduction of the airframe weight and, therefore, an increase in fuel efficiency and reduced pollution and acoustic emissions, and a reduction of maintenance requirements.

By the inherent characteristics of metallic airframes, the aircraft structures can easily support a lightning strike due to their high electrical conductivity that will dissipate the current without any major damage. On the other hand, carbon fibre composites have lower thermal and electrical conductivity than metals, thus resulting in higher vulnerability to lightning effects.

The introduction of composites has a strong impact in the lightning certification strategy for aircraft programs. Consequently, lightning tests are performed to assess the damage and to confirm a continuous safe flight and landing after severe lightning strike. However, these test campaigns are very expensive and time consuming, and must be replicated for coupon specimens as well as sub-assemblies.

One important step in the validation is the implementation of additional lightning protection solutions to create a conductive surface on the composite structure, typically using a metallic mesh on the external layer. Therefore, the implementation of these protection measures and their certification has an impact on the weight, on the design and manufacturing costs and on program delays.

Considering the expensive design, manufacturing, testing and certification processes, there is a progressive need for reliable computational models to increase the knowledge and predict the effect of lightning arcs on protected composite structures. Experimentally

validated numerical models that rely on the available experimental databases can be used to improve and optimize an aircraft structure and implemented towards virtual certification procedures.

1.2 Background

The use of lightweight carbon fibre reinforced composite materials in aircraft structures has been growing. Aluminium airframes are being progressively replaced with carbon fibre reinforced polymers (CFRP).

Aerospace companies spend a large amount of resources to ensure a safe design to the aircraft structures, with costs in the order of hundreds of million dollars [1]. Aiming to reduce the cost of assessing new configurations, multiple conservative safety factors and major inspection requirements are currently used, compromising the potential of composite materials.

Consequently, the process of validating the structural integrity of composite materials requires experimental tests combined with fatigue and fracture mechanics analyses. The safe-life analysis, guaranteeing an adequate life during its entire operation, requires a large amount of testing.

These tests are costly and time consuming, so there is an incontestable necessity to develop accurate analytical and numerical tools able to predict the mechanical response of composites. Advances in computational methods are key to the introduction of reliable analysis techniques in the current design and certification process. However, numerical models that predict the initiation and propagation of damage in composite materials need to properly account for the micro-structural mechanisms and their association to the material responses [2], typically based on progressive damage models [3].

A drawback of conventional composite laminates is the low impact resistance, leading to damage that remains undetectable by an outside visual inspection. Lightning strikes induce mechanical and thermal-mechanical loads that can be evaluated as conventional dynamic events, similarly to other impact events [4].

The excessive reliance on testing at all stages, from design and development, to certification and in-service inspection and repairs, encourage the development and improvement of numerical models to predict damage and to support the reliability and safety requirements of aerospace structures.

1.3 Objectives

The development of reliable models that accurately predict the main effects of lightning strikes in the context of damage tolerance criteria are essential in the current panorama of the aeronautical industry. As the industry moves towards hybrid experimental/numerical design and certification processes, these models need to be improved to support the industry.

Some specific aspects related to the effect of lightning strikes need to be assessed to contribute to the development of virtual certification. Therefore, the purpose of this work is the numerical analysis of the effect of the lightning parameters of simulated lightning strikes and of the effect of paint thickness on the damage induced on a protected carbon-fibre reinforced composite plate. The numerical analysis is performed using the Finite Element Method supported by semi-analytical models of the mechanical loads induced by lightning strikes.

1.4 Thesis layout

In Part II, the state-of-art and literature review is presented. The lightning phenomenon is introduced as well as the aircraft lightning certification proposed by civil certification authorities. A summary of the lightning strike damage to composite materials is presented, followed by a theoretical foundation of the basis of the models used in this study.

In Part III, the mechanical loads induced by a lightning strike event are presented. The finite element and constitutive models are described and validated using experimental data.

Part IV presents the numerical studies performed during this work: (i) to evaluate the use of the strong shock wave approximation to describe the shock waves generated by the expansion of the plasma channel, Computational Fluid Dynamics (CFD) computations are performed and compared with the analytical approximation; (ii) to assess the effect of paint thickness on the damage occurring during a lightning strike event on a protected carbon-fibre reinforced composite plate, simulations are performed considering different thicknesses of the paint layer and their effects; (iii) to evaluate the influence of the lightning parameters on the damage induced by a lightning strike, a parametric study is performed by comparing the results considering different peak currents and different action integrals.

In Part V, a case study is conducted to understand the application domain of the SAE aerospace recommended practice for lightning strike testing of aeronautical structures. A detailed sensitivity analysis is conducted considering six waveforms covering the testing domain of this standard to understand whether changes within the recommended lightning parameters lead to any significant change in the damage footprint in protected composite laminates..

Part VI presents the conclusions of the study carried out in this thesis, together with recommendations of future work for a better understanding and modelling of the damage occurring during lightning strike events on protected carbon-fibre reinforced composite plates.

Part II

State-of-art and literature review

Chapter 2

State of art

Contents

2.1 Lightning phenomenon

2.2 Aircraft lightning certification

2.2.1 Current waveforms

2.2.2 Zoning

2.3 Induced damage

2.3.1 Direct effects

2.3.2 Indirect effects

2.4 Laboratory tests

2.5 Lightning strike damage to composite materials

2.6 Modelling strategies

2.7 Conclusion

Objectives
This chapter describes the lightning strike phenomenon and its impact on aircraft certification used by aircraft manufacturers and aeronautical companies.
A theoretical approach to the damage induced to aircraft composite structures is presented. It explores the influence of several parameters inherent to a lightning strike event, supporting an understanding of the effects and the contributors to damage.

2.1 Lightning phenomenon

Lightning is a natural and atmospheric transient phenomenon that generates a high current and high voltage discharge, generating a path length and attempts to equalize regions of opposite electrical discharge [5; 6].

Lightning events can be classified depending on the regions between which the lightning takes place and the polarity of the charge transferred from one region to another [6; 7].

Intracloud lightning (IC): Lightning between two charged regions within a cloud, it is the most common.

Intercloud lightning (CC): Lightning between opposite charged regions of two different clouds.

Cloud-to-ground lightning (CG): Lightning between cloud and ground. This category can be divided in two subcategories by the polarity of the transported charges:

Negative ground lightning (-CG): Lightning flashes that strike ground come from the negative charged regions of clouds.

Positive ground lightning (+CG): Lightning flashes that strike ground come from the positive charged regions of clouds.

Figure 2.1 illustrates the different types of lightning flashes.

A lightning strike is due to the polarization of a cloud which unloads its excess of charges, which initiates an ionized channel of low current, called a leader. Under the effect

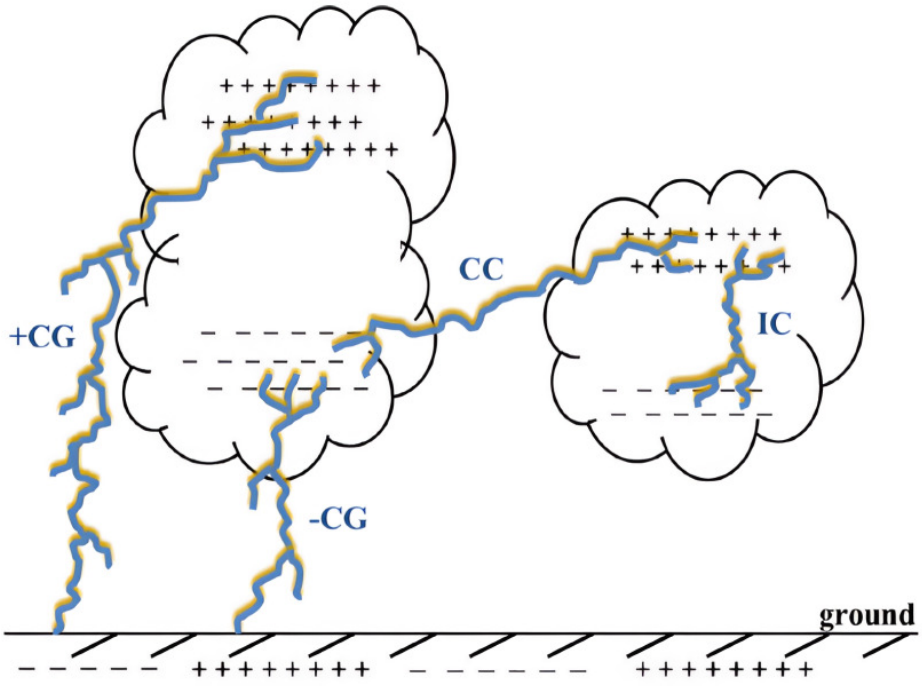


Figure 2.1: Different types of lightning flashes [8]

of this leader, the second region will also form a leader as a response that propagates in zigzag steps and possibly branches.

Subsequent strokes can be originated by the presence of multiple centres of charges in the cloud, forming a succession of discharges in the lightning event. The rise time is extremely short, about a few microseconds, and the decay time a few tens of microsecond. Between the different strokes, a lower current could be generated, named an intermediate current. At the end of the lightning flash, a continuous current remains.

The most regular scenario is due to the presence of an aircraft which is called triggered lightning, where the aircraft is the one which initiates the leader. Most of the lightning strikes happen during ascending and descending phases of the airplane, corresponding to intra-clouds strikes, the less dangerous.

Despite the increasing interest to this problem, the damage mechanisms related to lightning strikes and the structural response of the aircraft remain undetermined.

2.2 Aircraft lightning certification

The average probability of a lightning strikes an aircraft is about once to twice a year, for a commercial airliner. This represents one strike every 1000 to 10000 flight hours, shown by statistical analysis [9]. Nevertheless, this possibility depends on several factors such as geographical location, flight profile or type of aircraft.

A lightning strike on an aircraft is a hazard that needs to be consider when designing the aircraft once it could compromise the safety of the flight. Therefore, the design stages are based on certification methods that guarantee the aircraft's holding to an upper-bound lightning strike. Civil certification authorities, such as EASA (European Aviation Safety Agency) and FAA (Federal Aviation Administration), introduces basic recommendations to protect aircraft against catastrophic effects of lightning. Standard committees, such as EUROCAE (European Organization for Civil Aviation Equipment) and SAE (Society of Automotive Engineers), establish guides and normative documents that explain how to achieve these recommendations [10].

FAA and EASA have issued compulsory standards to define design criteria, FAR-25 [11] and CS-25 documents [12]. The FAR-25 contains basic regulations, and any additional material is contained within AC's (Advisory Circulars). The CS-25 1 contains certification specifications which are standard technical interpretations of the essential airworthiness requirements. The book is divided in subparts, being the subparts the B (Flight), C (Structure) and D (Design and Construction) the most important for loads and aeroelasticity concerns.

According to these guidelines' documentation, an evaluation of the strength, detail design and fabrication must show that catastrophic failure due to fatigue, corrosion or accidental damage will be avoided throughout the operational life of an airplane. The determination of structural properties or selected a material for aircraft requires a considerable amount of testing. This is a time-consuming task and costly, so virtual testing can be used to reduce the physical tests and determine allowable limits.

Some of the categories of material related airworthiness requirements are static strength, for example the capability to resist gust or manoeuvre, endurance, emergency landing, flutter, and accidental hazards, such as fire, lightning strikes, bird impact, accidental tool drop and fuselage impact.

Therefore, the aircraft lightning certification can be divided into three steps:

1. Definition of an idealized lightning environment, in particular defining a set of current components specifying a standardized current waveform.

2. Definition of the lightning strike zones on the aircraft, which are associated to the risk level of lightning strikes and the corresponding current intensities.

3. Definition of direct effect testing on materials, equipment, systems, and structures.

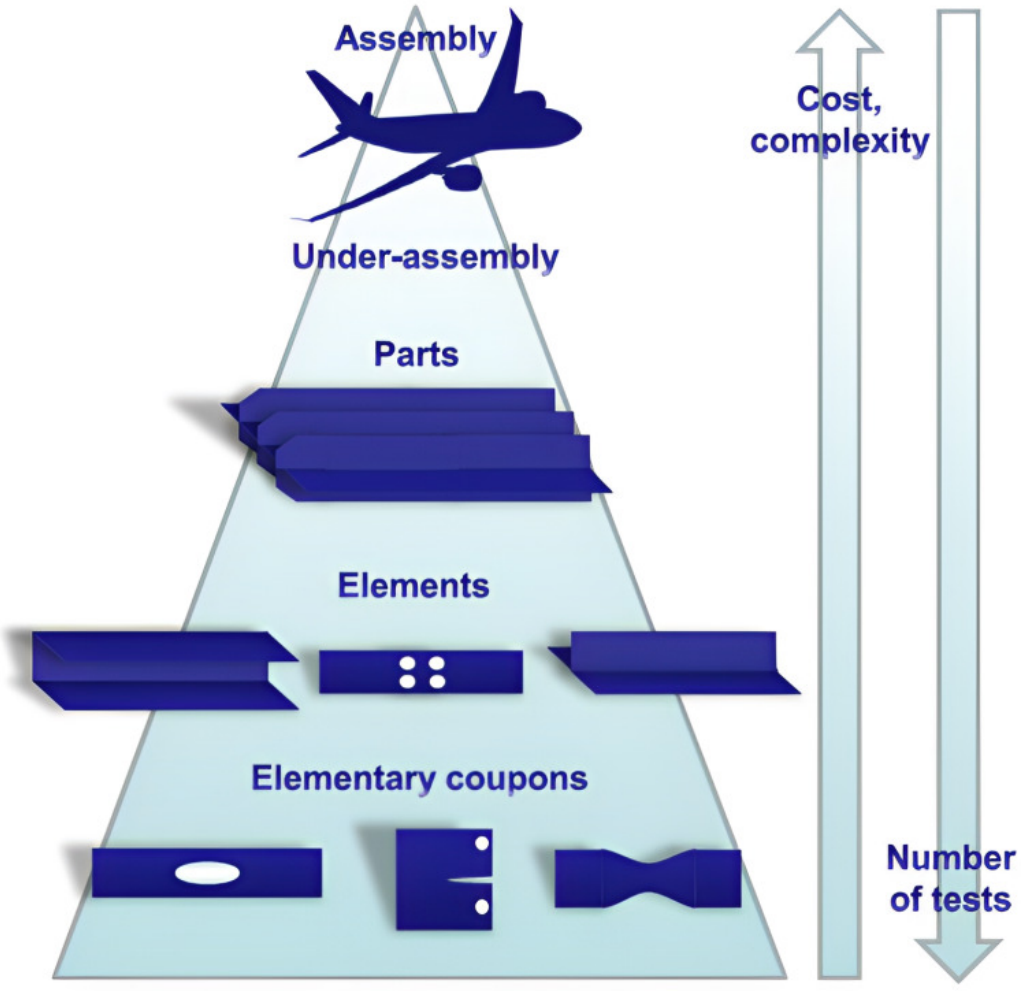


Figure 2.2: Building-block approach in composite certification [13]

2.2.1 Current waveforms

Taking into consideration that lightning is a natural phenomenon, the current levels and waveforms differ in the different lightning strikes. NASA (National Aeronautics and Space Administration – United States Government), FAA (Federal Aviation Administration – United State Department of Transportation) and aerospace industry work together to create a recommended procedure for aircraft lightning environment, the SAE ARP 5412 [14], for aircraft analysis and testing. This report is internationally considered as the unique standard concerning the lightning threat, determining the environment and levels which represent the minimum required by the certifying authorities.

This aerospace recommended practice introduce several current waveforms that depending in the lightning type. These current waveforms were obtained by available lightning data and analysis in order to represent the lightning environment, and to give upper bounds of the direct effects of lightning on aircraft.

Lightning is composed of an initial stroke, an impulse and a continuing current [15]. The lightning current waveform is defined by a composition of four current components, named A, B, C and D, and the Multiple Stroke (MS) and Multiple Burst (MB) waveform sets, which represent idealized environments whose effects upon aircraft are those expected from natural lightning. [5; 14].

The current wave is defined by the following parameters:

1. The intensity peak of the current.
2. The rise and descent times of the wave front.
3. The electrical load transferred equals to $\int i\,dt$).
4. The action integral equals to $\int i^2\,dt$ which represents the ability of the current to deposit energy on a resistive object.

Each component represents a different phase from the current of blasting [14] [16]:

Component A: Current of the first return stroke.

This component has a peak intensity of 200 kA ± 10%, an action integral of 2×10^6 A^2s ± 20% and a total duration of 500 µs at the maximum. The rise time from 10% to 90% of the peak value must be smaller than 50 s.
This component can cause damage by direct effects or indirect effects.

Component B: Intermediate current.

This component has an average amplitude of 2 kA ± 20% and an electrical load transferred of 10 C ± 10% during 5 ms ± 10%.
This component corresponds to a transition phase of the discharge.

Component C: Continuous current.

This component transfers an electrical load of 200 C ± 20% during a time between 0.25 and 1 second, with intensity from 200 to 800 A.
This component of limited amplitude can cause very important damages (in particular thermal ones) because of large quantity of electrical charges that it deposits.

Component D: Current of the subsequent return stroke.

This component has a peak intensity of 100 kA ± 10%, an action integral of 0.25×10^6 A^2s ± 20% and a total duration of 500 µs at the maximum. The time from 10% to 90% of the peak value must be smaller than 25 µs.
This component can cause damage by direct effects or indirect effects.

Aiming to examine and report the testing material resistance to impact of a lightning strike on aircraft parts and structures, manufacturers and researchers have to lead campaigns where subject a material to this standardized lightning strike. Although there is not any specific norm about all the parameters to consider during these tests to evaluate and certify appropriate behaviour of aircraft parts to lightning direct effects and/or indirect effects, generally guidelines as EUROCAE or SAE are used [5; 14].

2.2.2 Zoning

The distinct segments of an aircraft have non-identical probability to be exposed to different lightning current components, due to the lightning sweep stroke phenomenon. Factors as the local geometry and nature of the surface, the air flow or the current waveform influence the dwell time at each attachment point.

Since there are some regions on the aircraft where lightning is unlikely to attach, and others which will exposed to attachment for only a small portion of the total flash duration, it is appropriate to define the zones on the aircraft surface which will be exposed to different components of the flash and therefore receive different types and degrees of effects.

The classification of these zones is established by aircraft designer by reference to past in-flight experience of similar design or with the aid of lightning strike tests on scale models. The classification by a map zone of the structure, dividing the plane into different sections according to the impacted component of the lightning, represent a certification

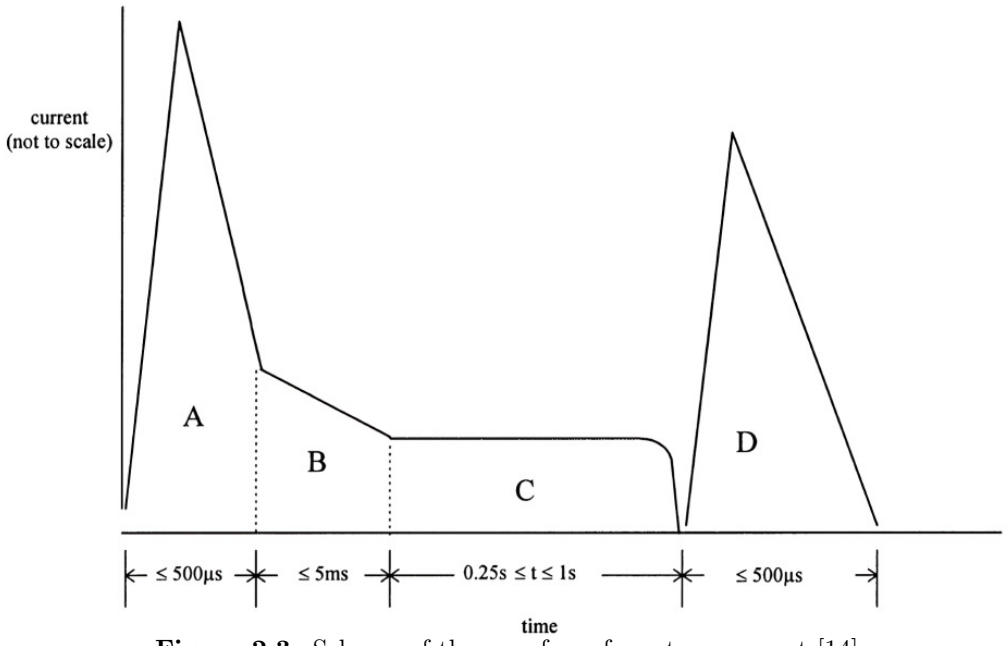


Figure 2.3: Scheme of the waveform for return current [14]

step on the regulation and allows to predict the susceptible zones, assistance the selection of more convenient protections to the structure.

The zones are defined with a number and a letter, regarding to their propensity to cause attachment and/or sweeping. The first label, numbered by 1 to 3, indicates the cause of the presence of the arc: (i) attachment for zone 1; (ii) sweeping regarding to zone 2; (iii) or neither of them to zone 3.

Supplementing the first label are linked a letter to describe the ability of the arc to sweep, if zone A, or to dwell, for zone B. In a simple way, classified as zone A if the time of stagnation of the arc root will be short, or zone B if the time of stagnation will be long. It could be included the letter C for a transition zone, mostly used in the literature.

Therefore, an airline can be divided into six zones. These zones are [5; 14; 17]:

Zone 1A: First Return Stroke Zone.

All areas of the airplane surfaces where a first return is likely during lightning channel attachment with a low expectation of flash hang on.
The current sequence associated to these zones is components A, B and C* (component C* is a shorter C-component associated to the dwell time and the surface coating).

Zone 1B: First Return Stroke Zone with Long Hang-On.

All areas of the airplane surfaces where a first return is likely during lightning channel attachment with a high expectation of flash hang on.
Those zones are subjected to the total standardized current sequence, component A, B, C and D.

Zone 1C: Transition Zone for First Return Stroke.

All areas of the airplane surfaces where a first return stroke of reduced amplitude is likely during lightning channel attachment with a low expectation of flash hang on.
The current sequence associated to this zone is component Ah, B and C* (component Ah is a reduced A-component associated to swept leaders at flight altitudes between 1500 and 3000 m).

Zone 2A: Swept Stroke Zone.

All areas of the airplane surfaces where a first return of reduced amplitude is likely during lightning channel attachment with a low expectation of flash hang on.
The current sequence associated to these zones is component B, C* and D.

Zone 2B: Swept Stroke Zone with Long Hang-On.

All areas of the airplane surfaces into which a lightning channel carry subsequent return stroke is likely to be swept with a high expectation of flash hang on.
The current sequence associated to these zones is component B, C and D.

Zone 3: Current Conduction Zone (Strike locations other than Zone 1 and Zone 2).

> Those surfaces not in Zone 1A, 1B, 1C, 2A, or 2B, where any attachment of the lightning channel is unlikely, and those portions of the airplane that lie beneath or between the other zones and/or conduct a substantial amount of electrical current between direct or swept stroke attachment points.

The majority parts subjected to an impact of lighting strike are the radome, a blister which is located at the level of the aircraft nose section, the wing-tips and the tail planes as well as the jet engines.

Lightning zoning test have the purpose of verify the resistance of the material. These tests are an integral part of the certification process nowadays, indicating that the aircraft is effectively protected from direct effects of lightning. Thus, this process provides the aircraft's manufacturer adapt the design of each zone and certify that different parts are resistant to the several components of the lightning current waveform.

In the current aerospace context, processes such as electrostatic field analysis and numerical simulations combined are used to perform lightning zoning certification. Analytical methods, like rolling sphere, are in lack of use.

One of the most current approaches considers the finite conductivity of the materials, which is important for CFRP structures, and the time-dependent behaviour of the external field.

2.3 Induced damage

Lightning strikes induce various effects on an aircraft. Both attachment and high current phases cause stresses and undesirable effects on the aircraft, that are generally divided into two categories, direct effects and indirect effects.

Figure 2.5 summarize the various damage mechanisms during a lightning strike impact.

There are three main mechanisms explaining the lightning strike heating [18]:

1. Thermal radiation from the plasma channel, which is absorbed by the surface surrounding the arc root.

2. Heat transfer from the plasma channel, inside the arc root.

3. Resistive Joule heating by the current flow in the material.

An explosive partial vaporization of the lightning protection layer as well as vaporization of the resin impregnating the first plies of the laminate are consequence of the rapid heat generation. In case of unprotected composite structures, this explosion is confined inside the composite.

The different phenomena relating to lightning strike heating provoke overpressure on the structure, which causes delamination, fibre and matrix cracks in CFRP structures.

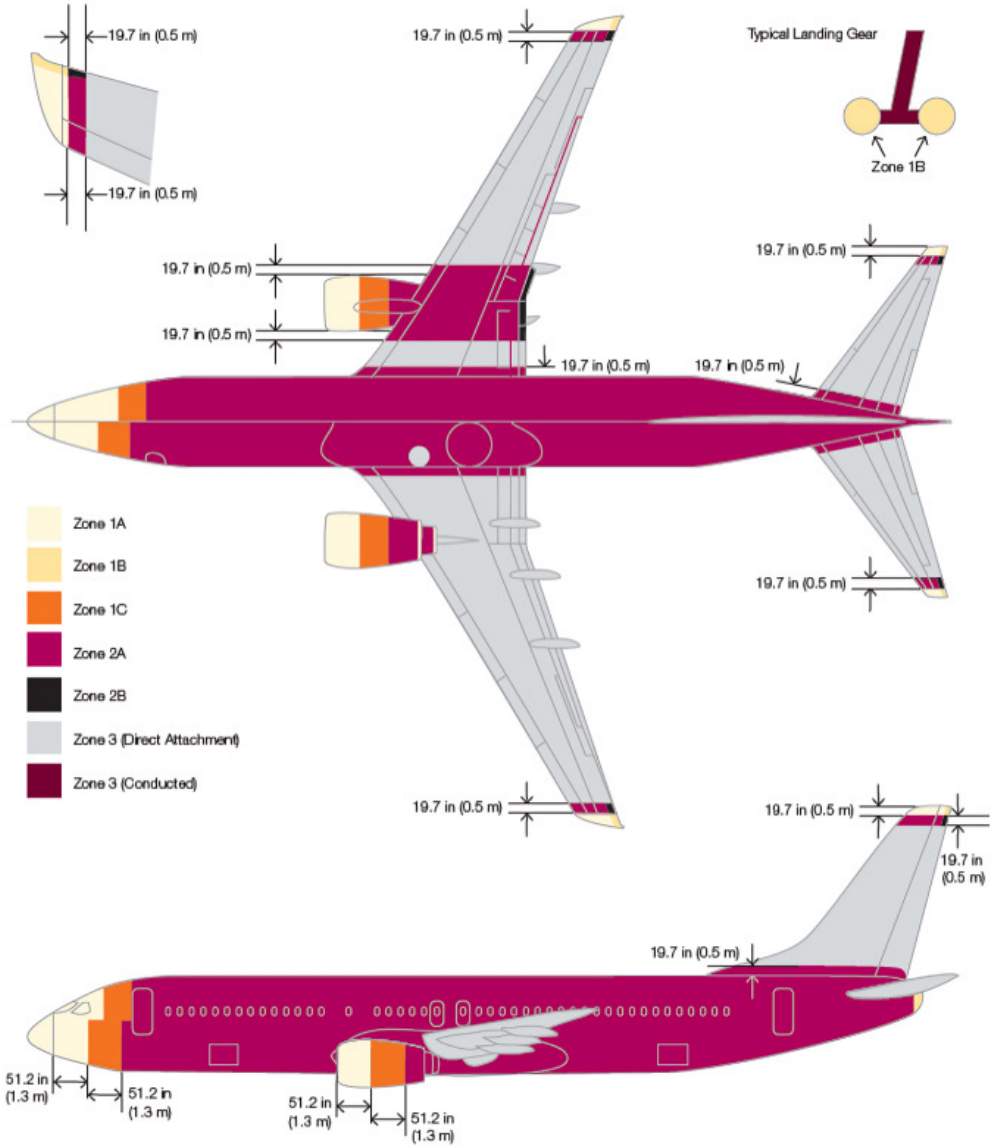


Figure 2.4: Airplane lightning zones [17]

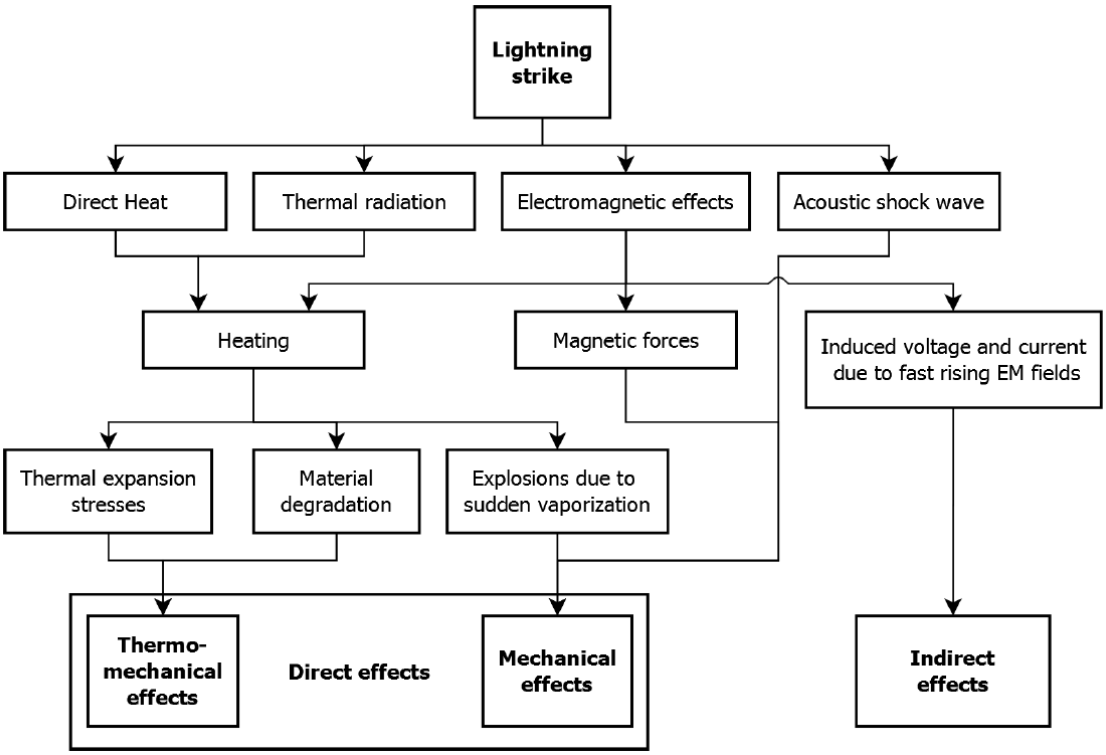


Figure 2.5: Damage mechanisms induced by a lightning strike [18]

Acknowledging the produced effects by the lightning strikes, it is recognised that the most severe damage to composites is caused by mechanical effects in the transient lightning components, especially due to the explosion of the protection layer [19; 20].

2.3.1 Direct effects

The direct effects of the lightning are associated with physical damage to structures and external devices due to the interaction of the electrical arc of the lightning and the structure. These effects induce electrical, thermal and mechanical damage to the composite at the attachment points of the arc on the structure, where the current is the most concentrated and intense.

Since the lightning is a complex phenomenon involving a thermal flow, magnetic pressure and acoustic waves, it is a major concern. CFRP composites have poor electrical and thermal conductivity, thus being susceptible of structural damage. The surface burns and leads to explosion of the laminate, causing break-up of the fibres around the attachment point and delamination of the composite material.

These effects can be divided in two main categories, thermal and mechanical effects.

Thermal effects originate from the fast increase in temperature of the material. They depend on the intensity of the current, so they are particularly important at the attachment points and other parts of the aircraft of high current flow.

These effects have three main sources, which can cause erosion, deformation, melting or puncture of the fuselage [21].

The first thermal effect corresponds to the heat dissipation by the Joule heating.

Another effect arises from the direct heat flux from the arc, including the heat flux by conduction and by electron or ion recombination.

The last source is the radiative flux emitted by the lightning channel.

Mechanical effects are particularly important during the current peaks. This can lead to failure, delamination and puncture of the aircraft materials. Similar to thermal effects, they occur at the attachment points and other parts of the aircraft of high current flow.

These effects have three main sources too:

The first mechanical effect is the overpressure due to the explosion in the lightning channel, which leads to the propagation of a strong shock wave in the radial direction of the arc. The explosion comes from the fast increase in the arc temperature in the channel, up to 30 000 K, within a time interval of a few microseconds [21].

Another effect is the magnetic force induced by the current circulation. The internal pressure of the arc column is reinforced by the concentric magnetic force, magnetic pinch, and the current owing in the structure which acts as an additional mechanical constraint on the skin, magnetic pressure.

The last source is the expansion due to the fast increase in temperature of material yields, leading to an additional contribution to the mechanical stress [21].
Although with less impact, other effects like dielectric breaking at the lightning attachment point or sparking at junctions and fasteners are included in the mechanical effects.

The different effects that occur at the attachment point are shown in figure Figure 2.6.

2.3.2 Indirect effects

Indirect lightning effects involve the electromagnetic (EM) effects following a lightning strike. This could be summarized as the interaction of high electromagnetic fields with electrical/electronic equipment in the aircraft, producing a phenomenon called EM coupling.

Direct effects of lightning are mostly applied at the entry point, with a large amplitude current injected. Besides the mechanical-effects and thermal-effects at the attachment point, the electric current then circulates over all electrically conducting parts of the structure until it finds the exit point. The current flow in the external surfaces and in the inner parts, this redistributed over the entire structure is called the induced current.

Although the significant damages drive from direct effects, indirect lightning can itself produce damage concerned with mechanical and thermal effects.

There are three main effects from the indirect lightning effects. [16; 22].

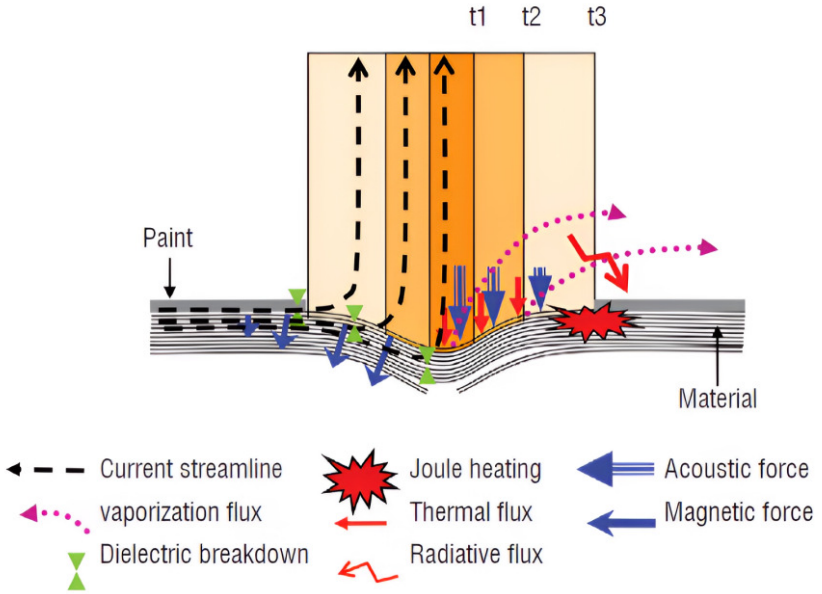


Figure 2.6: Illustration of the various direct effects at the attachment point [21]

Thermal effects: The induced current which flow through the structure increase the temperature along the path to the exit point. Thus, the current concentration lead to a intensive heating of the mechanical parts during the current flow.

Electrical discharges: During the circulation of the current along resistive and inductive paths, the electrical potential of the system's parts varies. Electrical breakdown and production of electrical discharges can be a consequence of this changes. These electrical discharges can occur in the vicinity of rivets and junctions between material parts and are particularly serious when occurring in fuel tanks [22].

Effects at electronic equipment level: The induced current can reach equipment connectors. This current flowing along cables results in dysfunction of electronic equipment, even though the mechanical and thermal effects, by a difference of potential on impedant systems. These currents are a main concern in Electromagnetic Compatibility (EMC) field, explaining the classification of an EM effect.

2.4 Laboratory tests

Aeronautical companies make use of laboratory test campaigns to assess the material resistance to a lightning event.

In order to study the consequences of a lightning strike on materials, high current tests, commonly designated by direct effects tests, are used. This requires experimental simulation in a laboratory employing the standardized current waveform according to the zoning defined previously. There is a recommended procedure for lightning tests following guidelines and norms defined by EUROCAE or SAE [5; 14].

This laboratory tests are very expensive, so the sample considered is not a real aircraft component but a flat sample with the minimum number of plies for the composite design to be validated.

The lightning arc is created between two electrodes, similar to the discharges in the lightning event. One is formed by the aeronautical object under test. The other, called jet diverter electrode is formed by a rod that is away from the panel, where the lighting current injected is initiated by a metallic wire.

Since the parameters during the test do not follow a fully standardised regulation of the test setup, the mechanical clamping and the electrical bonding of the sample can vary from one lab to another.

The most common and hazardous component current waveform for composite structures is component D. The impulse generated by the experimental test must be controlled and is frequently a component D to create a reliable situation. Nevertheless, components A, B and C can also be used. In order to generate such intensities or currents, HVG (High Voltage Generator) or HCG (High Current Generator) are used.

As a consequence of the high current intensity and temperatures reached by electric arc, the possible equipment to extract quantitative real-time data is very restricted. The available data come from the rear face of the sample where the displacement and the velocities during the electric shock could be measure.

To measure real-time deflection during the strike, Velocity Interferometer System for Any Reflector (VISAR) are used, such a technique allowing covering a velocity range of $10\,\mathrm{cm\,s^{-1}}$ to $3000\,\mathrm{m\,s^{-1}}$ with a precision better than 1%. An important analysis to performed after a lightning test is evaluate the delamination area. The most conventional method is an ultra-sonic scan, a Non-Destructive Test.

The lightning damage mechanism is complex and difficult to predict by the several physics phenomenon involved. Thus, these experimental tests during the development phase of aircraft program should be only used for the certification of the design.

2.5 Lightning strike damage to composite materials

Aircraft design is increasingly based on Carbon Fibre Reinforced Plastic (CFRP) composite structures. Nowadays, several parts of the aircraft, such as fuselage, wing boxes or structural spars, used composite materials in order to reduce the overall weight and additional fuel savings by their inherent characteristics of high strength and stiffness [8].

These components are highly exposed to lightning strikes, establishing new challenges in the design of aircraft structures. [15; 19]. Since the CFRP composites have low conductivity to electrical currents and temperature, it lead to the initiation and growth of structural damage.

In a CFRP, the electric conductivity highly depends of the direction of the carbon fibres. [23]. The electrical conductivities is generally defined by three values: (i) the parallel conductivity, in the direction of fibres, (ii) the transverse conductivity, transverse to fibres, but in the same ply and (iii) the perpendicular conductivity, transverse to fibres, directed between different layers. This dependence of the conductivity with the fibre directions could increase the resistivity of the material and consequently an increase of the thermal

constraints.

Lightning strikes are a possible origin of internal damage related to aircraft, which is an inconvenient of composite materials. This type of damage, like delamination and matrix cracks, develop significant strength degradation of the structure. Due to the complex multi-physical phenomenon relatable to an impact by lightning strikes, involving different thermal and mechanical constraints, it is difficult to predict damage induced to composite structures [24–26].

Two distinct categories of direct effects can be recognised, surface and bulk damage. In a brief resume, surface damage is induced by thermal effects mainly on the metallic protection, while bulk damage is induced by mechanical stresses propagating through the material [4].

Surface damage is based in a thermal model, involving heating, melting or vaporization of the metallic protection. Due to the Joule effect phenomenon and heat transfer from the plasma arc, fibre fracture, splitting, bulging, ply-lift and resin vaporization occur. This damage is confined to the surface and in the vicinity of the lightning attachment point [15; 24].

Bulk damage are expressed as fibre-resin debonding, transverse cracks, fibre rupture and ply delamination [25; 28]. The two main sources for this damage are the eletro-magnetic forces, also know as Laplace force, and mechanical forces due to air and surface explosion shock waves and explosive damage of the resin [20; 29]. These are the major contribution in the damage induced by lightning strikes.

There is a relation between the intensity of current and the damaged area. Feraboli et al. demonstrate that for high-energy current strikes, 50 to 200 kA, the composite revealed pronounced detectable damage. For intermediate energy strike, 30 to 50 kA, some visible damage occur and repairs will be required. Finally, for low-energy current strikes, 10 to



Figure 2.7: Damage due to lightning strikes on aircraft composite structure [27]

30 kA, non or barely visible damage is noted and no repairs are needed [15] (See Figure 2.8).

Summary, the damage observed in the composite after lightning can be divided in:

Fibre breakage and fibre damage, also known as **tuft** too, is mainly due to the shockwave induced by lightning strikes. The shockwave transmits a huge energy to the impacted surface, leading to an energy rises that dissipate as heat by Joule effect. The heating causes carbon fibres' sublimation that propagates through the laminate's thickness. The inner damage includes pyrolysed fibres, vaporized resin, and traces of inter and intra-ply arcing [15; 30].

Resin deterioration is the combined effect of the resistive heating of the surface layer and high atmospheric temperature due to insulation breakdown of air. [24]. This deterioration could lead to additional explosion with gas release.
Atmospheric temperature around the ionized leader channel of a natural lightning strike can heat up to 30 000 K which is fifty times higher that the pyrolysis temperature for conventional epoxy resin, 600 K [24].
The resin pyrolysis release gas inside the composite and its evaporation is responsible for the characteristic explosive fracture in the vicinity of the lightning attachment point [16].

Delamination is a critical failure of the material. Since the fibres have good conductivity compared to the resin matrix, the lightning current propagates along fibre direction. Thus, it generates Joule heating leading to a serious damage in the interfacial adhering of the matrix with its nearby fibres.
This damage is related to the shock wave and explosion on the surface that leads to a high overpressure induced by the vaporization of the materials [25]. Since the interlaminar fracture toughness caused by thermal decomposition of the matrix resin, delamination can progress fluently [28].
These coupled phenomena lead to a loss of mechanical properties of the structure, which could loss the resistance to sustain flight loads and their integrity compromise, affect flight safety.
Therefore, the interlaminar damage is a critical aspect of composite airframe design. An additional problematic concern about the non-visible damage, requiring



Figure 2.8: Current intensity effect [15]

non-destructive test device such as ultra-sonic scanning which defines the projected delamination of the panel.

Various parameters can influence the damage occurring during a lightning strike event. Some studies have been already presented in literature, even though an extended evaluation is needed in certain parameters considering the aircraft lightning certification.

Lay-up parameters, like ply thickness and relative fibre angle, have influence on the damage induced by lightning strikes. Several authors demonstrate that based in experimental tests.

Regarding to the ply thickness effect, Hirano et al. [24] found little influence of the variation of the testing panels size and thickness on the damage response for each damage mode. Hosokawa et al. [31] concluded that thicker pitch-based carbon fibre skin layers have higher resistance to lightning-induced damage. Furthermore, Kawakami et al. [32] and Yamashita et al. [33] concluded that thicker ply blocks usually lead to a larger projected damage area.

Additional, Mamizu et al. [34] performed tests on different uni-directional specimens and compared the results with multi-directional specimens. Li et al. [30] reported that the stacking sequence could influence the failure behaviour significantly in the case of unprotected CFRPs. The same study concluded that different fibre relative angles produced dissimilar delamination and fibre damage patterns. Kawakami et al. [32] concluded that the stacking sequence influences the projected damage area by changing its shape. Also, even though the projected damage area is dependent on this parameter of the lay-up, the damage maximum depth is not.

Lightning parameters, identifying as the maximum current of the waveform, electrical discharge and action integral, with a physical meaning of specific energy, was also a purpose of study. Hirano et al. [24], Li et al. [30], Yamashita et al. [33] and Li et al. [35] studies show strong relationship between lightning parameters and certain damages modes. Summary, fibre damage are relatable to a peak current of a lightning strike, a resin deterioration region with an electrical charge, and the delamination damage area by the action integral of the waveform.

Moreover, a relevant parameter in the evaluation develop is the paint thickness effect. Murillo et al. [36] and Bigand et al. [26; 37] show that paint thickness influences the confinement of explosive gases and has a strong relation with damage. In a brief resume, the damage increases with the paint thickness.

Other consideration presented in the literature is the influence of stacking sequence in the effect of hygrothermal ageing on the mechanical properties. Li et al. [35] showed that the stacking sequence has a great effect on the behaviour of composites subjected to water absorption.

2.6 Modelling strategies

Modelling the damage mechanism that occur during a lightning strike event is a complex problem. In order to design reliable models, theories of damage processes have been de-

velop in the lightning community.

The first and best-known theory is based on eletro-thermal physics. This theory considered the temperature as a criterion for the damage in the composite panel, the increase of temperature due to Joule heating is evaluate. The second approach assess the lightning strike impact as a pressure applied on the surface, so it is consider a mechanical criteria of the laminate with a composite damage model.

Therefore, different simulations models have been proposed in the literature.

Thermal damage modelling
Thermal-electric models are the most common type of lightning damage modelling and focused in eletro-thermal constraints. These models are usually implemented in Finite Element (FE) software by apply current to a composite specimen resulting in thermal decomposition of the epoxy matrix (degradation and conversion to gaseous products) and sublimation (transition directly from solid to the gas phase) of carbon fibres [38].
In these models the flow of electrical current is described by Ohm's:

$$J = \sigma E \tag{2.1}$$

where σ is the electrical conductivity, E is the electric field tensor and J is the electric current density tensor. The material to which electric current is being applied resists the flow of current. When electric current flows through a material, electrical energy is converted to heat energy by resistive or Joule heating (Q_j):

$$Q_j = JE \tag{2.2}$$

The heat conduction is governed by the energy balance equation:

$$\rho C_p \frac{dT}{dt} = \nabla(k\nabla T) + Q_j \tag{2.3}$$

where ρ, C_p, k are the instant density, specific heat, and directional thermal conductivity of the composite material, all of which are temperature-dependent [39].
The majority of the lightning strike simulations by thermal-electrical models focussed in waveform A, although reduced authors also focussed in waveform B, waveform C and waveform D. As well some works have focussed on multiple or sequential waveforms applied to the specimen, however there are lack of supporting experimental research. The specimen layup and geometry as the experimental work of Hirano et al. [24] are the most common used in the thermal-electric damage models in literature $150 \times 100 \times 4.704\,\text{mm}$ and $[45/0/-45/90]_{4S}$.
Relatable to the presence of lightning strike protections layers, the majority of the works modelled unprotected specimens, although a small number of authors have included some protection layers in their studies.
The main methods to describe thermal damage are temperature points or fields to define the damage predicted in a simulation and compared surface temperature contours from simulations and experimental surface damage results. The first approach, presented by Ogasawara et al. [40], used 300 °C and 500 °C temperature fields to compare the predicted damage depth in simulations with delamination areas in experiments. However, Foster identified some concerns (i) no methodology had been

defined to identify the depth of temperature fields in experimental work, (ii) the temperatures used corresponded to resin decomposition using one low heating rate, not representative of a lightning strike, (iii) and there was a factor of two difference between the experimental and simulation action integrals [38; 41]. This lead to a underestimated the experimental delamination area.
The second approach defined two zones. The first zone considered a 500 °C contour, named as *severe damage* that expecting this zone to encompass char residue as a result of resin thermal decomposition, frayed or fractured fibres and fibre blow out due to mechanical force, and the second second zone, labelled the *moderate damage* as zone was expected to contain resin thermal decomposition and align with the 300 °C simulation contour [42].

Mechanical damage modelling
Mechanical models, known as mechanical pressure or shock wave pressure loading models, consider the structural effects due to the shock wave impact on the composite surface. These models are equivalent to mechanical loading on composites, nevertheless only a few authors develop models focus on lightning strikes analysis.
The equations proposed to reproduce the effect of the shock wave or pressure load on the surface of the composite during a lightning strike can be divided into two types, (i) electromagnetic pinch (ii) and electromagnetic flux. Assuming that the lightning strike was a perfect cylinder and the air had a fixed magnetic permeability, an generic equation can be obtained with a numerical division factor divergent from the several auhtors.

$$\Delta p = \frac{\mu_0 I^2}{8\pi^2 r^2} \tag{2.4}$$

where I is the electric current and μ_0 is the magnetic permeability constant of air and r is the arc radius.
The mechanical models presented used waveform A and D, the most severe current waveforms to induced damage in a composite structure. The specimens tended to have larger dimensions compared to the thermal-electric models, the most common in-plane size is 450×450 mm with a lay-up sequence of $[45/0/-45/90]_S$.
It is interesting to note that Karch et al. [43] is the only one group used protected specimens with shock wave loading models.
Similar to thermal damage modelling, the pressure load is derived from the SAE waveform and applied directly to the specimen surface, neglecting any lightning plasma surface.

Thermal-expansion modelling
Thermal-expansion models are the least researched in the simulations models proposed. These models are associated to thermal-eletric models and are concern on the expansion of the composite specimen due to rapid heating and its constraints relative to the experimental boundary conditions, producing thermal strains:

$$\epsilon_{thermal} = \alpha \Delta T \tag{2.5}$$

where $\epsilon_{thermal}$ is the thermal strain, α is the thermal expansion coefficient and ΔT is the change in temperature [38].
Typically, summing up, the essential approach is to conduct a thermal-electric analysis and transfer the results forward to thermal expansion analyses.

Heretofore, waveform D studies with this approach are not presented. However, some groups published about waveform A and B (see []) and waveform C* (see []). Sun et al. [44] combined thermal-electric and mechanical simulations to predict damage for waveform A. Since this approach are linked to the thermal-electric models, the specimens used are identical. It is interesting to note that the damage area increased when thermal expansion effects were included with thermal-eletric effects (see [42; 45; 46]).

2.7 Conclusion

Based on aircraft certification, the aeronautical industry and the manufacturers need a better understanding of the physical phenomenon associated to the aircraft structural damage. Lightning is a complex multi-physics phenomenon involving coupling of various physical mechanisms, such as electromagnetic, thermal and mechanical effects. Several types of damage, like fibre tufting, resin decomposition, delamination and matrix cracking are caused in composite structures subjected to lightning strikes.

To study the influence of each parameter inherent to lightning strikes, laboratory tests have strong limitations, especially concerning the generation of a strong electromagnetic field and the very high temperature that a lightning can reach.

Alternatively, numerical models can be a promise solution for aircraft certification. The review of the lightning related literature showed that lightning strike damage and direct effects on composite panels have been studied mostly based on electro-thermal approaches. These techniques reproduce the electrical current flow and the generated thermal flux, which induce thermal damage to the structure. These models were subsequently refined by considering the degradation of the resin by pyrolysis, for example.

However, electro-thermal approaches are unable to predict mechanical damage which can have the most detrimental effect for the integrity of the structure. Moreover, to obtain reliable numerical predictions, not only the composite system, but also the lightning strike protection and paint layers need to be considered.

The research developed in this work aims to explore the different parameters involved in a lightning strike event and consequently their effect on mechanical damage. In particular, this study will focus on the development of a mechanical numerical model validated by experimental laboratory tests.

Part III

Numerical model

Chapter 3

Lightning loads

Contents

3.1 Lightning strike phenomena
3.2 Lightning current
3.3 Root radius
3.4 Near-surface explosion of the lightning protection layer
3.5 Supersonic plasma expansion
3.6 Magnetic forces

Objectives
This chapter presents the semi-analytical approach to obtain the mechanical pressure induced by a transient D current waveform.
The lightning current load characteristics and the three main mechanical contributions are introduced, where the loads are assumed to be axisymmetric and time-dependent. Available experimental data supports the physical mechanisms presented in this chapter.

3.1 Lightning strike phenomena

A lightning strike is a natural phenomenon that generates a high current and high voltage discharge. Due to its complex phenomenology, the research in this field involves multi-physical disciplines. [5; 14].

To assess the damage to metallic and composite materials used in airframe structures based on aircraft safety it is fundamental to focus on the intense pressure pulse in the vicinity of the lightning discharge [29].

The most severe mechanical damage at and around the lightning attachment area of protected and unprotected airframe composite parts is caused by the lightning current components during the transient A or D. Consequently, the assessment neglects thermal effects, which are mainly present in the continuous current components B and C.

Therefore, it is required reliable models that can predict the response of non-thermal damage mechanisms of protected CFRP structures caused by transient lightning strike current components. Thermal and thermal-mechanical effects can be disregarded once mechanical damage is mainly caused by purely mechanical effects.

The mechanical constraints responsible for the damage imposed on the structures have three main origins: (i) overpressure due to the near-surface explosion of the lightning protection layer, (ii) shock waves caused by the supersonic expansion of the hot plasma channel, and (iii) magnetic forces induced by the current flow in the electrically conducting structures. Although the contributions of the swift increase in temperature and magnetic pressures are lower than the surface explosion, the major cause of damage, cannot be neglected [21; 43; 47].

The presented study is supported by Karch's model [20], which is an improvement of the model proposed by Lepetit et al. [19] that describes the damage mechanism of CFRP structures due to transient lightning strike current. Lepetit's model included experimental VISAR data which are validated by numerical and Finite Element calculation [20; 43; 47].

To reproduce the experimental data, the samples used by Lepetit and Karch are the same, CFRP samples made from 8 unidirectional (UD) T700/M21 plies with a quasi-isotropic lay-up. It was used two lightning strike protection (LSP) layers, expanded copper foil (ECF) with diamond mesh shape: (i) surface weights of $73.3\,\mathrm{g\,m^{-2}}$, 2Cu4-100FA (ECF 73); •(ii) $195.3\,\mathrm{g\,m^{-2}}$, 3Cu7-100FA (ECF 195). The samples were painted with polyurethane paint with a surfacing film of 300 µm of thickness. The equations used to compute the pressure distributions for a transient D current waveform with a time to peak of 26.8 µs, a decay time of 48.5 µs, and a peak current of 96.4 kA are described below [19].

3.2 Lightning current

According to the SAE Aerospace Recommended Practice for aircraft lightning environment and related test waveforms [14], the standard equation to describe the lightning transient current waveform D is:

$$I(t) = c\left(e^{-at} - e^{-bt}\right) \tag{3.1}$$

However, this equation cannot describe accurately enough the measured current waveforms tested by Lepetit et al. [19]. Hence, a modified double exponential was proposed by Karch et al. [43]:

$$J(t) = \begin{cases} c\left(e^{-at} - e^{-bt}\right) & , \quad t < t_{max} \\ c\left(e^{-af(t-\upsilon)} - e^{-bf(t-\upsilon)}\right) & , \quad t \geq t_{max} \end{cases} \tag{3.2}$$

where t_{max} is the time at the current peak and the parameter υ is defined by $\upsilon = t_1\left(1 - \frac{1}{f}\right)$. Note that according to SAE Aerospace Recommended Practice [14] a waveform is determined by the time to peak which represents 100% of the lightning current, t_1, time to half value which represents 50% of the lightning current, t_2, and the peak current value, I_{max}. To sum up, the waveform is normally defined as t_1/t_2 µs, I_{max} kA.

The graphical visualization of the double exponential waveform fittings are shown in Figure 3.1.

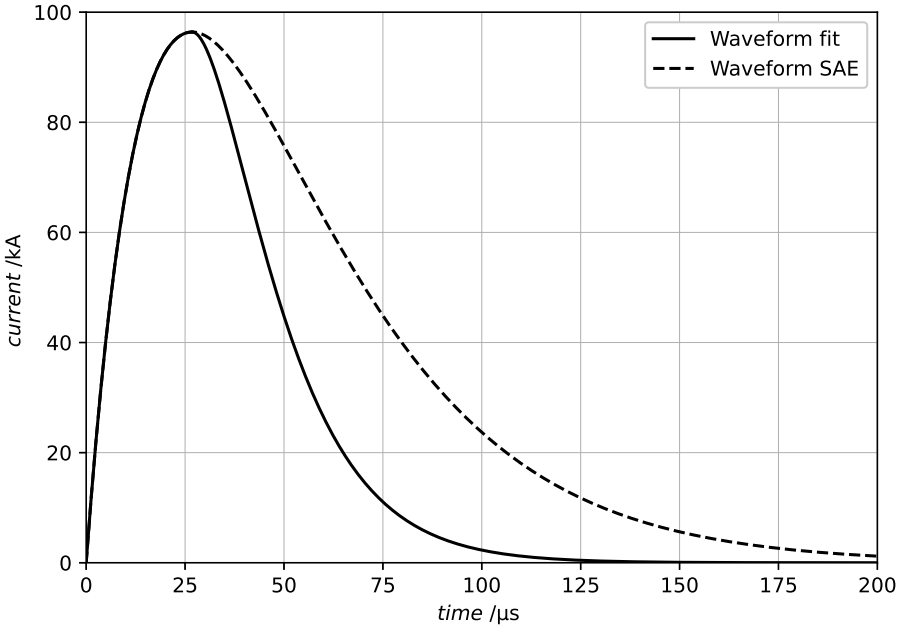


Figure 3.1: Double exponential waveform fittings for a time to peak of 26.8 µs, a decay time of 48.5 µs and a peak current of 96.4 kA using the SAE recommended fit in Equation 3.1 [14] (dashed lines) and the fitting equation proposed by Karch et al. in Equation 3.2 [43] (solid lines).

The parameters of the modified double exponential function are numerical optimize as well as the specifications for the transient D current components by SAE ARP5412 with a peak amplitude $I_{max} = 100\,\text{kA}(\pm 10\%)$, an action integral of $0.25 \times 10^6\,\text{A}^2\text{s}$ ($\pm 20\%$) and a maximum time duration of $t_{max} \leq 500\,\mu\text{s}$ [14].

The parameters for the D current waveform with a time to peak of 26.8 µs, a decay time of 48.5 µs and a peak current of 96.4 kA, are given in Table 3.1.

Table 3.1: Waveform parameters for the waveform 26.8 µs/48.5 µs, 96.4 kA

a /s^{-1}	b /s^{-1}	c /A	f /-	υ /s	t_{max} /s
33 833.1	41 024.7	1 361 710.5	2.081	1.392×10^{-5}	2.68×10^{-5}

Connected to the lightning current, the action integral is a critical factor in the extent of damage related to the energy deposited or absorbed in a system [14].

$$AI(t) = \int I^2 \, dt \tag{3.3}$$

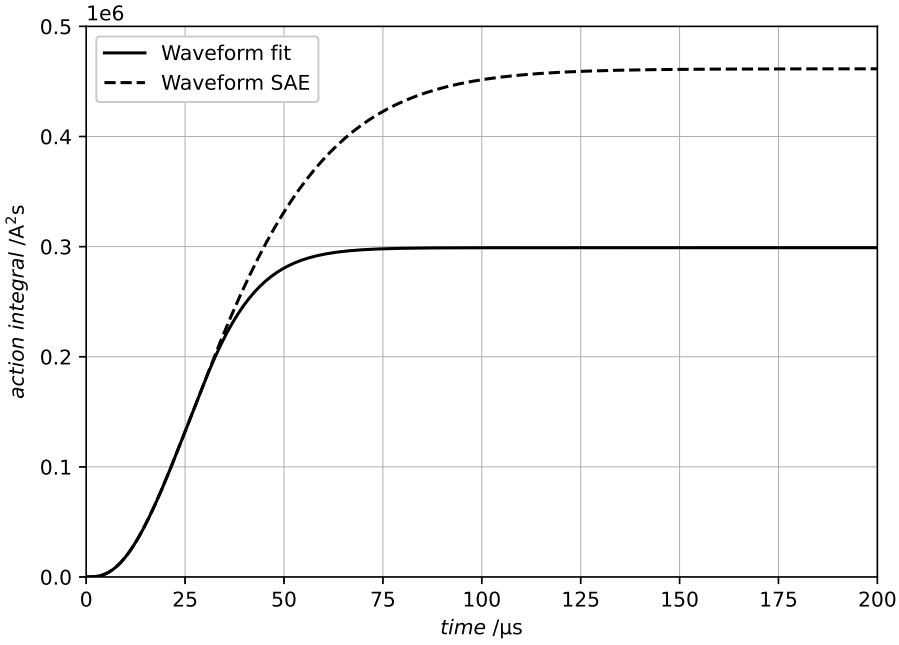


Figure 3.2: Action integral for a time to peak of 26.8 µs, a decay time of 48.5 µs and a peak current of 96.4 kA using the SAE recommended fit in Equation 3.1 [14] (dashed lines) and the fitting equation proposed by Karch et al. in Equation 3.2 [43] (solid lines).

3.3 Root radius

For the case of waveforms A and D, the arc root radius is an important factor in the damage zone size and for numerical implementation [30; 48]. The arc root behaviour depends on the current waveform and the surface properties of the sample. Figure 3.3 gives a clear graphical visualization explanation of the arc root expansion phenomenon (See [49] for further investigation).

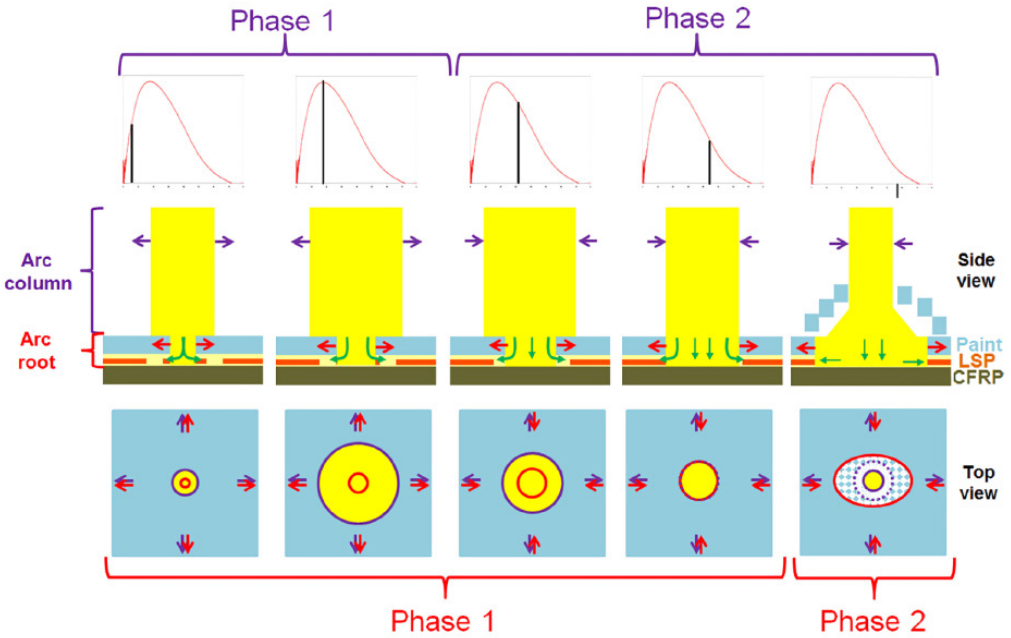


Figure 3.3: Arc expansion theory: (i) arc column phases - axisymmetric expansion, dependent oft the lightning current; (ii) arc root phases - dependent on the LSP electrical conductivity, state and paint

The root radius expansion is calculated using the finite volume degradation approach by defining the temperature at which the material of the lightning protection is assumed to turn to plasma [43]. The initial temperature of 293.16 K, degradation temperature of 1380 K and an initial arc root radius, radius of streamer-leader transition channel, of 0.5 mm are proposed by Karch et al. [43].

This implementation is computed for the expanded copper foils (ECFs) 2Cu4-100FA, (ECF 73) and 3Cu7-100FA, 195.3 g m^{-2} (ECF 195) such as the experimental measurements of Lepetit et al. [19]. The root radius data are fitted using a double exponential function until a time t_s, where it approaches a constant value $c = R_{R_0} + ae^{t_s} + be^{t_s}$:

$$R_R(t) = \begin{cases} R_{R_0} + ae^{\alpha t} + be^{\beta t} & , \quad t < t_s \\ c & , \quad t > t_s \end{cases} \tag{3.4}$$

To ensures an initial root radius of 0.5 mm the root radius equation proposed by Karch et al. [43] need to be modified. So the Equation 3.4 can be rewritten as:

$$R_R(t) = \begin{cases} R_{R_0} + a\left(e^{\alpha t} + e^{\beta t}\right) & , \quad t < t_s \\ c & , \quad t > t_s \end{cases} \tag{3.5}$$

Thus, the initial arc root radius R_{R_0} is independently of the parameters a, α and β obtained during curve fitting.

The parameters of the fitting function in Equation 3.5 are obtained using the curve fitting application from MATLAB [50]. These parameters are shown in Table 3.2.
The fitted root radii as a function of time are plotted in Figure 3.4.

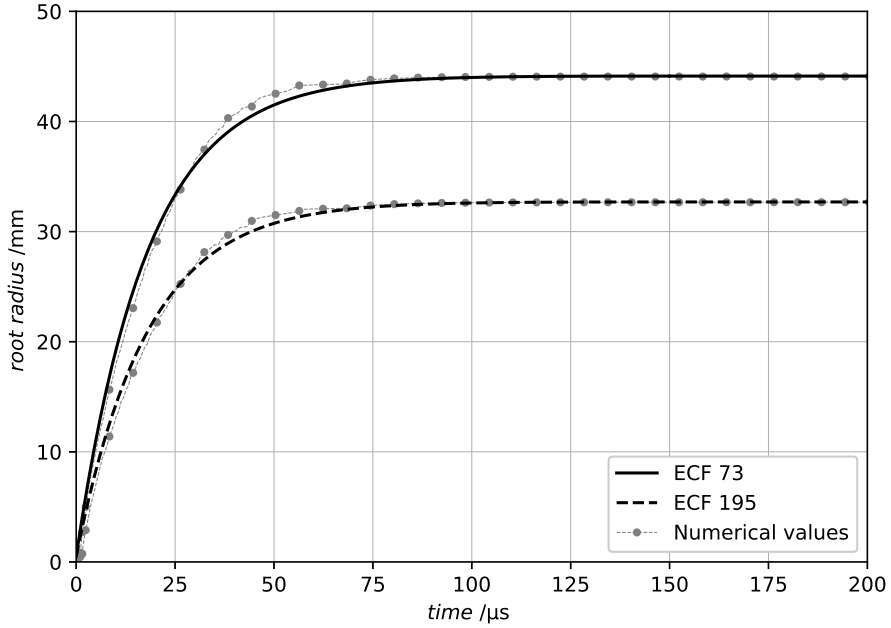


Figure 3.4: Fitted root radii as a function of time for the transient D current waveform with a time to peak of 26.8 µs, a decay time of 48.5 µs and a peak current of 96.4 kA [19].

Analogous to Lepetit et al. experiments [19], the root radius of the ECF 73 is larger than that of the ECF 195. The protection layer is a hybrid ECF/epoxy resin layer, in the case of ECF 73 it used 73.3 g/m^2 of copper, while in the case of ECF 195 it used 195.3 g/m^2 of copper. This variation leads to a difference in the behaviour and the size of the arc root radius, a higher surface conductivity reduces the arc root size. The lower the mass value of copper in the lightning protection layer, the faster the copper mesh degrades, and the more difficult will be the expanding movement of the arc root [21; 43].

According to Landfried et al. [51], the equivalent voltage drop recommend for describing the direct heat input from the plasma channel is about 12 V. Therefore, the same value is used in the root radius expansion data computed.

Table 3.2: Parameters for root radius fit for the transient D current waveform with a time to peak of 26.8 µs, a decay time of 48.5 µs and a peak current of 96.4 kA [19].

	a /mm	α /µs^{-1}	β /µs^{-1}	R_{R_0} /mm	t_s /µs	c /mm
ECF 73	43.6	-1.49×10^{-6}	-0.058	0.5	181.60	44.08
ECF 195	32.2	-9.37×10^{-7}	-0.060	0.5	183.60	32.66

3.4 Near-surface explosion of the lightning protection layer

The explosion of the lightning protection layer is the most significant contribution to the mechanical damage, its influence is well reported in the literature [19; 20; 52]. The explosion of the LSP layer is assumed to be caused mainly by the rapid vaporization of the

metallic mesh of the lightning protection layer due to Joule resistive heating.

Karch et al. [20] added the contributions from the direct heat transfer from the plasma channel to the previous models that described the near-surface explosion phenomena [19; 53]. It is assumed that the spatial distribution of the expanding plasma pressure can be approximated by a Gaussian bell-shaped curve:

$$p_e(r,t) = p_e(t)\ k^{-2}\ exp\left[-\frac{r^2}{(k\ R_R(t))^2}\right] \tag{3.6}$$

where the effective plasma overpressure $p_e(t)$ is numerically determined as described by Karch et al. [43]. The parameter $k \leq 1$ in Equation 3.6 is used to limit the pressure distribution mainly to the arc root area $\pi R_R(t)^2$.

Note that the effective plasma overpressure is directly dependent on the root radius, so it is necessary to calculate the pressure, force, and impulse considering both ECFs. Thus, the model is able to generate effective plasma overpressure considering protected CFRP without paint and with paint thickness of 200 µm, 300 µm and 400 µm for the lightning protection layers ECF 73 and ECF 195. The effective plasma overpressure is fitted to the sum of six Gauss functions, as proposed by Karch et al. [43] and shown at Figure 3.5.

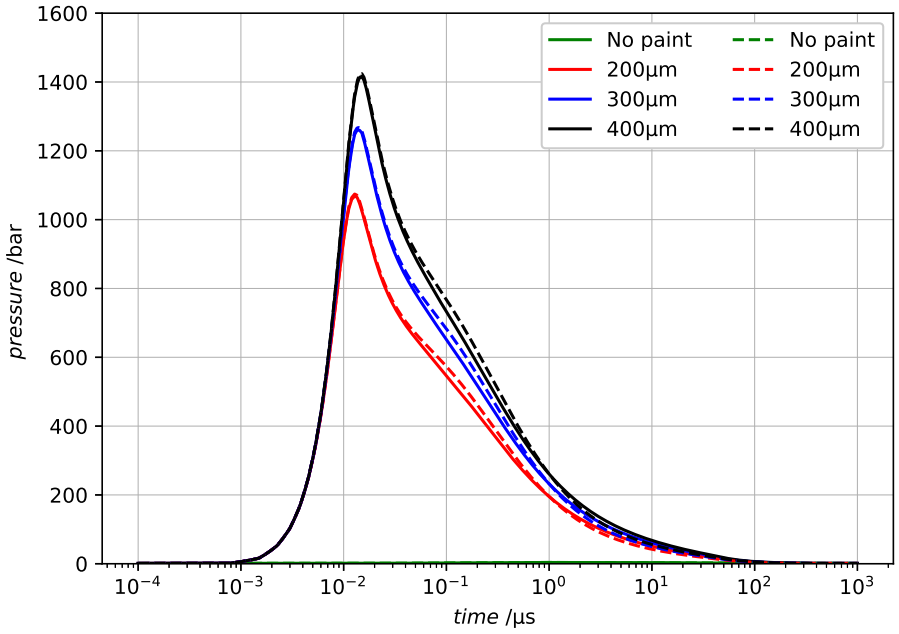


Figure 3.5: Calculated overpressure caused by explosion of lightning protection layers as a function of time for the transient D current waveform with a time to peak of 26.8 µs, a decay time of 48.5 µs and a peak current of 96.4 kA, where the solid lines represent ECF 73 and the dashed lines represent ECF 195.

Consequently, the forces caused by explosion of lightning protection layers and the respectively impulse magnitude could be calculated based on the mathematical foundation

of:

$$Force = \int_A Pressure\, dA \tag{3.7}$$

$$Impulse = \int_{\Delta t} Force\, dt \tag{3.8}$$

The visual representation of the force magnitude and the impulse magnitude as a function of time is shown in Figure 3.6 and Figure 3.7, respectively.

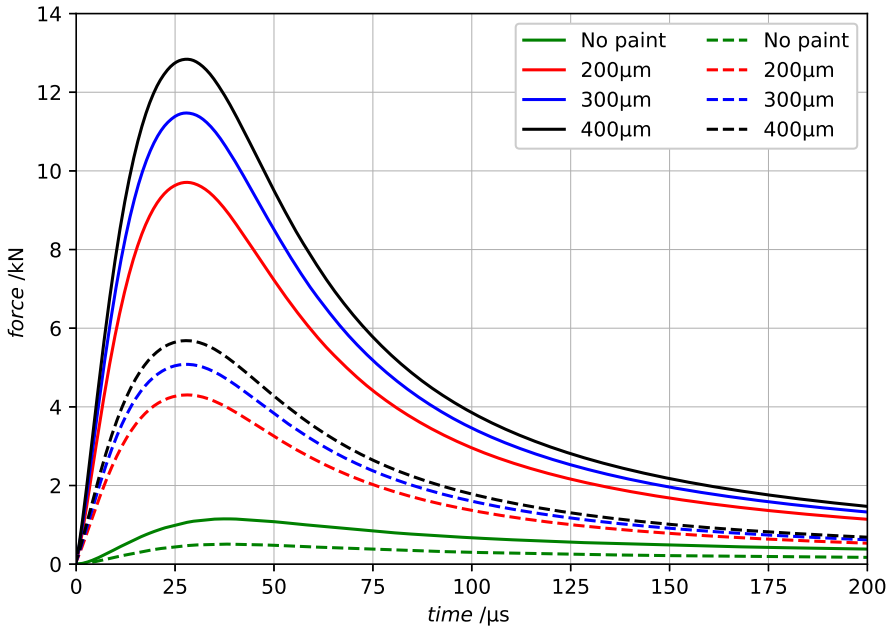


Figure 3.6: Force magnitude caused by explosion of lightning protection layers as a function of time for the transient D current waveform with a time to peak of 26.8 µs, a decay time of 48.5 µs and a peak current of 96.4 kA, where the solid lines represent ECF 73 and the dashed lines represent ECF 195.

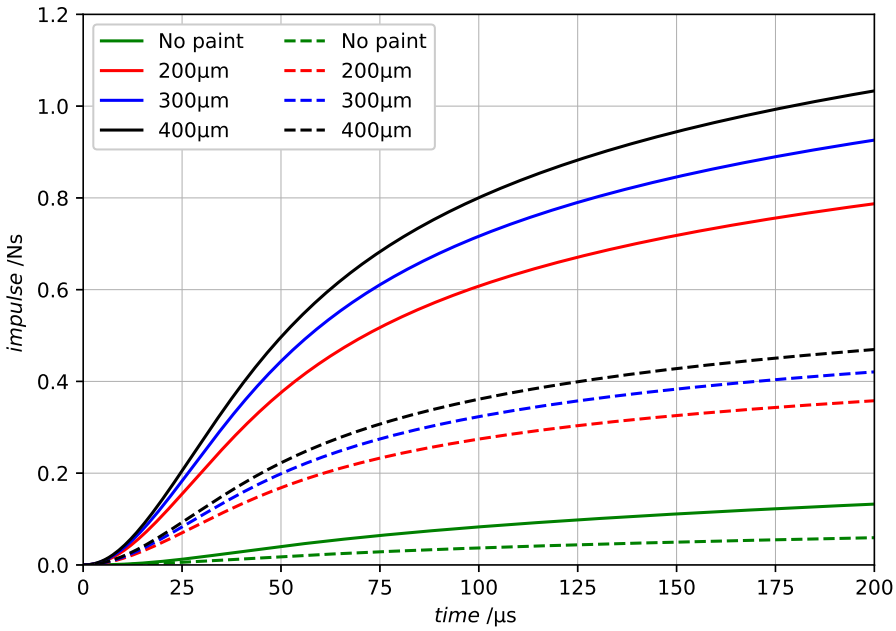


Figure 3.7: Impulse magnitude caused by explosion of lightning protection layers as a function of time for the transient D current waveform with a time to peak of 26.8 µs, a decay time of 48.5 µs and a peak current of 96.4 kA, where the solid lines represent ECF 73 and the dashed lines represent ECF 195.

3.5 Supersonic plasma expansion

The electrical discharge rapidly heats and expands the air into plasma, producing supersonic shock waves. Therefore, a rapid temperature rise of a few microseconds causes an increase of the plasma channel pressure.

The supersonic shock wave expansion of a lightning strike has been studied for a long time by several authors ([54–56]). Following Lin's approach [55], the shock wave model used here is given by the extension from Karch et al. [57].

This overpressure creates a cylindrical shock wave that expands radially at supersonic velocity [20]. The shock position $R(t)$ as a function of time is given by:

$$R(t) \cong 1.004 \left(\frac{E_0}{\rho_0} \right)^{0.25} t^{0.5} \tag{3.9}$$

where E_0 is the initial channel energy density and ρ_0 the initial mass (air) density. The following relationship between the initial channel energy density E_0 ($\mathrm{J\,m^{-1}}$) and the lightning current peak I_{max} (A) can be established [29; 57]:

$$E_0 \cong 0.45 \times 10^{-2} \, (I_{max})^{1.25} \tag{3.10}$$

The shock wave pressure is described by

$$p(\eta, t) \cong 0.180\ (\rho_0 E_0)^{0.5} f(\eta)\ t^{-1} \tag{3.11}$$

where $f(\eta)$ is the dimensionless pressure function and the dimensionless radius $\eta = r/R(t)$ [57].

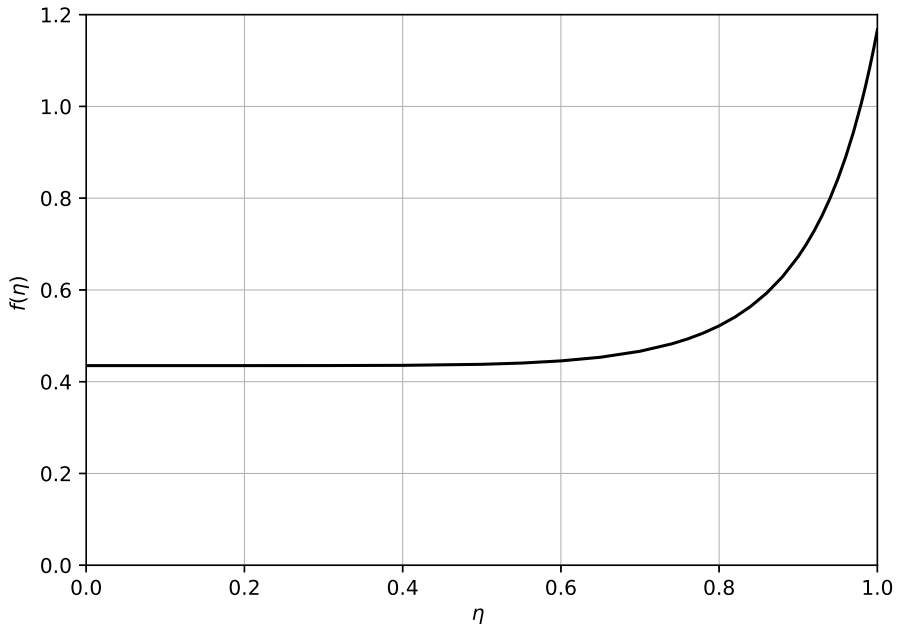
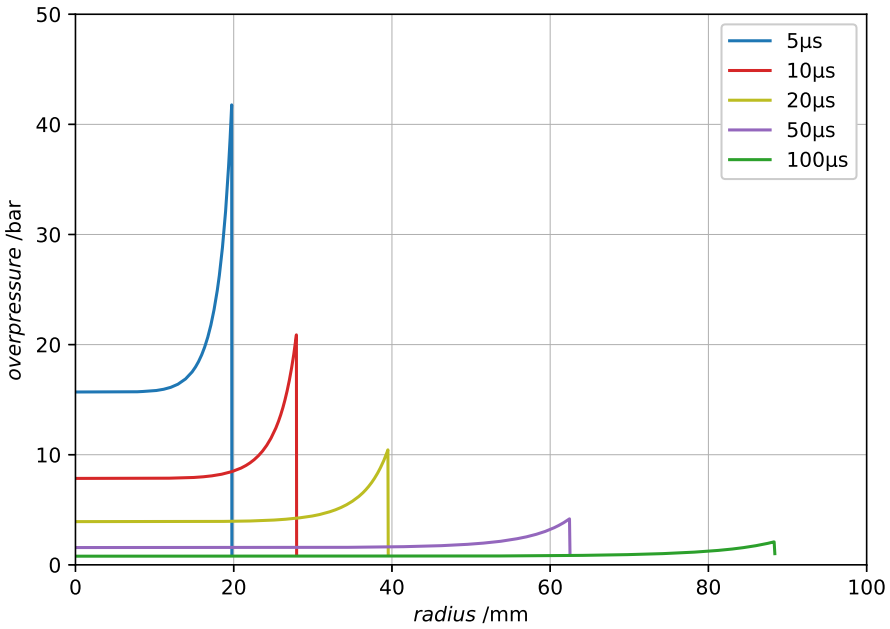


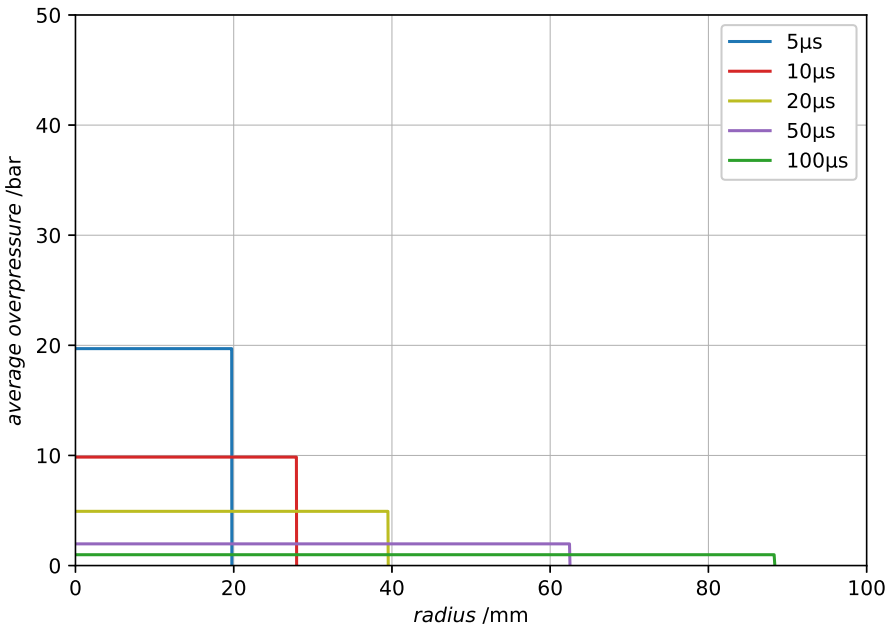
Figure 3.8: Dimensionless pressure function

The peak pressure approaches $+\infty$ for $t \to 0$. This behaviour is caused by the assumption that the energy is released instantaneously at $r = 0$ and $t = 0$.

Figure 3.9a shows the corrected radial overpressure profile at various times. For a better transfer into the finite element model the radial dependency is averaged so that the total generated force and impulse stay constant, shown in Figure 3.9b.



(a) Shock wave pressure



(b) Average shock wave pressure

Figure 3.9: Shock wave overpressure for the transient D current waveform with a time to peak of 26.8 µs, a decay time of 48.5 µs and a peak current of 96.4 kA over the radius for different times. (a) Correct radial overpressure profile (b) Average radial overpressure profile

The expanding shock wave radius (Equation 3.9) can be rewritten as:

$$R(t) \cong \begin{cases} 1.004 \left(\frac{E_0}{\rho_0}\right)^{0.25} \sqrt{0.5} & , \quad t < 0.5\,\mu s \\ 1.004 \left(\frac{E_0}{\rho_0}\right)^{0.25} \sqrt{t} & , \quad t \geqslant 0.5\,\mu s \end{cases} \tag{3.12}$$

assuming a constant value for $t < 0.5\,\mu s$, as showing in Figure 3.10.

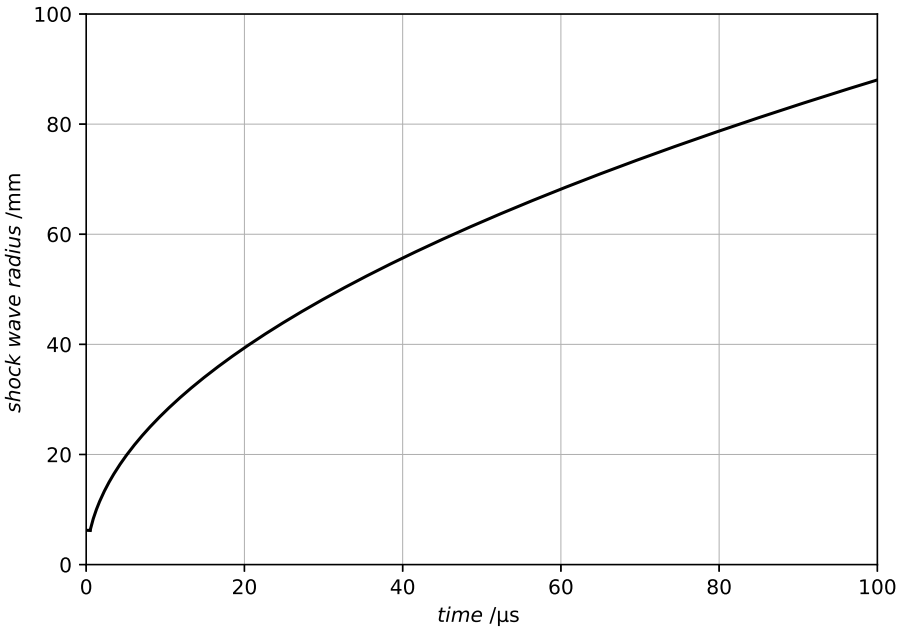


Figure 3.10: Computed shock wave radius for the transient D current waveform with a time to peak of 26.8 µs, a decay time of 48.5 µs and a peak current of 96.4 kA evolution with time

Assuming that the actual distribution of the pressure of the shock wave up to the shock front $R(t)$ can be replaced by a spatially uniform pressure distribution, the analytical approximation reads (see Figure 3.11):

$$p(\eta, t) \cong \begin{cases} \beta \cdot t & , \quad t < 0.5\,\mu s \\ 0.180\ (\rho_0 E_0)^{0.5} f(\eta)\ t^{-1} - 1 & , \quad t \geqslant 0.5\,\mu s \\ 0 & , \quad t > 100\,\mu s \end{cases} \tag{3.13}$$

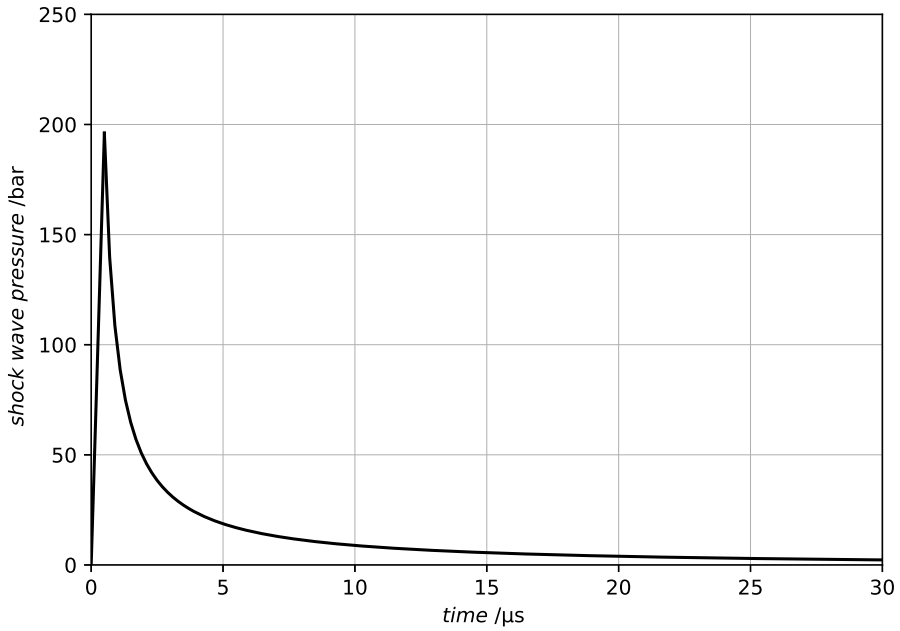


Figure 3.11: Mean cylindrical shock wave pressure for the transient D current waveform with a time to peak of 26.8 µs, a decay time of 48.5 µs and a peak current of 96.4 kA evolution with time

Time-integration of the pressure profiles gives the total force acting on the surface of the sample, representing in Figure 3.12.

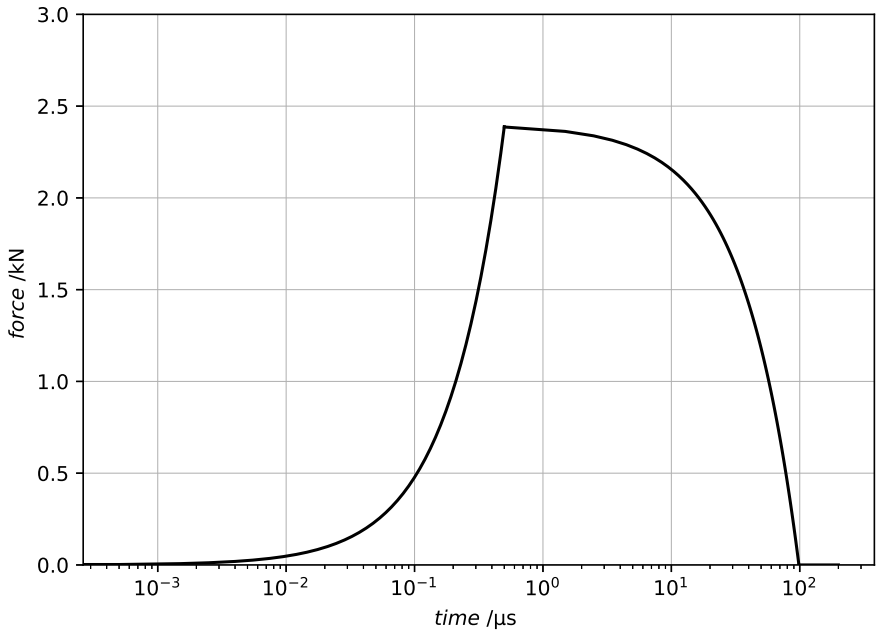


Figure 3.12: Force magnitude caused by supersonic expansion as a function of time for the transient D current waveform with a time to peak of 26.8 µs, a decay time of 48.5 µs and a peak current of 96.4 kA

The approach proposed allows neither determining the time when the shock wave detaches from the expanding hot, high pressure plasma channel nor the correct pressure distribution within the channel up to this point in time.

Using the mathematical foundation as Equation 3.8, the impulse magnitude due to supersonic plasma expansion can be calculated (see Figure 3.13).

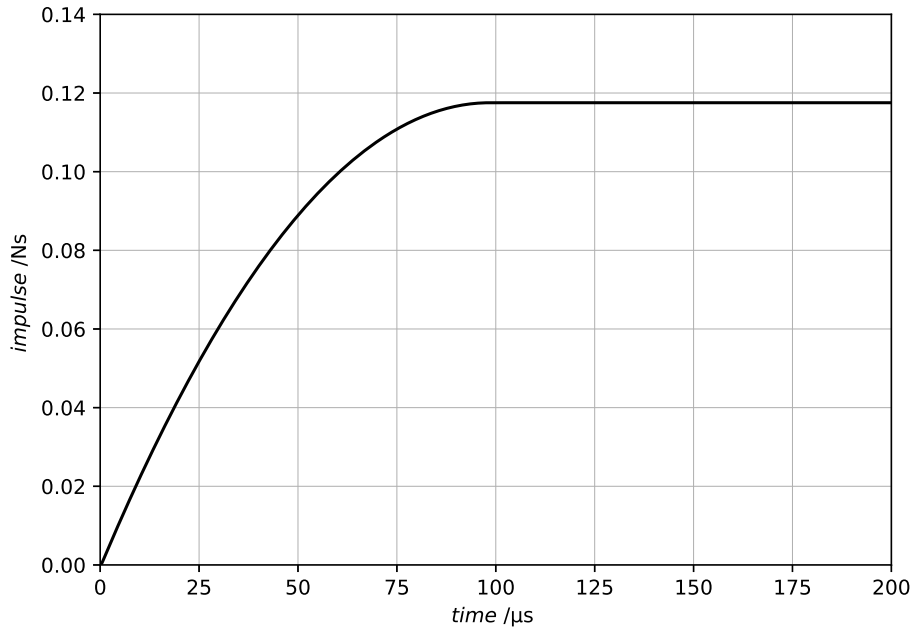


Figure 3.13: Impulse magnitude caused by supersonic expansion as a function of time for the transient D current waveform with a time to peak of 26.8 µs, a decay time of 48.5 µs and a peak current of 96.4 kA

Note that the shock wave pressure only depends on the peak current I_{max} of the waveform. This mechanical load from the supersonic plasma expansion does not depend on the properties of the lightning protection layer used [57].

3.6 Magnetic forces

For composite structures, in particularly CFRP structures, the lightning current flow is mainly constrained within the high-conduction protection layer [57].

The current flow depends on the arc root radius $R_R(t)$. The lightning stream progresses from the plasma channel into the metallic protection layer through the arc root surface [20].

Therefore, the magnetic pressure depends on the region of the sample under ($0 < r < R_R(t)$ – region 1) or beyond the arc root radius ($r > R_R(t)$ – region 2)), see Figure 3.14.

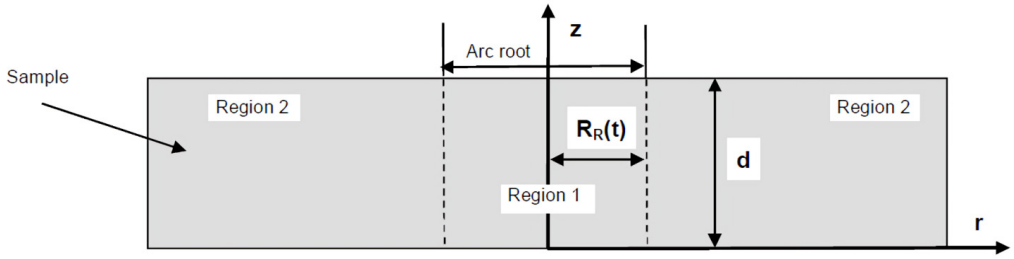


Figure 3.14: Scheme of the sample: region 1 under the arc root and region 2 beyond the arc root [20]

Taking this into account, the effective magnetic surface pressure acting on the upper side of the LSP layer is given as:

$$p_m(r,t) = \begin{cases} \frac{\mu_r \mu_0 J(t)^2}{8\pi^2} \frac{r^2}{R_R(t)^4} & , \quad 0 < r < R_R(t) \\ \frac{\mu_r \mu_0 J(t)^2}{8\pi^2} & , \quad r > R_R(t) \end{cases} \tag{3.14}$$

where $\mu_0 = 4\pi \times 10^{-7}$ Hm^{-1} is the permeability of the free space, $\mu_r = 1$ is the relative permeability of the non-magnetic LSP layer, and $J(t)$ is the total lightning current amplitude, here approximated by the modified double exponential function in Equation 3.2 [43].

This magnetic pressure has a maximum at the arc root radius R_R, where the maximum magnetic pressure distribution is shown in Figure 3.15.

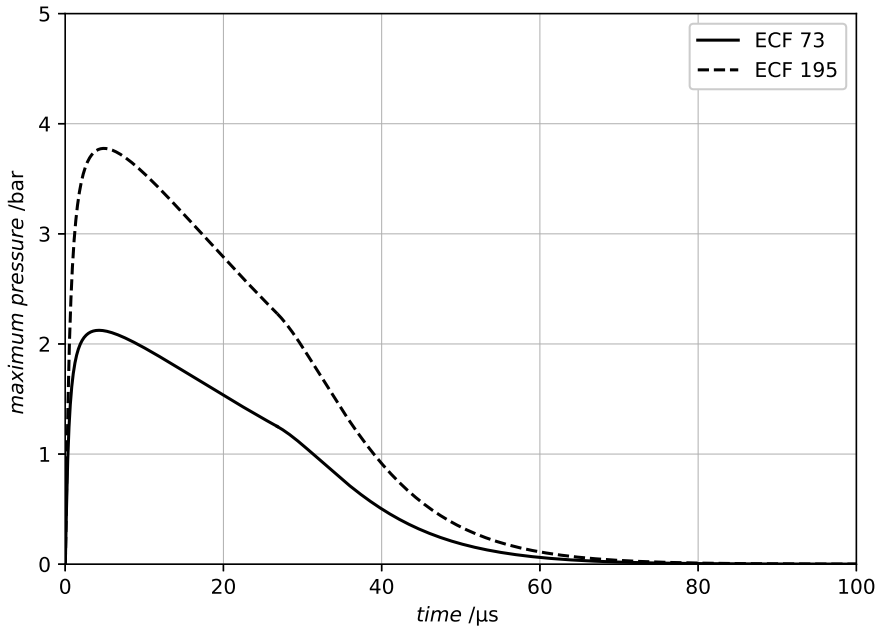


Figure 3.15: Maximum magnetic pressure evolution with time for the transient D current waveform with a time to peak of 26.8 µs, a decay time of 48.5 µs and a peak current of 96.4 kA

To obtain the total magnetic force in both regions, the magnetic pressure has to be integrated over the area of the arc root radius R_R and the area between the arc root radius R_R and the edge radius R of the sample: (see [43])

$$\begin{aligned} F(t) &= \int_0^{R_R} 2\pi r \frac{\mu_r \mu_0 J(t)^2}{8\pi^2} \frac{r^2}{R_R(t)^4}\, dr + \int_{R_R}^{R} 2\pi r \frac{\mu_r \mu_0 J(t)^2}{8\pi^2 r^2}\, dr \\ &= \frac{\mu_r \mu_0 J(t)^2}{4\pi} \left[\frac{1}{4} + \ln\left(\frac{R}{R_R(t)} \right) \right] \end{aligned} \tag{3.15}$$

The graphical visualization of the force magnitude caused by magnetic forces as a function of time are shown in Figure 3.16.

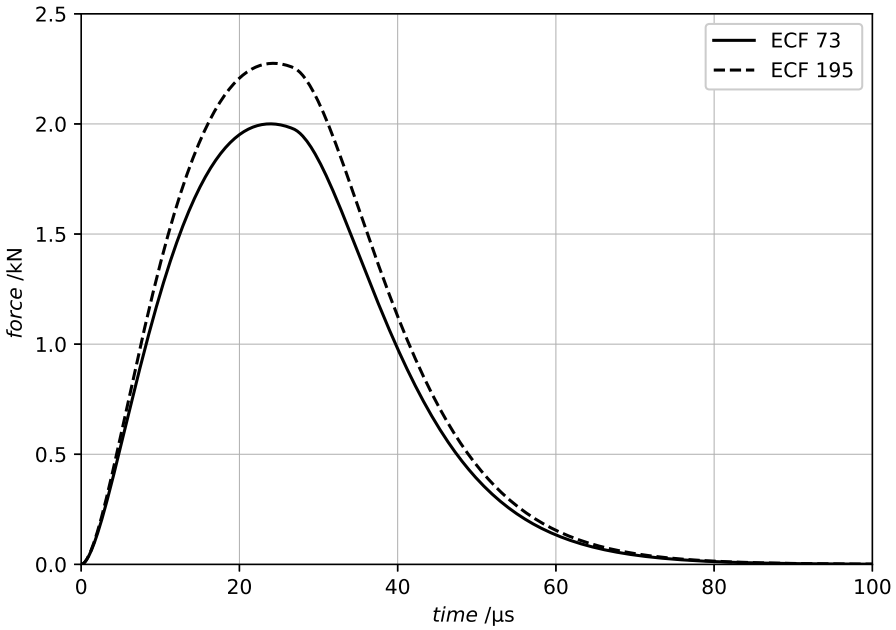


Figure 3.16: Force magnitude caused by magnetic forces as a function of time for the transient D current waveform with a time to peak of 26.8 µs, a decay time of 48.5 µs and a peak current of 96.4 kA

The magnetic impulse amplitude is simply determined by time-integration of Equation 3.15, and it is plotted in Figure 3.17.

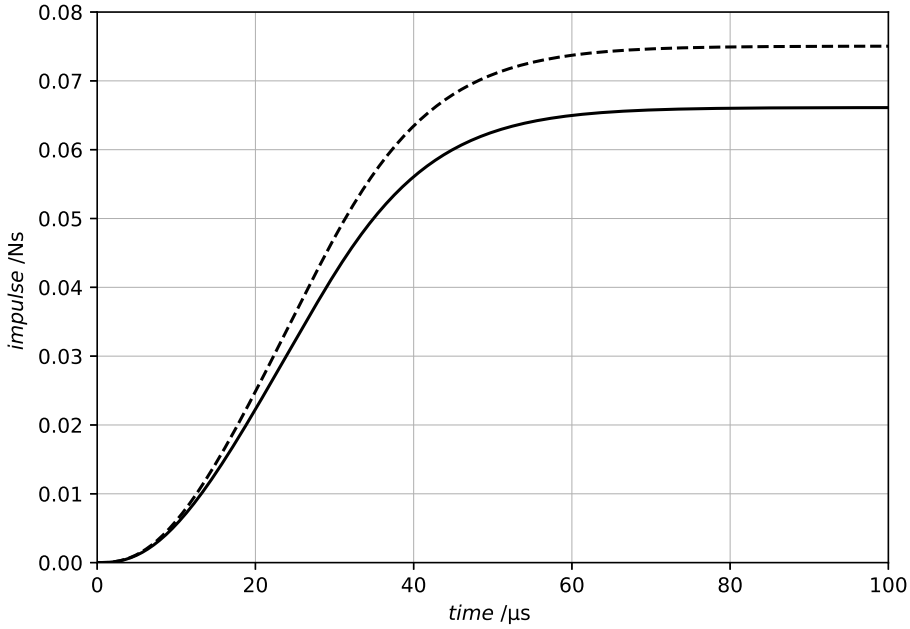


Figure 3.17: Impulse magnitude caused by magnetic forces as a function of time for the transient D current waveform with a time to peak of 26.8 µs, a decay time of 48.5 µs and a peak current of 96.4 kA

Chapter 4

Finite element analysis and validation

Contents

4.1 Finite element model

4.2 Continuum damage mechanics model

4.2.1 Constitutive model

4.2.2 Damage activation functions

4.2.3 Damage laws

4.2.4 Delamination

4.3 Experimental setup

4.4 Mass scaling

4.4.1 Reference model verification

4.5 Model validation

4.5.1 Conclusion

Objectives
This chapter presents an overview of the finite element model, the constitutive models, and the validation with experiments.
The finite element model definitions are presented, as well as the foundations of the continuum damage mechanics model. A sensitivity study regarding the use of mass scaling is presented, and the model predictions validated with experimental results.

4.1 Finite element model

A finite element model with solid elements was used in conjunction with a modification [58] to the continuum damage mechanics model proposed by Maimí et al. [59; 60] to represent failure of the composite plies. This damage model represents the onset of each intralaminar damage mechanism by means of appropriate damage initiation criteria [58; 59] and damage accumulation through appropriate damage evolution laws [58; 60]. Each ply, which is assumed transversely isotropic, must be represented explicitly in the finite element model. To account for ply thickness effects, *in-situ* strengths are defined as a function of ply thickness according to Camanho et al. [61].

The composite laminate is modelled using 8-node C3D8R 3D brick elements with reduced integration are used to model each layer of the composite structure under consideration, including the lightning strike protection layer. Considering the assumed *in-situ* effect [61], successive plies with the same fibre orientation, forming ply clusters, are modelled by a single element through the thickness. Also, the effect of paint is not explicitly in the finite element model once the repercussions on the mechanical response of the composite plate is negligible.

The pressure distributions described in chapter 3 are appplied to the top surface of the compsite plate using a user-defined subroutine, VDLOAD, of the finite element solver Abaqus/Explicit [62]. The equations are programmed into this subroutine that is used to define the variation of the distributed load magnitude as a function of position and time on the top surface of the finite element model. The time scale of the induced mechanical forces/pressures caused by transient current components is about 50 µs. Despite that, the mechanical response of the CFRP laminate has to be considered at least ten times higher. In order to have a proper time discretization of the applied surface pressures, the numerical simulation is divided into several steps with a total time of 550 µs, summarized in Table 4.1. Note that the mechanical pressure induced by the explosion of the lightning strike protection layer and by the supersonic shock wave expansion, which depends both on time and space, act independently, neglecting any possible interactions between them.

Table 4.1: Time duration of the FE model

Step name	Elapsed time /µs
Near-surface explosion	0.1
Shock pressure	0.9
Magnetic pressure	9
Final expansion	40
Over stressing	500

4.2 Continuum damage mechanics model

The modified version of the continuum damage mechanics model [58] has a decoupled longitudinal tensile and compressive elastic behaviour that accounts for different stiffness in tension and in compression parallel to the fibre direction, and it uses bilinear softening laws to model longitudinal damage growth in tension and in compression (according to the parameters f_{XT} and f_{XC}), including a residual stress plateau in compression to more

accurately capture crushing effects.

The formulation of the continuum damage model starts by the definition of a potential (the complementary free energy density) as a function of damage variables associated to the different failure modes. It is also necessary to define the damage activation functions, i.e. the conditions that lead to the onset of inelastic response, and the damage evolution functions.

Maimí et al. [59; 60] assumed that the out-of-plane stress components are too small to promote damage, and therefore only the in-plane stress components of the stress tensor activate damage. However, this assumption is not suitable for test cases where the triaxiality of the stress state is not negligible. Therefore, to improve the ability to accurately predict damage initiation and evolution in 3D test cases, the 3D invariant based failure criterion for fibre kinking proposed by Camanho et al. [63] is used to define an artificial in-plane shear strength S_L^{ef} that represents the effect of hydrostatic pressure on the shear response of the polymer matrix [58]. This 3D invariant-based failure criterion for fibre kinking is also used to scale the fracture toughness for longitudinal compression $\mathcal{G}_{1-}$ and the longitudinal compressive strength ratio at the inflection point f_{XC} as a function of the applied hydrostatic pressure [58].

Experimental evidence also shows that the mode II fracture toughness virtually increases when the cracking faces are compressed against each other. Therefore, an effective fracture toughness for in-plane shear is defined to account for the effect of transverse compressive stresses on the fracture toughness associated with in-plane shear fracture $\mathcal{G}_6$.

Finally, an energy regularization approach based on the fracture energy associated to each failure mechanism and based on the characteristic length of the finite elements is used to ensure mesh independent results after damage onset [64]. This model is implemented in a user-defined subroutine VUMAT for the commercial explicit finite element solver Abaqus/Explicit [62]. Element deletion is set when $d_1 \approx 1$.

These modifications are described in the following sections, with full details of the original model are available in [59; 60; 65].

4.2.1 Constitutive model

The constitutive equations are based in the thermodynamics of irreversible processes. The constitutive law is defined by a scalar function, which must be positive definite and zero at the origin with respect to the free variables and the complementary free energy density in the material. The scalar function corresponding to the ply complementary free energy density, accounting for the different longitudinal Young's moduli in tension and compression reads:

$$\begin{aligned} G = &\frac{\langle \sigma_{11} \rangle^2}{2(1-d_1)E_1} + \frac{\langle -\sigma_{11} \rangle^2}{2(1-d_1)E_{1c}} - \nu_{12}\sigma_{22}\left(\frac{\langle \sigma_{11} \rangle}{E_1} + \frac{\langle -\sigma_{11} \rangle}{E_{1c}}\right) + \\ &\frac{\sigma_{22}^2}{2(1-d_2)E_2} + \frac{\sigma_{12}^2}{2(1-d_6)G_{12}} + (\alpha_{11}\sigma_{11} + \alpha_{22}\sigma_{22})\,\Delta T + (\beta_{11}\sigma_{11} + \beta_{22}\sigma_{22})\,\Delta M \end{aligned} \tag{4.1}$$

where E_1, E_2, E_3, ν_{12}, ν_{13}, ν_{23}, G_{12}, G_{13} and G_{23} are the in-plane elastic orthotropic properties of a unidirectional lamina. Subscript 1 denotes the longitudinal (fibre) direction and 2 denotes the transverse direction. α_{11} and α_{22} are the coefficients of thermal expansion in the longitudinal and transverse directions, respectively. β_{11} and β_{22} are the coefficients of hygroscopic expansion in the longitudinal and transverse directions, respectively. ΔT and ΔM are the differences of temperature and moisture content with respect to the corresponding reference values. σ_{ij} $(i, j = 1, 2)$ are the stress components and d_i $(i = 1, 2, 6)$ are the scalar damage variables, related to longitudinal, transverse and shear damage modes, respectively. Also, and $\langle\bullet\rangle$ stands for the Macaulay brackets, which return the argument $\bullet$ if positive, and zero otherwise.

The potential in Equation 4.1 is the basis for establishing the relation between the stress and the strain tensors. To ensure the thermodynamic irreversibility of the damage process, the rate of change of the complementary free energy $\dot{G}$ minus the externally supplied work to the solid at constant strains, $\dot{\sigma} : \epsilon$, must not be negative:

$$\dot{G} - \dot{\sigma} : \varepsilon \geq 0 \tag{4.2}$$

The strain tensor reads:

$$\epsilon = \frac{dG}{d\sigma} = H : \sigma + \alpha\Delta T + \beta\Delta M \tag{4.3}$$

Since the effects of temperature and moisture not considered in the model, the strain tensor are:

$$\epsilon = \frac{dG}{d\sigma} = H : \sigma \tag{4.4}$$

H is the lamina compliance tensor:

$$H = \frac{\partial^2 \mathcal{G}}{\partial \sigma^2} = \begin{bmatrix} \frac{1}{(1-d_1)|\sigma_{11}|}\left(\frac{\langle\sigma_{11}\rangle}{E_1} + \frac{\langle-\sigma_{11}\rangle}{E_{1c}}\right) & -\frac{\nu_{12}}{|\sigma_{11}|}\left(\frac{\langle\sigma_{11}\rangle}{E_1} + \frac{\langle-\sigma_{11}\rangle}{E_{1c}}\right) & 0 \\ -\frac{\nu_{12}}{|\sigma_{11}|}\left(\frac{\langle\sigma_{11}\rangle}{E_1} + \frac{\langle-\sigma_{11}\rangle}{E_{1c}}\right) & \frac{1}{(1-d_2E_2)} & 0 \\ 0 & 0 & \frac{1}{(1-d_6)G_{12}} \end{bmatrix} \tag{4.5}$$

To account for closure of longitudinal and transverse cracks under load reversal, four damage variables associated with longitudinal (d_{1+} and d_{1-}) and transverse (d_{2+} and d_{2-}) damage are considered to define the d_1 and d_2:

$$d_1 = d_{1+}\frac{\langle\sigma_{11}\rangle}{|\sigma_{11}|} + d_{1-}\frac{\langle-\sigma_{11}\rangle}{|\sigma_{11}|} \tag{4.6}$$

$$d_1 = d_{2+}\frac{\langle\sigma_{22}\rangle}{|\sigma_{22}|} + d_{2-}\frac{\langle-\sigma_{22}\rangle}{|\sigma_{22}|} \tag{4.7}$$

Since shear damage represents transverse cracks which do not close under shear stresses, only one variable is considered for shear damage ($d6$).

4.2.2 Damage activation functions

This model assumed that the elastic domain is enclosed by the four surfaces of each failure mechanism: longitudinal and transverse fracture under tension and compression. The surfaces of the domain are materialized by damage activation functions based on the LaRC03 criteria [66] and the 3-D invariant-based failure criteria [63].

The continuum damage model predicts four intralaminar failure mechanisms: longitudinal tensile failure (F_{1+}), longitudinal compressive failure (F_{1-}), transverse failure where the crack plane is perpendicular to the mid-plane of the laminate (F_{2+}), and transverse failure where the crack plane is not perpendicular to the mid-plane of the laminate (F_{2-}) [59]. The respective activation functions are defined as:

$$\begin{aligned} F_{1+} &= \phi_{1+} - r_{1+} \leq 0 \\ F_{1-} &= \phi_{1-} - r_{1-} \leq 0 \\ F_{2+} &= \phi_{2+} - r_{2+} \leq 0 \\ F_{2-} &= \phi_{2-} - r_{2-} \leq 0 \end{aligned} \tag{4.8}$$

The four loading functions, ϕ_i ($i = 1+; 1-; 2+; 2-$), define the failure surfaces, and are established in terms of strain tensor depend on the material elastic and strength properties, using an approximation of the LaRC03 failure criteria [66]. Also, r_n are the elastic domain thresholds, associated with the relative failure mechanism, $n = 1+; 1-$ for longitudinal mode and $n = 2+; 2-$ for transverse mode. (for full details on their definition and their physical meaning see [59; 60; 65]).

4.2.3 Damage laws

A different stress/strain relations response is considered for each damage mechanism in order to obtain a precisely prediction of the mechanical response of a unidirectional (UD) composite lamina before and after initiation of the different failure modes. The uniaxial response is presented in Figure 4.1, where [58]:

Figure 4.1a presents a linear-elastic response followed by a bi-linear softening law after longitudinal tensile damage initiation, under longitudinal tensile loading.

Figure 4.1b presents a under longitudinal compressive loading the initially linear-elastic response, preceding kink band formation, which is followed by linear softening, corresponding to the propagation of a kink band, until reaching a plateau. It is based in experimental findings of Moran et al. [67].

Figure 4.1c presents an linear softening law following an initially linear-elastic response for the transverse tensile and compressive stress-strain relations.

Figure 4.1d represented by a reduced slope in the stress-strain curve to account for the inelastic response caused by plastic deformation, followed by a linear softening law. A nonlinear elasto-plastic response is assumed.

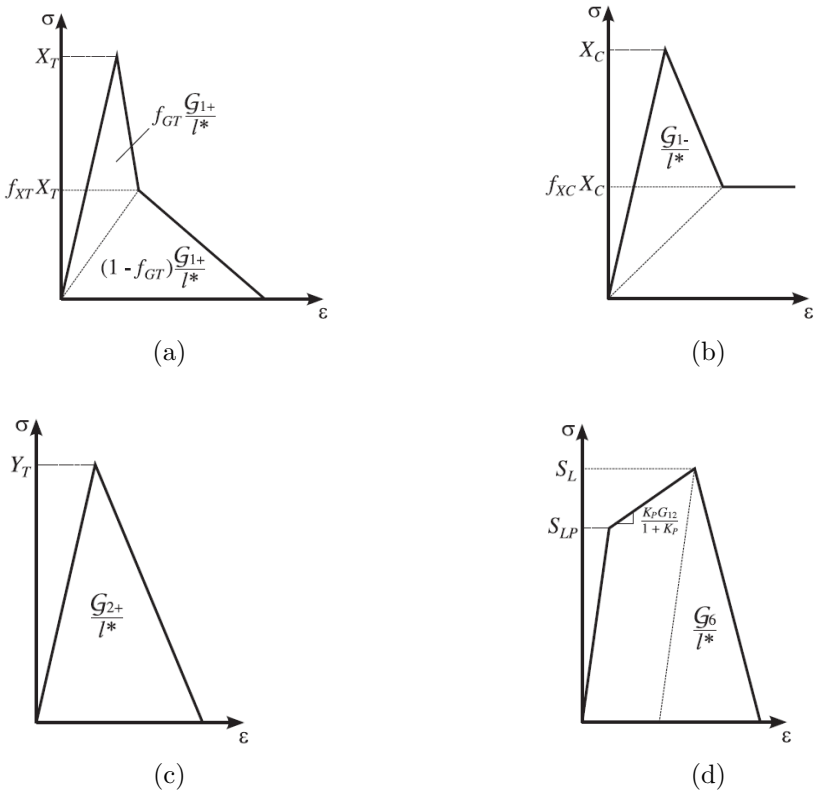


Figure 4.1: Uniaxial response in (a) longitudinal tension, (b) longitudinal compression, (c) transverse tension or compression and (d) in-plane shear [43]

To ensure correct energy dissipation during damage propagation and to avoid mesh-size dependency of the numerical solution, the slopes of the softening laws are determined as a function of the fracture toughness $\mathcal{G}_c$ associated with each failure mechanism and as a function of the characteristic length l^* of the finite elements [64].

4.2.4 Delamination

Delamination between plies is modelled using the interaction properties with cohesive behaviour available in Abaqus [62]. The cohesive interaction is defined by a bilinear traction separation damage law accounting for mode dependency according to the B-K law [68]. Mode-dependent (mode I and mode II) strengths and fracture energies are considered. The onset of interlaminar damage is predicted by a quadratic stress-based criterion, and to account for friction between delaminating interfaces subjected to sliding movements, tangential friction is assigned to the cohesive surface interactions. A friction coefficient of 0.3 is assumed.

Turon et al. [69] demonstrated that changes in the local mode ratio in the evolution of damage during mixed mode loading might lead to erroneous calculation of the energy dissipation. For this reason, the shear strengths $\tau_1 = \tau_2$ are not fully independent material properties, but instead they are determined as a function of the mode I and mode II fracture toughness, $\mathcal{G}_{Ic}$ and $\mathcal{G}_{IIc}$ respectively, and the normal strength τ_3:

$$\tau_1 = \tau_2 = \tau_3 \sqrt{\frac{\mathcal{G}_{IIc}}{\mathcal{G}_{Ic}}} \tag{4.9}$$

4.3 Experimental setup

Lepetit et al. [19] performed at Airbus France a several lightning strikes tests to improve understanding of the damage mechanisms induced by lightning strikes in carbon fiber composite materials. Composite samples were subjected to transient lightning components via a lightning transient generator.

The tested CFRP samples are made from 8 unidirectional (UD) T700/M21 plies with a quasi-isotropic $[45/0/-45/90]_S$ lay-up are considered in this study. The samples are square laminates plates with the size of 450×450 mm and each ply is 0.262 mm. For the lightning protection layer, expanded copper foils (ECF) with a diamond mesh shape and surface weights of $73.3\,\mathrm{g\,m^{-2}}$, 2Cu4-100FA (ECF 73), and $195.3\,\mathrm{g\,m^{-2}}$, 3Cu7-100FA (ECF 195), were used. A polyurethane paint layer with a thickness of 300 µm, including surfacing film was applied to each reference model sample.

The samples were painted with polyurethane paint with a total thickness of the paint system including the surfacing film of 300 µm. The samples were subjected to standard arc attachments tests, with a transient D current waveform as the lightning load. The current load has a time to peak of 26.8 µs, a decay time of 48.5 µs, and a peak current of 96.4 kA as described previously [19] [43].

Airbus identified this project as ALDER 18 for the samples which used the expanded copper foil of $195.3\,\mathrm{g\,m^{-2}}$ (ECF 195) and ALDER 19 for the samples that used the expanded copper foil of $73.3\,\mathrm{g\,m^{-2}}$ (ECF 73). The schematic drawing of the experiments realized by Lepetit et al. is shown in the Figure 4.2. The laminated plate is fixed by screws along a circumference with 370 mm diameter, concentring with the central circular opening with 340 mm diameter of the support plate.

Velocity Interferometer System for Any Reflector (VISAR) are used, a tool which uses laser interferometry to determine surface velocities of objects moving with high speed [55]. Five measuring points, named IDF 1 to IDF 5, were chosen in the rear face of the sample to record the velocities normal to the plane.

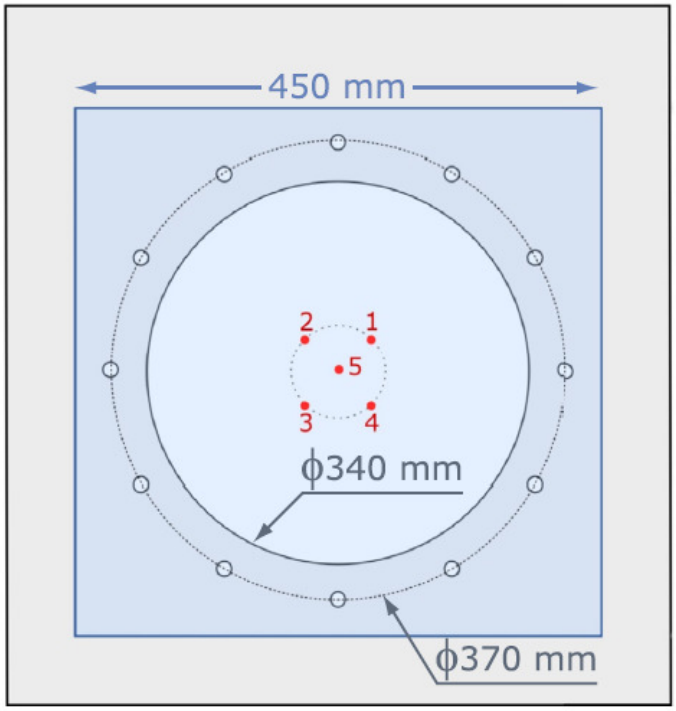


Figure 4.2: Configuration of the lightning strike test support and sample [43]

4.4 Mass scaling

Several sectors of the industry and research groups use numerical simulations to predict the behaviour of structures or systems affected by many physical effects, such as mechanical stress, mechanical vibration, fatigue, heat transfer, fluid flow or electrostatics. Finite element software is very helpful nowadays, leading to a expensive and time consuming experiments to a large level can be eliminated.

The use of most refined mesh in finite element models, creating small size elements directly affects the time step of the solution. Therefore, aiming to increase computational efficiency the mass scaling option in Abaqus is often used in the Abaqus/Explicit solver. The size and dimensions of these small elements control the stable time steps of the solution and cause the dissolution time to increase dramatically.

The use of mass scaling can be used for different purposes, (i) scale the mass of the entire model or individual elements, (ii) scale the mass at the beginning of the solution or during the solution process, and (iii) in a specific step or stage, normally in analysis with several steps [62].

For these objectives, the diverse techniques could be leading:

1. Use a user-defined constant factor to scaling the mass of all elements.
2. Scale the mass of the specified elements at the same quantity, so that the minimum stable time step for solving each of the specified elements in this set is equal to the time step defined by the user.
3. Scale the mass of all specified elements, so that the stable time increments for solving is the same as the number defined by the user.

4. Scale only the mass of the elements in a set that cause the stable time step of the solution to be less than the value specified by the user, so that the stable time step to solve these elements is equal to the value defined by the user.

5. Perform the Mass Scaling process automatically based on the mesh geometry and the initial conditions of the problem

4.4.1 Reference model verification

In order to verify the potentiality of use a mass scaling procedure in this work, a reference model was selected to performed a numerical simulation with and without mass scaling technique.

As a reference model, the model of an 8-plies CFRP plate $[45/0/-45/90]_S$ that used the expanded copper foil of $73.3\,\mathrm{g\,m^{-2}}$ was used. The interface between different plies is defined by cohesive elements, forming interlaminar layers, which is considerably smaller than the thickness of a ply. The large computational time of the simulation is caused by the low stable time increment of the interlaminar elements with a very small characteristic length.

The selective mass scaling procedure available in Abaqus/Explicit [62] was used to avoid unacceptably small stable time increments occurring due to the collapse of a small number of volumetric elements below the impact point of the lightning strike. Because this procedure applies mass scaling just to the elements whose stable time increment is below a specified value, it was possible to limit the relative mass change to just 2×10^{-9}.

The assessment of the mass scaling procedure was establish by the kinetic energy, internal energy, and displacement and velocity of the panel, presented in Figure 4.3, Figure 4.4 and Figure 4.5, respectively.

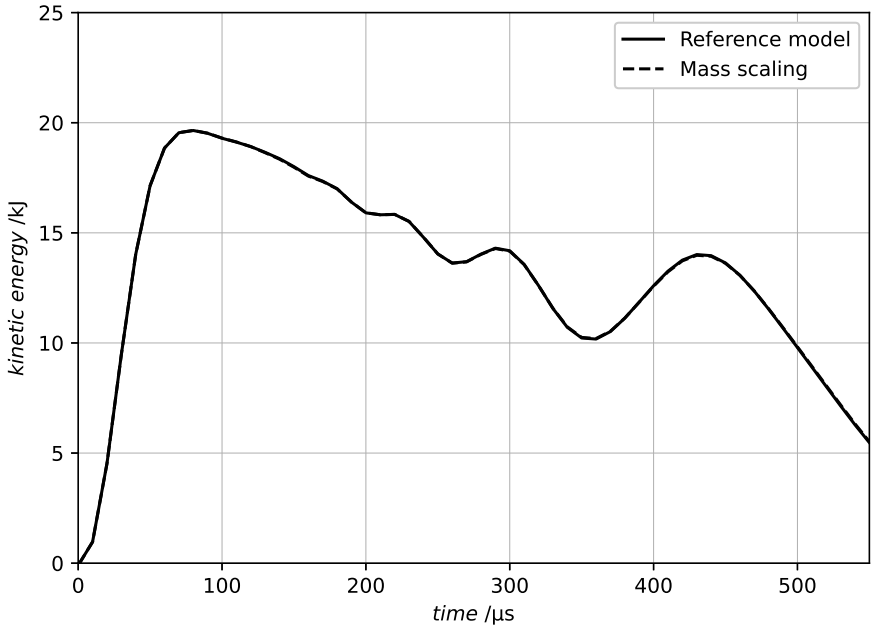


Figure 4.3: Comparison of the kinetic energy between reference model (solid lines) and mass scaling model (dashed lines)

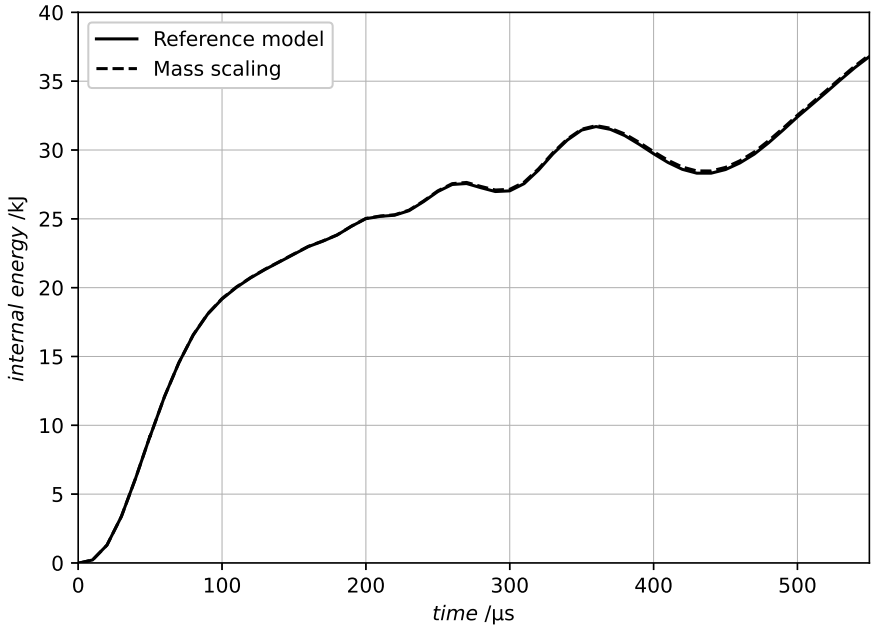
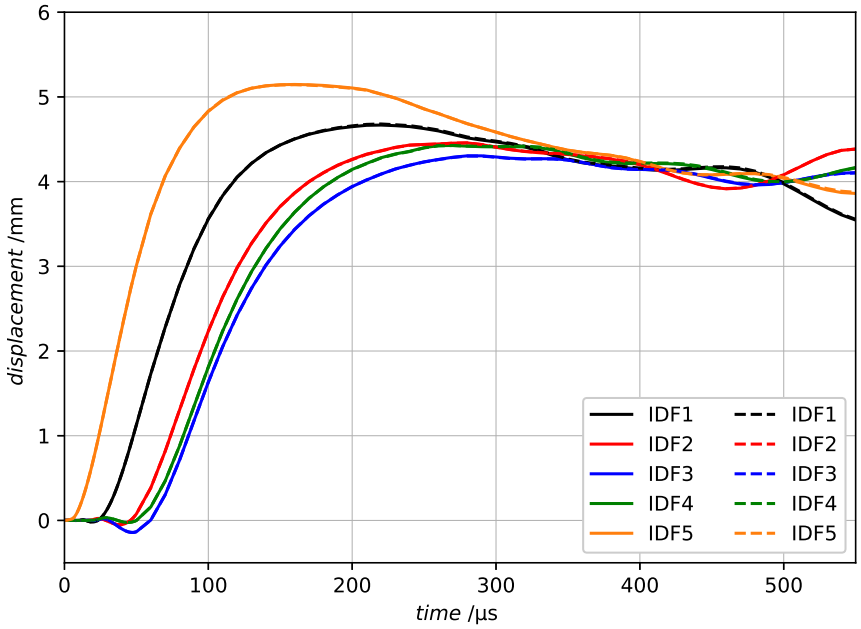
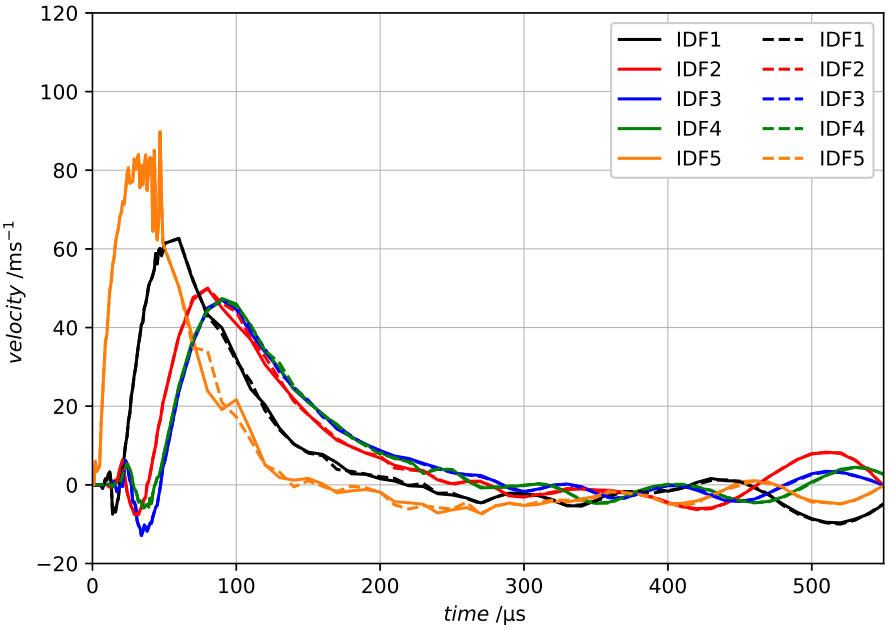


Figure 4.4: Comparison of the internal energy between reference model (solid lines) and mass scaling model (dashed lines)



(a) Displacement



(b) Velocity

Figure 4.5: Finite element predictions comparison between reference model (solid lines) and mass scaling model (dashed lines)

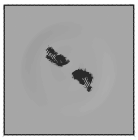
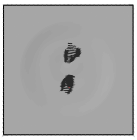
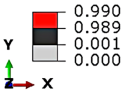
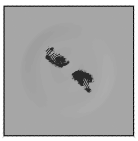
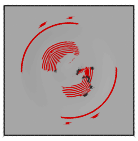
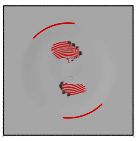
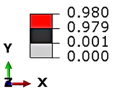
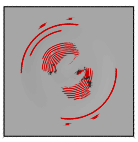
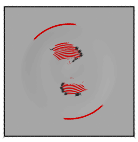
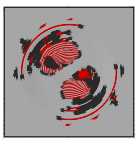
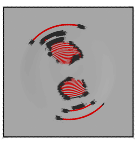
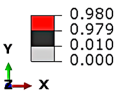
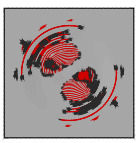
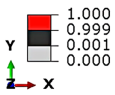
Moreover, a damage map analysis, Table 4.2, was done to demonstrate the correlation between the two models, with and without the mass scaling technique. This assessment approach will be important for the numerical model analysis developed in this work, this is a suggested methodology to evaluate the damage in all the layers of the laminate. Since this analysis intends only to verify the application of mass scaling, only the first and the second topmost layer, the most affected by lightning strikes, are presented. Although, during the present work the damage map assessment is performed for all the layers of the composite laminate.

In the following damage analysis damage onset, partially damaged interfaces/elements ($0 < d_i \lesssim 1$), is represented by the color black and full cracks, fully damaged elements $d_i \approx 1$, by a red color (each damage variable specifies the range of values used for damage onset and full cracks).

Due to the sample size, a progressively coarser mesh was used as the distance to the centre of the sample increased, which renders the damage onset maps inaccurate in the coarse regions, hence the extensive areas showing damage onset and closer to the supporting edge.

Nevertheless, the damage patterns are those usually observed on CFRP samples subjected to simulated lightning strikes and attributed to mechanical effects: damage tends to concentrate below the region of the initial attachment, mainly interlaminar and matrix damage at the middle and bottom plies, and to spread away from the initial attachment point predominantly at the top plies.

Table 4.2: Damage map assessment for the four damage variables comparing the reference model (first row) and the model with mass scaling (second row) for ECF 73

	Layer 8	Layer 7
Longitudinal damage		
		
Transverse damage		
		
Shear damage		
		
Delamination		
		

4.5 Model validation

The CFRP sample is modelled fixing the out-of-plane displacements on the supported area outside the circular opening and fixing the nodes along the circumference where the screws are placed, see Figure 4.6.

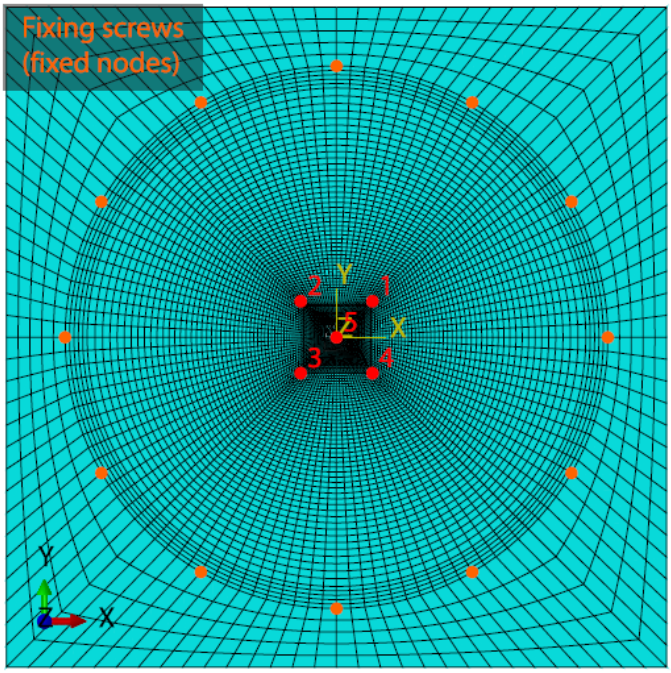


Figure 4.6: Composite plate finite element mesh

The UD ply elastic properties and the strength and material degradation properties used in the simulations are presented in Table 4.3 and Table 4.4, where:

S_L^p: in-plane yield strength

K_p: shear modulus degradation factor

X_T: longitudinal tensile strength

X_C: compressive plain strength

f_{XT}: pull-out (tension) strength factors

f_{XC}: crushing (compression) strength factors

Y_T: UD transverse tensile strength

Y_C: UD transverse compressive strength

α_0: composite fracture angle in uniaxial transverse compression

S_L: UD in-plane shear strength

$\mathcal{G}_{1+}$: longitudinal tensile fracture toughness

$f_{\mathcal{G}_{1+}}$: fraction of the fracture toughness dissipated in the second arm of the bilinear softening law

$\mathcal{G}_{1-}$: longitudinal compressive fracture toughness

$\mathcal{G}_{2+}$: transverse tensile fracture toughness

$\mathcal{G}_6$: in-plane shear fracture toughness

Table 4.3: T700/M21 UD ply density, Young's moduli, shear modulus and Poisson's ratios

density /tonne m^{-3}		
1.15×10^{-9}		
E_1 /MPa	E_2 /MPa	E_3 /MPa
116 500	8900	8900
G_{12} /MPa	G_{13} /MPa	G_{23} /MPa
5300	5300	6700
ν_{12} /−	ν_{13} /−	ν_{23} /−
0.33	0.33	0.35

Table 4.4: T700/M21 strengths and material degradation properties used in the modified continuum damage mechanics model

X_T /MPa	X_C /MPa	α_0/rad	f_{XT} /−	f_{XC} /−
2000	1300	0.925	0.086	0.6
Y_T /MPa	Y_C /MPa	S_L /MPa	S_L^p /MPa	K_p /−
76	256	81	50	0.29
$\mathcal{G}_{1+}$ /N mm^{-1}	$\mathcal{G}_{1-}$ /N mm^{-1}	$\mathcal{G}_{2+}$ /N mm^{-1}	$\mathcal{G}_6$ /N mm^{-1}	$f_{\mathcal{G}_{1+}}$ /−
133.3	95	0.35	1.209	0.52
$f_{f_{xc}}$ /−	η_G /−			
0.05	0.0245			

and $f_{f_{xc}}$ is a frictional parameter used to scale f_{XC} as a function of the hydrostatic pressure, i.e., $f_{f_{xc}}$ can be calibrated using the experimental curves from a bearing or filled-hole compression test and from an open-hole compression test:

$$f_{XC}^{ef} = \min\left\{1, f_{XC}\left(1 - f_{f_{xc}}\langle -I_3\rangle\right)\right\} \tag{4.10}$$

Where $I_3 = \sigma_{22} + \sigma_{22}$ is the third invariant of the 3D invariant-based failure criterion [63].

Also, η_G is a material dependent empirically derived enhancement factor used in the definition of an effective fracture toughness for in-plane shear in the presence of transverse compressive stresses, σ_{22}:

$$\mathcal{G}_6^{ef} = \mathcal{G}_6\left(1 - \eta_G\langle -\sigma_{22}\rangle\right) \tag{4.11}$$

Table 4.5 shows the interlaminar properties used in the simulations, where K is the stiffness of the cohesive surfaces before damage onset, and η_{B-K} is the mixed-mode parameter of the B-K law [68].

Table 4.5: T700/M21 interlaminar properties

K /N mm^{-3}	$\mathcal{G}_{Ic}$ /N mm^{-1}	$\mathcal{G}_{IIc}$ /N mm^{-1}	η_{B-K} /−	τ_3 /MPa
1×10^5	0.545	1.387	1.5	60

For the lightning strike protections layers modelling are assumed homogeneous orthotropic linear-elastic solids. Following Karch et al. [43], the effective properties of ECF 73 and ECF 195

filled with epoxy resin M21 were determined using a micro-mechanical

finite element homogenization approach. The properties used in the simulations for both lightning strike protections layers are given in Table 4.6.

Table 4.6: Effective properties of ECF 73 and ECF 195 filled with epoxy resin M21

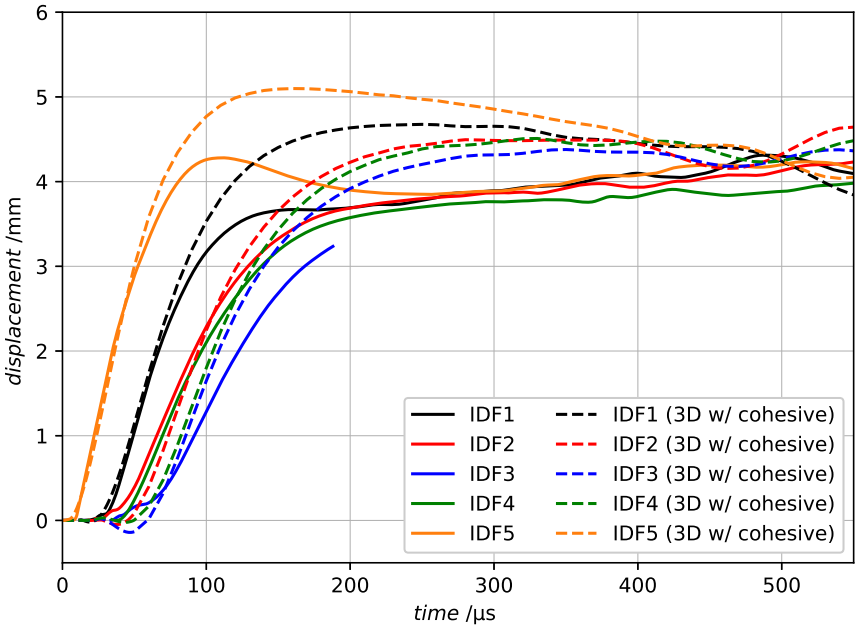
ECF 73	density /tonne m^{-3}		thickness /mm
	3.543×10^{-9}		0.051
	E_1 /MPa	G_{12} /MPa	ν_{12} /−
	12 057.5	5602.63	0.870 739
	E_2 /MPa	G_{23} /MPa	ν_{23} /−
	4802.54	3444.56	0.073 341
	E_3 /MPa	G_{13} /MPa	ν_{13} /−
	23 661.6	7179.23	0.174 582
ECF 195	density /tonne m^{-3}		thickness /mm
	2.474×10^{-9}		0.076
	E_1 /MPa	G_{12} /MPa	ν_{12} /−
	23 765.3	8796.59	0.992 35
	E_2 /MPa	G_{23} /MPa	ν_{23} /−
	6435.77	5263.77	0.055 93
	E_3 /MPa	G_{13} /MPa	ν_{13} /−
	41 292.9	13 031.3	0.196 641

The VISAR deflection measurements conducted by Lepetit et al. [19] strongly indicate that the lightning strike did not initiate from the middleof the CFRP samples. Therefore, motivate to validate the proposed mechanical model, Karch et al. [43] used a 2D symmetric Gauss function to fit the deflection in the measurement points IDF1 to IDF5 (see Figure 4.2) for different times. An averaged the time dependent offset coordinates was carried out, resulting in the values presented in Table 4.7.

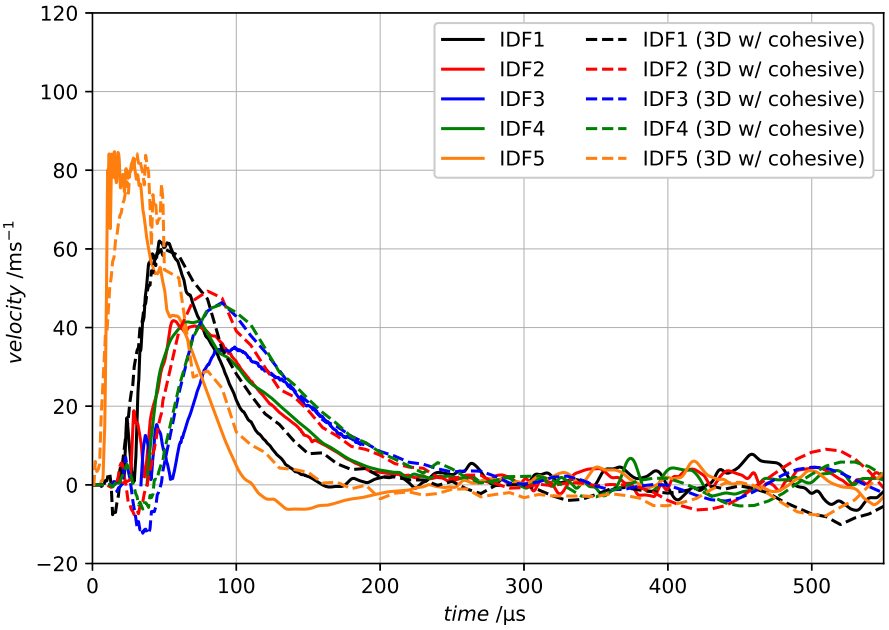
Table 4.7: Offset coordinates for ECF 73 and ECF 195.

	x_0 /mm	y_0 /mm
ECF 73	5.4	6.8
ECF 195	12.5	11.1

In order to validate the finite element model a comparison between numerical results and the experimental VISAR measurements for ECF 73 and ECF 195 performed by Lepetit et al. [19], showing in Figure 4.7 and Figure 4.8, respectively.

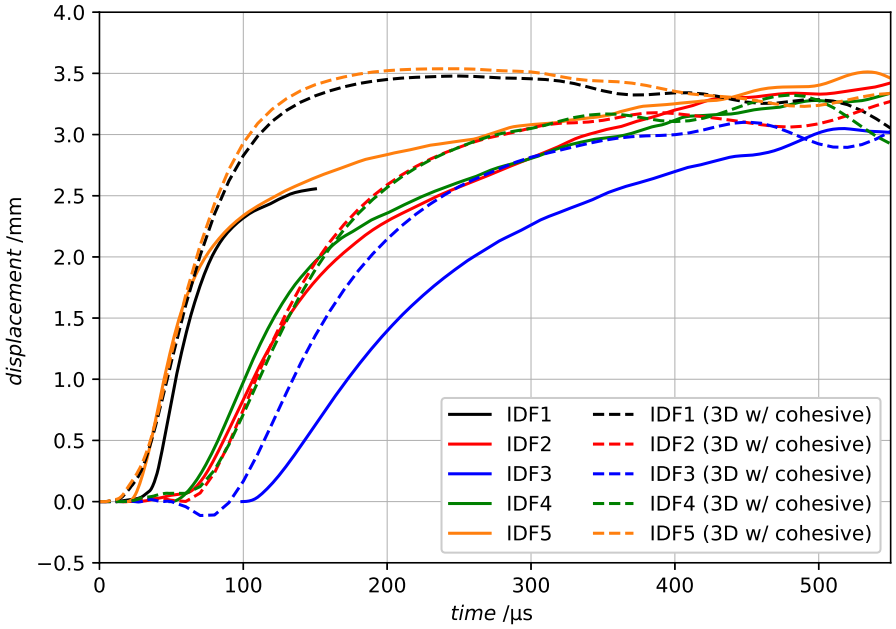


(a) Displacement

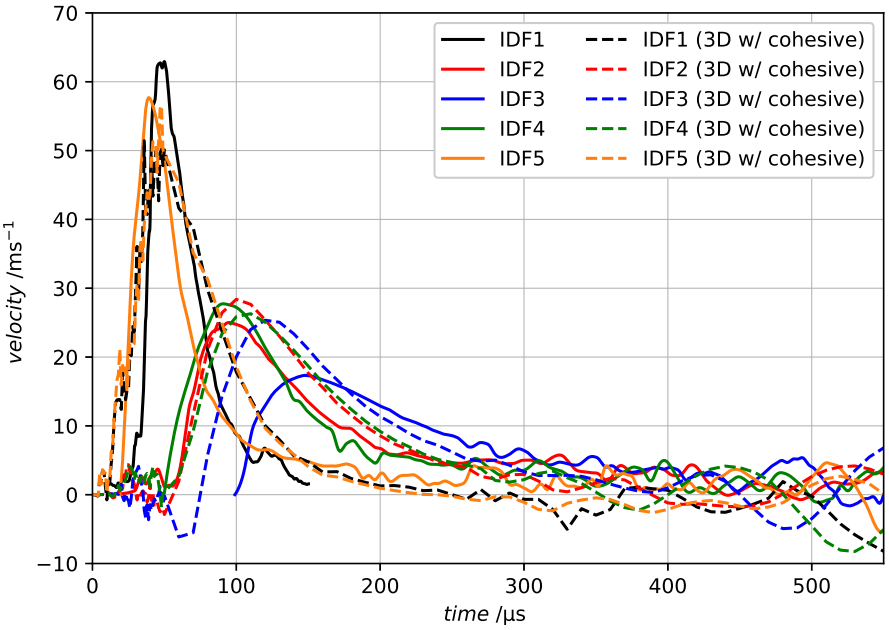


(b) Velocity

Figure 4.7: Finite element predictions (dashed lines) and VISAR measurements [19] (solid lines) for ECF 73



(a) Displacement



(b) Velocity

Figure 4.8: Finite element predictions (dashed lines) and VISAR measurements [19] (solid lines) for ECF 195

Note that the parameter k in the Equation 3.6 was set to 0.4 and 0.1 for ECF 73 and ECF 195 respectively, implying differences on how the pressure distribution caused by the explosion of LSP layers with $73.3\,\mathrm{g\,m^{-2}}$ and $195.3\,\mathrm{g\,m^{-2}}$ follow the arc root area.

The predictions of the out-of-plane velocity reproduce very well the experimental results at the different measurement points, in particular the peak velocities. Regarding the predicted deflections, although they exceed the experimental results at the initial 50 µs to 300 µs, the results then converge at around 500 µs, see Figure 4.7 and Figure 4.8.

These results demonstrate that the model of the lightning loads used for this study can accurately represent the mechanical contributions from a lightning strike, in particular when used together with detailed damage models for CFRPs.

4.5.1 Conclusion

Since the elements with reduced characteristic lengths suffer significant amounts of deformation near the impact zone, a smaller global time increment leads to an unreasonably large computational time. In Abaqus, mass scaling is a controlled procedure allowing the user to define an allowable minimum time step. The selective mass scaling is very efficient by only increasing the density of the elements causing the reduction of the maximum stable time increment in the model, meaning that the increase of mass in the whole model is as minimal as required. The value of the minimum stable time increment selected to activity selective mass scaling does not affect the response of the system, however reducing the CPU time by a factor of 4.

Part IV

Numerical study

Chapter 5

CFD analysis

Contents

5.1 Introduction

5.2 CFD approach

5.3 Finite element calculations

5.3.1 Pressure profile

5.4 Numerical results

5.4.1 Expanded copper foil 73

5.4.2 Damage maps

5.4.3 Expanded copper foil 195

5.4.4 Damage maps

5.5 Discussion

5.6 Conclusion

Objectives
This chapter evaluates the accuracy of the implementation of a strong shock wave approximation to characterize the supersonic expansion of the hot plasma channel. The analytical equation will be compared with Computational Fluid Dynamics (CFD) computations to assess the representation of the supersonic plasma expansion phenomenon.

5.1 Introduction

The temporal and spatial propagation of the shock waves and pressures required for the simulation of lightning-induced mechanical damage to composite structures can be derived from semi-analytical or numerical CFD computations. As presented in section 3.5, the mechanical load generated by the rapid temperature rise of the lightning plasma channel can be introduced by a strong shock wave approximation (Equation 3.12).

In order to evaluate the use of the strong shock wave approximation as an adequate and reliable approach to accurately describe the mechanical damage on composite structures, numerical Computational Fluid Dynamics (CFD) computations are performed. These experiments provided by AIRBUS support the numerical finite element calculations in this work to assess the use of an analytical shock wave approximation instead of more sophisticated and complex methods.

5.2 CFD approach

The theoretical establishment of this study is the Riemann problem, so the software used of CFD analysis must provide the ability to user or implement appropriate equations of state (EOS).

For the CFD calculations, the blastFoam solver from the open-source toolbox blastFoam Version 5.0 [70] , which is based on the OpenFOAM® framework [71], was used [72]. The numerical method is depended on full finite volume discretization and takes for the present work advantage of the HLLC flux discretization introduced by Toro [73].

The solver lastFoam solves generally the compressible Navier- Stokes equations for a large variety of fluid and explosion models in three dimensions. Note that Navier-Stokes equations with zero viscosity and zero thermal conductivity are known as Euler equations too [74]. It is important once the propagation of shock waves generated by lightning discharges can be derived from Eulerian equations of mass, momentum and energy conservation [75].

Three different EOS were applied and compared in the finite element calculations.

Ideal gas assumption: Perfect gas with constant heat capacity C_p =1004 J kg^{-1} K^{-1}, specific gas constant R=287 J kg^{-1} K^{-1}, and γ =1.4.

Doan-Nickel: The EOS of Doan and Nickel [76] includes changes in the composition of air at high temperatures and the variation of the specific heat ratio due to dissociation of molecules.

Plooster: The “air2” EOS of Plooster [77; 78], which also accounts for molecular changes, is stated by means of two equations, (i) expressing the specific internal energy as a function of temperature and (ii) expressing the pressure as a function of temperature and density. However, to use the equations in the blastfoam solver, the equations must be numerically solved for temperature and pressure as a function of the specific internal energy and density with high accuracy [72].

5.3 Finite element calculations

To impose a cylindrical symmetry, the numerical domain in the CFD computations is modelled as a wedge with a 2 m of radius. Thus, only one cell layer is necessary for the axial direction. On the other hand, in the radial direction used a graded mesh with 2500 cells and an expansion ratio of 40 from the innermost to the outermost cell length turned out, ensuring mesh independency of the numerical results.

Some conditions are imposed such as symmetry and zero gradient boundary conditions for pressure, temperature and velocity are applied at the domain boundaries, and the centre axis so the pressure wave leaves the domain without reflection. The resultant fields are interpolated to the cell centres of the grid, while in the remaining domain, atmospheric pressure and the ambient temperature of 300 K were applied.

As an output from the computational measurements with this information are a [2500 × 701] matrix, which represented the location on the sample from the attachment point to 2 m, representing the wedge, within a time run of 3.5 µs, respectively the lines and columns of the matrix.

5.3.1 Pressure profile

To understand the difference between the strong shock wave and the three cases performed by CFD calculations, a graphical approach for the pressure profile evolution over the radius, assuming the initial value the attachment point, was done for 5 instant times: 5 µs, 10 µs, 20 µs, 50 µs and 100 µs. For this analysis, the corrected radial overpressure profile was used, as **??** shows.

Therefore, the pressure profile of the three EOS *Ideal gas assumption*, EOS *Doan-Nickel* and EOS *Plooster* are presented in Figure 5.1, Figure 5.2 and Figure 5.3, respectively.

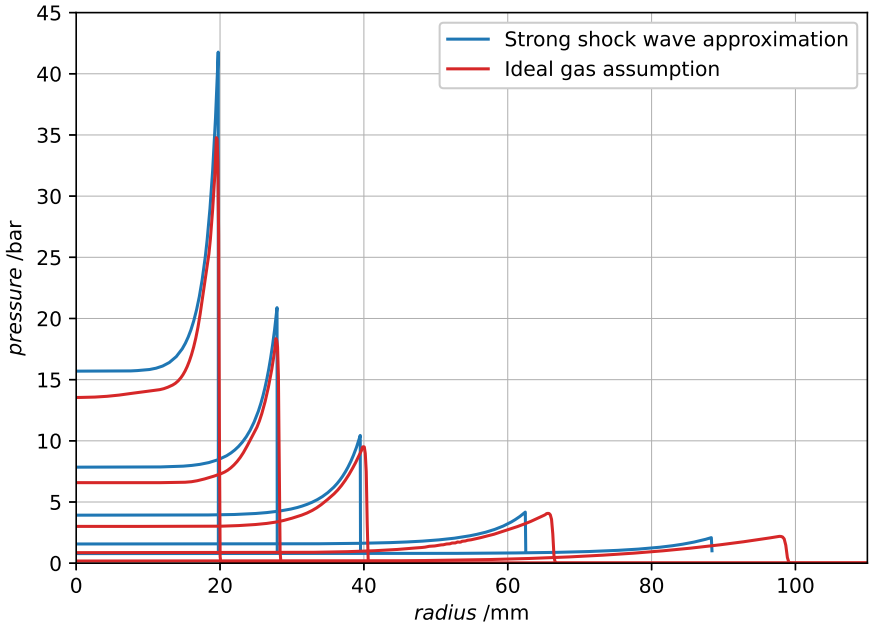


Figure 5.1: Pressure profile of the EOS *Ideal gas assumption*, and comparison with the strong shock wave approximation

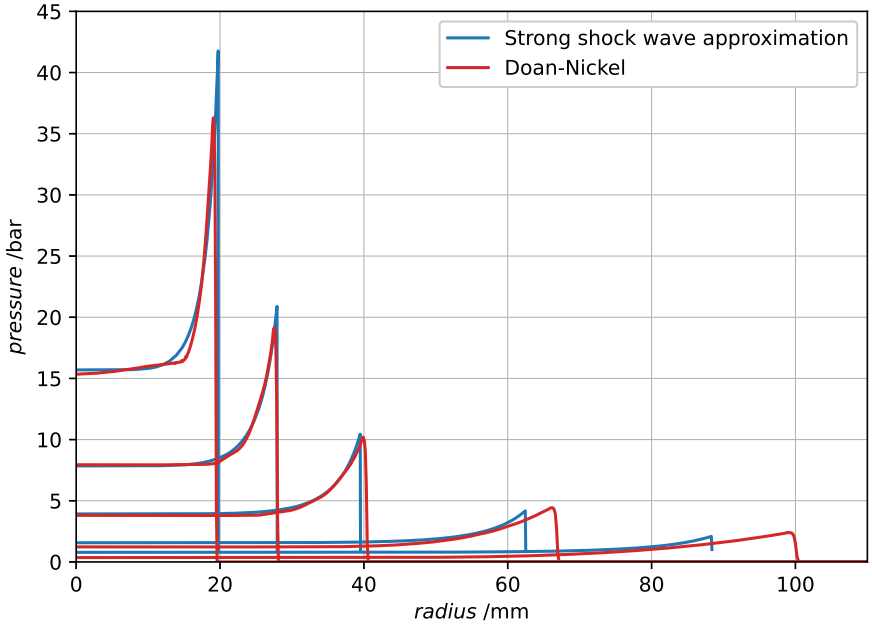


Figure 5.2: Pressure profile of the EOS *Doan-Nickel*, and comparison with the strong shock wave approximation

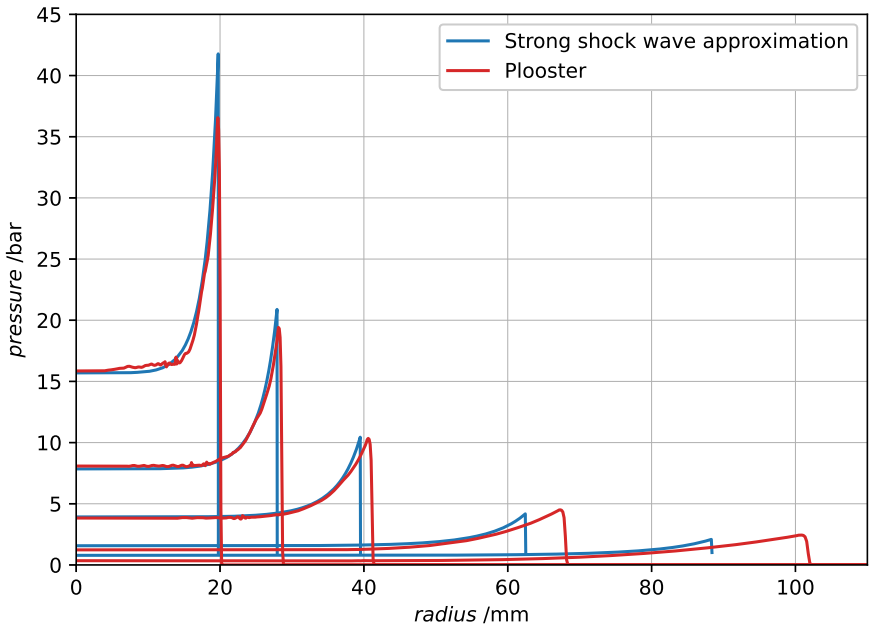


Figure 5.3: Pressure profile of the EOS *Plooster*, and comparison with the strong shock wave approximation

5.4 Numerical results

To replace the analytical equation of the strong shock wave approximation with the data given by the CFD calculations some modifications in the the FORTRAN VDLOAD subroutine were performed to read a $[2500 \times 701]$ matrix and use the overpressure value given by the CFD measurements.

The overpressure of the supersonic plasma expansion is then determined by the use of a bilinear interpolation. The theoretical approach is summarised in Equation 5.1 and Figure 5.4.

$$\begin{aligned} f(x,y) \approx & \frac{f(Q_{11})}{(x_2-x_1)(y_2-y_1)}(x_2-x)(y_2-y) \\ & + \frac{f(Q_{21})}{(x_2-x_1)(y_2-y_1)}(x-x_1)(y_2-y) \\ & + \frac{f(Q_{12})}{(x_2-x_1)(y_2-y_1)}(x_2-x)(y-y_1) \\ & + \frac{f(Q_{22})}{(x_2-x_1)(y_2-y_1)}(x-x_1)(y-y_1) \end{aligned} \tag{5.1}$$

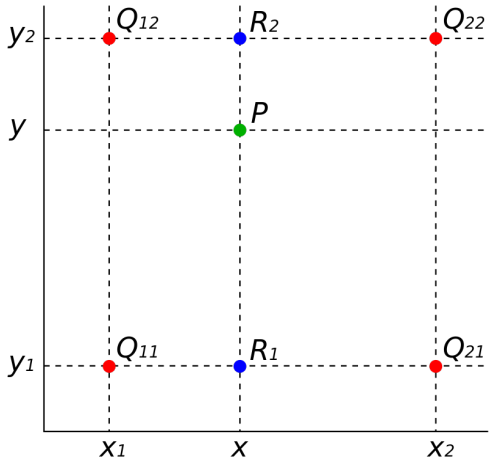


Figure 5.4: Bilinear interpolation foundation

The investigation carried out was performed for two lightning strike protections, the expanded copper foil 73 ($73.3\,\mathrm{g\,m^{-2}}$ of copper) and for the expanded copper foil 195 ($195.3\,\mathrm{g\,m^{-2}}$ of copper). The numerical results are divided in two analysis: (i) a numerical analysis of the displacement and velocity at the five IDFs points already defined, adding a graphical visualization of the displacement development during 500 µs for each case, and (ii) a damage map analysis for each layer of the laminate, exploring the induced damage of the lightning strike through the thickness of the structure.

5.4.1 Expanded copper foil 73

5.4.1.1 CFD - Ideal gas assumptions

Figure 5.5 presents the displacement map obtained with the EOS *Ideal gas assumption*, and Figure 5.6 compares the finite element predictions for the strong shock wave approximation and the EOS *Ideal gas assumption*. A slightly larger displacement is predicted when considering the EOS *Ideal gas assumption* for time periods above 100 µs.

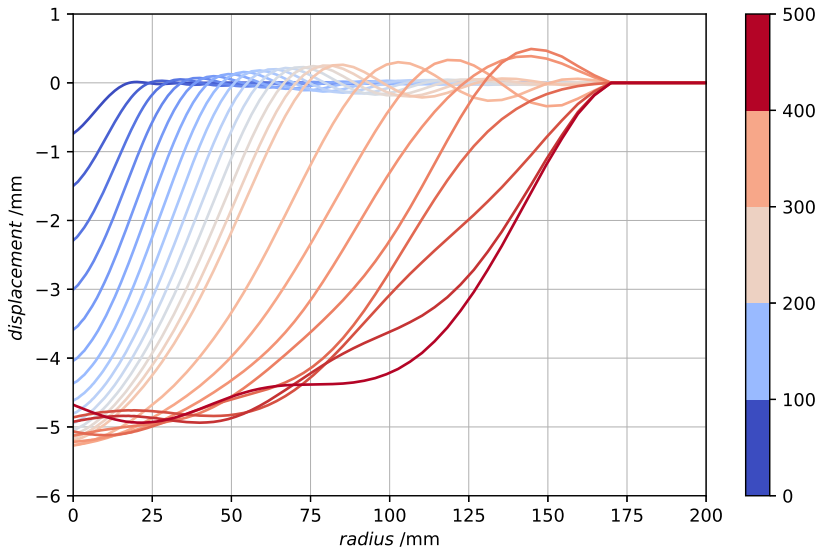
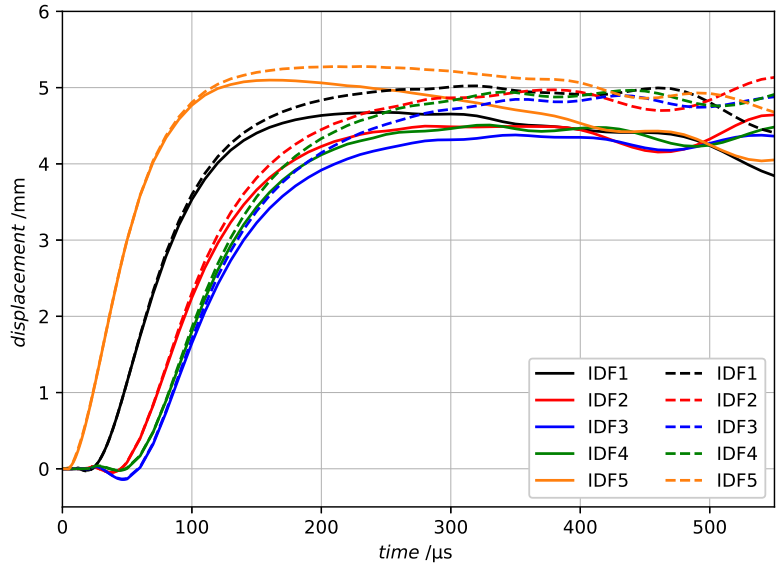
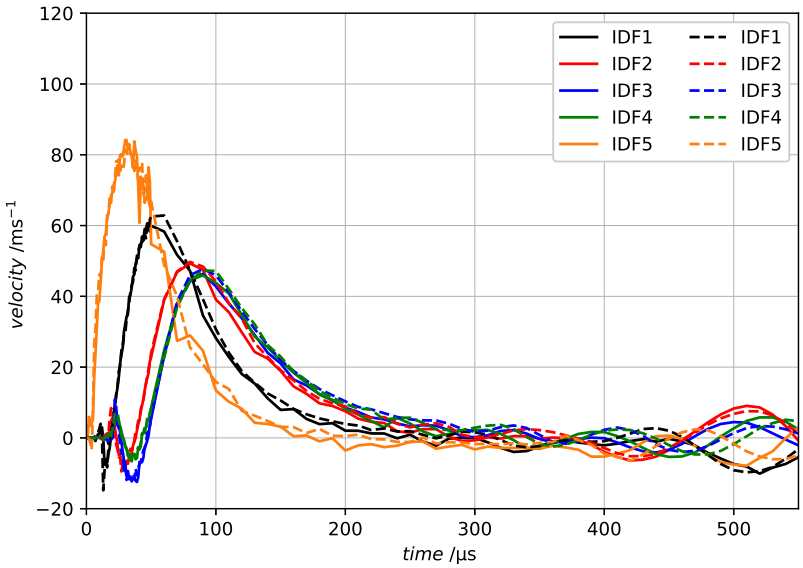


Figure 5.5: Displacement map for ECF 73 within a time $t \leq 500\,\mu s$ (colour bar) of the EOS *Ideal gas assumption*



(a) Displacement



(b) Velocity

Figure 5.6: Finite element predictions with analytical approximation (solid lines) and CFD calculations of the EOS *Ideal gas assumption* (dashed lines) for ECF 73

5.4.1.2 CFD - Doan Nickel

Figure 5.7 presents the displacement map obtained with the EOS *Doan-Nickel*, and Figure 5.8 compares the finite element predictions for the strong shock wave approximation and the EOS *Doan-Nickel*. Similar trends to the previous EOS are observed.

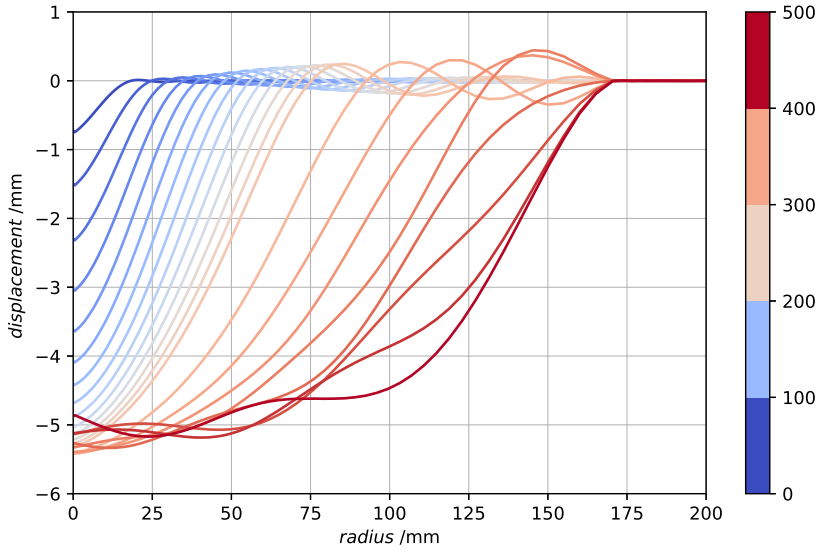
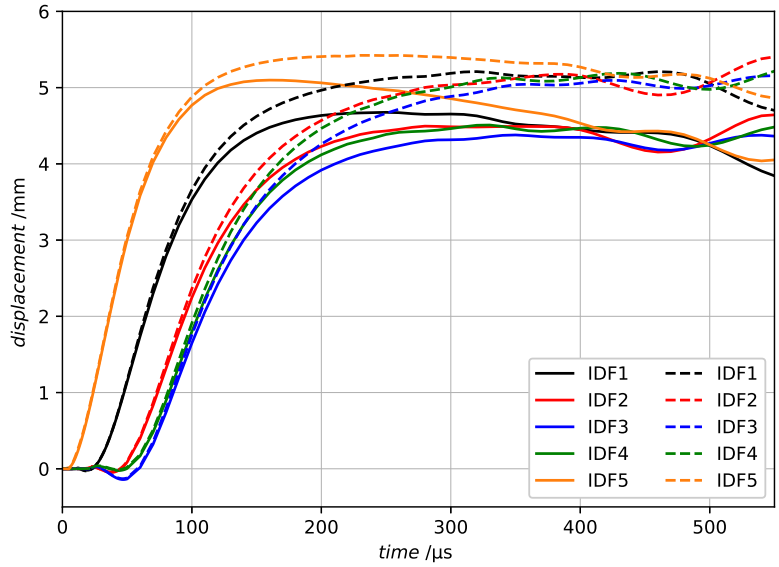
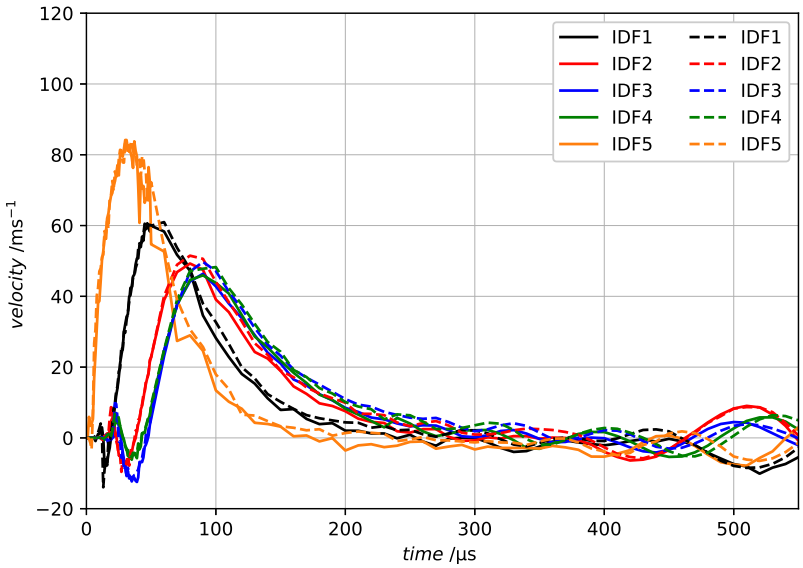


Figure 5.7: Displacement map for ECF 73 within a time $t \leq 500\,\mu s$ (colour bar) of the EOS *Doan-Nickel*



(a) Displacement



(b) Velocity

Figure 5.8: Finite element predictions with analytical approximation (solid lines) and CFD calculations of EOS *Doan-Nickel* (dashed lines) for ECF 73

5.4.1.3 CFD - Plooster

Figure 5.9 presents the displacement map obtained with the EOS *Plooster*, and Figure 5.10 shows the finite element predictions for the strong shock wave approximation and the EOS *Plooster*. Similar trends to the previous EOS are observed.

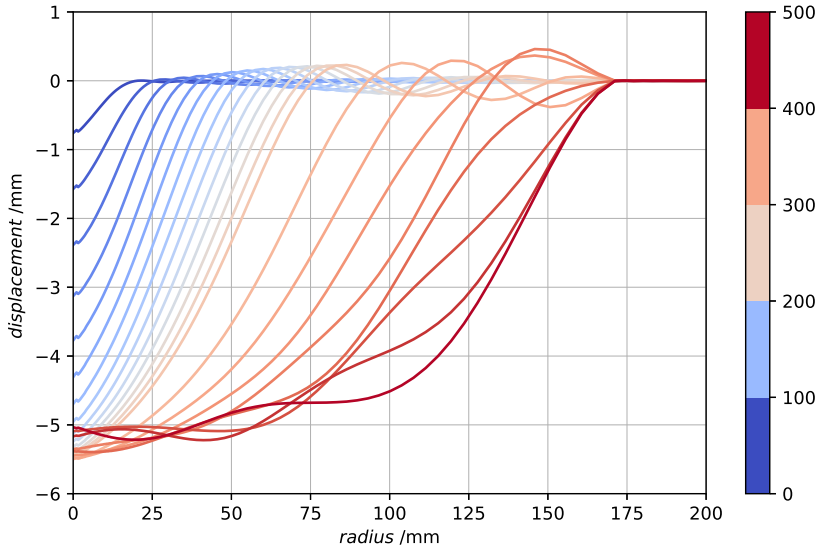
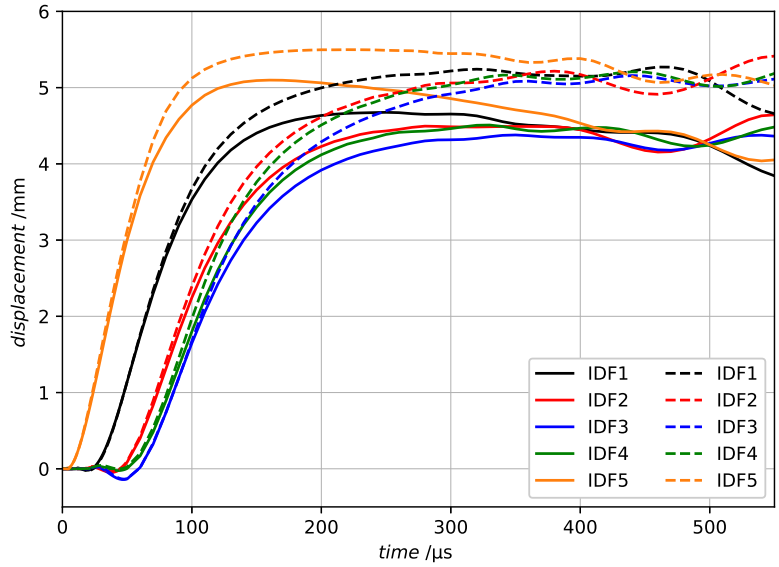
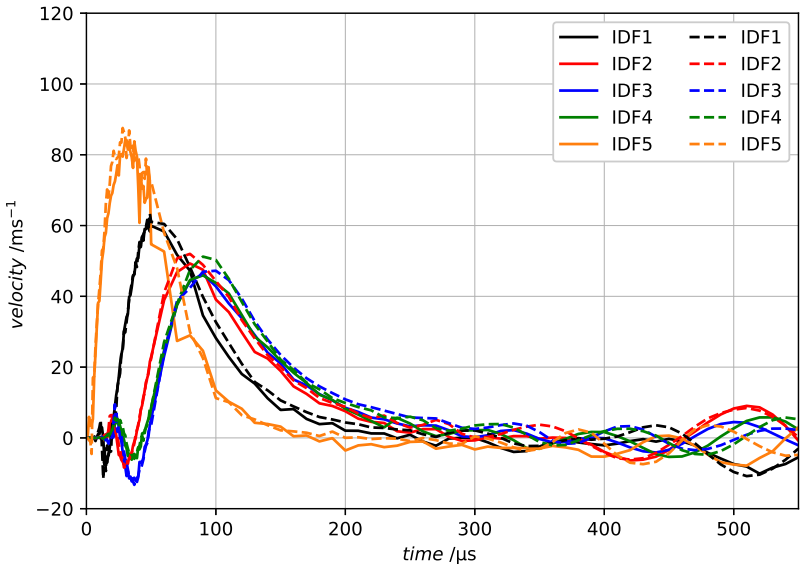


Figure 5.9: Displacement map for ECF 73 within a time $t \leq 500\,\mu s$ of the EOS *Plooster*



(a) Displacement



(b) Velocity

Figure 5.10: Finite element predictions with analytical approximation (solid lines) and CFD calculations of the EOS *Plooster* (dashed lines) for ECF 73

5.4.2 Damage maps

The damage map assessment was performed to evaluate the onset of damage, and possible failure, considering the damage variables in the longitudinal direction (d_1), transverse direction (d_2), shear (d_6) and delamination (d).

Table 5.1: Damage map assessment of the damage variable in the longitudinal direction (d_1) for the strong shock wave approximation and CFD calculations for ECF 73

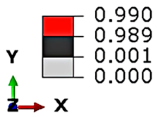
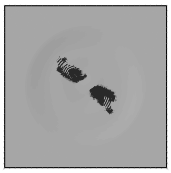
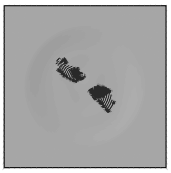
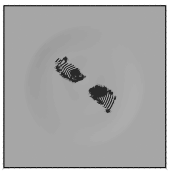
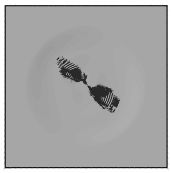
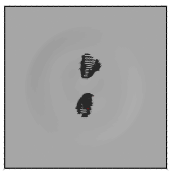
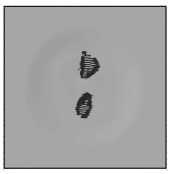
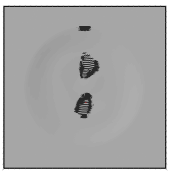
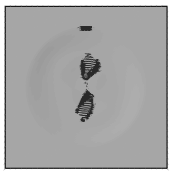
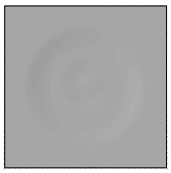
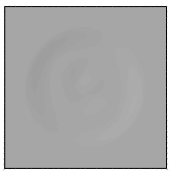
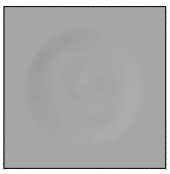
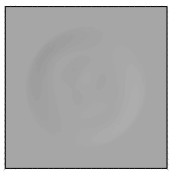
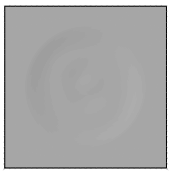
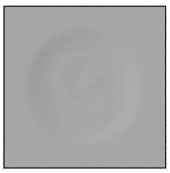
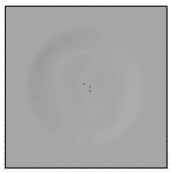
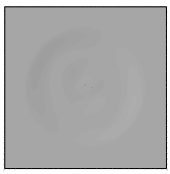
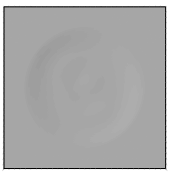
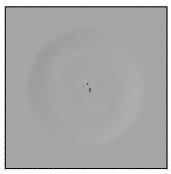
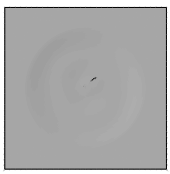
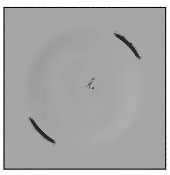
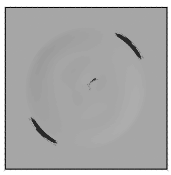
	Strong shock wave approximation	CFD - Ideal gas	CFD - Doan Nickel	CFD - Plooster
Layer 8				
Layer 7				
Layer 6				
Layer 4 and 5				
Layer 3				
Layer 2				
Layer 1				

Table 5.2: Damage map assessment of the damage variable in the transverse direction (d_2) for the strong shock wave approximation and CFD calculations for ECF 73

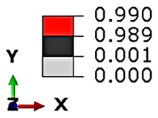
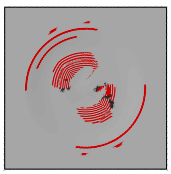
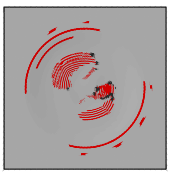
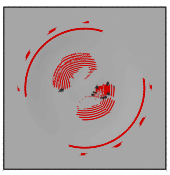
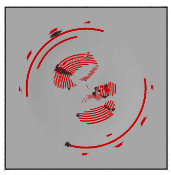
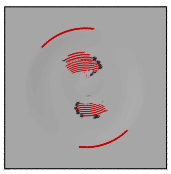
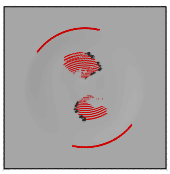
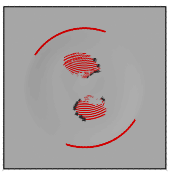
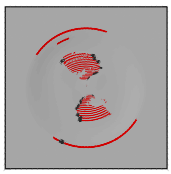
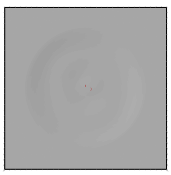
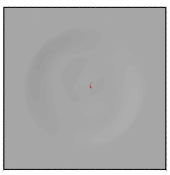
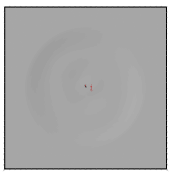
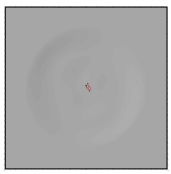
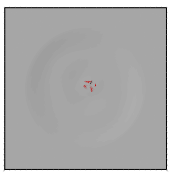
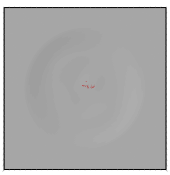
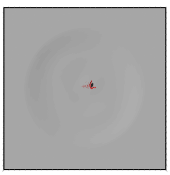
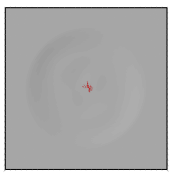
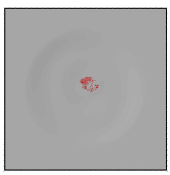
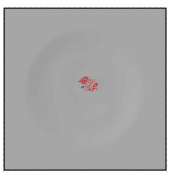
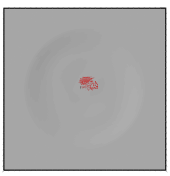
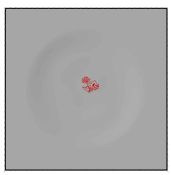
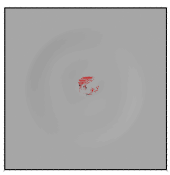
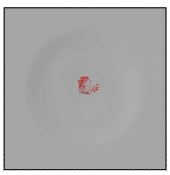
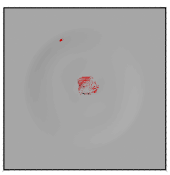
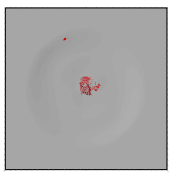
	Strong shock wave approximation	CFD - Ideal gas	CFD - Doan Nickel	CFD - Plooster
Layer 8				
Layer 7				
Layer 6				
Layer 4 and 5				
Layer 3				
Layer 2				
Layer 1				

Table 5.3: Damage map assessment of the shear damage variable (d_6) for the strong shock wave approximation and CFD calculations for ECF 73

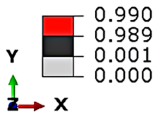
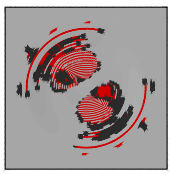
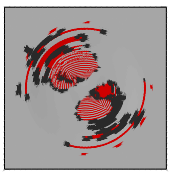
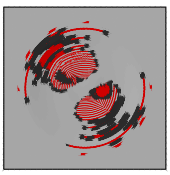
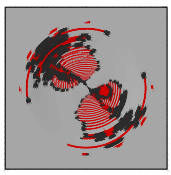
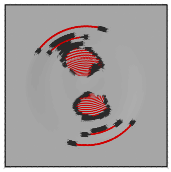
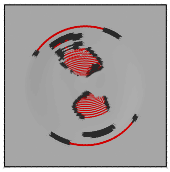
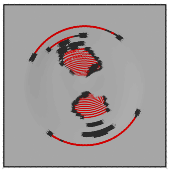
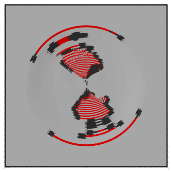
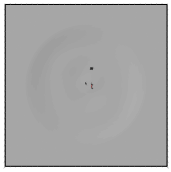
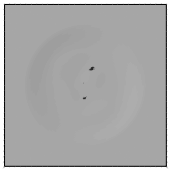
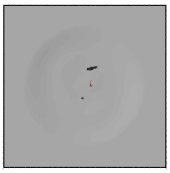
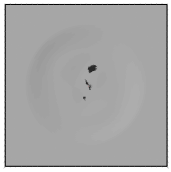
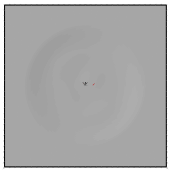
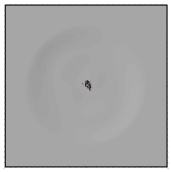
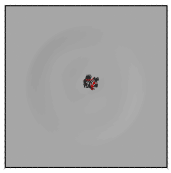
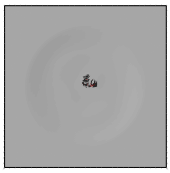
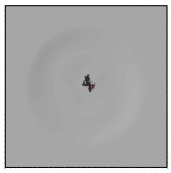
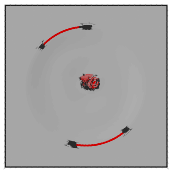
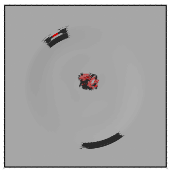
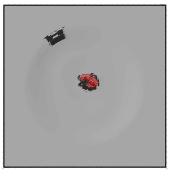
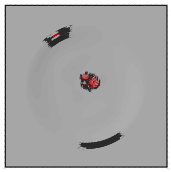
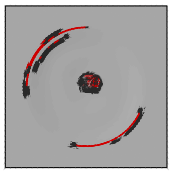
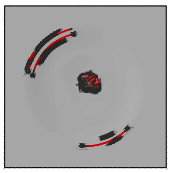
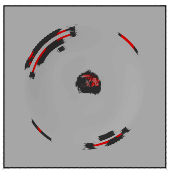
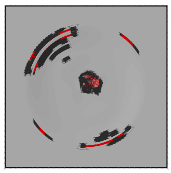
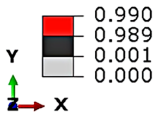
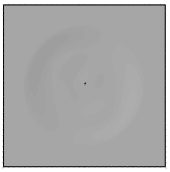
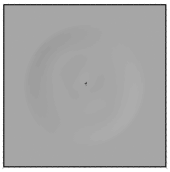
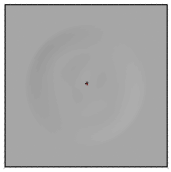
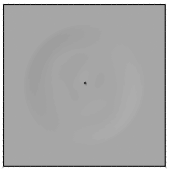
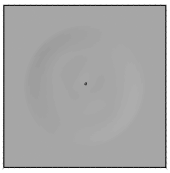
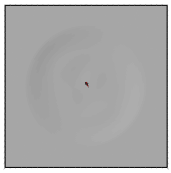
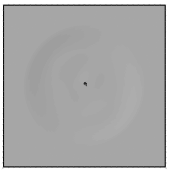
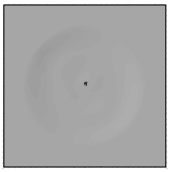
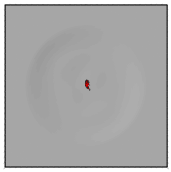
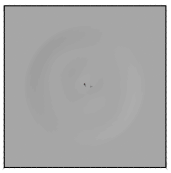
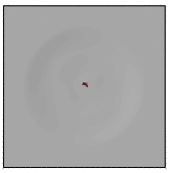
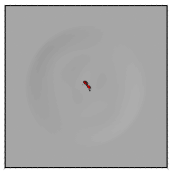
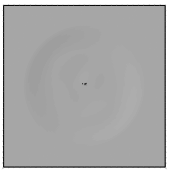
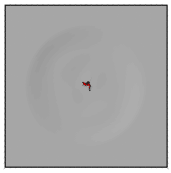
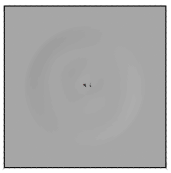
	Strong shock wave approximation	CFD - Ideal gas	CFD - Doan Nickel	CFD - Plooster
Layer 8				
Layer 7				
Layer 6				
Layer 4 and 5				
Layer 3				
Layer 2				
Layer 1				

Table 5.4: Damage map assessment of the damage variable for cohesive surfaces (d) for the strong shock wave approximation and CFD calculations for ECF 73

	Strong shock wave approximation	CFD - Ideal gas	CFD - Doan Nickel	CFD - Plooster
Layer 8				
Layer 7				
Layer 6				
Layer 4 and 5				
Layer 3				
Layer 2				
Layer 1				

5.4.3 Expanded copper foil 195

5.4.3.1 CFD - Ideal gas assumption

Figure 5.11 presents the displacement map obtained with the EOS *Ideal gas assumption*, and Figure 5.12 shows the finite element predictions for the strong shock wave approximation and the EOS *Ideal gas assumption*. Slightly lower displacements are obtained for the initial time periods.

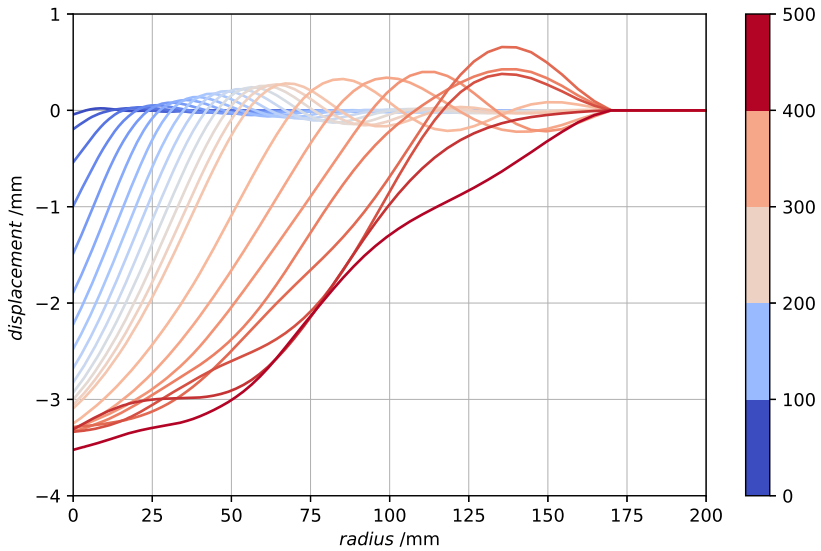
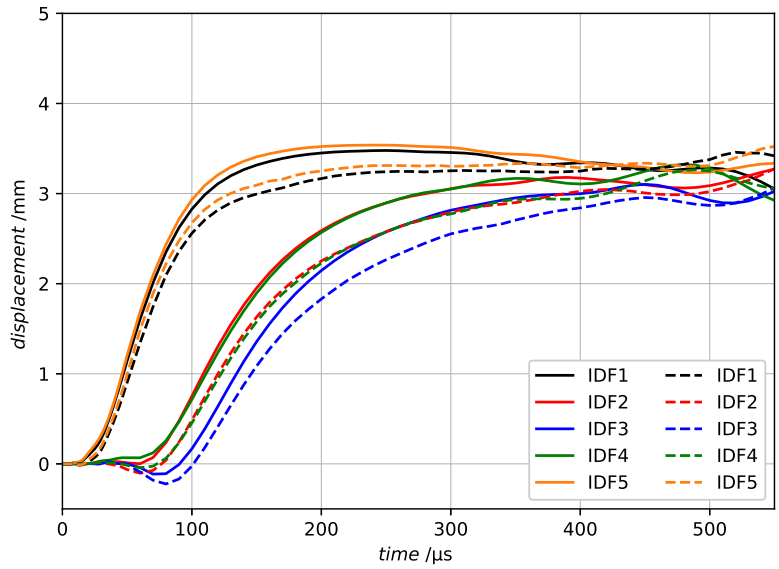
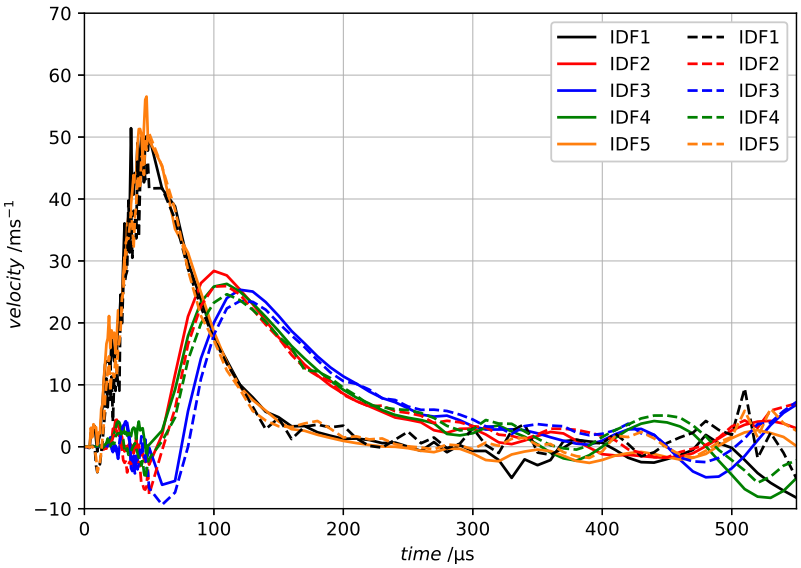


Figure 5.11: Displacement map for ECF 195 within a time $t \leq 500\,\mu s$ (colour bar) of the EOS *Ideal gas*



(a) Displacement



(b) Velocity

Figure 5.12: Finite element predictions with analytical approximation (solid lines) and CFD calculations of the EOS *Ideal gas* (dashed lines) for ECF 195

5.4.3.2 CFD - Doan Nickel

Figure 5.13 presents the displacement map obtained with the EOS *Doan-Nickel*, and Figure 5.14 shows the finite element predictions for the strong shock wave approximation and the EOS *Doan-Nickel*. In this case, a slightly larger displacement is predicted with the EOS *Doan-Nickel* for time periods above 100 µs.

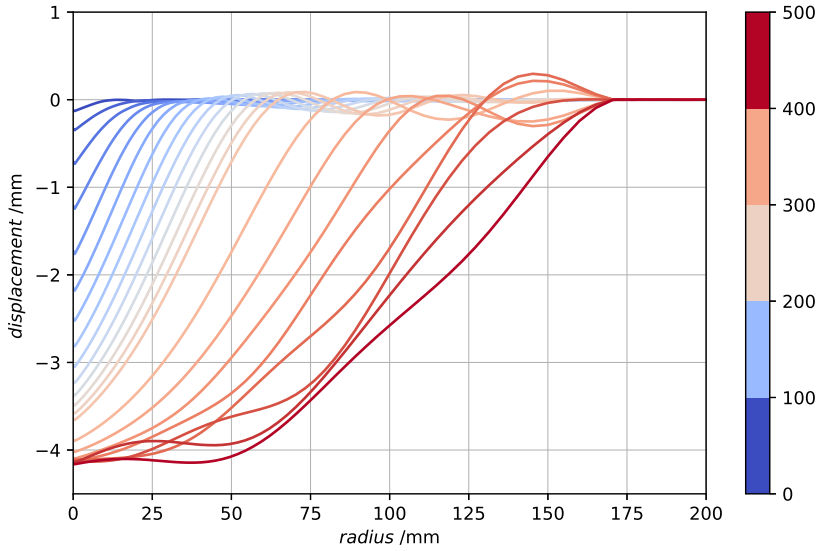
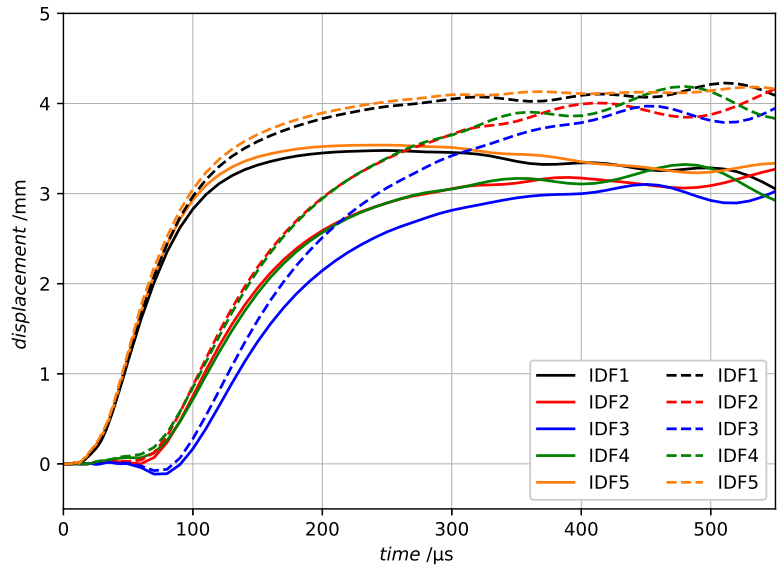
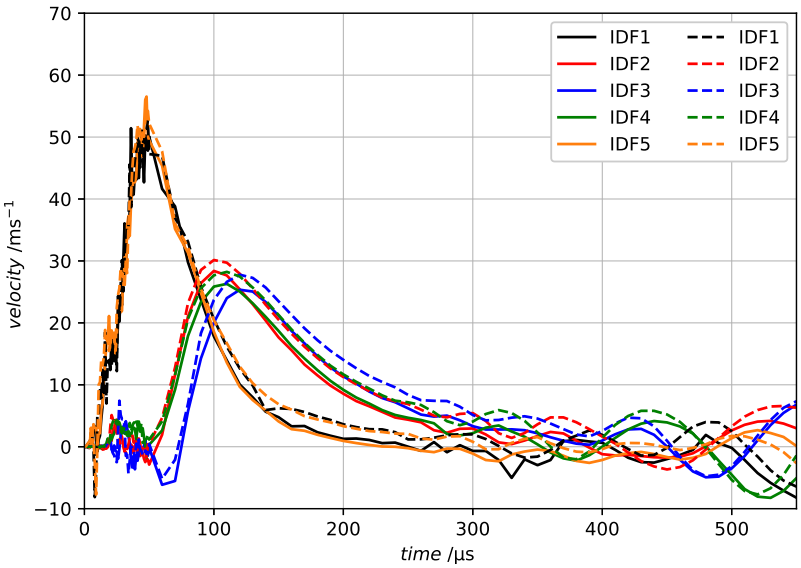


Figure 5.13: Displacement map for ECF 195 within a time $t \leq 500\,\mu s$ (colour bar) of the EOS *Doan-Nickel*



(a) Displacement



(b) Velocity

Figure 5.14: Finite element predictions with analytical approximation (solid lines) and CFD calculations of the EOS *Doan-Nickel* (dashed lines) for ECF 195

5.4.3.3 CFD - Plooster

Finally, Figure 5.15 presents the displacement map obtained with the EOS *Plooster*, and Figure 5.16 shows the finite element predictions for the strong shock wave approximation and the EOS *Plooster*. Similar trends to the ones predicted by the EOS *Doan-Nickel* are observed.

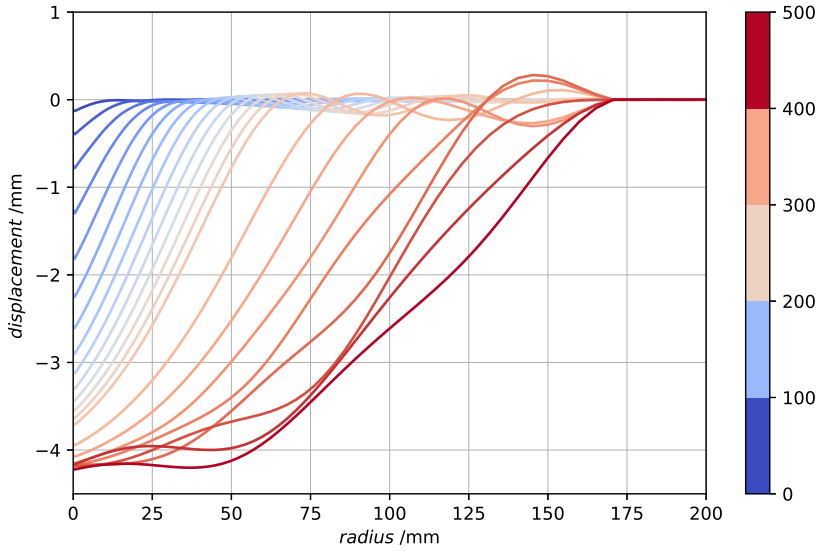
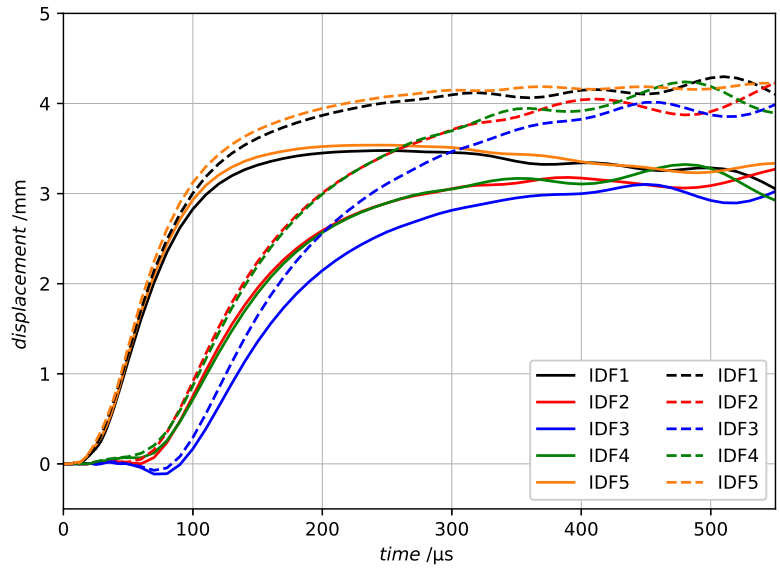
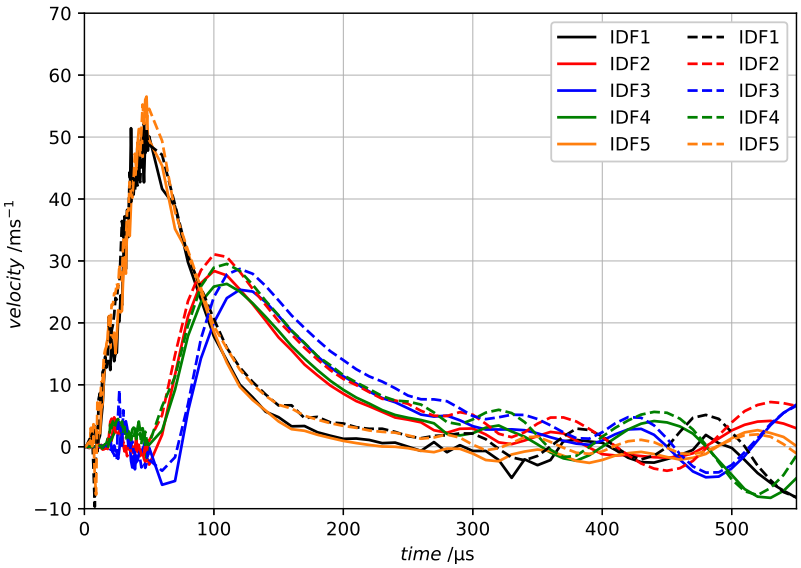


Figure 5.15: Displacement map for ECF 195 within time $\leq 500\,\mu s$ of the EOS *Plooster*



(a) Displacement



(b) Velocity

Figure 5.16: Finite element predictions with analytical approximation (solid lines) and CFD calculations of the EOS *Plooster* (dashed lines) for ECF 195

5.4.4 Damage maps

Similar to ECF 73, a damage map assessment is performed here to evaluate the onset of damage, and possible failure, by plotting the damage variables in the longitudinal direction (d_1), transverse direction (d_2), shear (d_6) and delamination (d).

Table 5.5: Damage map assessment of the damage variable in the longitudinal direction (d_1) for the strong shock wave approximation and CFD calculations for ECF 195

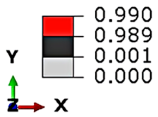
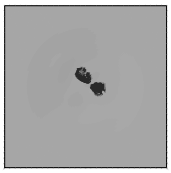
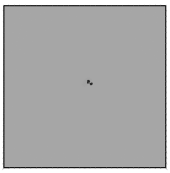
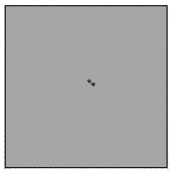
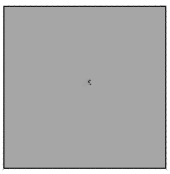
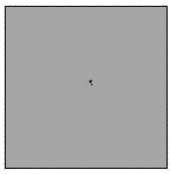
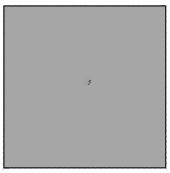
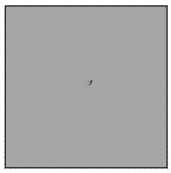
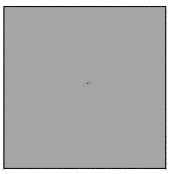
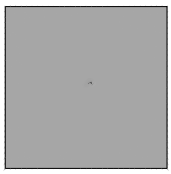
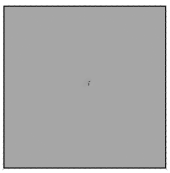
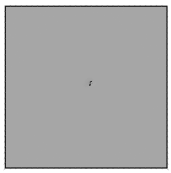
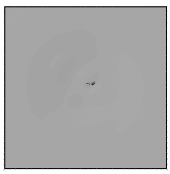
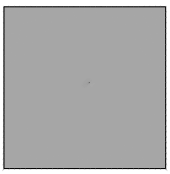
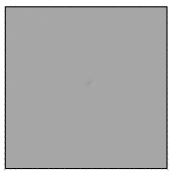
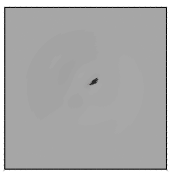
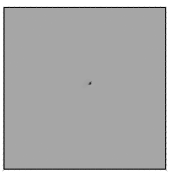
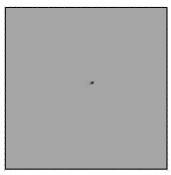
	Strong shock wave approximation	CFD - Ideal gas	CFD - Doan Nickel	CFD - Plooster
Layer 8				
Layer 7				
Layer 6				
Layer 4 and 5				
Layer 3				
Layer 2				
Layer 1				

Table 5.6: Damage map assessment of the damage variable in the transverse direction (d_2) for the strong shock wave approximation and CFD calculations for ECF 195

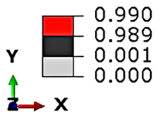
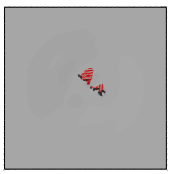
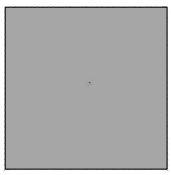
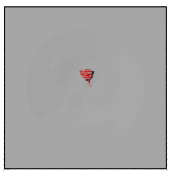
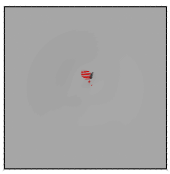
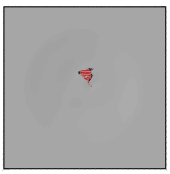
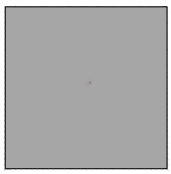
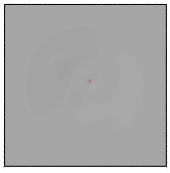
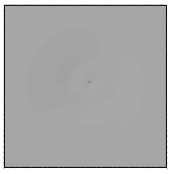
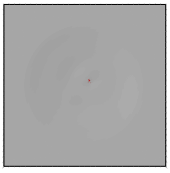
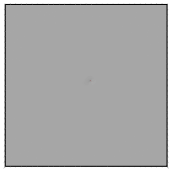
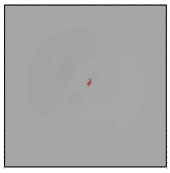
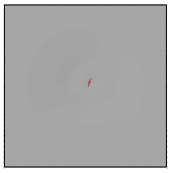
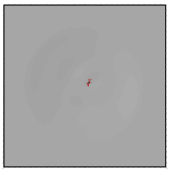
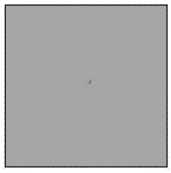
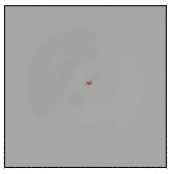
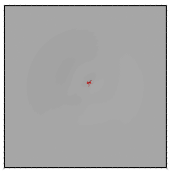
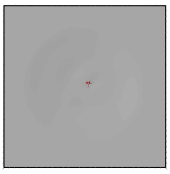
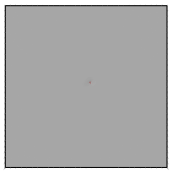
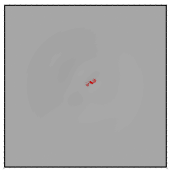
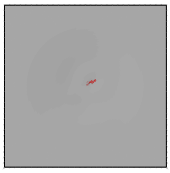
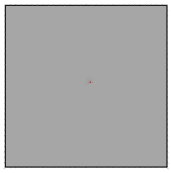
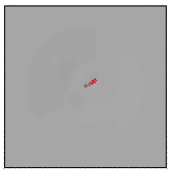
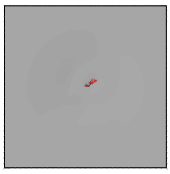
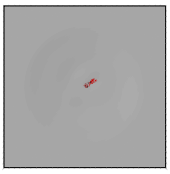
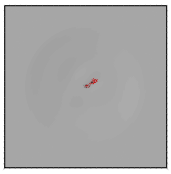
	Strong shock wave approximation	CFD - Ideal gas	CFD - Doan Nickel	CFD - Plooster
Layer 8				
Layer 7				
Layer 6				
Layer 4 and 5				
Layer 3				
Layer 2				
Layer 1				

Table 5.7: Damage map assessment of the shear damage variable (d_6) for the strong shock wave approximation and CFD calculations for ECF 195

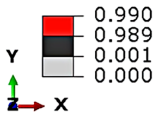
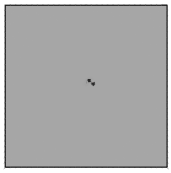
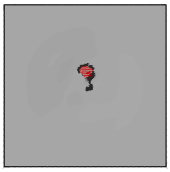
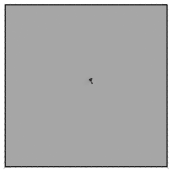
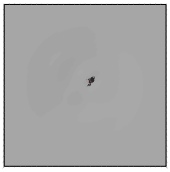
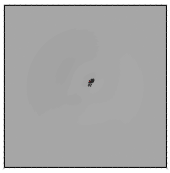
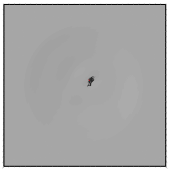
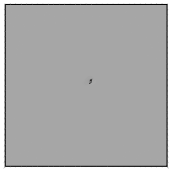
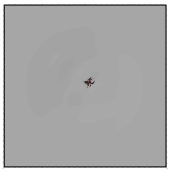
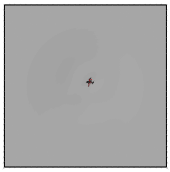
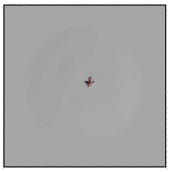
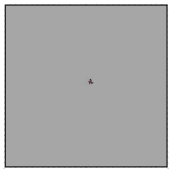
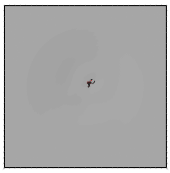
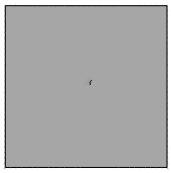
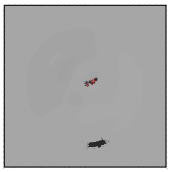
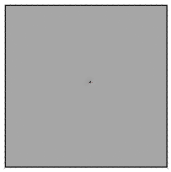
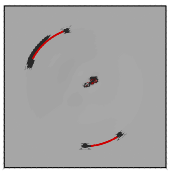
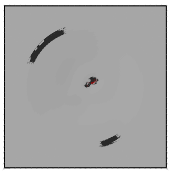
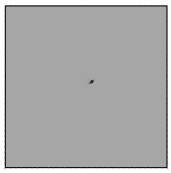
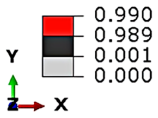
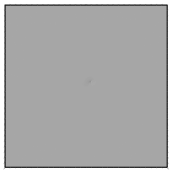
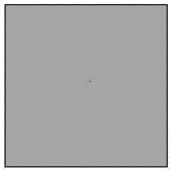
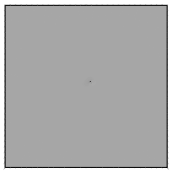
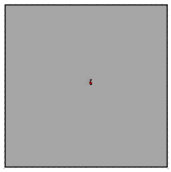
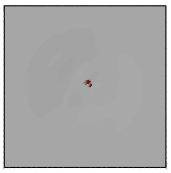
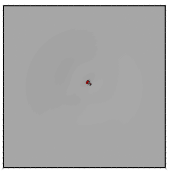
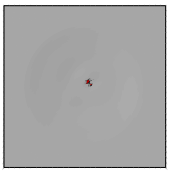
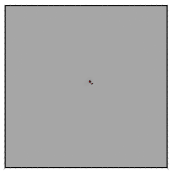
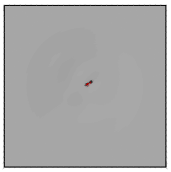
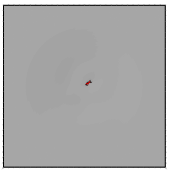
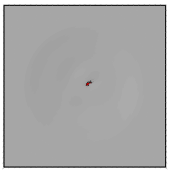
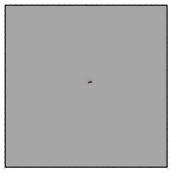
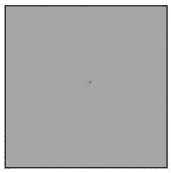
	Strong shock wave approximation	CFD - Ideal gas	CFD - Doan Nickel	CFD - Plooster
Layer 8				
Layer 7				
Layer 6				
Layer 4 and 5				
Layer 3				
Layer 2				
Layer 1				

Table 5.8: Damage map assessment of the damage variable for cohesive surfaces (d) for the strong shock wave approximation and CFD calculations for ECF 195

	Strong shock wave approximation	CFD - Ideal gas	CFD - Doan Nickel	CFD - Plooster
Layer 8				
Layer 7				
Layer 6				
Layer 4 and 5				
Layer 3				
Layer 2				
Layer 1				

5.5 Discussion

Through a pressure profile analysis, some divergences are notorious in the peak pressure at the different instant times selected. Despite the expected improvements of the accuracy of the mechanical simulations, the need to read and interpolate external data during the mechanical finite element simulations leads to a significant increase of the run time in some cases reaching a factor of 7.

For the six different simulations that used CFD calculations presented in this analysis, a numerical assessment methodology was replicated and compared to the reference model of each lightning strike protection. The displacement and velocity at the five points of the rear surface panel previously defined were used to compare the analytical approach based on a strong shock wave approximation and the CFD calculations.

The strong shock wave approximation is based on the theoretical approach of Karch et al. [20] that use the cylindrical blast shock wave model of a lightning return stroke developed by Lin [55] for an ideal problem. So, as expected, the equation of state for a perfect gas achieves similar quantitative results for displacement and velocity. The discrepancy observed can be reduced by an optimization of the input parameters in the equation of the strong shock wave approximation.

For the cases considering the EOS from *Doan-Nickel* and *Plooster*, higher values of displacement are predicted. Nevertheless, the agreement of the analytical equation with the numerical CFD computations is observed for the expanded copper foil 73 ($73.3\,\mathrm{g\,m^{-2}}$ of copper) and also for the expanded copper foil 195 ($195.3\,\mathrm{g\,m^{-2}}$ of copper).

Finally, the evaluation of the damage induced on each layer of the laminate, considering the damage variables in the longitudinal direction (d_1), transverse direction (d_2), shear (d_6) and delamination (d), shows very similar results in all cases.

5.6 Conclusion

This part of the work aimed to support and validate the use of a strong shock wave approximation to predict mechanical damage on composite structures caused by the supersonic expansion of the hot plasma channel. Based on three different EOS, CFD analyses were used to determine the overpressure generated. Using a modified non-uniform pressure distribution obtained from reading the CFD data, the predictions of the analytical strong shock wave approximation were compared with those obtained using the CFD calculations.

The assessment of the pressure profiles, the numerical predictions of the displacement and velocity of the previously validated test cases, and the analysis of the predicted damage maps show that, for the both lightning strike protection layers, the strong shock wave approximation provides a reasonably good description of the effects of the supersonic plasma expansion loads. This is particularly important considering that the use of an analytical model for the overpressure allows avoiding the additional step comprising CFD calculations, at the same time it reduces the cost of the mechanical computations..

Chapter 6

Effect of paint thickness

Contents

6.1 Introduction

6.2 Surface explosion theory

6.3 Literature background

6.4 Numerical results

6.4.1 Expanded copper foil 73

6.4.2 Expanded copper foil 195

6.5 Discussion

6.6 Conclusion

Objectives
The objective of this chapter is to evaluate the effect of the paint thickness in the damage induced by lightning strikes. The confinement effect of the paint is a significant parameter affecting the damage in composite structures. In this chapter, unpainted structures and three different thicknesses of the paint layer are considered.

6.1 Introduction

In the aircraft industry, it is common to paint the skin of the structures, either to protect the surface from environmental effects or simply to personalize the aircraft. In the case of composites structures, particularly CFRP frames, the use of paint becomes even more necessary to create a uniform exterior surface.

Paints are generally insulative and may influence the mechanism of damage to CFRP structures after lightning strikes. It is important to take into consideration the thickness of these paints. This parameter has a significant responsibility on the dissipation of the incident lightning current on the surface, which can reduce the performance of the LSP drastically [26][79].

Thus, it is necessary to control the paint thickness. For aircraft applications, an extensive set of material specifications is defined [80]. The first part of the specifications concerns the physical and chemical properties of the individual components of the paint. Note that the paint is made from two components, the base and the hardener. The second part concerns the physical properties of the liquid paint before application. A final part concerns the dry film properties with cosmetic requirements and tests to assess its resistance to the aeronautical environment, as no blisters or cracks should be produced.

Since the main function of paint is cosmetic, very few specifications concern the mechanical properties of the paint for aeronautical applications. The adhesion is estimated following ISO 2409 [81], the resistance to impact is assessed based on ISO 6272 [82], the resistance to scratch is measured with ISO 1518 [83] and the flexibility is tested according to ISO1519 [84].

Altogether, the effect of paint thickness is an important parameter to study on the damage induced by lightning strikes in composites plates.

6.2 Surface explosion theory

While composite laminates with a LSP layer are more efficient than a unprotected composite panels when subjected to lightning strikes [85], the efficiency of the LSP layer decreases with the paint thickness [26; 79]. The Joule heating of the metallic protection is considered the cause for this phenomenon, leading to its explosion [20]. Since paint has influence on the damage imposed due to the confinement of explosive gases, the damage induced by lightning strikes are dependent of the paint thickness [26; 36].

The presence of the paint adds a further complexity to the lightning strike event, which could be approximate to a thick dielectric film over the metallic protection. This produces two effects:

1. Dielectric constriction effect of the lightning arc and energy dissipation into the metal protection [36; 86].
2. Confinement of the surface explosion. The slow ejection of the paint compared to the explosion propagation in the LSP will enhance the shock wave generated by the

explosion induced by the sudden vaporisation of the metallic protection due to Joule effect, leading to additional damage [19; 49].
Therefore, the parameters that will affect the overpressure enhancement are the density and the paint thickness. Otherwise, the thickness of the panel does not have influence on the surface phenomena [36].

The damage induced can be separated in two sections: surface damage and structural damage. The surface damage can be measured by visual inspection, where vaporisation of the LSP and ejection of the paint, and dry fibres (tufting) due to resin deterioration and broken fibres be able to be inspected [49]. This damage is mainly due to the electro-thermal effect of the lightning current in the LSP and in the composite [16][19]. On the other hand, the structural damage needs a specialized procedure for the assessment. A common inspection is ultrasonic C-scan [24] or X-ray [87] analysis to measure the delamination. Although the thermal damage concentrated in the centre of the impact, the lightning strike is a far more complex phenomenon than thermal damage due to current flow in the structure. An significant damage to be assess is the delamination that has a mechanical origin [16].

6.3 Literature background

Several studies have already been reported about the influence of the paint thickness in lightning damage, including composite materials, or aluminium structures in aircraft. It is clear that the type and the thickness of the paint layer are some of the most important factors in the damage induced from lightning strikes to the aircraft structures [16; 37]

Bigand and Duval [26] clearly demonstrates that the damage increase with the paint thickness. In this study was used thin carbon laminate panels protected with Expanded Copper Foil. Murillo et al. [36] showed that a variation of the paint thickness can lead to an increase in the size of the damage induced. The same work also proves the importance of the thickness of the dielectric layer in the mechanical loads suffered by the panel, with a thicker paint layer is associated to a faster deflection of the panel.

Lepetit et al. [19] show that the paint layer enhances the shock waves due to the concentrated arc, with a detrimental effect on the damage caused by lightning strikes.

A few more authors studied the paint thickness effect using aluminium panels. Chemartin et al. [21] studied aluminum and composite panels. In both cases a correlation was found between the increase of damage and the thicker paint layer of the panels tested. Superficial damage was identified for lower paint thicknesses, while the panel was punctured for thicker paint layers.

Lago [88] used stereo digital image correlation to study the paint thickness effect on the deformation. The thicker the paint layer, the larger the deflection. Moupfouma [48] studied the effect of paint thickness on lightning swept stroke damages, correlated paint thickness, lightning dwell time, and aircraft skin thickness.

Lepetit et al. [19] developed the first model considering the confinement effect due to the paint on the overpressure, which was improved by Karch et al. [20]. In this approach,

the paint is considered as a mass, which leads to an inertial effect on the overpressure occurring on the surface. Alternatively, Espinosa et al. [89] used thermomechanical numerical simulations to assess the effect of an overpressure due to the presence of paint on the damage suffered by the composite. The paint confinement contribution was simulated by an equivalent pressure.

Experiments shows, supported by high-speed camera analysis, that an explosion occurred on the surface due to the rapid vaporisation of the LSP layer [19]. Similar, Bigand et al. [37] performed specific tests that demonstrate the expansion of the lightning arc and hot gases, the shock front propagation from the lightning arc and the ejection of pieces of paint.

6.4 Numerical results

Considering an unpainted plate and plates with different thicknesses, the contributions of the near-surface explosion, supersonic plasma expansion and magnetic forces are determined and implemented in the VDLOAD subroutine used in the finite element model. The predicted displacements and the predicted velocities are then compared, as well as the damage induced on the unpainted plate and on the plates with different paint thicknesses.

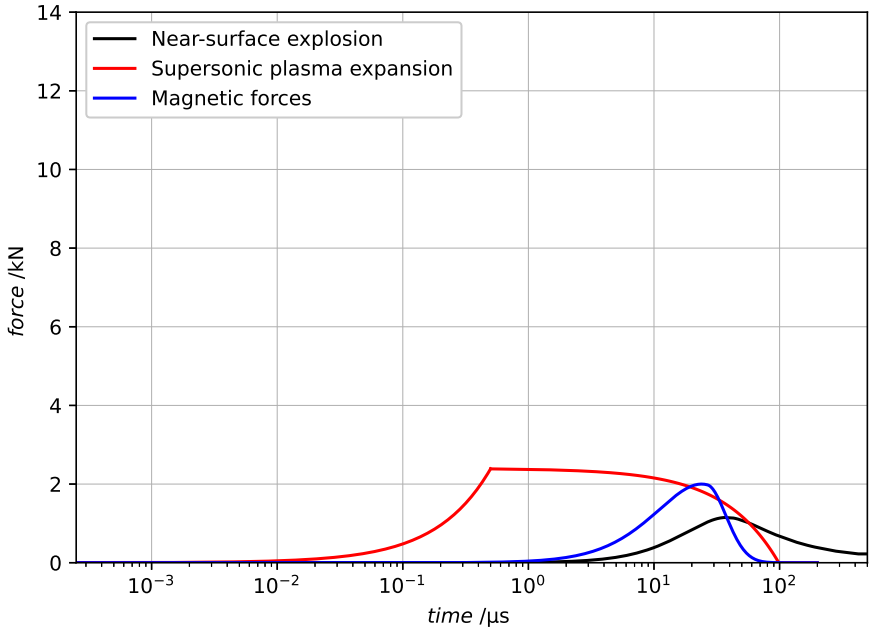
Although the objective of this work is not the comparison between lightning strike protections, to reinforce the assessment of the paint thickness effect the two alternatives of lightning strike protections implemented in the previously validated finite element model were used.

It is important to note that the overpressure due to the near-surface explosion of the lightning protection layer, the mechanical effect providing the major contribution in the reference case (chapter 3 and chapter 4), is the lightning pressure contribution directly affected by the thickness of the paint layer. Therefore, this is the contribution that needs to be recalculated for all the cases in study: unpainted, 200 µm, 300 µm and 400 µm paint layer thickness for the two lightning protection layers, ECF 73 and ECF 195. Considering an unpainted plate and plates with different thicknesses, the contributions of the near-surface explosion, supersonic plasma expansion and magnetic forces are determined and implemented in the VDLOAD subroutine used in the finite element model. The predicted displacements and the predicted velocities are then compared, as well as the damage induced on the unpainted plate and on the plates with different paint thicknesses..

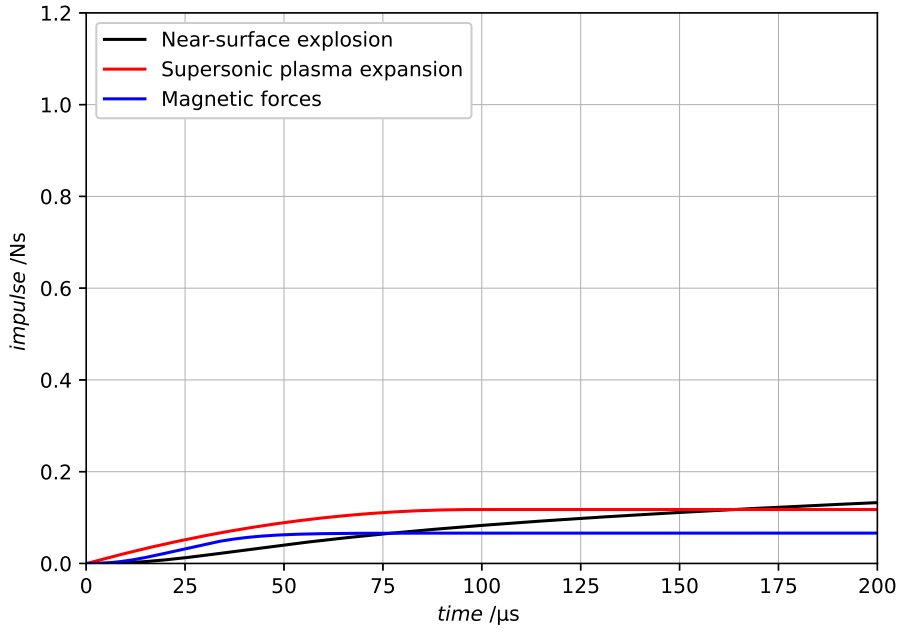
6.4.1 Expanded copper foil 73

6.4.1.1 No paint

Figure 6.1 and Figure 6.2 summarize the numerical results performed for the case of unpainted panels. It is interested to note that the near-surface explosion of the lightning protection layer, the mechanical constraint with major of the damage imposed, are lower than the other two contributions, the supersonic plasma expansion and the magnetic forces.

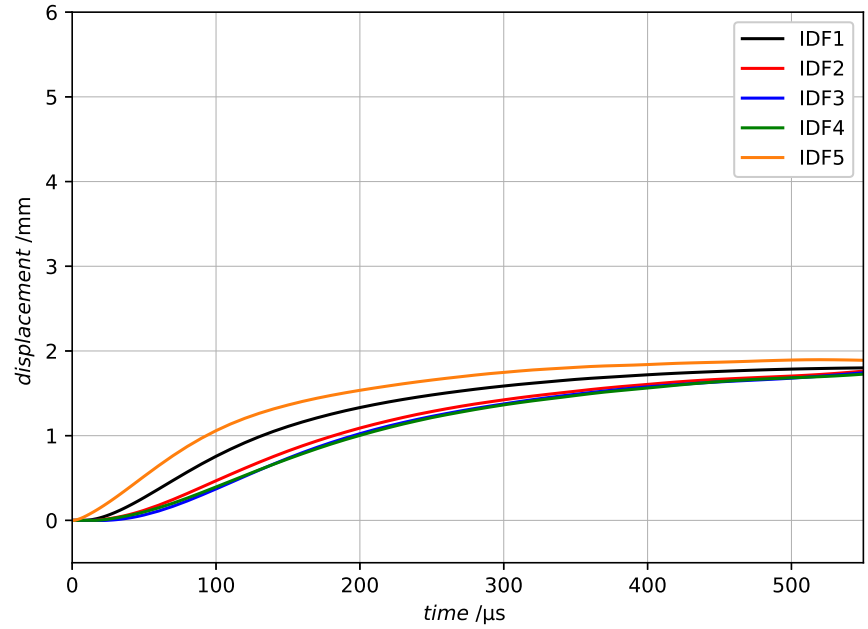


(a) Force magnitude

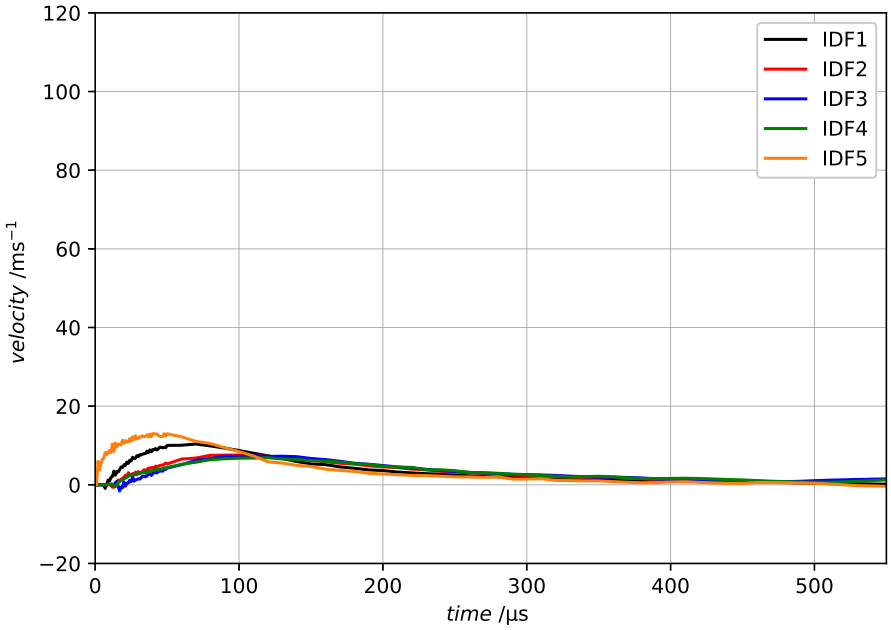


(b) Impulse magnitude

Figure 6.1: Mechanical contributions for the unpainted sample of ECF 73



(a) Displacement

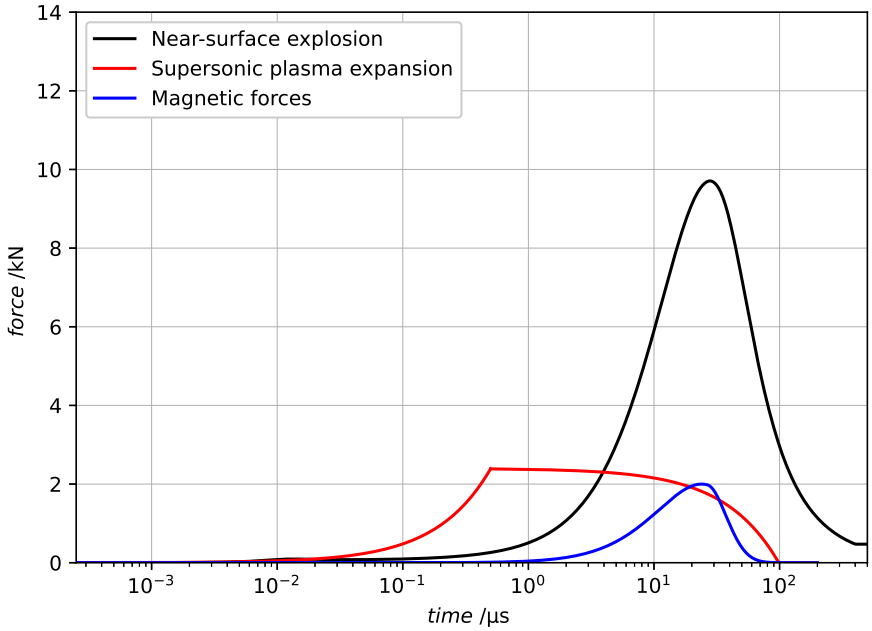


(b) Velocity

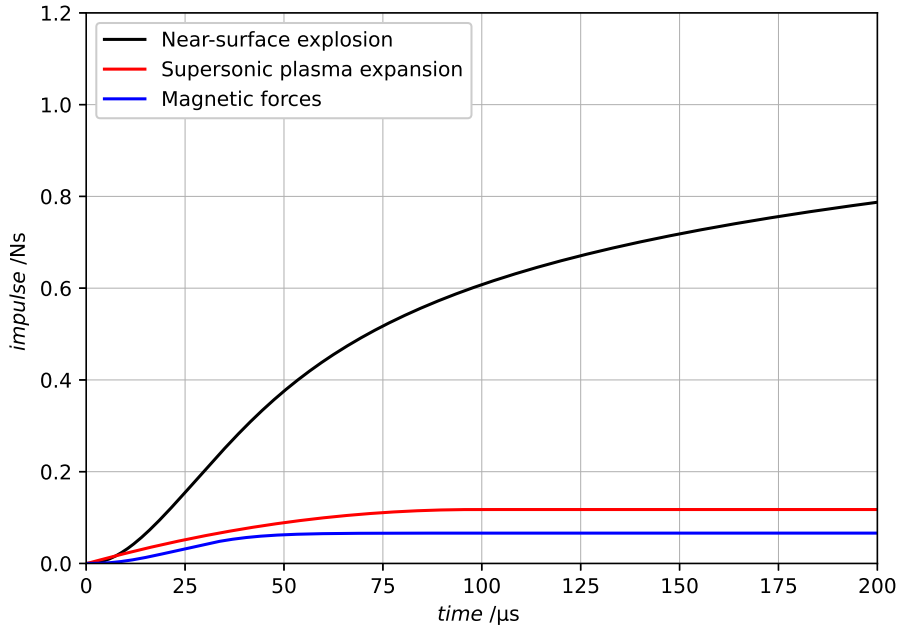
Figure 6.2: Finite element predictions for the unpainted sample of ECF 73

6.4.1.2 200 µm paint thickness

Figure 6.3 and Figure 6.4 summarize the numerical results performed for the case of 200 µm of paint thickness. It is clear that the presence of paint generate more notable impact, the force magnitude by the near-surface explosion of the lightning protection layer is almost ten times higher than the case of unpainted samples.

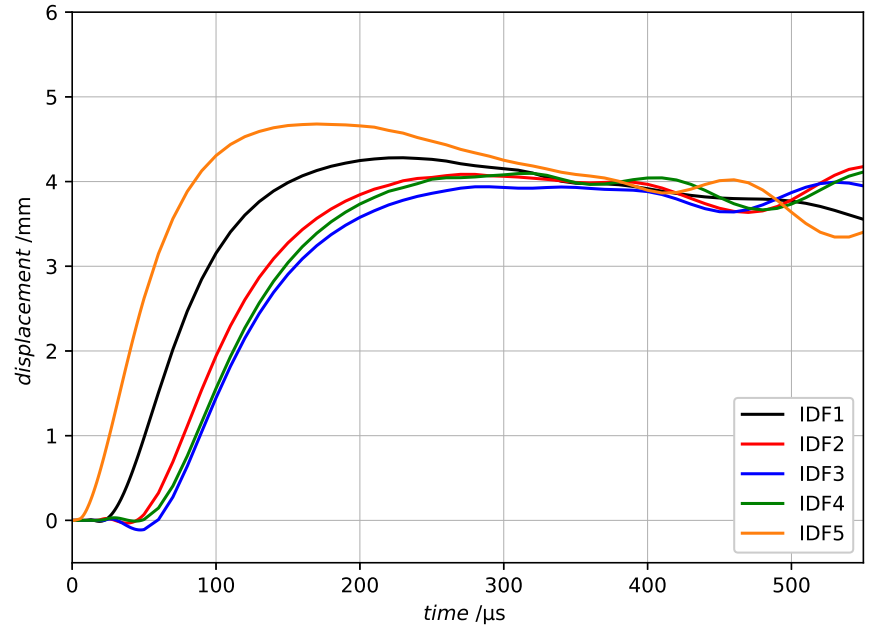


(a) Force magnitude

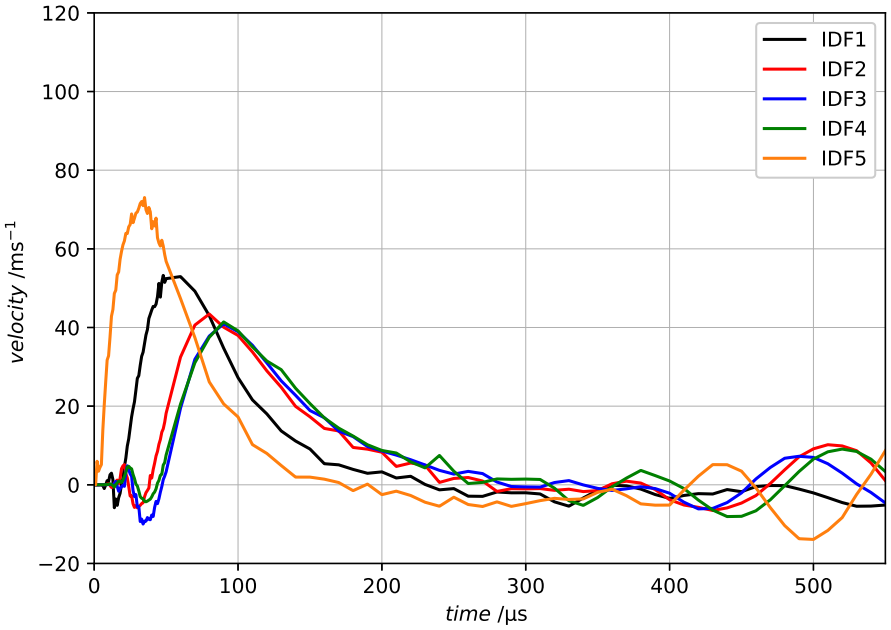


(b) Impulse magnitude

Figure 6.3: Mechanical contributions for the sample with 200 µm paint thickness of ECF 73



(a) Displacement

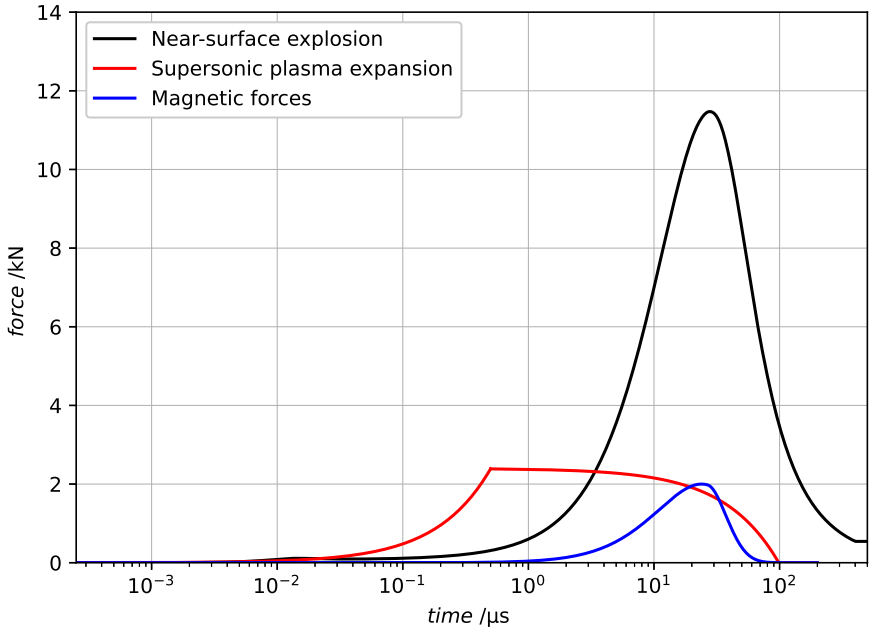


(b) Velocity

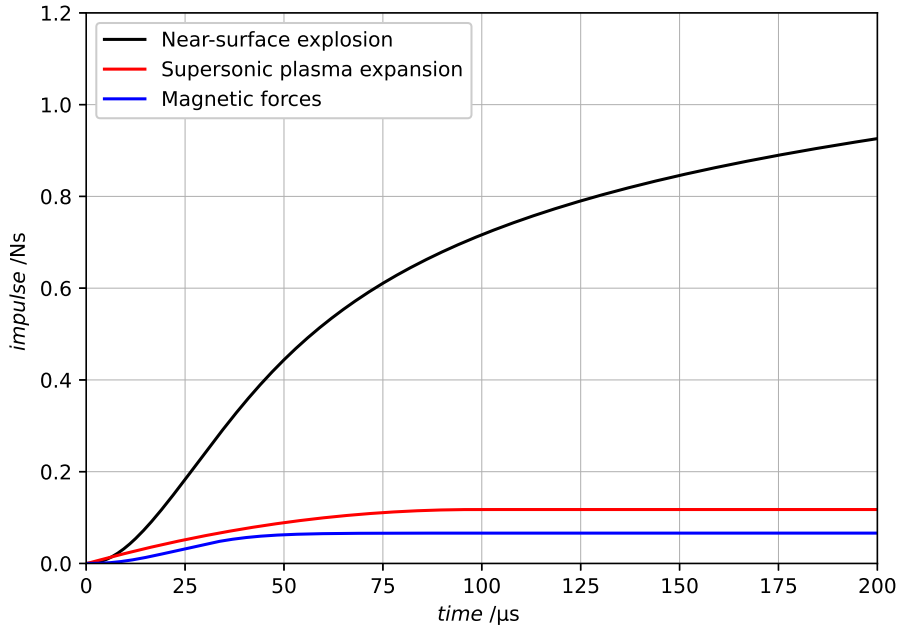
Figure 6.4: Finite element predictions for the sample with 200 µm paint thickness of ECF 73

6.4.1.3 300 µm paint thickness

Keeping the same approach, Figure 6.5 and Figure 6.6 summarize the numerical results performed for the case of 300 µm of paint thickness. Even the force and impulse magnitude generated by the near-surface explosion of the lightning protection layer or the deflection analysis demonstrate the influence with a increase of 100 µm in the thickness of the paint layer.

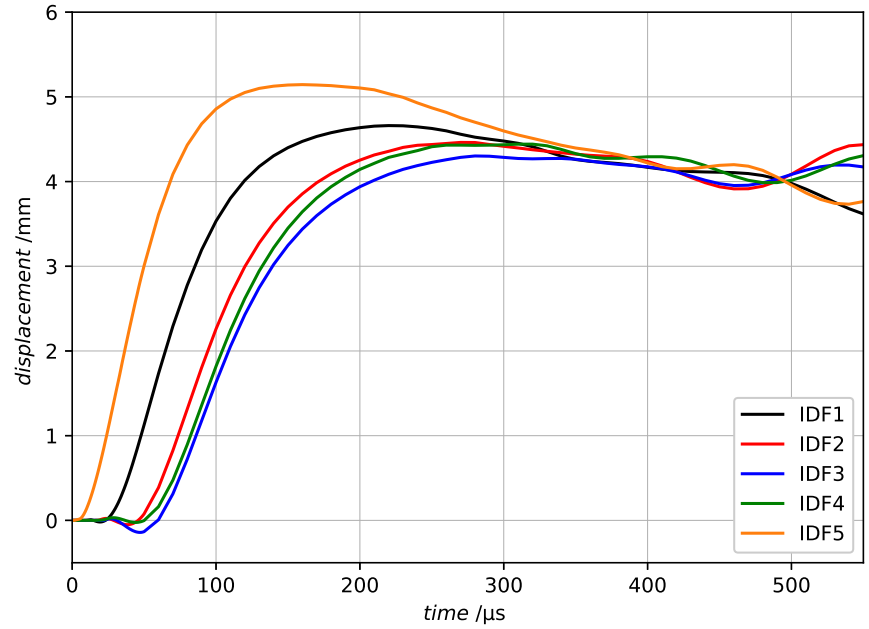


(a) Force magnitude

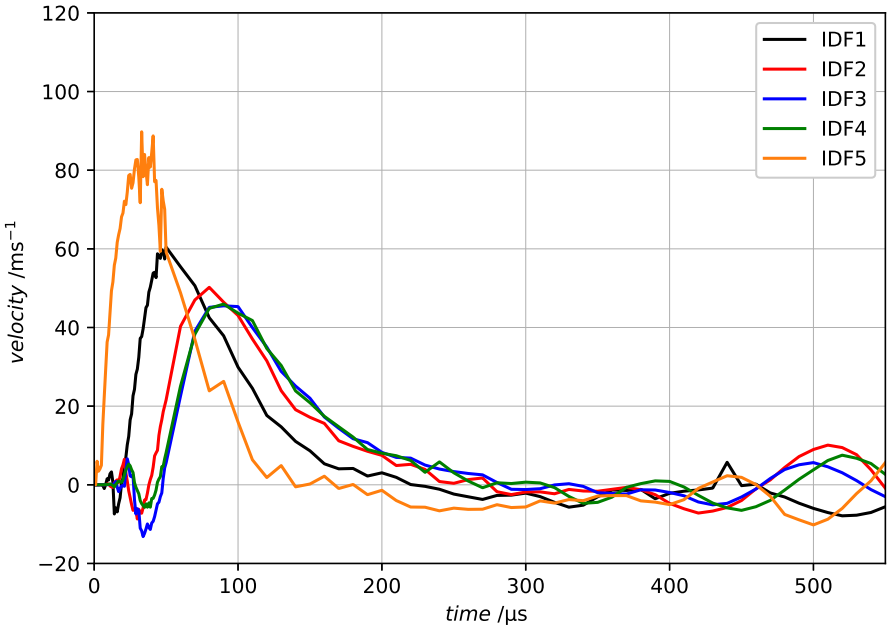


(b) Impulse magnitude

Figure 6.5: Mechanical contributions for the sample with 300 µm paint thickness of ECF 73



(a) Displacement

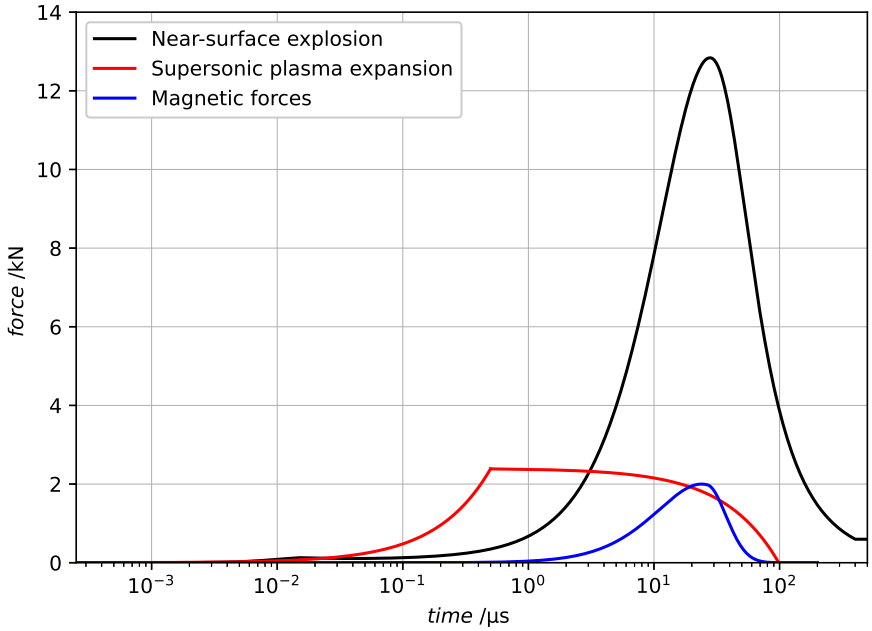


(b) Velocity

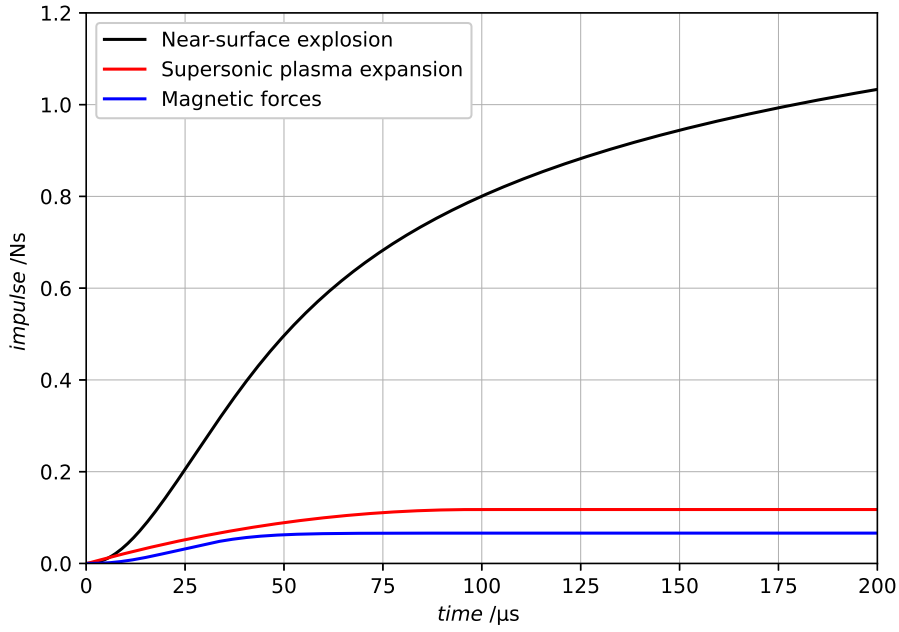
Figure 6.6: Finite element predictions for the sample with 300 µm paint thickness of ECF 73

6.4.1.4 400 µm paint thickness

Following the trend observed in the previous analyses, the case of 400 µm of paint thickness presents the higher values of force and impulse magnitude, and also for deflection. Figure 6.7 and Figure 6.8 demonstrate this fact.

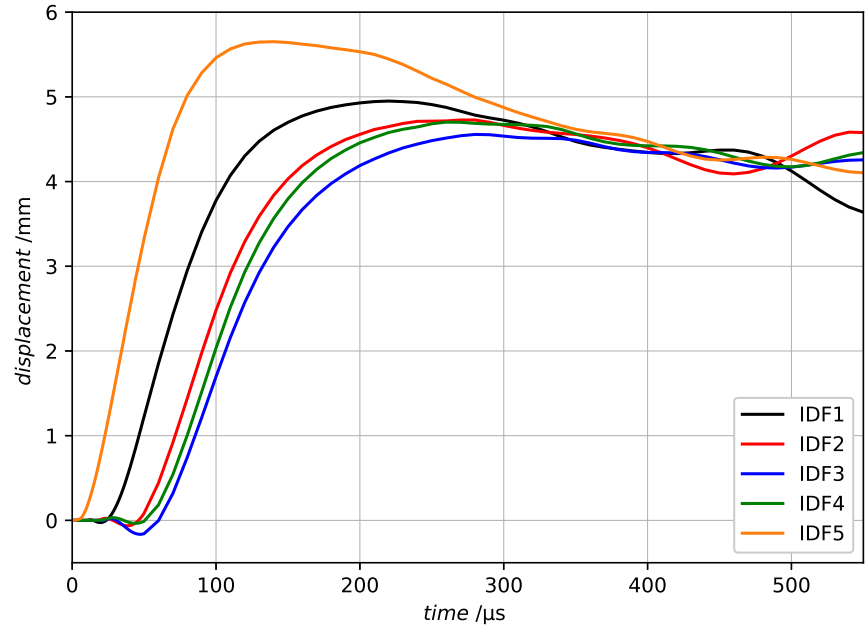


(a) Force magnitude

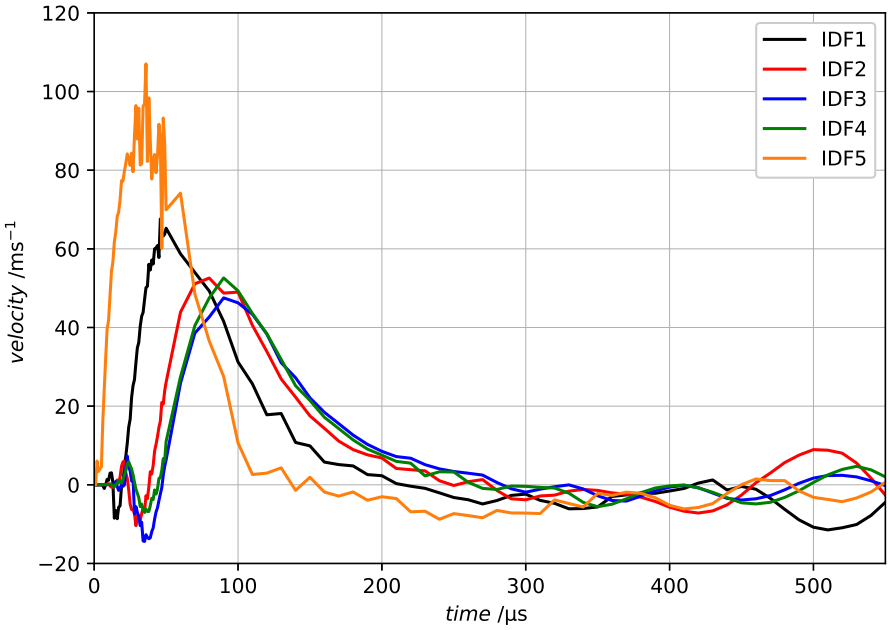


(b) Impulse magnitude

Figure 6.7: Mechanical contributions for the sample with 400 µm paint thickness of ECF 73



(a) Displacement



(b) Velocity

Figure 6.8: Finite element predictions for the sample with 400 µm paint thickness of ECF 73

6.4.1.5 Damage maps

An illustrative evaluation of the induced longitudinal, transverse, shear and interlaminar damage is shown, respectively, in Table 6.1, Table 6.2, Table 6.3 and Table 6.4.

Table 6.1: Damage map assessment considering the effect of paint thickness for the damage variable in the longitudinal direction (d_1) for ECF 73

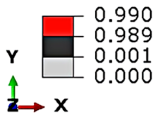
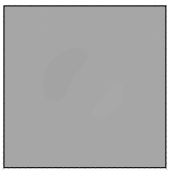
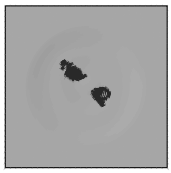
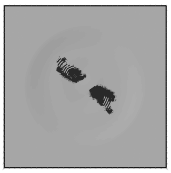
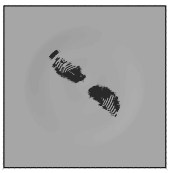
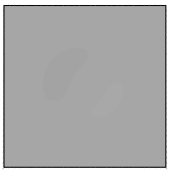
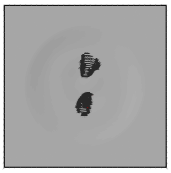
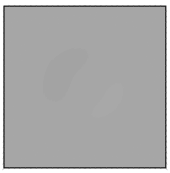
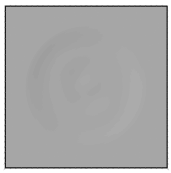
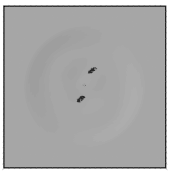
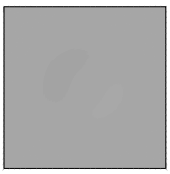
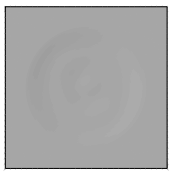
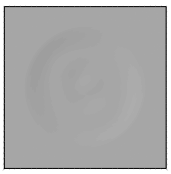
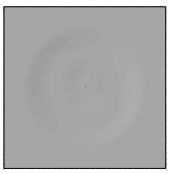
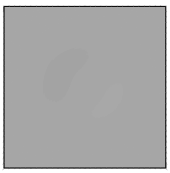
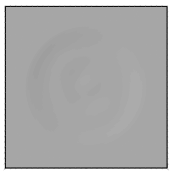
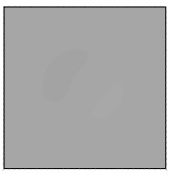
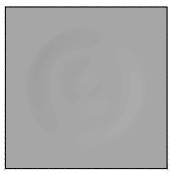
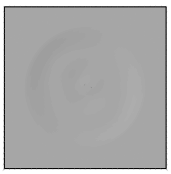
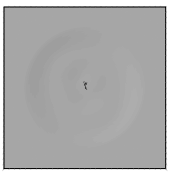
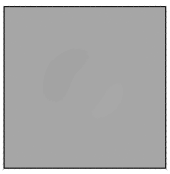
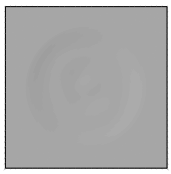
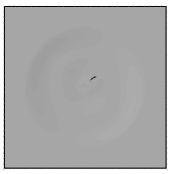
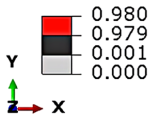
	No paint	200 µm	300 µm	400 µm
Layer 8				
Layer 7				
Layer 6				
Layer 4 and 5				
Layer 3				
Layer 2				
Layer 1				

Table 6.2: Damage map assessment considering the effect of paint thickness for the damage variable in the transverse direction (d_2) for ECF 73



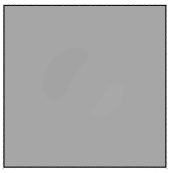
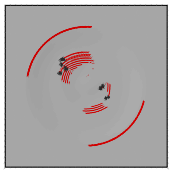
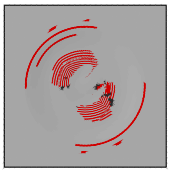
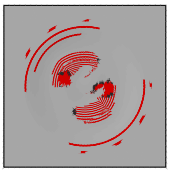
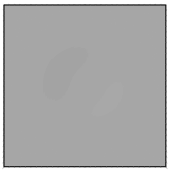
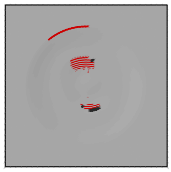
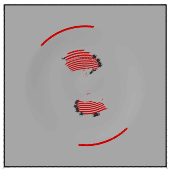
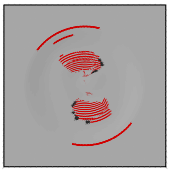
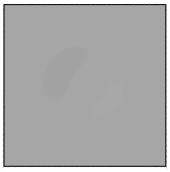
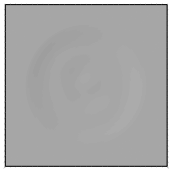
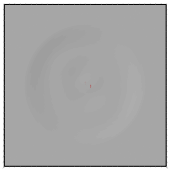
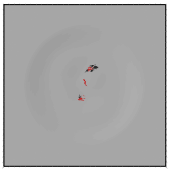
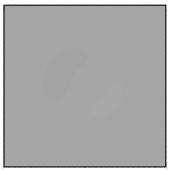
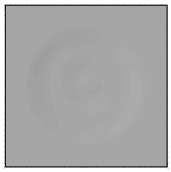
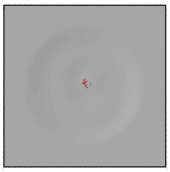
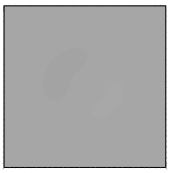
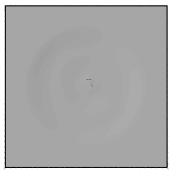
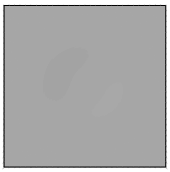
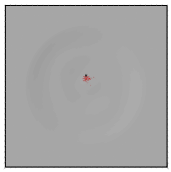
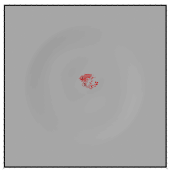
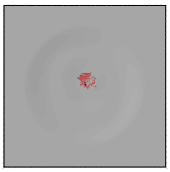
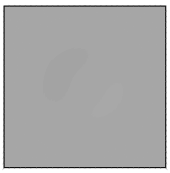
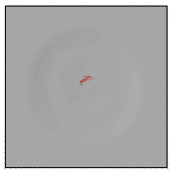
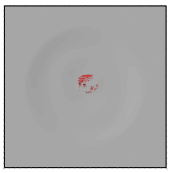
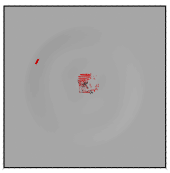
	No paint	200 µm	300 µm	400 µm
Layer 8				
Layer 7				
Layer 6				
Layer 4 and 5				
Layer 3				
Layer 2				
Layer 1				

Table 6.3: Damage map assessment considering the effect of paint thickness for the shear damage variable (d_6) for ECF 73

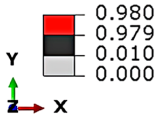
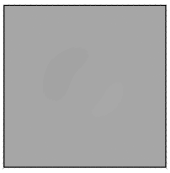
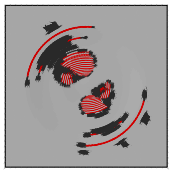
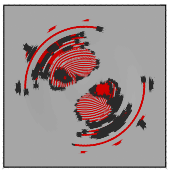
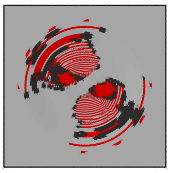
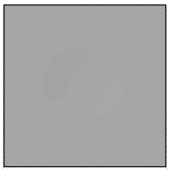
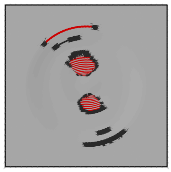
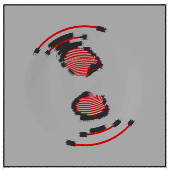
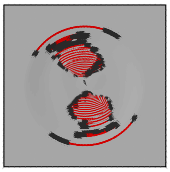
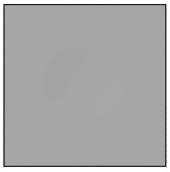
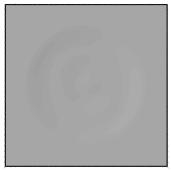
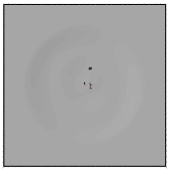
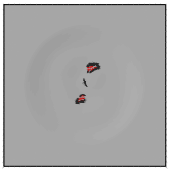
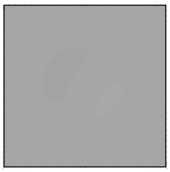
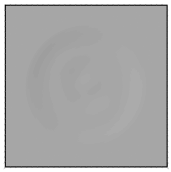
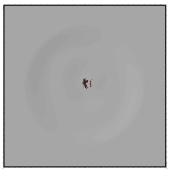
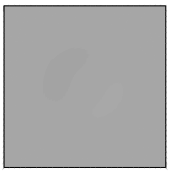
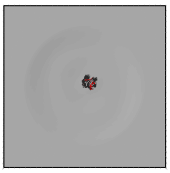
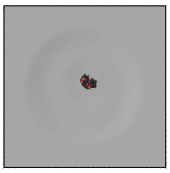
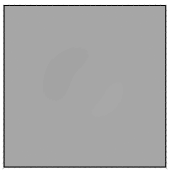
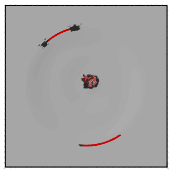
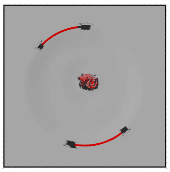
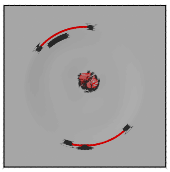
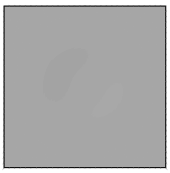
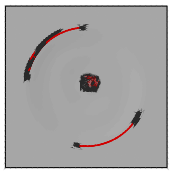
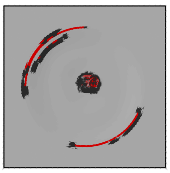
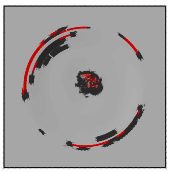
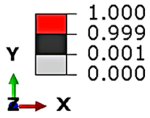
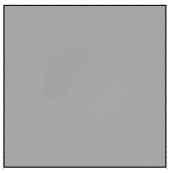
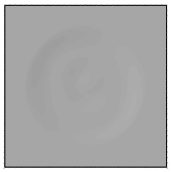
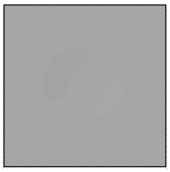
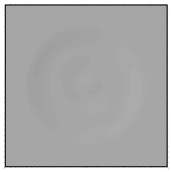
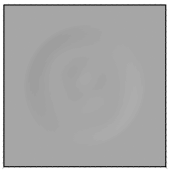
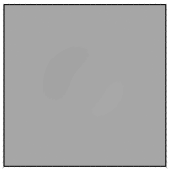
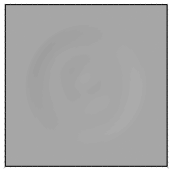
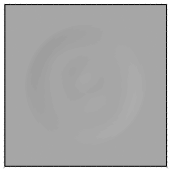
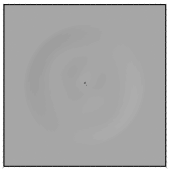
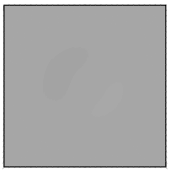
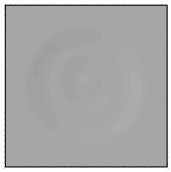
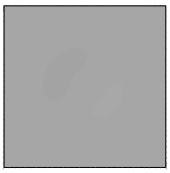
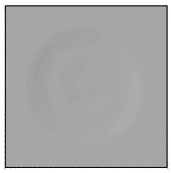
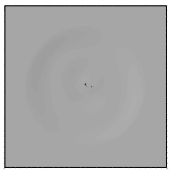
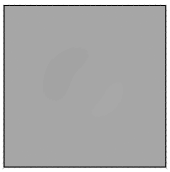
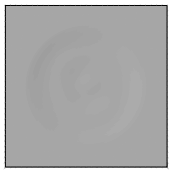
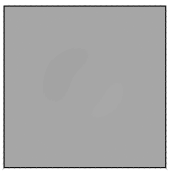
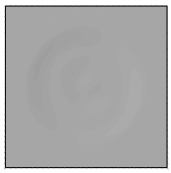
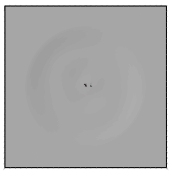
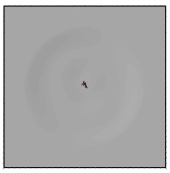
	No paint	200 µm	300 µm	400 µm
Layer 8				
Layer 7				
Layer 6				
Layer 4 and 5				
Layer 3				
Layer 2				
Layer 1				

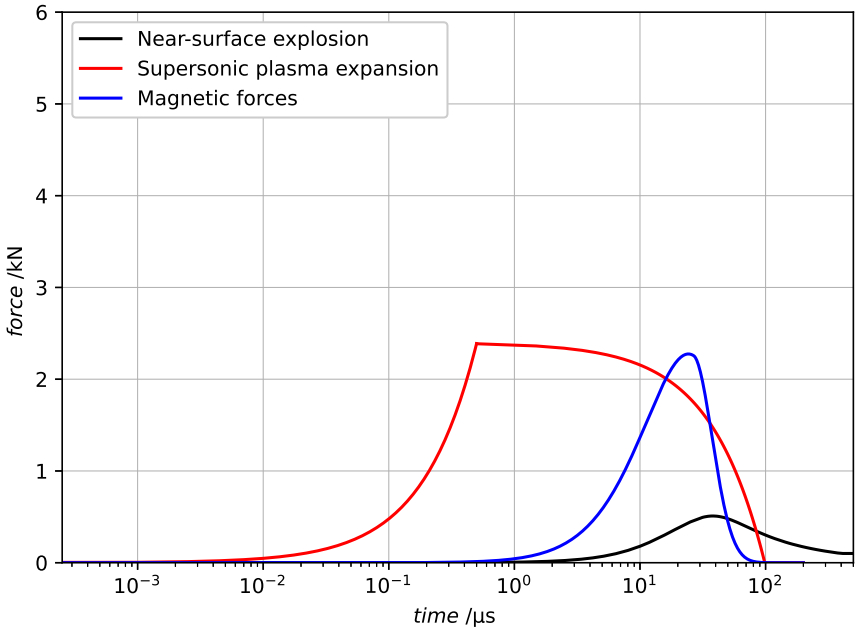
Table 6.4: Damage map assessment considering the effect of paint thickness on delamination (d) for ECF 73

	No paint	200 µm	300 µm	400 µm
Layer 8				
Layer 7				
Layer 6				
Layer 4 and 5				
Layer 3				
Layer 2				
Layer 1				

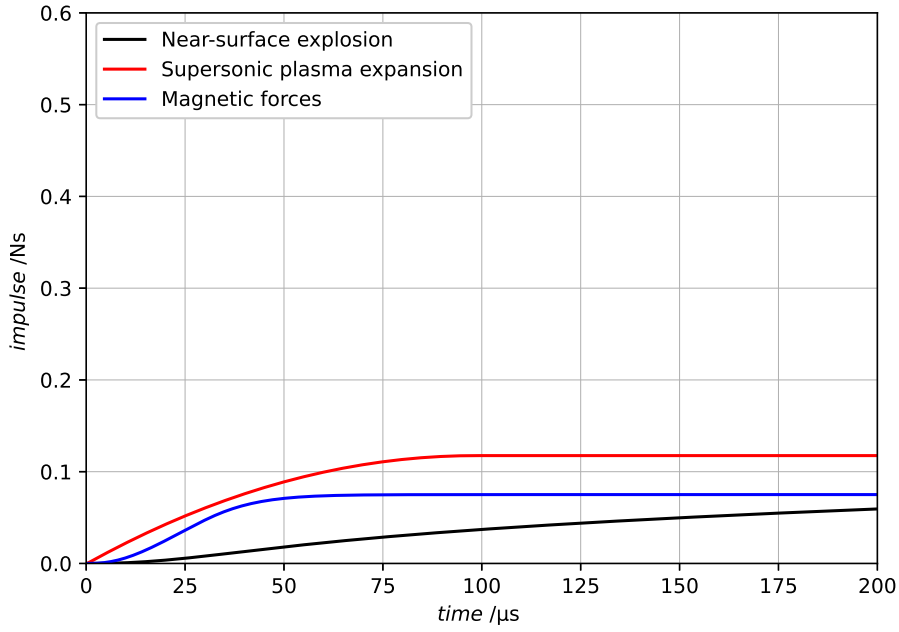
6.4.2 Expanded copper foil 195

6.4.2.1 No paint

Similar to the ECF 73 approach, an analytical evaluation based in the mechanical loads and a numerical assessment provided by the finite element model were performed. In this case, the near-surface explosion of the lightning protection layer has a lower contribution than the supersonic plasma expansion and the magnetic forces, leading to an overall low deformation, see, respectively, Figure 6.9 and Figure 6.10.

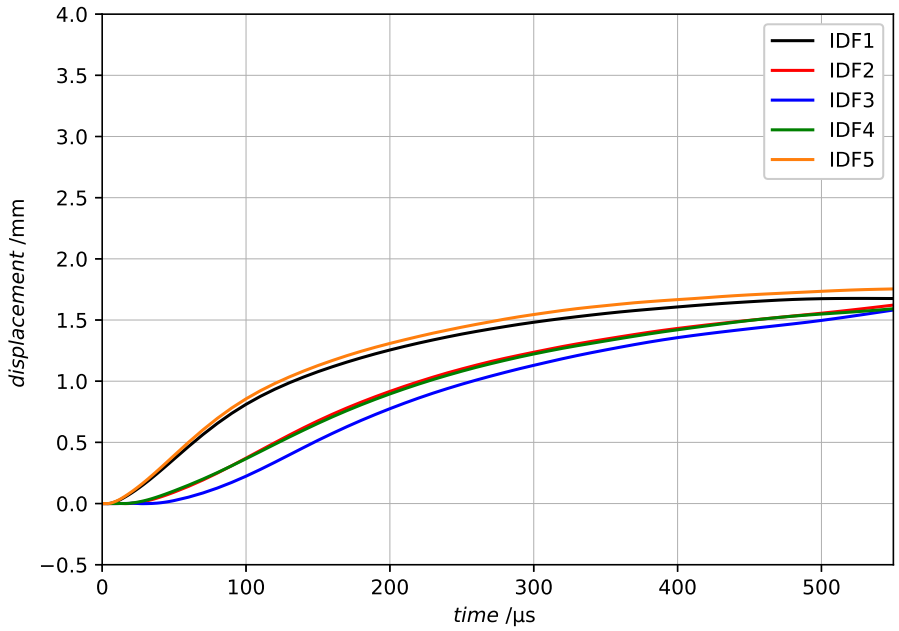


(a) Force magnitude

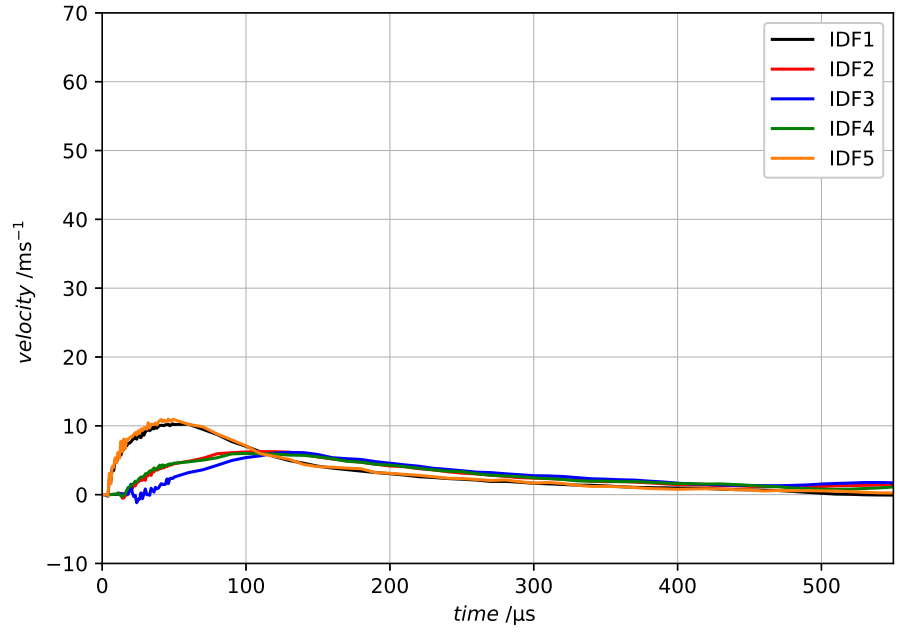


(b) Impulse magnitude

Figure 6.9: Mechanical contributions for unpainted sample of ECF 195



(a) Displacement

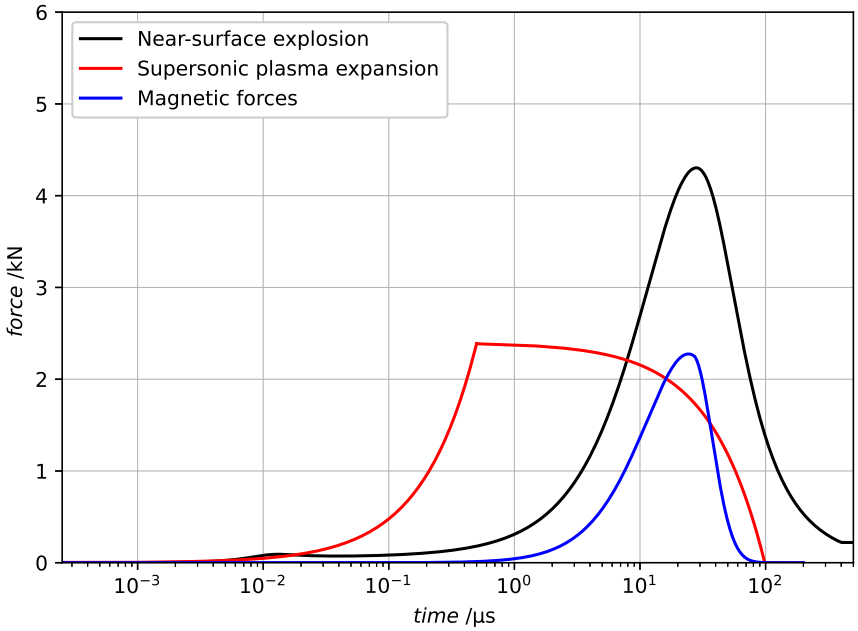


(b) Velocity

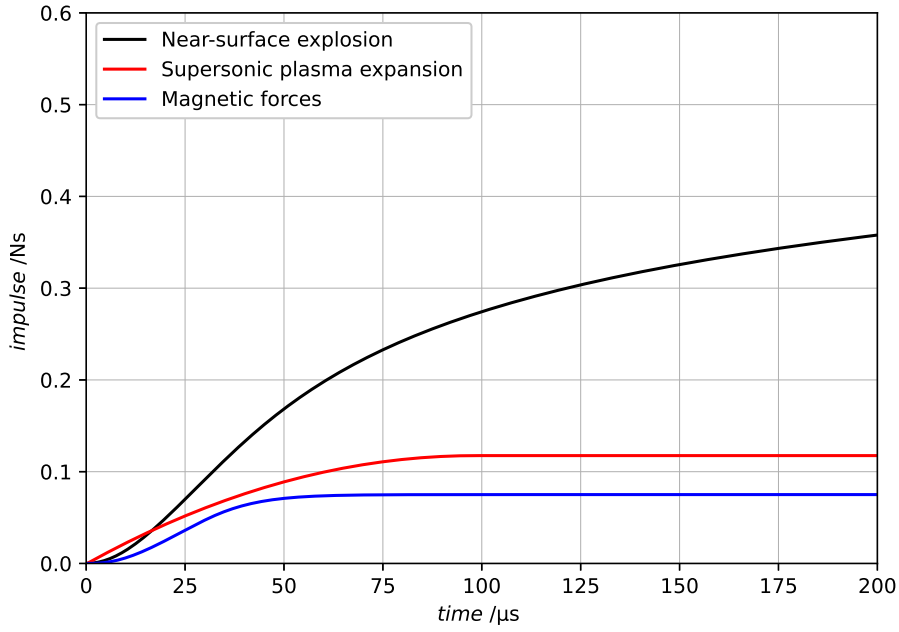
Figure 6.10: Finite element predictions for unpainted sample of ECF 195

6.4.2.2 200 µm paint thickness

Once again it is demonstrate that the presence of paint clear generated higher impact, as Figure 6.11 and Figure 6.12 shown.

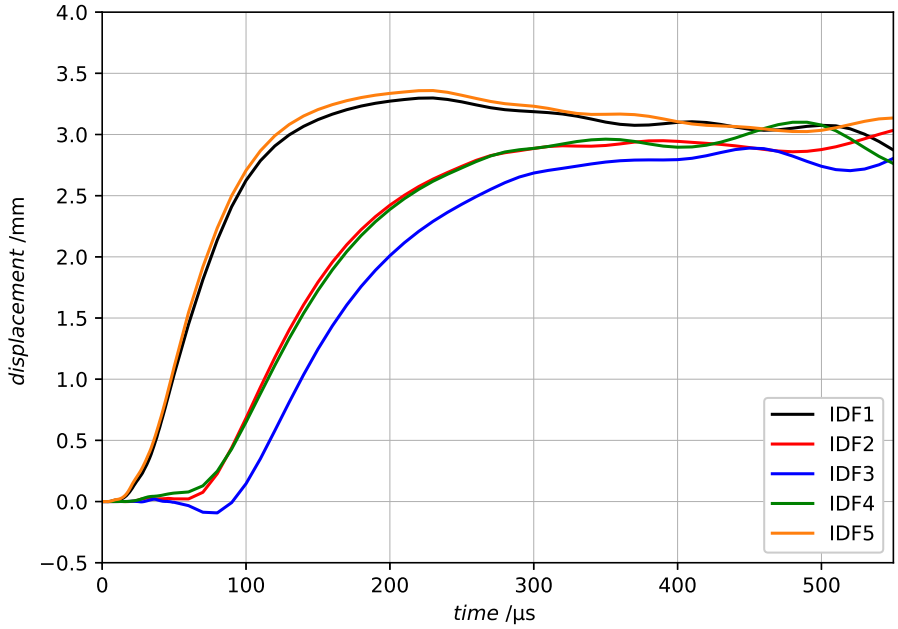


(a) Force magnitude

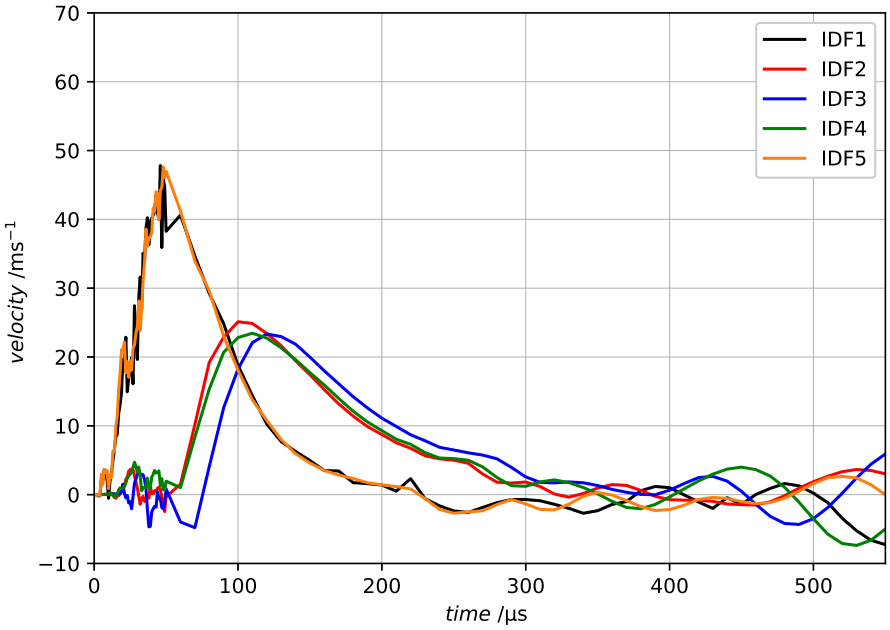


(b) Impulse magnitude

Figure 6.11: Mechanical contributions for the sample with 200 µm paint thickness of ECF 195



(a) Displacement

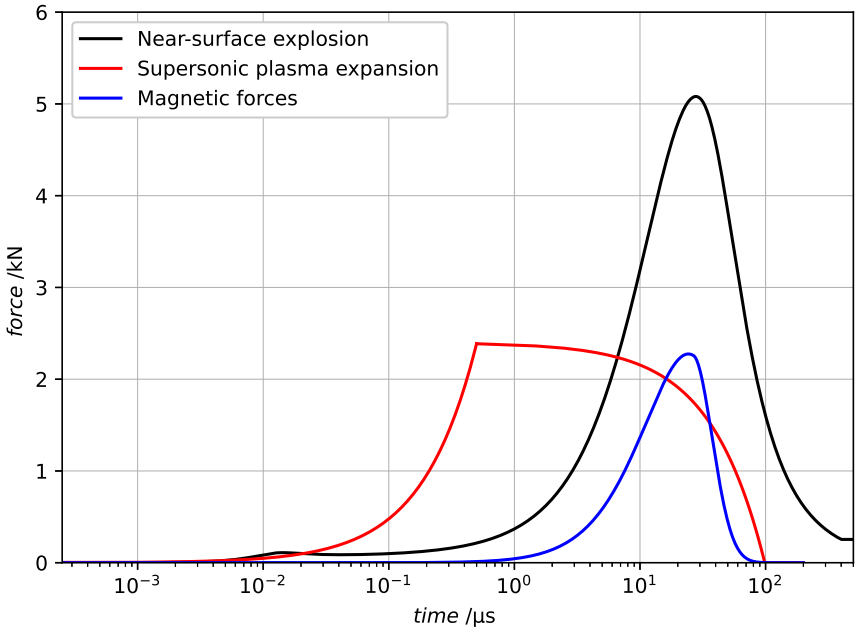


(b) Velocity

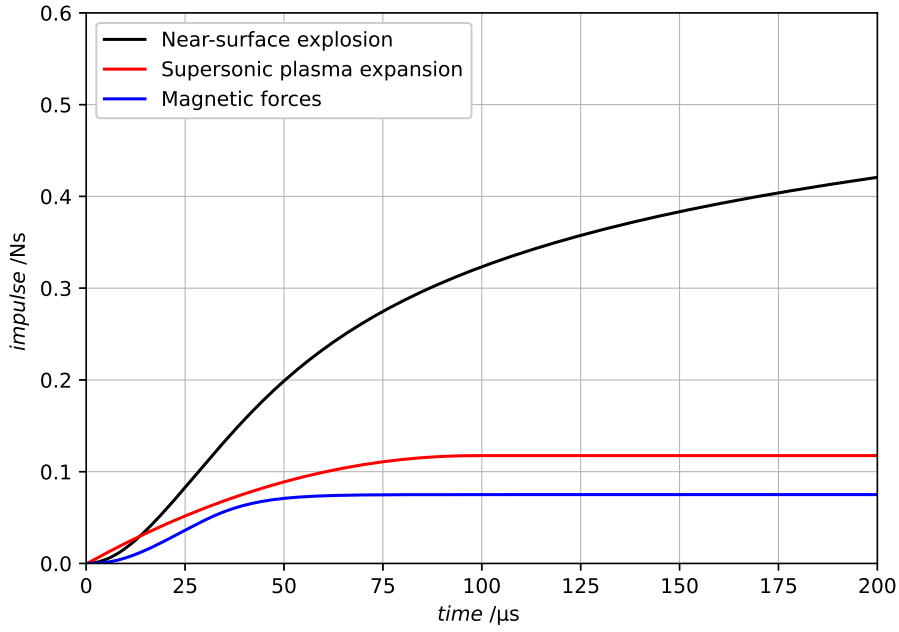
Figure 6.12: Finite element predictions for the sample with 200 µm paint thickness of ECF 195

6.4.2.3 300 µm paint thickness

Figure 6.13 and Figure 6.14 summarize the numerical results performed for the case of 300 µm of paint thickness, with a clear increase of the pressure contributions and mechanical loads and displacements.

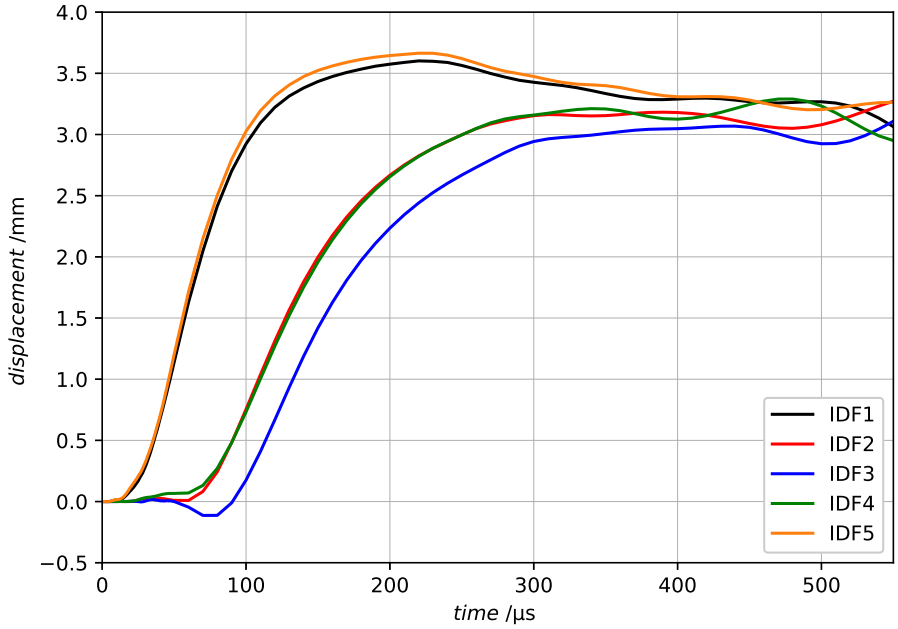


(a) Force magnitude

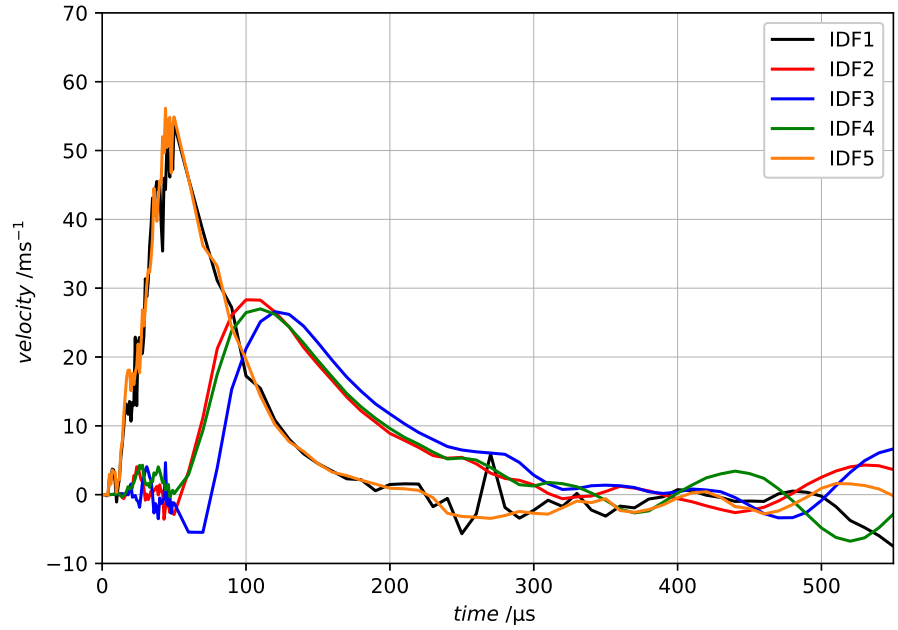


(b) Impulse magnitude

Figure 6.13: Mechanical contributions for the sample with 300 µm paint thickness of ECF 195



(a) Displacement

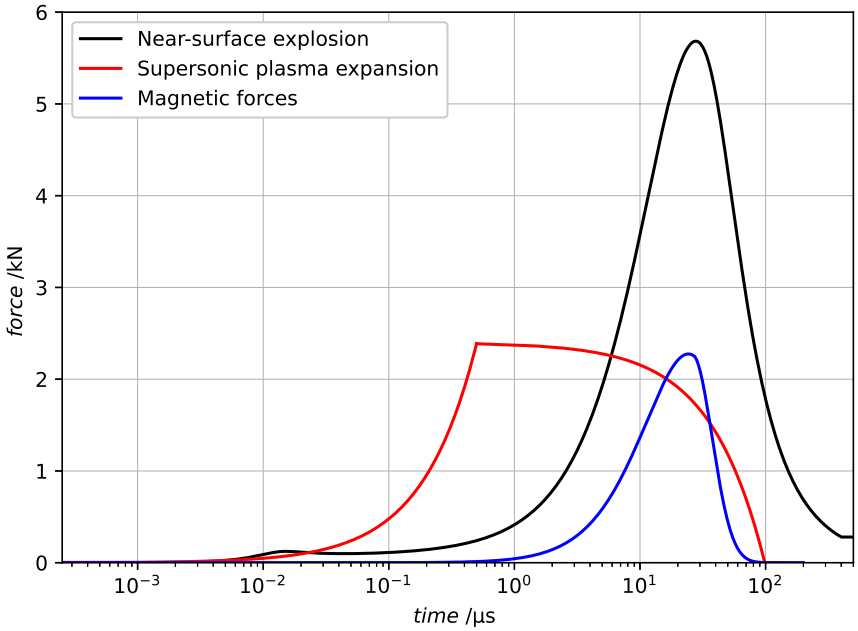


(b) Velocity

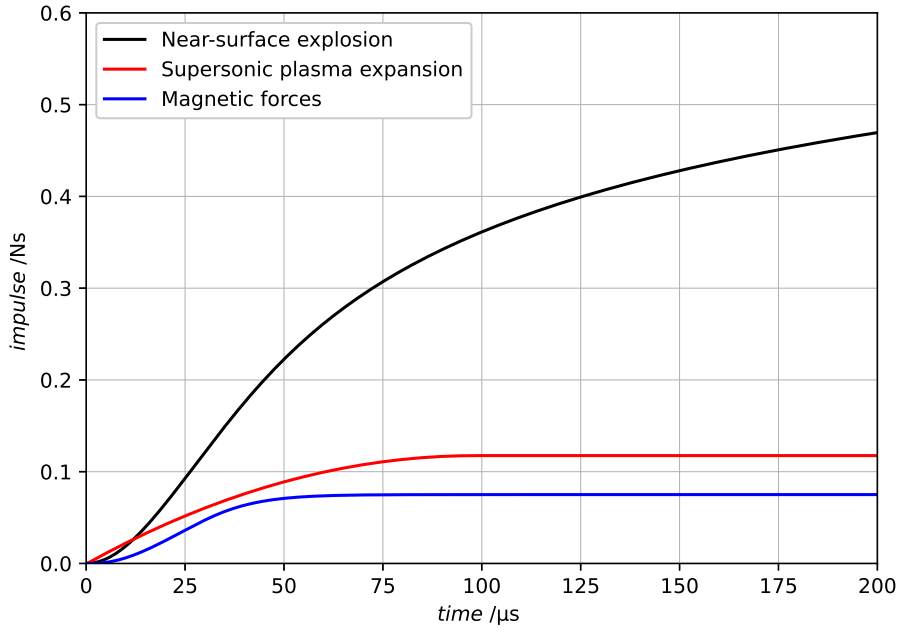
Figure 6.14: Finite element predictions for the sample with 300 µm paint thickness of ECF 195

6.4.2.4 400 µm paint thickness

Finally, the case of 400 µm of paint thickness layer presents again the higher values of force and impulse magnitude, as well as induced deflection. Figure 6.7 and Figure 6.8 demonstrate this fact clearly.

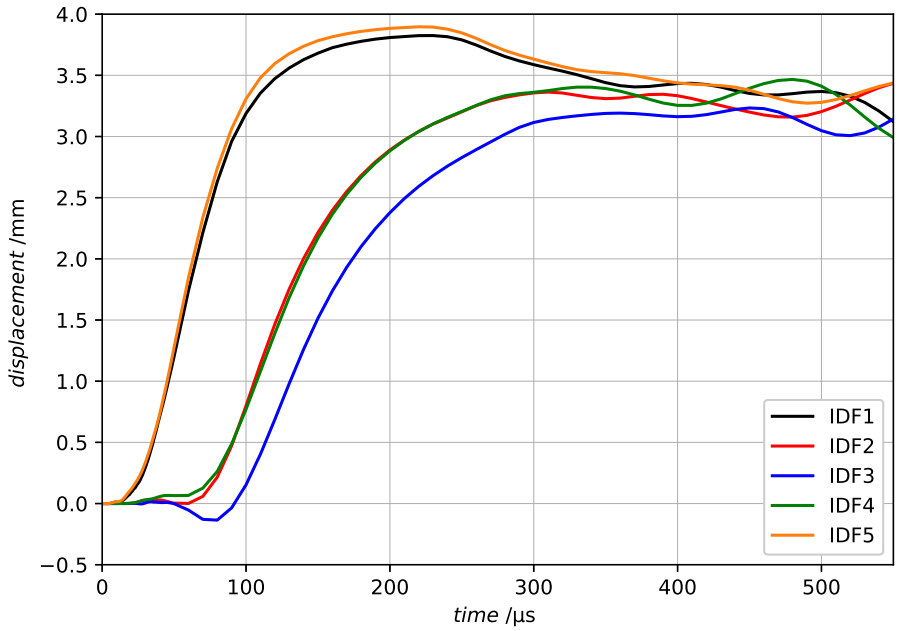


(a) Force magnitude

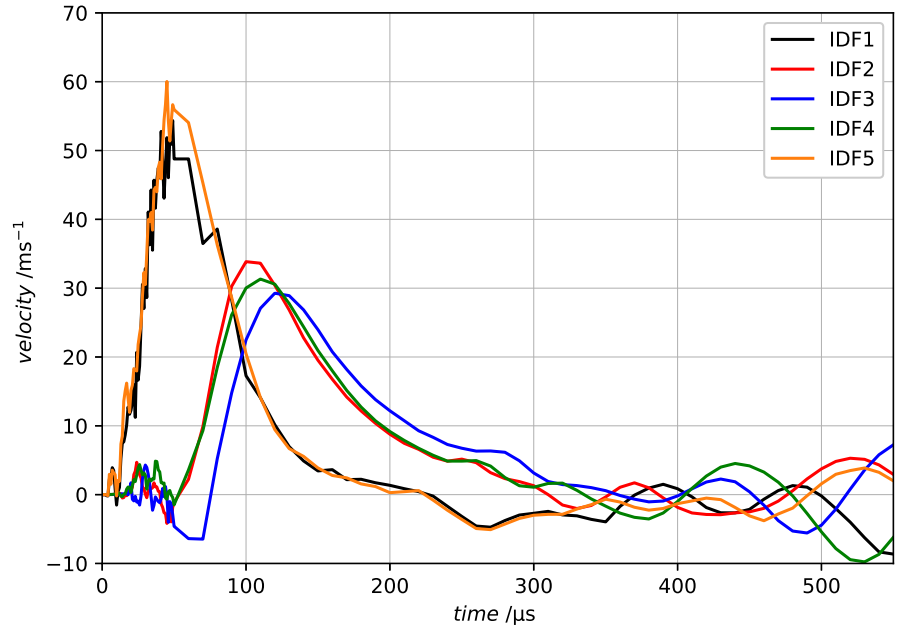


(b) Impulse magnitude

Figure 6.15: Mechanical contributions for the sample with 400 µm paint thickness of ECF 195



(a) Displacement



(b) Velocity

Figure 6.16: Finite element predictions for the sample with 400 µm paint thickness of ECF 195

6.4.2.5 Damage maps

An illustrative evaluation of the induced longitudinal, transverse, shear and interlaminar damage is shown, respectively, in Table 6.5, Table 6.6, Table 6.7 and Table 6.8.

Table 6.5: Damage map assessment considering the effect of paint thickness for the damage variable in the longitudinal direction (d_1) for ECF 195

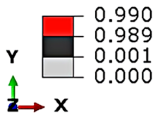
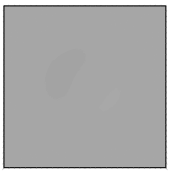
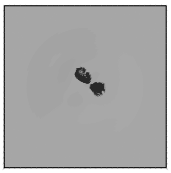
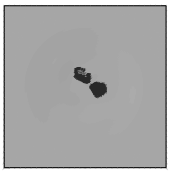
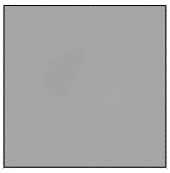
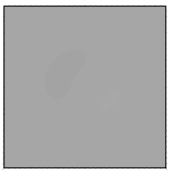
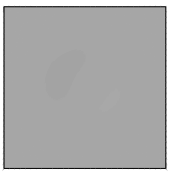
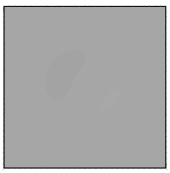
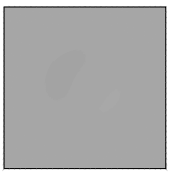
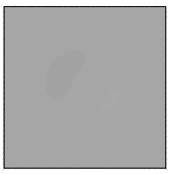
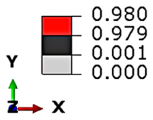
	No paint	200 µm	300 µm	400 µm
Layer 8				
Layer 7				
Layer 6				
Layer 4 and 5				
Layer 3				
Layer 2				
Layer 1				

Table 6.6: Damage map assessment considering the effect of paint thickness for the damage variable in the transverse direction (d_2) for ECF 195



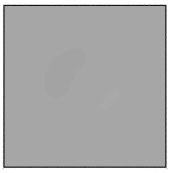
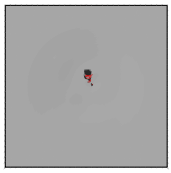
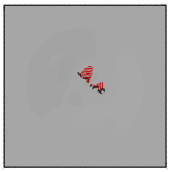
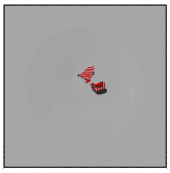
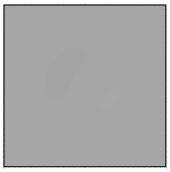
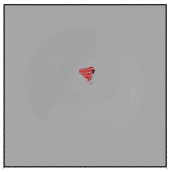
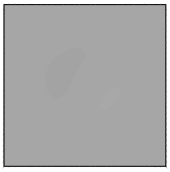
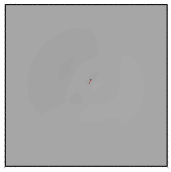
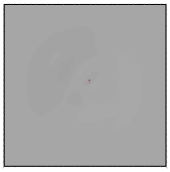
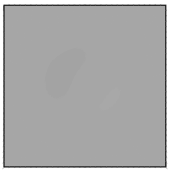
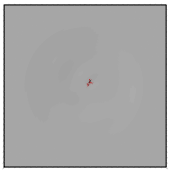
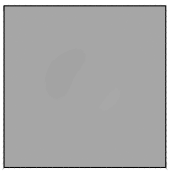
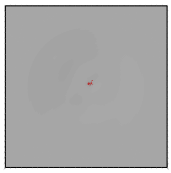
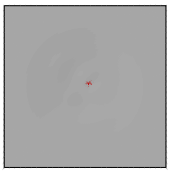
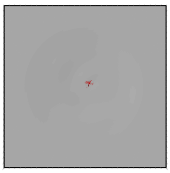
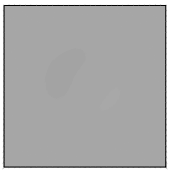
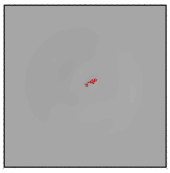
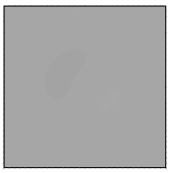
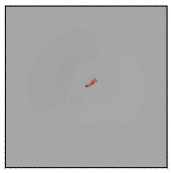
	No paint	200 µm	300 µm	400 µm
Layer 8				
Layer 7				
Layer 6				
Layer 4 and 5				
Layer 3				
Layer 2				
Layer 1				

Table 6.7: Damage map assessment considering the effect of paint thickness for the shear damage variable (d_6) for ECF 195

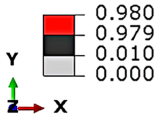
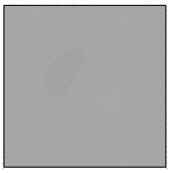
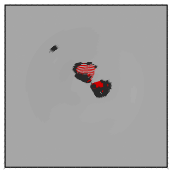
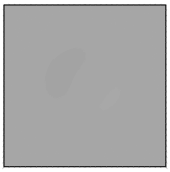
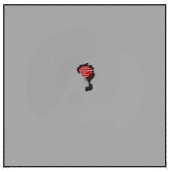
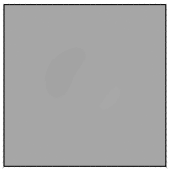
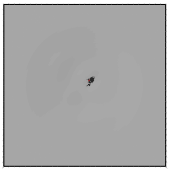
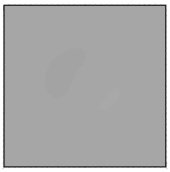
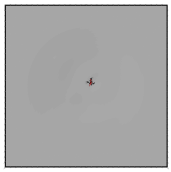
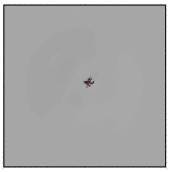
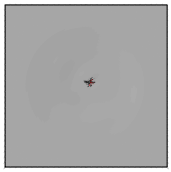
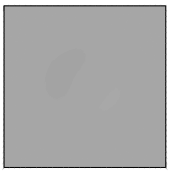
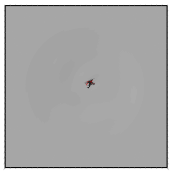
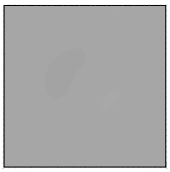
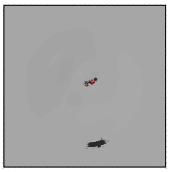
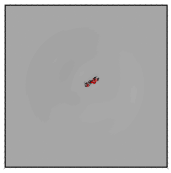
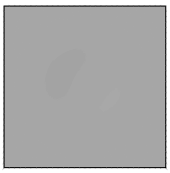
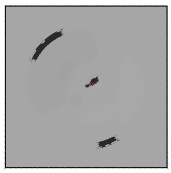
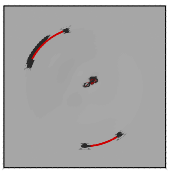
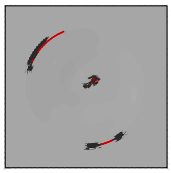
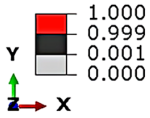
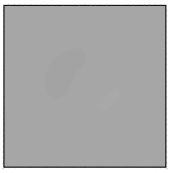
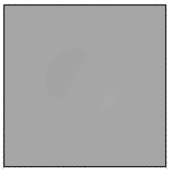
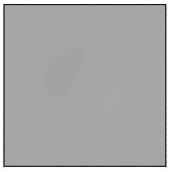
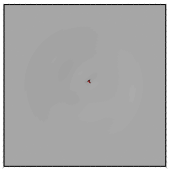
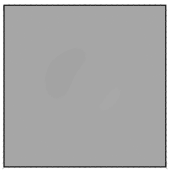
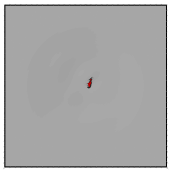
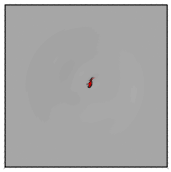
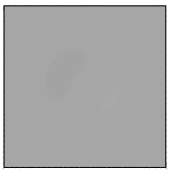
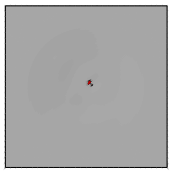
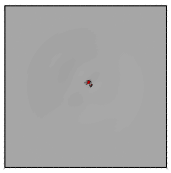
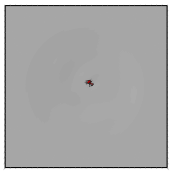
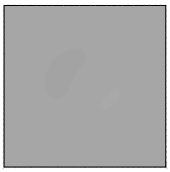
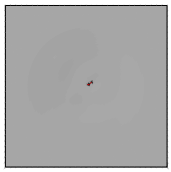
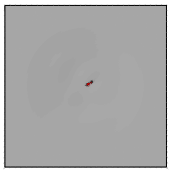
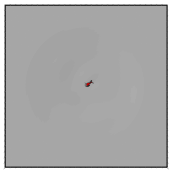
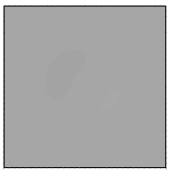
	No paint	200 µm	300 µm	400 µm
Layer 8				
Layer 7				
Layer 6				
Layer 4 and 5				
Layer 3				
Layer 2				
Layer 1				

Table 6.8: Damage map assessment considering the effect of paint thickness on delamination (d) for ECF 195

	No paint	200 µm	300 µm	400 µm
Layer 8				
Layer 7				
Layer 6				
Layer 4 and 5				
Layer 3				
Layer 2				
Layer 1				

6.5 Discussion

Since the model for the shock waves generated by the explosion of the LSP layer can account for the effect of ply thickness, distinct pressure magnitudes are captured, which grow with the increase of paint thickness. It is clearly demonstrate the disparity of values from the case of unpainted panels to a 400 µm paint layer.

The predicted mechanical responses then show that the deflection imposed to the panel with 400 µm paint layer is about three times higher than the unpainted case for the expanded copper foil 73, and 2.2 times for the expanded copper foil 195.

The damage maps also show a clear increase of damage extent with the increase of paint thickness. While the unpainted panels do not show any type of damage, all panels with a paint layer, independently of the thickness, exhibit all types of damage, in the longitudinal direction (d_1), in the transverse direction (d_2), in shear (d_6) and delamination (d), except for the samples with a 200 µm paint layer, which do not exhibit delamination (d).

Moreover, these results show that a small variation of the paint thickness will have impact on the damage induced by lightning strikes, motivated mainly by the rapid vaporization of the metallic mesh of the lightning protection layer due to Joule resistive heating. As the protection layer is confined between the composite and a surface paint layer, the resulting explosion shock wave is reflected back, leading to a much more severe phenomenon than without a covering coating layer.

6.6 Conclusion

The effect of paint thickness on the damage occurring during a lightning strike event on a protected carbon-fibre reinforced composite plate was well-defined, and it becomes unquestionable that thicker paint layers generate more damage. These numerical results are corroborated by the experimental observations reported earlier in this chapter. Finally, it is important to mention that the possibility to have a tool that is capable of predicting the effect of paint thickness on the damage induced by lightning strikes is a key asset for the optimization of the paint layer thickness, whose criteria cannot be solely based on static electricity and environmental protection, but should as well take into account its effect in the event of a lightning strike and the selection of an appropriate lightning protection measure.

Chapter 7

Waveform parameters

Contents

7.1 Introduction

7.2 Parametric study

7.3 Peak current variation

7.3.1 Expanded copper foil 73

7.3.2 Expanded copper foil 195

7.4 Action integral variation

7.4.1 Expanded copper foil 73

7.4.2 Expanded copper foil 195

7.5 Discussion and conclusions

Objectives
This chapter presents a parametric study to assess the influence of the lightning waveform parameters in the damage induced by a lightning strikes. Considering a baseline D-current waveform the effects of the peak current and of the action integral on the damage induced in a protected composite plate are evaluate.

7.1 Introduction

According to the literature [24; 30; 32], the lightning parameters defining simulated lightning strikes are the maximum current of the waveform (or peak current), the electrical discharge and the action integral, which represents the specific energy.

A parametric analysis to ascertain the variation on the damage induced by the direct effects of mechanical forces originated by a lightning strike on a CFRP plate is the purpose of this work. The transient D current waveform with a time to peak of 26.8 µs, a decay time of 48.5 µs, and a peak current of 96.4 kA already defined, was used. In this work, the analysis concerns the following lightning parameters: (i) peak current and (ii) action integral.

Based on the experimental tests performed by Hirano et al. [24] on unprotected CFRP, a comparison between the numerical simulations and observed trends can be establish.

Trend 1: Influence of the peak current. The value of the peak current is modified, keeping the same action integral and the same stacking sequence. Note that to keep the same value of action integral, the decay time needs to be adjusted.

Trend 2: Influence of the action integral. The value of the decay time is modified to adjust the action integral value, keeping the same peak current value and the same stacking sequence.

7.2 Parametric study

According to the SAE Aerospace Recommended Practice about aircraft lightning environment and related test waveforms [14], the maximum peak current amplitude should be 100 kA±(10%) and the action integral 0.25×10^6 A^2s ±(20%) in a time duration $t \leq 500$ µs to describe the lightning transient current waveform D. Implementing the same acceptable range taking the waveform 26.8/48.5 µs, 96.4 kA as nominal reference for the peak current and action integral, and keeping the value of t_1, it was possible to determine the following alternative waveforms:

26.8/41 µs, 106.04 kA - Maximum peak current, nominal action integral

26.8/58.6 µs, 86.76 kA - Minimum peak current, nominal action integral

26.8/57.1 µs, 96.4 kA - Nominal peak current, maximum action integral

26.8/39.9 µs, 96.4 kA - Nominal peak current, minimum action integral

Because the value of t_1 is the same in all the waveforms, the main parameters to change are the constant c and the constant f. The parameter c can be introduced as $c = A \times I_{max}$, directly dependent on the peak current (see section 3.2).

The waveform 26.8/48.5 µs, 96.4 kA takes the value of 96.4 kA as peak current and 0.3×10^6 A^2s of action integral, and t_1 is 26.8 µs. The waveform parameters are shown in Table 7.1.

Table 7.1: Waveform parameters for 26.8/48.5 µs, 96.4 kA

	a /s^{-1}	b /s^{-1}	c /A	f /(−)	v /s
26.8/48.5 µs, 96.4 kA	33 833.1	41 024.7	1 361 710.5	2.081	1.39×10^{-5}

7.3 Peak current variation

To assess the effect of the peak current, two alternative waveforms were defined considering 96.4 kA ± (10%), while keeping the nominal value of the action integral unchanged The graphical visualization of the proposed waveforms are shown in Figure 7.1 and the waveform parameters is shown in Table 7.2.

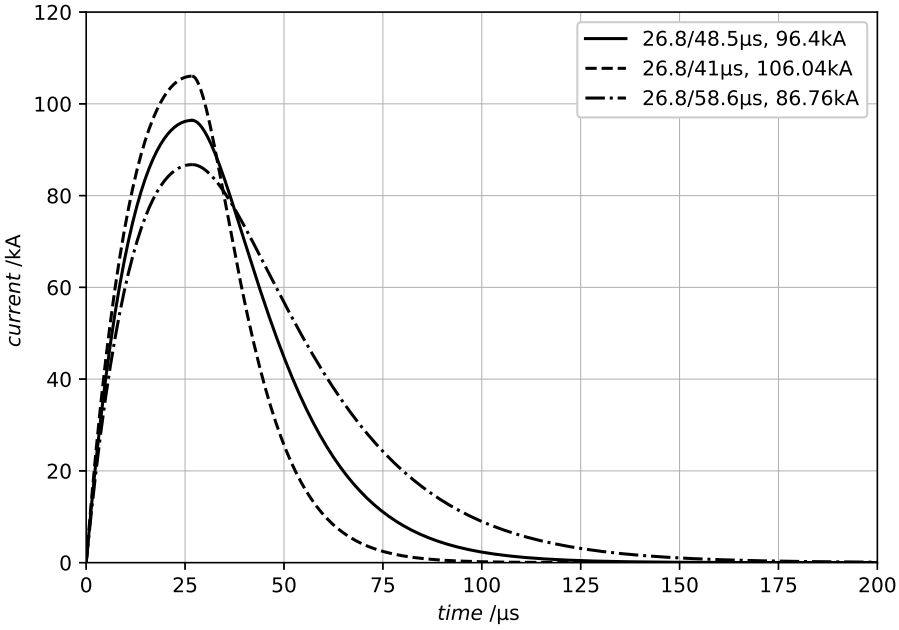


Figure 7.1: Waveforms considering different currents

Table 7.2: Waveforms parameters for peak current variation cases

	a /s^{-1}	b /s^{-1}	A /-	I_{max} /A	c /A
26.8/41 µs, 106.04 kA	33 833.1	41 024.7	14.1256	106040	1 497 875.9
26.8/58.6 µs, 86.76 kA	33 833.1	41 024.7	14.1256	106040	1 225 534.8

Table 7.2: Waveforms parameters for peak current variation cases

	f /−	v /s
26.8/41 µs, 106.04 kA	3.181	1.838×10^{-5}
26.8/58.6 µs, 86.76 kA	1.419	7.915×10^{-6}

An analytical analysis is shown below for the three contributions: (i) overpressure due to the near-surface explosion of the lightning protection layer; (ii) shock waves caused by the supersonic expansion of the hot plasma channel; and (iii) magnetic forces.

7.3.1 Expanded copper foil 73

7.3.1.1 Root radius

The fitted root radii as a function of time for waveform alternatives to assess peak current influence are plotted in Figure 7.2 and Table 7.3 presents the respective parameters.

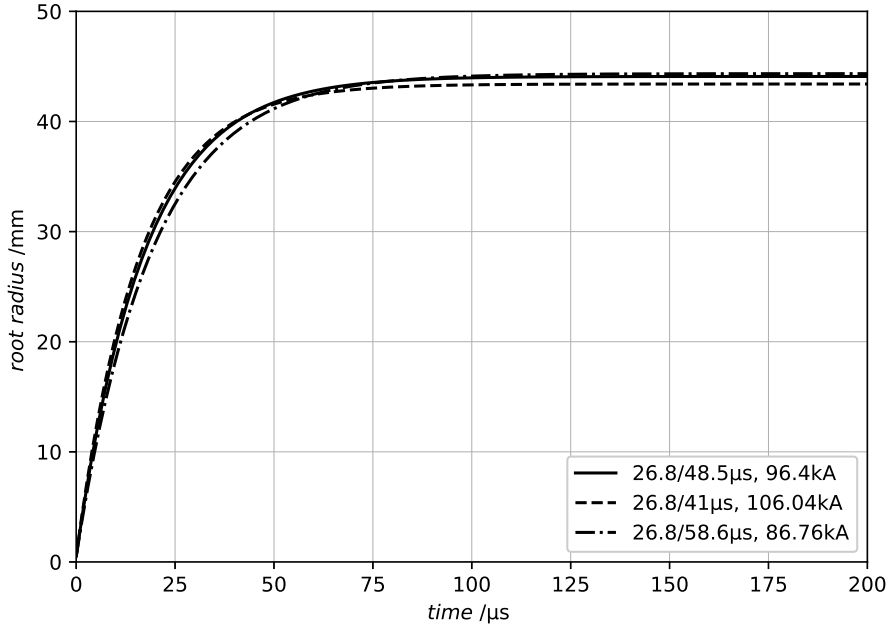


Figure 7.2: Root radius for waveform alternatives to assess peak current influence for ECF 73

Table 7.3: Root radius parameters for waveform alternatives to assess peak current influence for ECF 73

	a /mm	α /μs^{-1}	β /μs^{-1}	R_{R_0} /(mm)
26.8/41 µs, 106.04 kA	42.91	-8.53×10^{-7}	$-0.063\,02$	0.5
26.8/58.6 µs, 86.76 kA	43.86	-1.69×10^{-6}	$-0.052\,39$	0.5

Table 7.3: Root radius parameters for waveform alternatives to assess peak current influence for ECF 73

	t_s /μs	c /mm
26.8/41 µs, 106.04 kA	177.59	43.41
26.8/58.6 µs, 86.76 kA	197.66	44.34

7.3.1.2 Near-surface explosion

For the near-surface explosion of the lightning protection layer contribution the pressure, force and impulse magnitude are presented in Figure 7.3, Figure 7.4 and Figure 7.5, respectively.

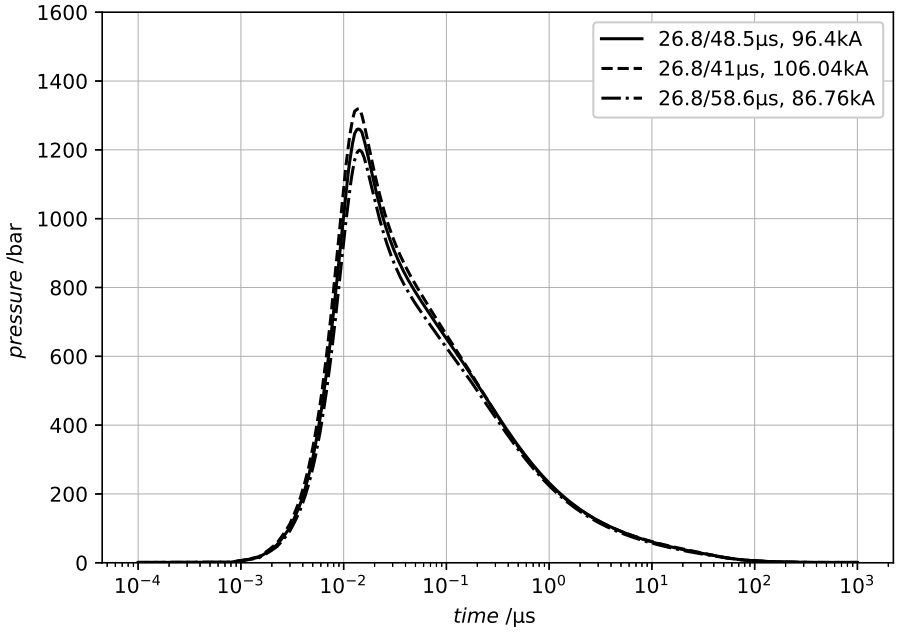


Figure 7.3: Overpressure caused by explosion of lightning protection layers as a function of time for waveform alternatives to assess peak current influence for ECF 73

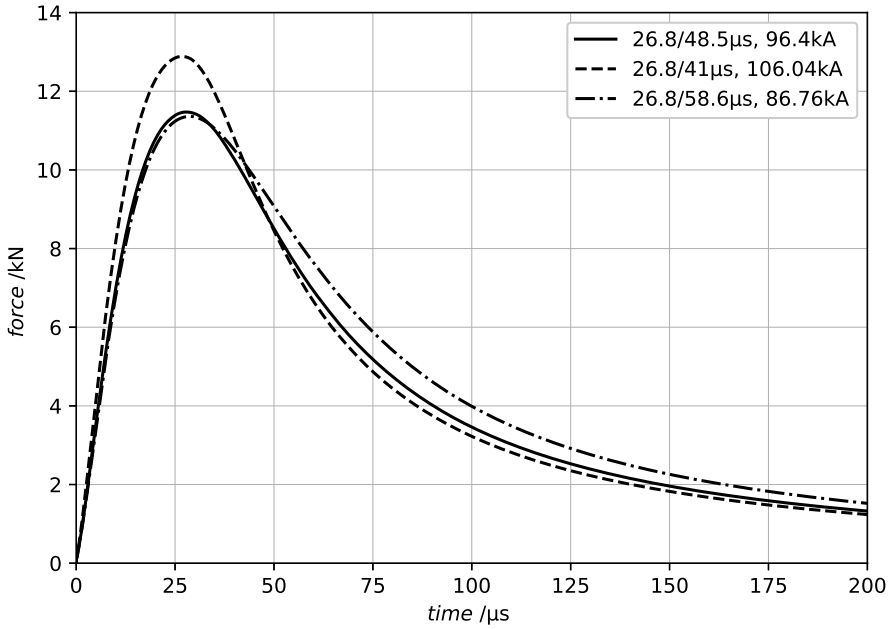


Figure 7.4: Force magnitude caused by explosion of lightning protection layers as a function of time for waveform alternatives to assess peak current influence for ECF 73

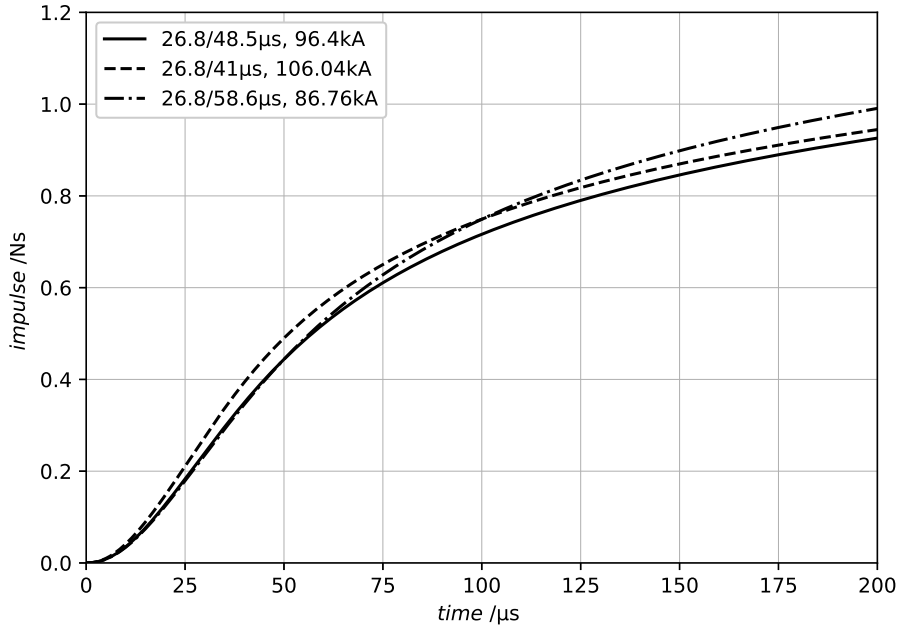


Figure 7.5: Impulse magnitude caused by explosion of lightning protection layers as a function of time for waveform alternatives to assess peak current influence for ECF 73

7.3.1.3 Supersonic plasma expansion

The parameters of the strong shock wave approximation are present in Table 7.4.

Table 7.4: Cylindrical shock wave parameters for waveform alternatives to assess peak current influence for ECF 73

	α_s /mm $\mu s^{-1/2}$	α /bar μs	β /bar μs^{-1}
26.8/41 µs, 106.04 kA	9.0701	104.5475	416.4966
26.8/58.6 µs, 86.76 kA	8.5188	92.2242	367.1670

Figure 7.6 represents the computed shock radius for the reference and waveforms in study, and Figure 7.7, Figure 7.8 and Figure 7.9 shown the pressure, force and impulse magnitudes generated by the supersonic plasma expansion, respectively.

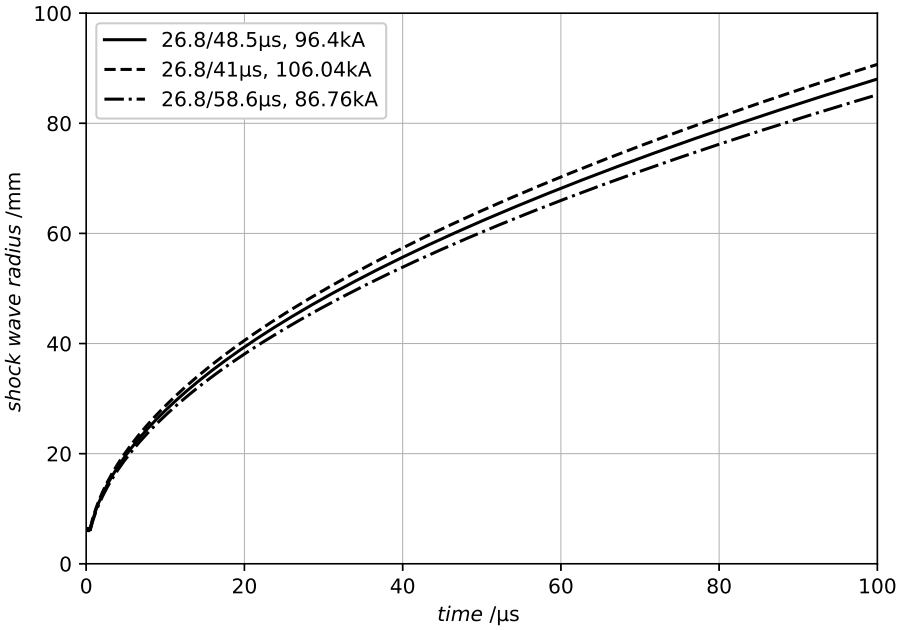


Figure 7.6: Computed shock radius for waveform alternatives to assess peak current influence for ECF 73

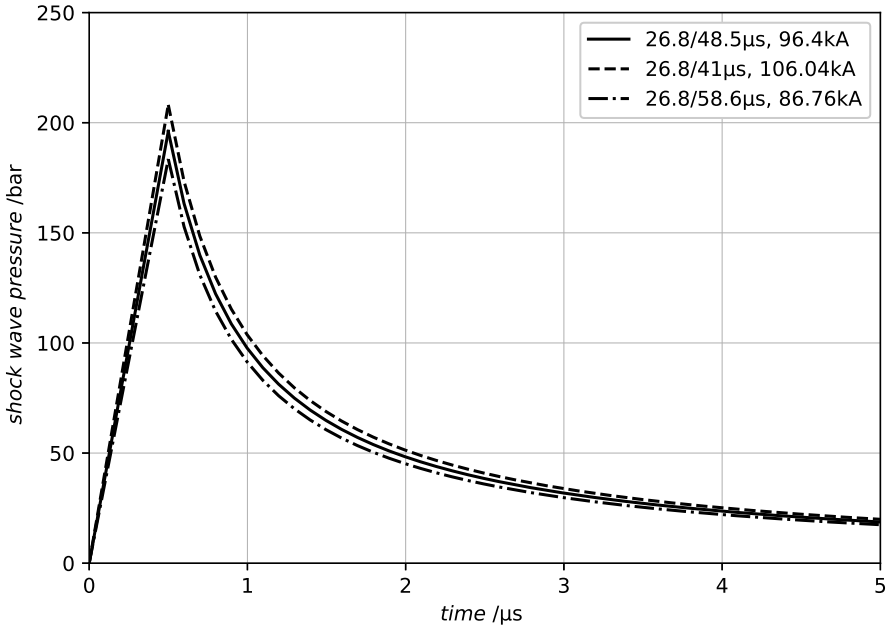


Figure 7.7: Mean cylindrical shock wave pressure as a function of time due to supersonic plasma expansion for waveform alternatives to assess peak current influence for ECF 73

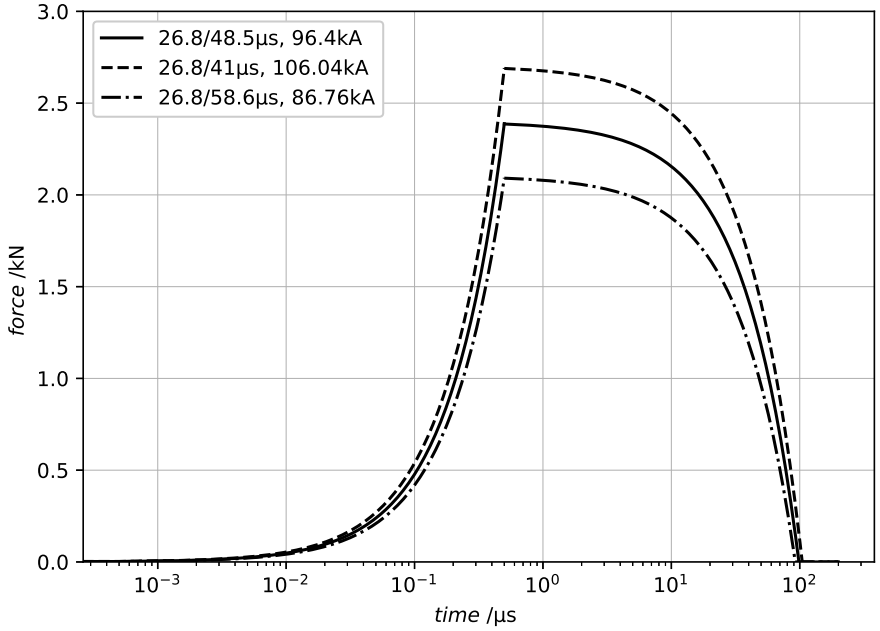


Figure 7.8: Force magnitude caused by supersonic plasma expansion as a function of time for waveform alternatives to assess peak current influence for ECF 73

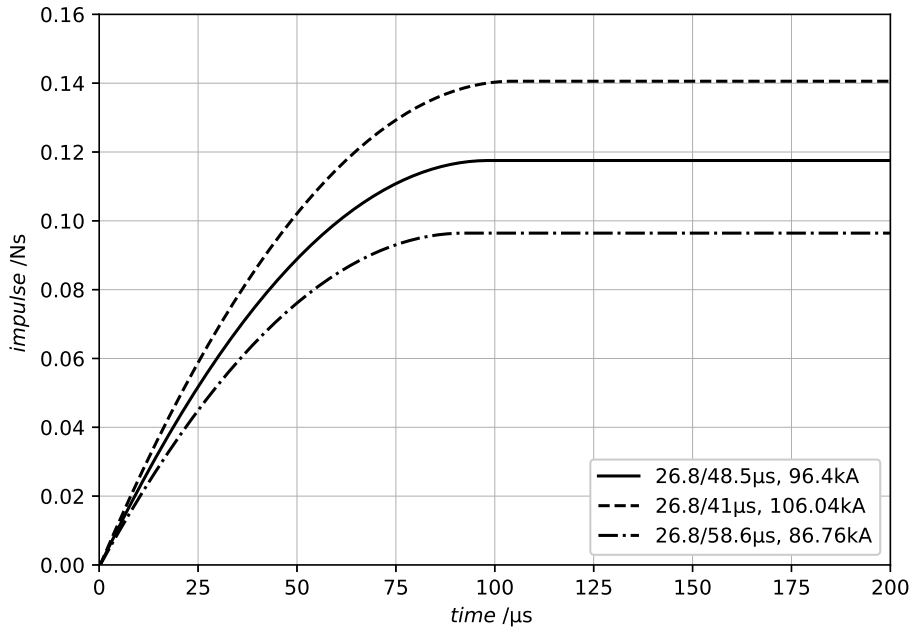


Figure 7.9: Impulse magnitude caused by supersonic plasma expansion as a function of time for waveform alternatives to assess peak current influence for ECF 73

7.3.1.4 Magnetic forces

To a complete analysis, pressure, force and impulse magnitudes generated by the magnetic forces contribution are presented in Figure 7.10, Figure 7.11 and Figure 7.12, respectively.

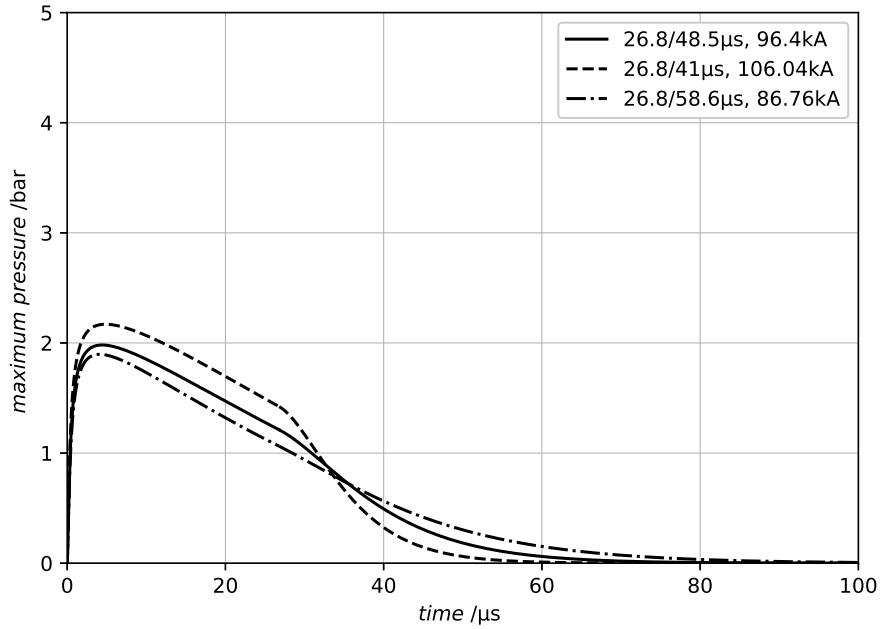


Figure 7.10: Maximum magnetic pressure evolution with time for waveform alternatives to assess peak current influence for ECF 73

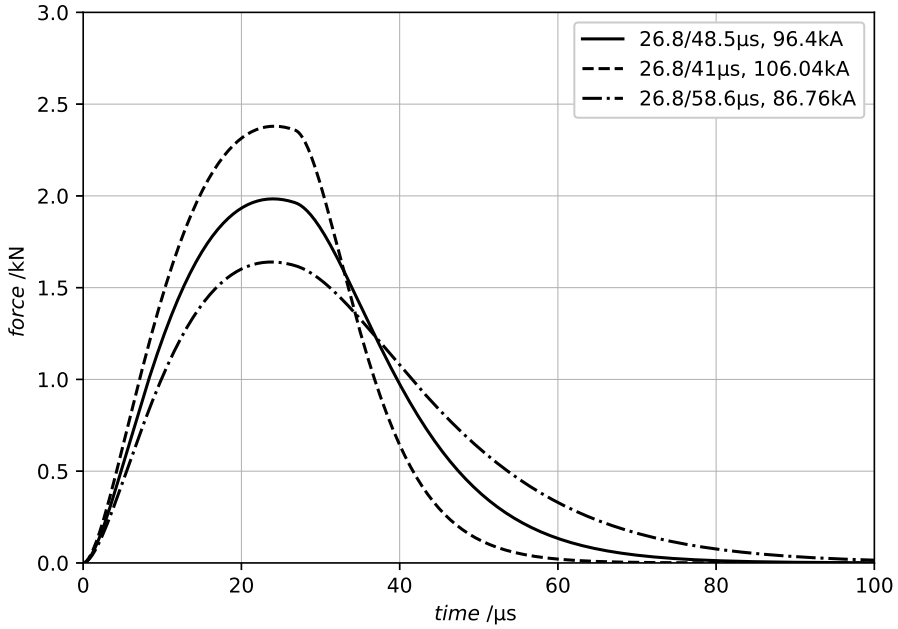


Figure 7.11: Force magnitude caused by magnetic forces as a function of time for for waveform alternatives to assess peak current influence for ECF 73

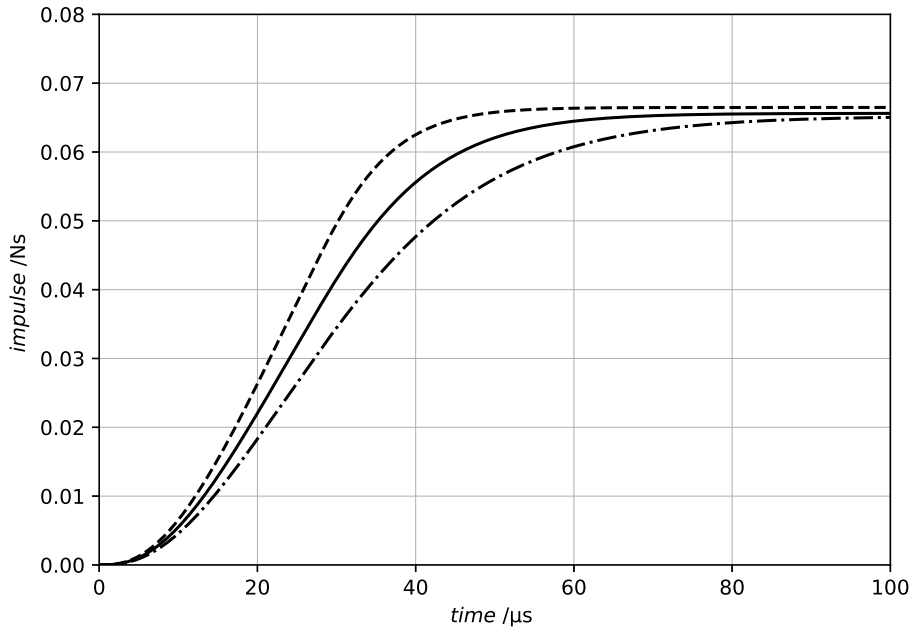
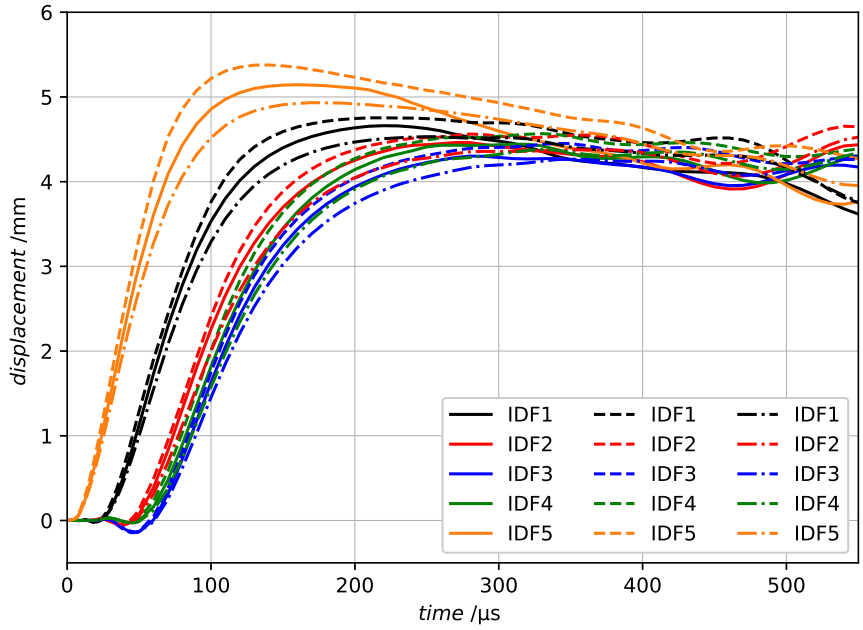


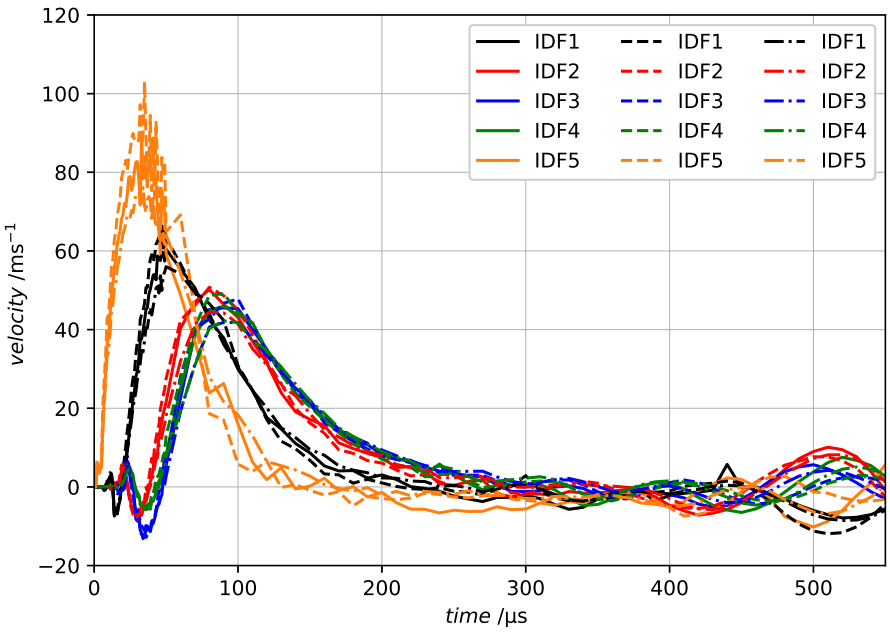
Figure 7.12: Impulse magnitude caused by magnetic forces as a function of time for waveform alternatives to assess peak current influence for ECF 73

7.3.1.5 Finite element predictions

The evaluation of the displacement and velocity of the five points already considered in the previously validated models are also performed, see Figure 7.13.



(a) Displacement



(b) Velocity

Figure 7.13: Finite element predictions for waveform alternatives to assess peak current influence, where solid lines represents the waveform 26.8/48.5 µs, 96.4 kA, dashed lines the waveform 26.8/41 µs, 106.04 kA and dashed dotted lines the waveform 26.8/58.6 µs, 86.76 kA for ECF 73

7.3.1.6 Damage maps

Consistent to previous analysis, an illustrative evaluation of the damage induced is shown. For each layer of the laminate, the damage variables in the longitudinal direction (d_1), Table 7.5, transverse direction (d_2), Table 7.6, shear (d_6), Table 7.7, and delamination (d), Table 7.8.

Table 7.5: Damage map assessment for damage variable in the longitudinal direction (d_1) for waveform alternatives to assess peak current influence for ECF 73

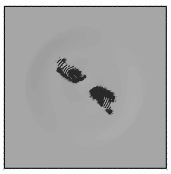
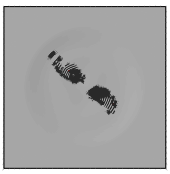
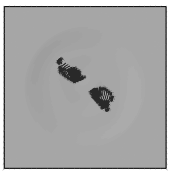
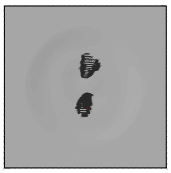
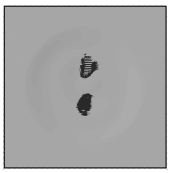
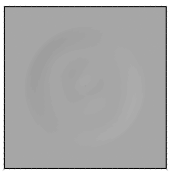
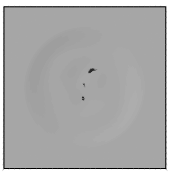
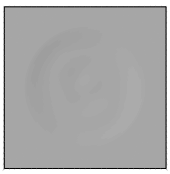
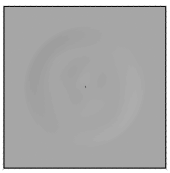
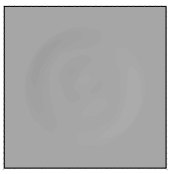
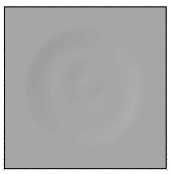
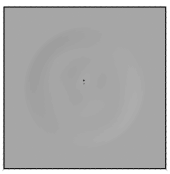
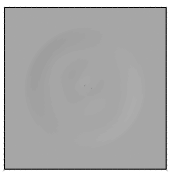
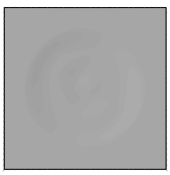
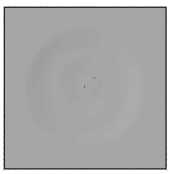
0.990 0.989 0.001 0.000 Y Z X	26.8/48.5 µs, 96.4 kA	26.8/41 µs, 106.04 kA	26.8/58.6 µs, 86.76 kA
Layer 8			
Layer 7			
Layer 6			
Layer 4 and 5			
Layer 3			
Layer 2			
Layer 1			

Table 7.6: Damage map assessment for damage variable in the transverse direction (d_2) for waveform alternatives to assess peak current influence for ECF 73

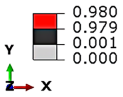
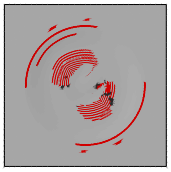
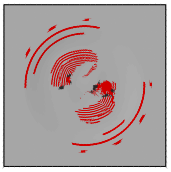
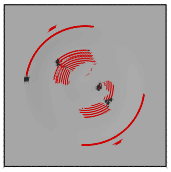
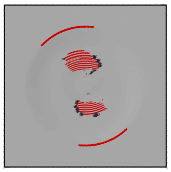
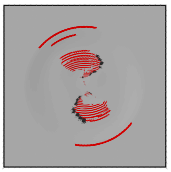
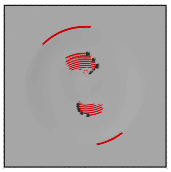
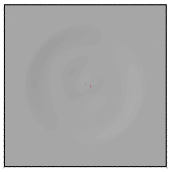
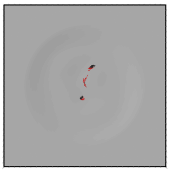
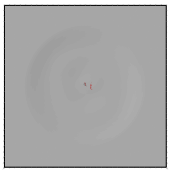
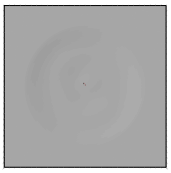
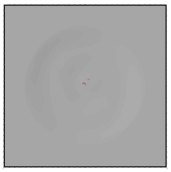
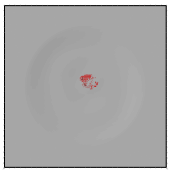
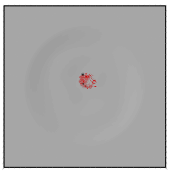
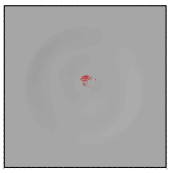
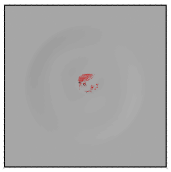
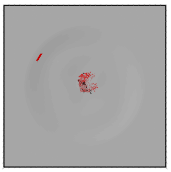
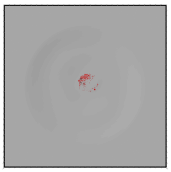
	26.8/48.5 µs, 96.4 kA	26.8/41 µs, 106.04 kA	26.8/58.6 µs, 86.76 kA
Layer 8			
Layer 7			
Layer 6			
Layer 4 and 5			
Layer 3			
Layer 2			
Layer 1			

Table 7.7: Damage map assessment for shear damage variable (d_6) for waveform alternatives to assess peak current influence for ECF 73

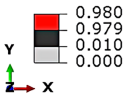
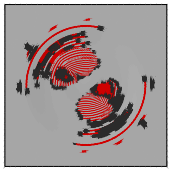
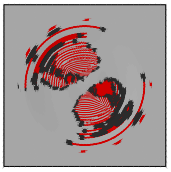
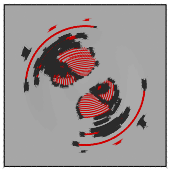
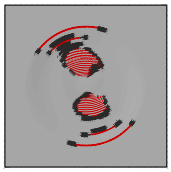
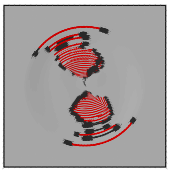
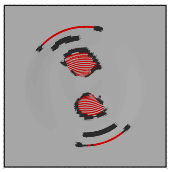
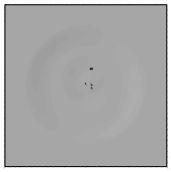
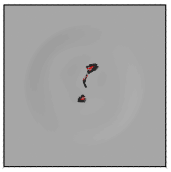
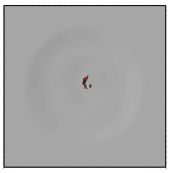
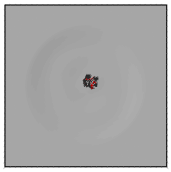
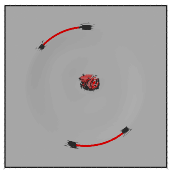
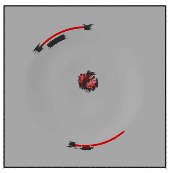
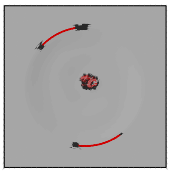
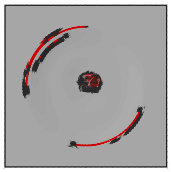
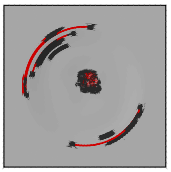
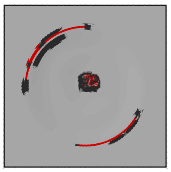
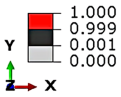
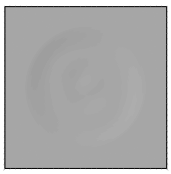
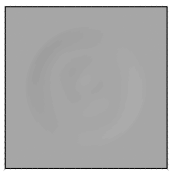
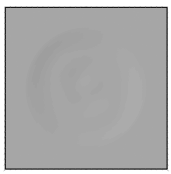
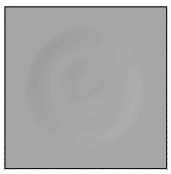
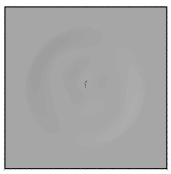
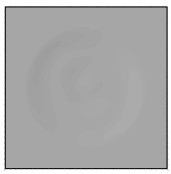
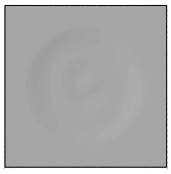
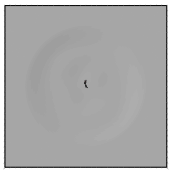
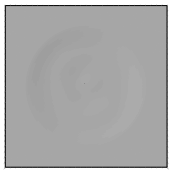
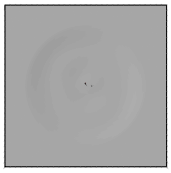
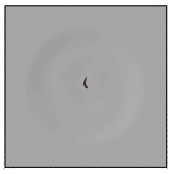
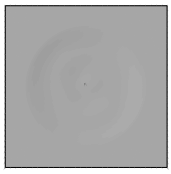
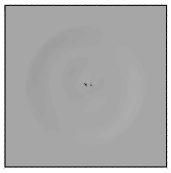
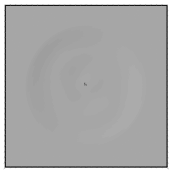
	26.8/48.5 µs, 96.4 kA	26.8/41 µs, 106.04 kA	26.8/58.6 µs, 86.76 kA
Layer 8			
Layer 7			
Layer 6			
Layer 4 and 5			
Layer 3			
Layer 2			
Layer 1			

Table 7.8: Damage map assessment for delamination (d) for waveform alternatives to assess peak current influence for ECF 73

	26.8/48.5 µs, 96.4 kA	26.8/41 µs, 106.04 kA	26.8/58.6 µs, 86.76 kA
Layer 8			
Layer 7			
Layer 6			
Layer 4 and 5			
Layer 3			
Layer 2			
Layer 1			

7.3.2 Expanded copper foil 195

7.3.2.1 Root radius

Carried out the simulations of the waveform alternatives to assess peak current influence for the ECF 195, the fitted root radii as a function of time are plotted in Figure 7.14 and Table 7.9 presents the respective parameters.

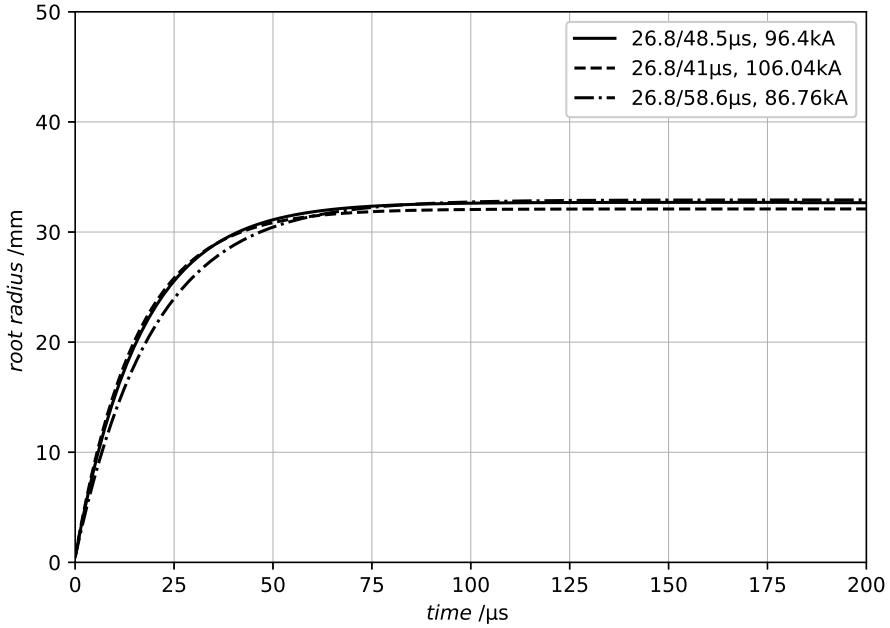


Figure 7.14: Root radius for waveform alternatives to assess peak current influence for ECF 195

Table 7.9: Root radius parameters for waveform alternatives to assess peak current influence for ECF 195

	a /mm	α /μs^{-1}	β /μs^{-1}	R_{R_0} /(mm)
26.8/41 µs, 106.04 kA	31.60	-6.73×10^{-7}	$-0.064\,66$	0.5
26.8/58.6 µs, 86.76 kA	32.43	-2.37×10^{-6}	$-0.051\,43$	0.5

Table 7.9: Root radius parameters for waveform alternatives to assess peak current influence for ECF 195

	t_s /μs	c /mm
26.8/41 µs, 106.04 kA	177.59	32.10
26.8/58.6 µs, 86.76 kA	194.65	32.91

7.3.2.2 Near-surface explosion

For the near-surface explosion of the lightning protection layer contribution the pressure, force and impulse magnitude are presented in Figure 7.15, Figure 7.16 and Figure 7.17, respectively.

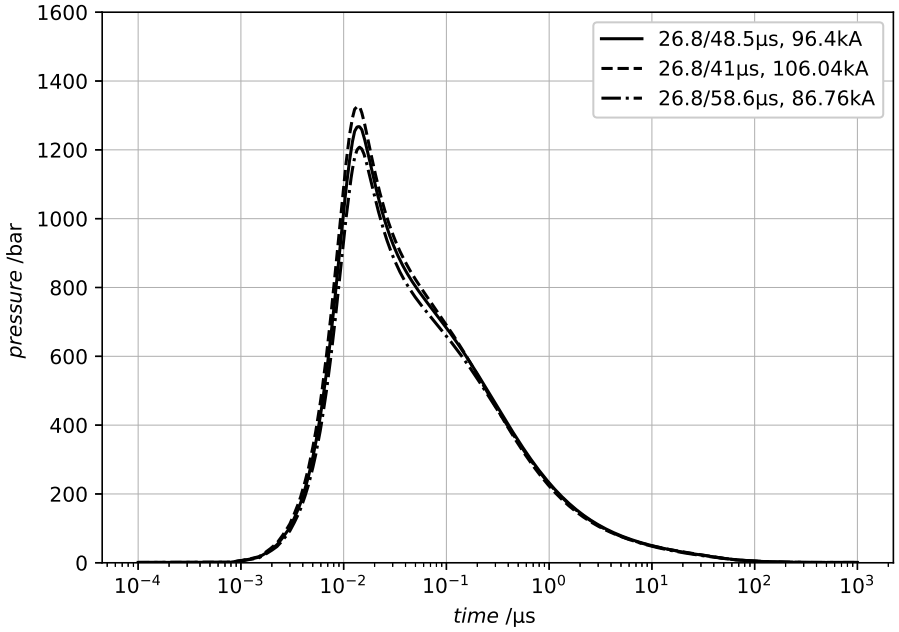


Figure 7.15: Overpressure caused by explosion of lightning protection layers as a function of time for waveform alternatives to assess peak current influence for ECF 195

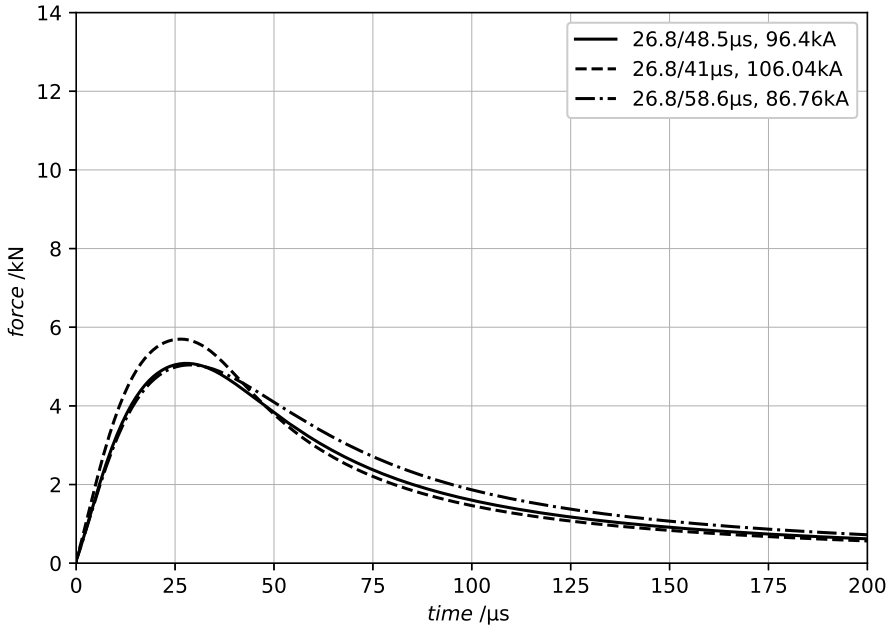


Figure 7.16: Force magnitude caused by explosion of lightning protection layers as a function of time for waveform alternatives to assess peak current influence for ECF 195

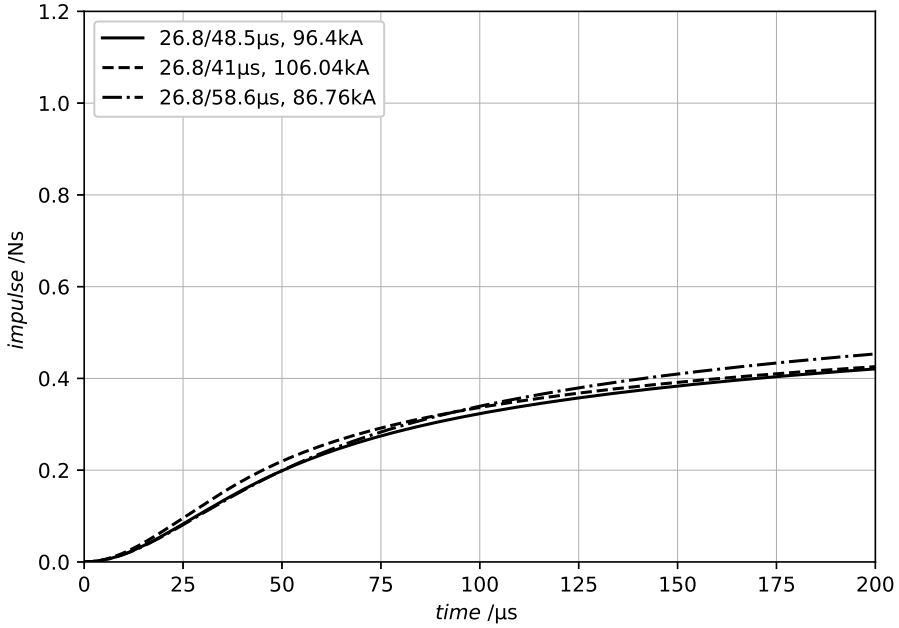


Figure 7.17: Impulse magnitude caused by explosion of lightning protection layers as a function of time for waveform alternatives to assess peak current influence for ECF 195

7.3.2.3 Supersonic plasma expansion

The parameters of the strong shock wave approximation are present in Table 7.10.

Table 7.10: Cylindrical shock wave parameters for waveform alternatives to assess peak current influence for ECF 195

	α_s /mm $\mu s^{-1/2}$	α /bar μs	β /bar μs^{-1}
26.8/41 µs, 106.04 kA	9.0701	104.5475	416.4966
26.8/58.6 µs, 86.76 kA	8.5188	92.2242	367.1670

Figure 7.18 represents the computed shock radius for the reference and waveforms in study, and Figure 7.19, Figure 7.20 and Figure 7.21 shown the pressure, force and impulse magnitudes generated by the supersonic plasma expansion, respectively.

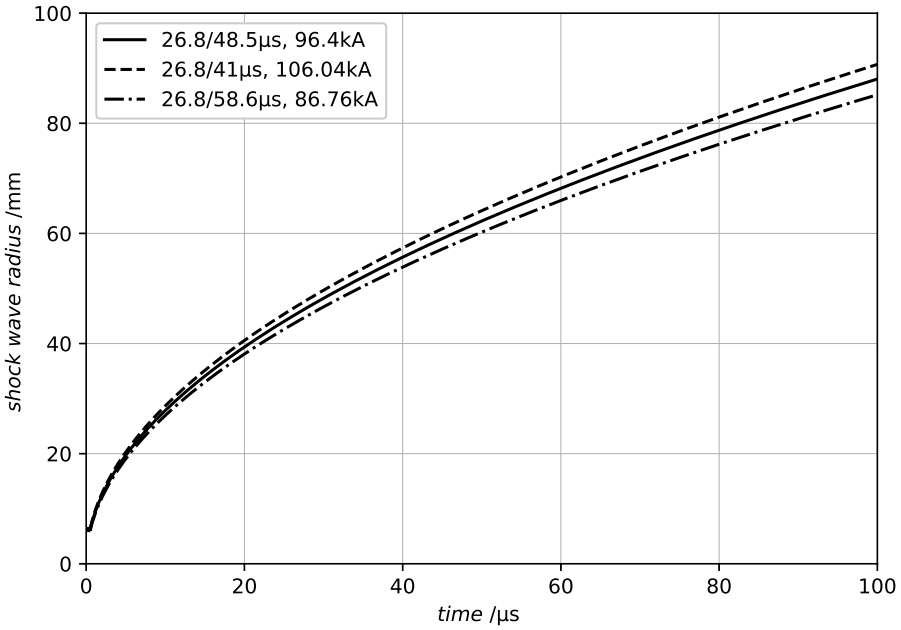


Figure 7.18: Computed shock radius for waveform alternatives to assess peak current influence for ECF 195

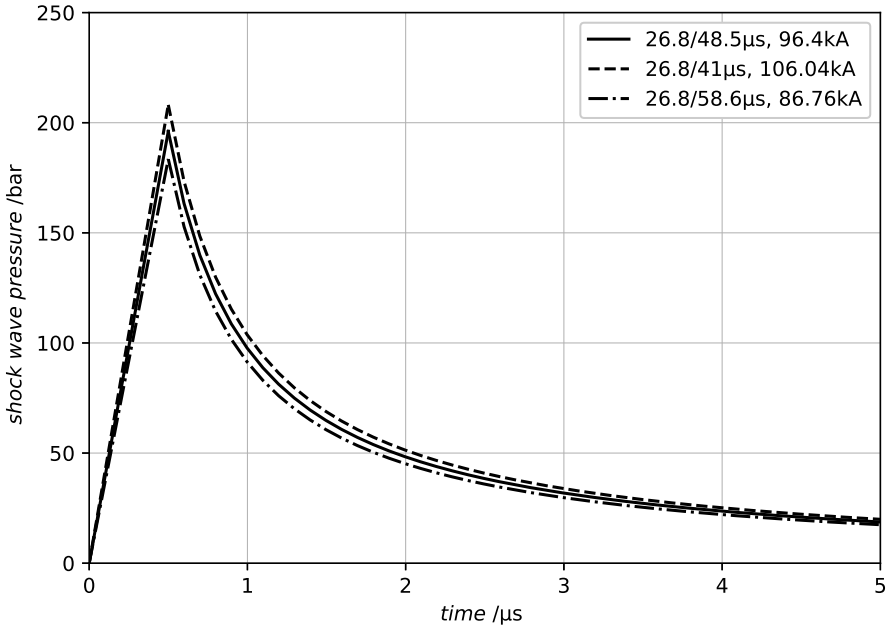


Figure 7.19: Mean cylindrical shock wave pressure as a function of time due to supersonic plasma expansion for waveform alternatives to assess peak current influence for ECF 195

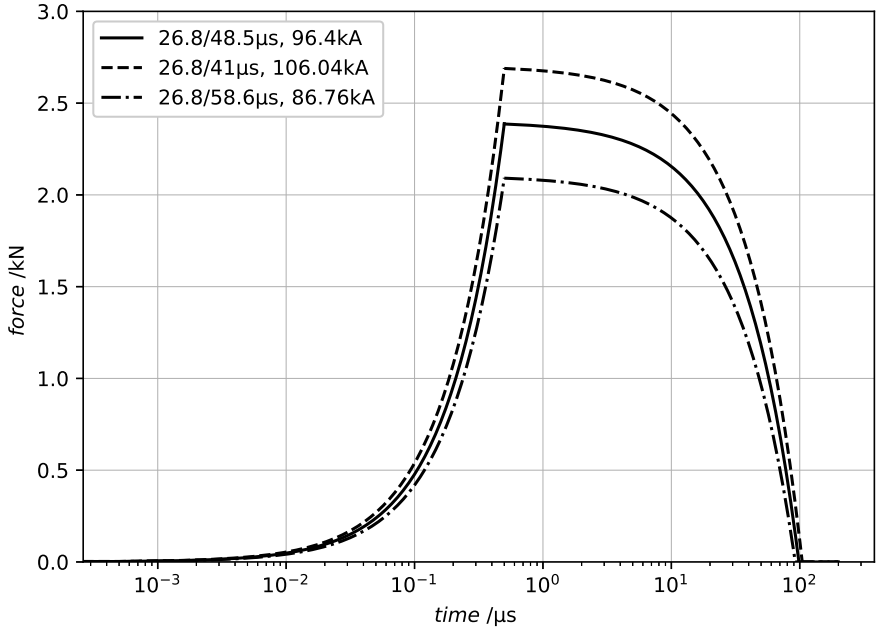


Figure 7.20: Force magnitude caused by supersonic plasma expansion as a function of time for waveform alternatives to assess peak current influence for ECF 195

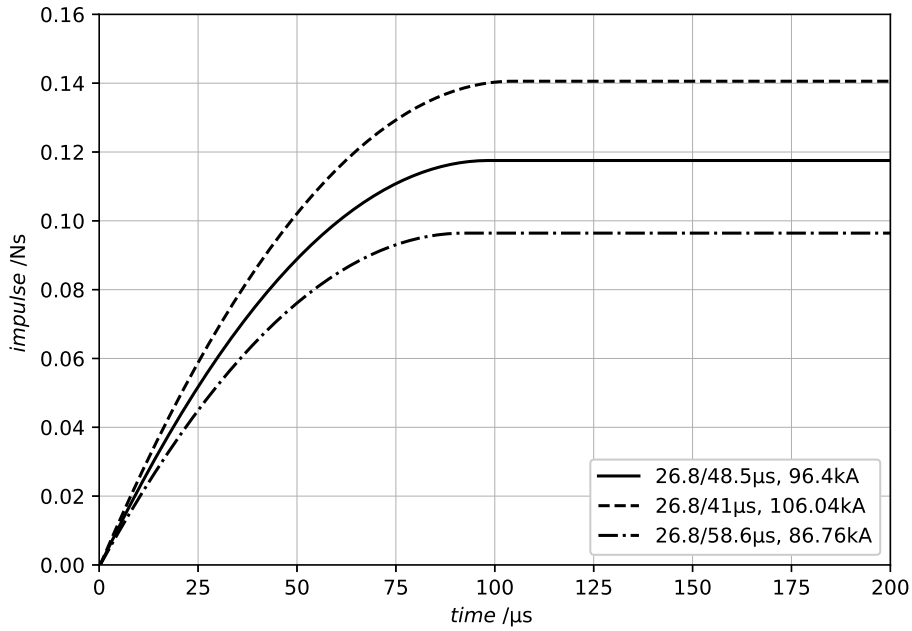


Figure 7.21: Impulse magnitude caused by supersonic plasma expansion as a function of time for waveform alternatives to assess peak current influence for ECF 195

7.3.2.4 Magnetic forces

To a complete analysis, pressure, force and impulse magnitudes generated by the magnetic forces contribution are presented in Figure 7.22, Figure 7.23 and Figure 7.24, respectively.

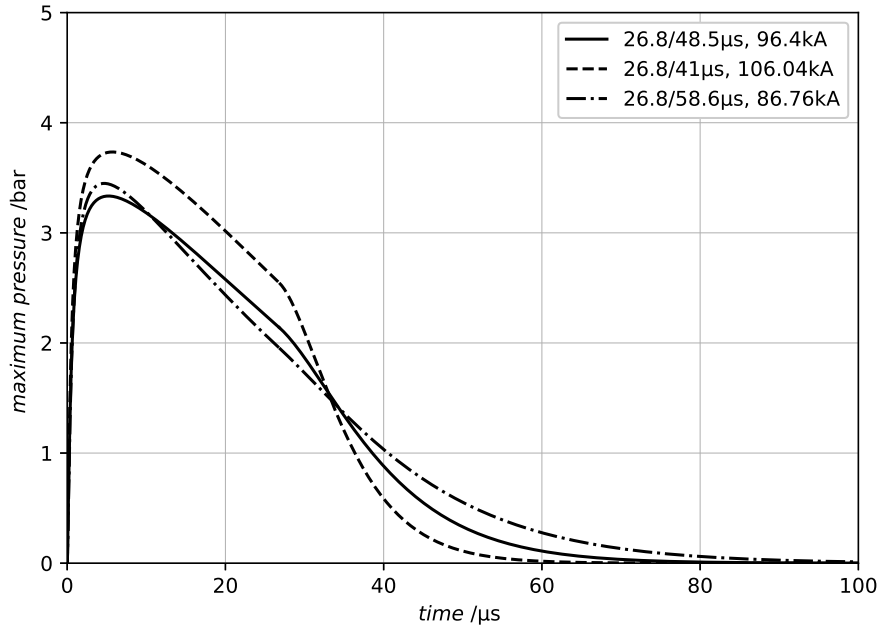


Figure 7.22: Maximum magnetic pressure evolution with time for waveform alternatives to assess peak current influence for ECF 195

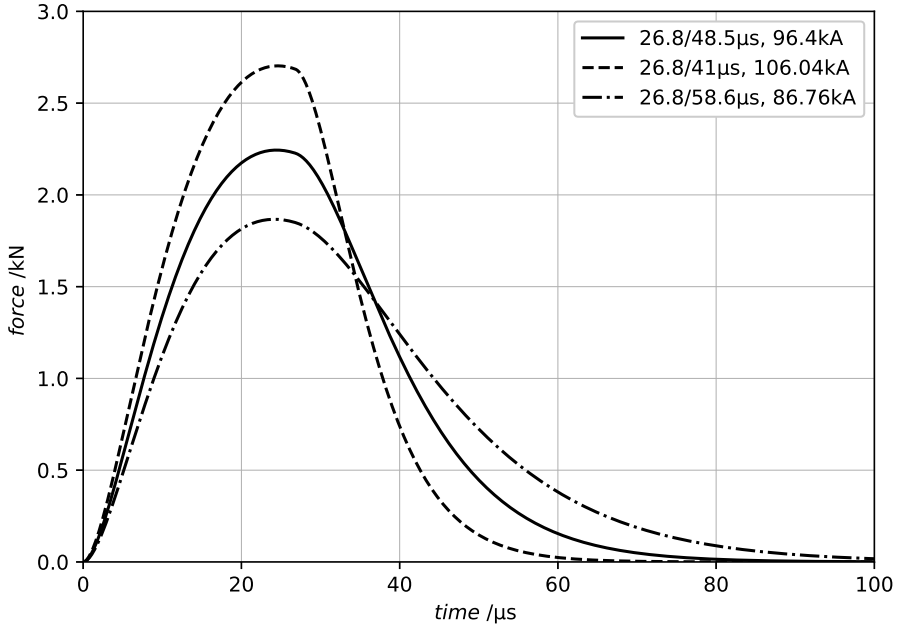


Figure 7.23: Force magnitude caused by magnetic forces as a function of time for for waveform alternatives to assess peak current influence for ECF 195

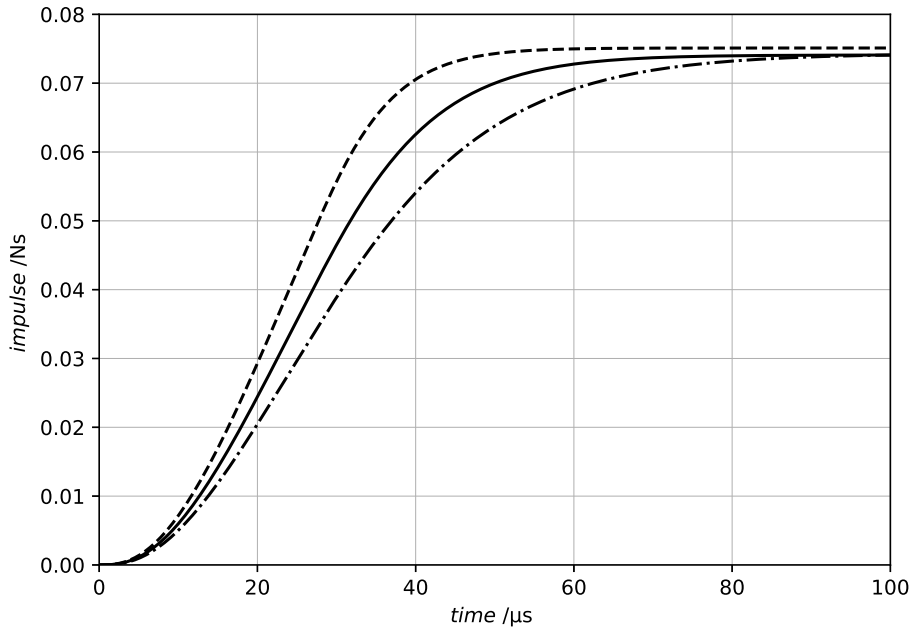
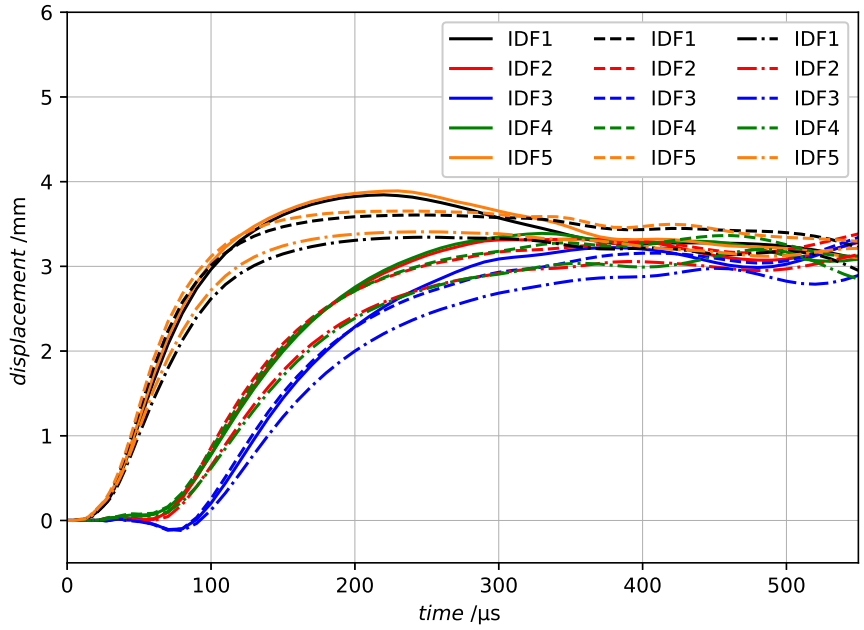


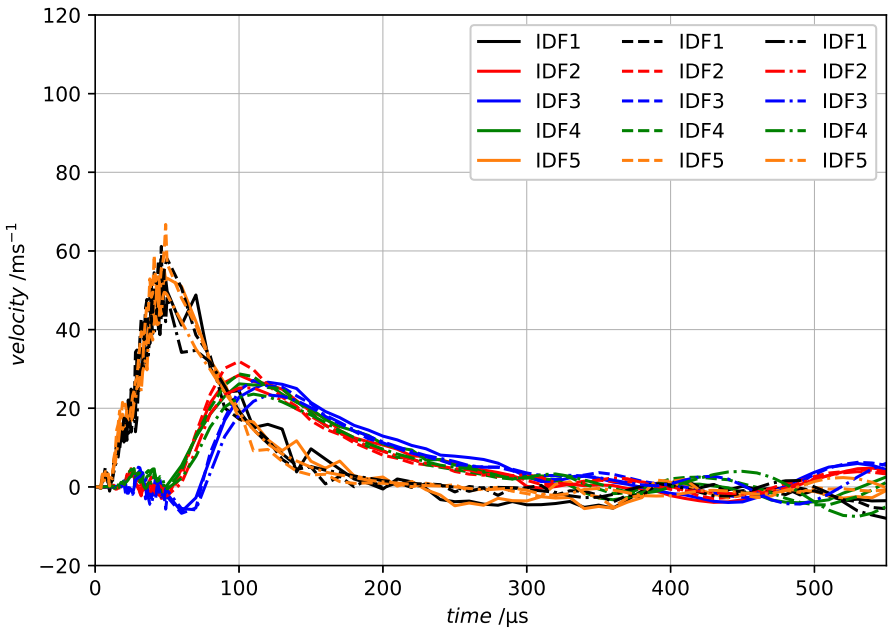
Figure 7.24: Impulse magnitude caused by magnetic forces as a function of time for waveform alternatives to assess peak current influence for ECF 195

7.3.2.5 Finite element predictions

The evaluation of the displacement and velocity of the five points already considered in the previously validated models and in the analysis with ECF 73 are also performed for ECF 195, see Figure 7.25.



(a) Displacement



(b) Velocity

Figure 7.25: Finite element predictions for waveform alternatives to assess peak current influence, where solid lines represents the waveform 26.8/48.5 µs, 96.4 kA, dashed lines the waveform 26.8/41 µs, 106.04 kA and dashed dotted lines the waveform 26.8/58.6 µs, 86.76 kA for ECF 195

7.3.2.6 Damage maps

The damage map assessment was also performed for ECF 195. For each layer of the laminate, the damage variables in the longitudinal direction (d_1), Table 7.11, transverse direction (d_2), Table 7.12, shear (d_6), Table 7.13, and delamination (d), Table 7.14.

Table 7.11: Damage map assessment for damage variable in the longitudinal direction (d_1) for waveform alternatives to assess peak current influence for ECF 195

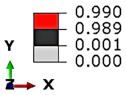
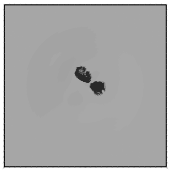
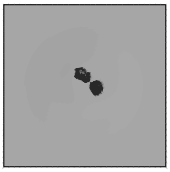
	26.8/48.5 µs, 96.4 kA	26.8/41 µs, 106.04 kA	26.8/58.6 µs, 86.76 kA
Layer 8			
Layer 7			
Layer 6			
Layer 4 and 5			
Layer 3			
Layer 2			
Layer 1			

Table 7.12: Damage map assessment for damage variable in the transverse direction (d_2) for waveform alternatives to assess peak current influence for ECF 195

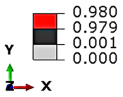
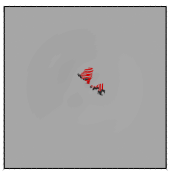
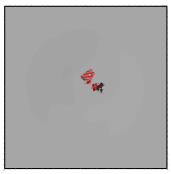
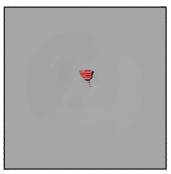
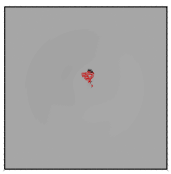
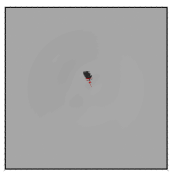
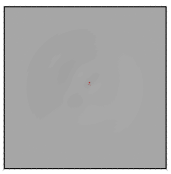
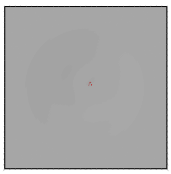
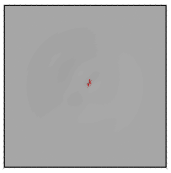
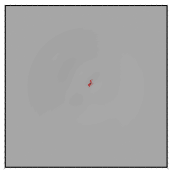
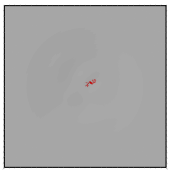
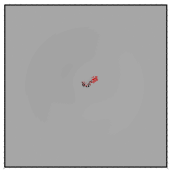
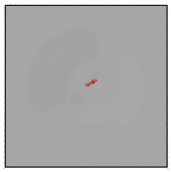
	26.8/48.5 µs, 96.4 kA	26.8/41 µs, 106.04 kA	26.8/58.6 µs, 86.76 kA
Layer 8			
Layer 7			
Layer 6			
Layer 4 and 5			
Layer 3			
Layer 2			
Layer 1			

Table 7.13: Damage map assessment for shear damage variable (d_6) for waveform alternatives to assess peak current influence for ECF 195

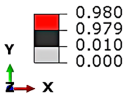
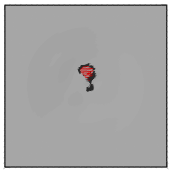
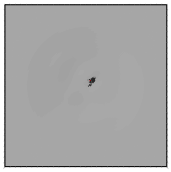
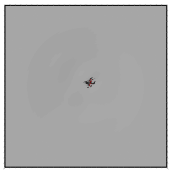
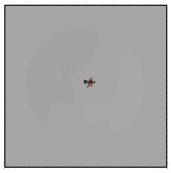
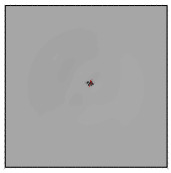
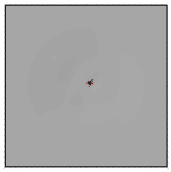
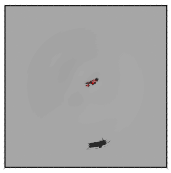
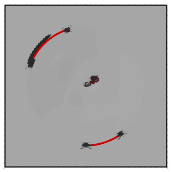
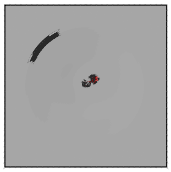
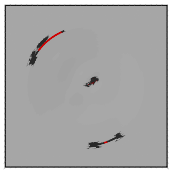
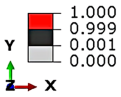
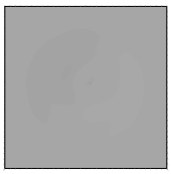
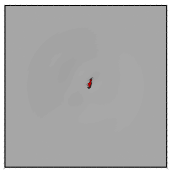
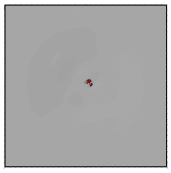
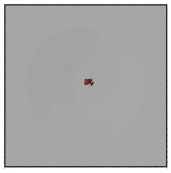
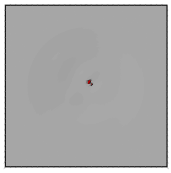
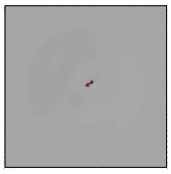
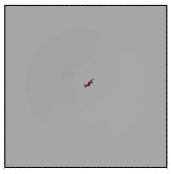
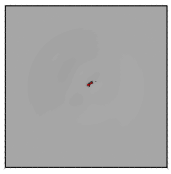
	26.8/48.5 µs, 96.4 kA	26.8/41 µs, 106.04 kA	26.8/58.6 µs, 86.76 kA
Layer 8			
Layer 7			
Layer 6			
Layer 4 and 5			
Layer 3			
Layer 2			
Layer 1			

Table 7.14: Damage map assessment for delamination (d) for waveform alternatives to assess peak current influence for ECF 195

	26.8/48.5 µs, 96.4 kA	26.8/41 µs, 106.04 kA	26.8/58.6 µs, 86.76 kA
Layer 8			
Layer 7			
Layer 6			
Layer 4 and 5			
Layer 3			
Layer 2			
Layer 1			

7.4 Action integral variation

To assess the effect of the action integral, the peak current was kept at 96.4 kA and the action integral took values of 0.3×10^6 A^2s $\pm(20\%)$. The graphical visualization of the proposed waveforms is shown in Figure 7.26 and the waveform parameters are shown in Table 7.15.

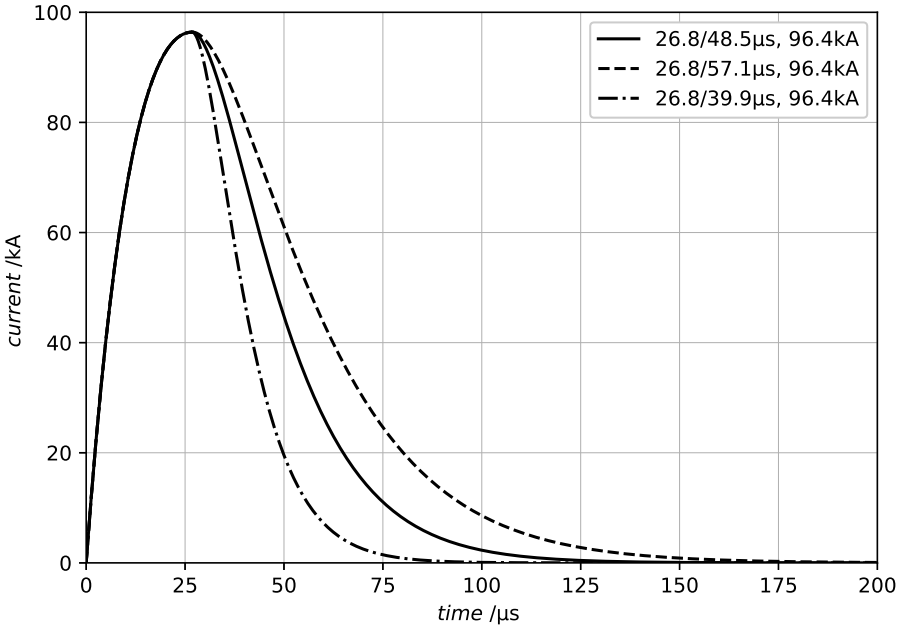


Figure 7.26: Waveforms considering different action integrals

Table 7.15: Waveform parameters for for different action integrals

	a (s^{-1})	b (s^{-1})	A (-)	I_{max} (A)	c (A)
26.8/57.1 µs, 96.4 kA	33833.1	41024.7	14.1256	96400	1361705.4
26.8/39.9 µs, 96.4 kA	33833.1	41024.7	14.1256	96400	1361705.4

Table 7.15: Waveform parameters for for different action integrals

	f (−)	v (s)
26.8/57.1 µs, 96.4 kA	1.4890	8.801×10^{-6}
26.8/39.9 µs, 96.4 kA	3.4594	1.905×10^{-5}

7.4.1 Expanded copper foil 73

7.4.1.1 Root radius

The fitted root radii as a function of time for waveform alternatives to assess action integral influence are plotted in Figure 7.27 and Table 7.16 presents the respective parameters.

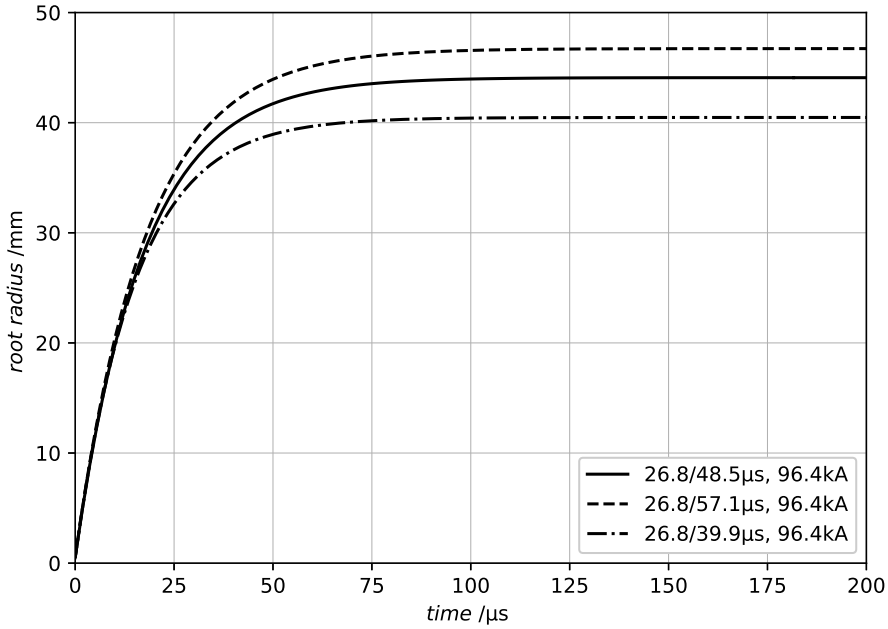


Figure 7.27: Root radius for waveform alternatives to assess action integral influence for ECF 73

Table 7.16: Root radius parameters for waveform alternatives to assess action integral influence for ECF 73

	a /mm	α /μs^{-1}	β /μs^{-1}	R_{R_0} /(mm)
26.8/57.1 µs, 96.4 kA	46.24	-1.30×10^{-6}	−0.056 11	0.5
26.8/39.9 µs, 96.4 kA	39.98	-6.26×10^{-7}	−0.065 16	0.5

Table 7.16: Root radius parameters for waveform alternatives to assess action integral influence for ECF 73

	t_s /μs	c /mm
26.8/57.1 µs, 96.4 kA	190.64	46.73
26.8/39.9 µs, 96.4 kA	177.59	40.4752

7.4.1.2 Near-surface explosion

For the near-surface explosion of the lightning protection layer contribution the pressure, force and impulse magnitude are presented in Figure 7.28, Figure 7.29 and Figure 7.30, respectively.

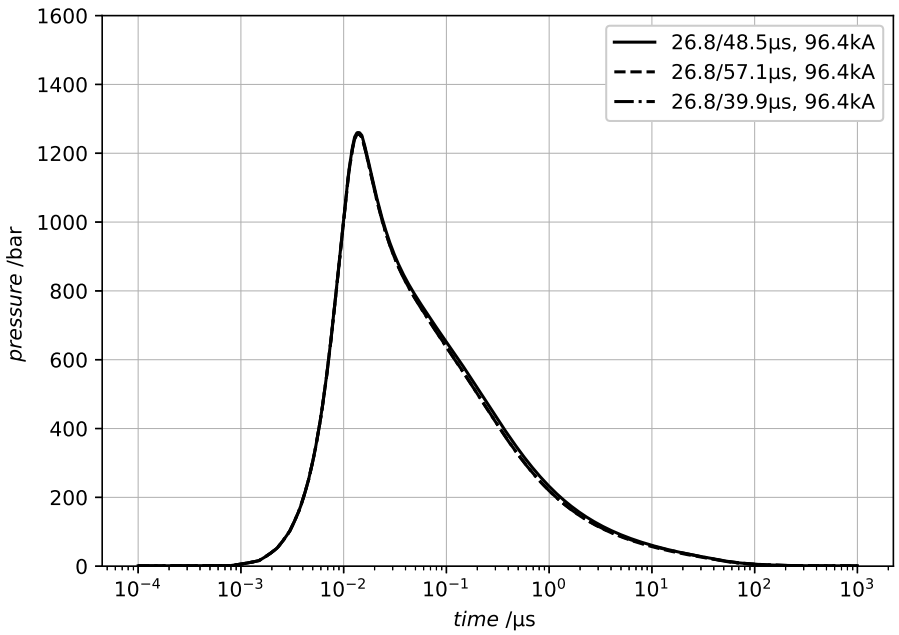


Figure 7.28: Overpressure caused by explosion of lightning protection layers as a function of time for waveform alternatives to assess action integral influence for ECF 73

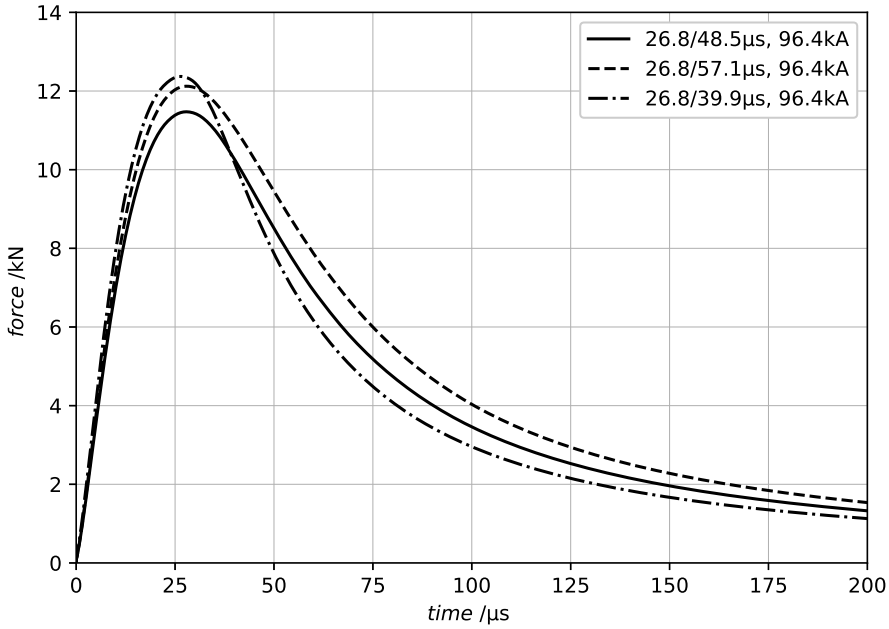


Figure 7.29: Force magnitude caused by explosion of lightning protection layers as a function of time for waveform alternatives to assess action integral influence for ECF 73

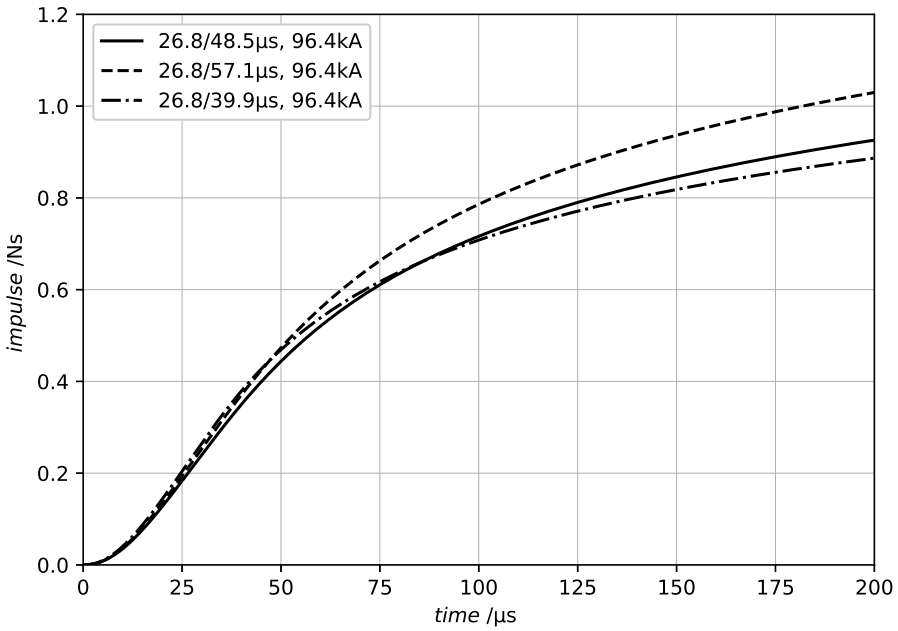


Figure 7.30: Impulse magnitude caused by explosion of lightning protection layers as a function of time for waveform alternatives to assess action integral influence for ECF 73

7.4.1.3 Supersonic plasma expansion

The parameters of the strong shock wave approximation are present in Table 7.17.

Table 7.17: Cylindrical shock wave parameters for waveform alternatives to assess action integral influence for ECF 73

	α_s /mm $\mu s^{-1/2}$	α /bar μs	β /bar μs^{-1}
26.8/41 µs, 106.04 kA	8.8040	98.5016	392.2952
26.8/58.6 µs, 86.76 kA	8.8040	98.5016	392.2952

Figure 7.31 represents the computed shock radius for the reference and waveforms in study, and Figure 7.32, Figure 7.33 and Figure 7.34 shown the pressure, force and impulse magnitudes generated by the supersonic plasma expansion, respectively.

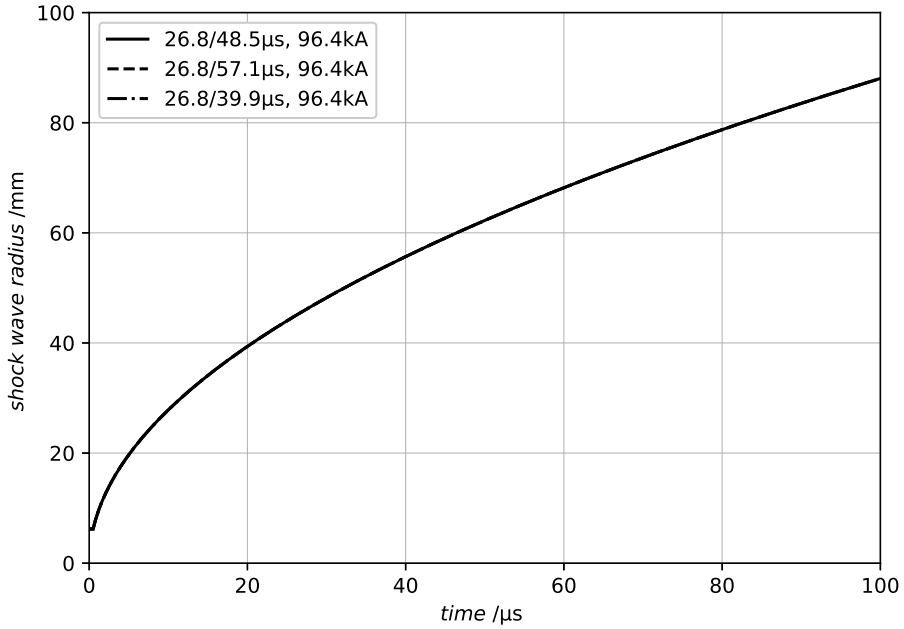


Figure 7.31: Computed shock radius for waveform alternatives to assess action integral influence for ECF 73

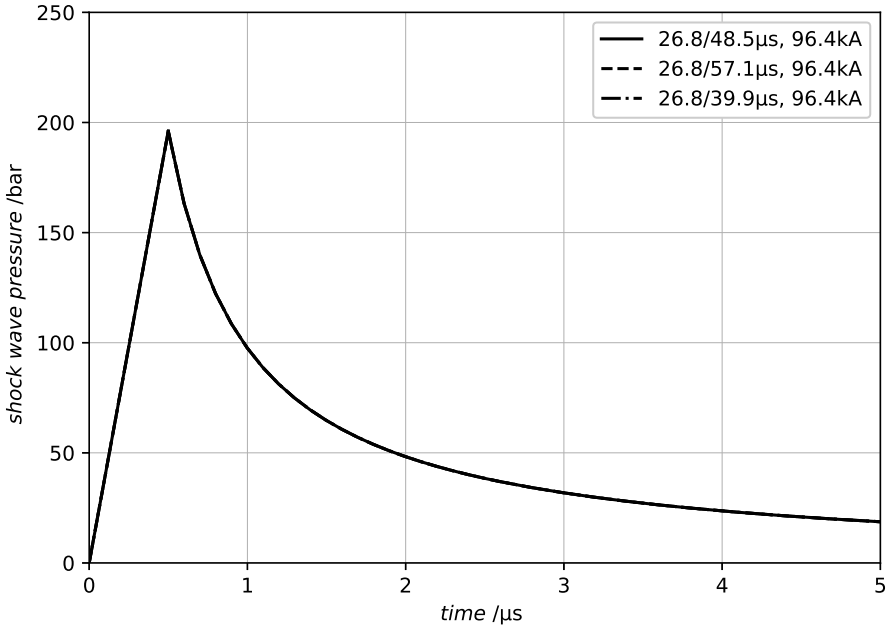


Figure 7.32: Mean cylindrical shock wave pressure as a function of time due to supersonic plasma expansion for waveform alternatives to assess action integral influence for ECF 73

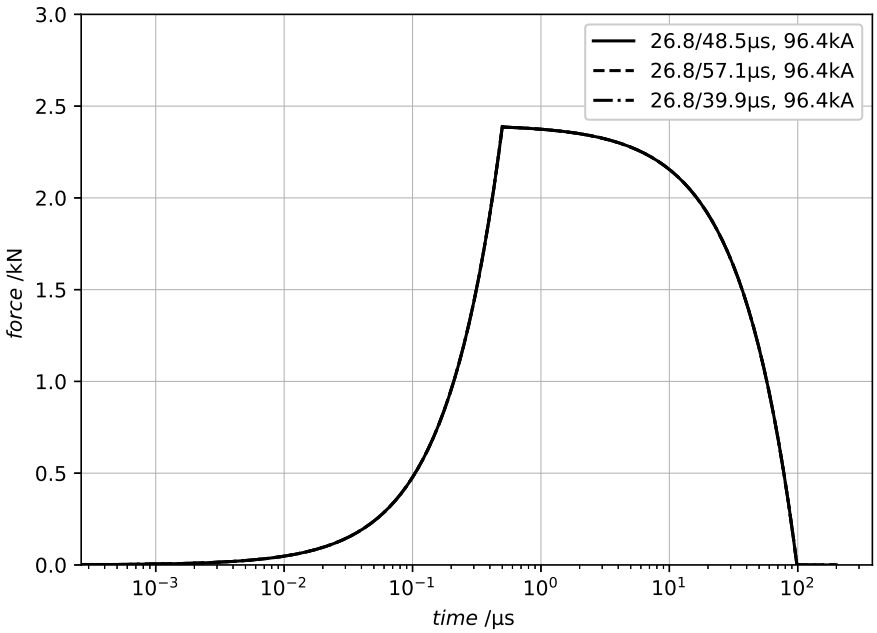


Figure 7.33: Force magnitude caused by supersonic plasma expansion as a function of time for waveform alternatives to assess action integral influence for ECF 73

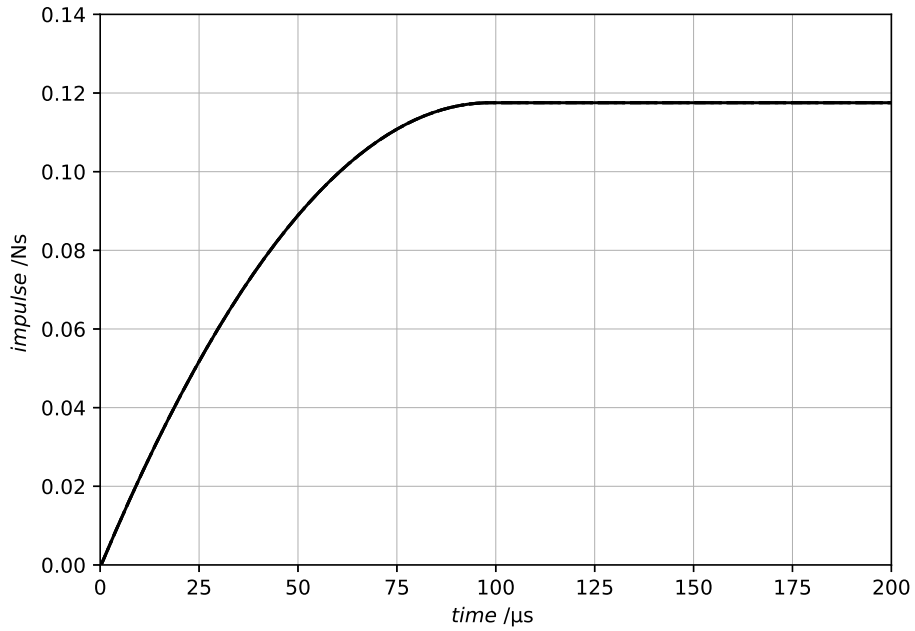


Figure 7.34: Impulse magnitude caused by supersonic plasma expansion as a function of time for waveform alternatives to assess action integral influence for ECF 73

7.4.1.4 Magnetic forces

To a complete analysis, pressure, force and impulse magnitudes generated by the magnetic forces contribution are presented in Figure 7.35, Figure 7.36 and Figure 7.37, respectively.

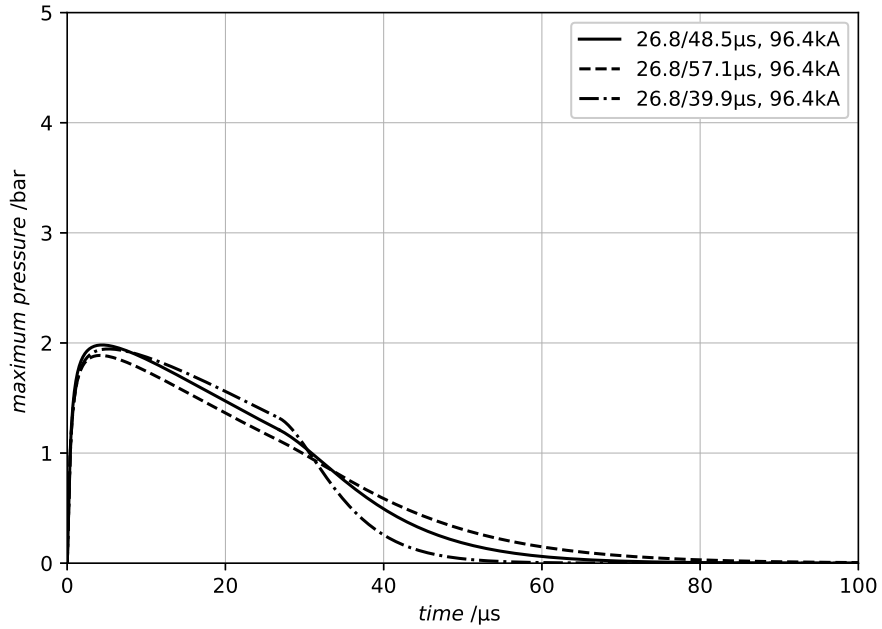


Figure 7.35: Maximum magnetic pressure evolution with time for waveform alternatives to assess action integral influence for ECF 73

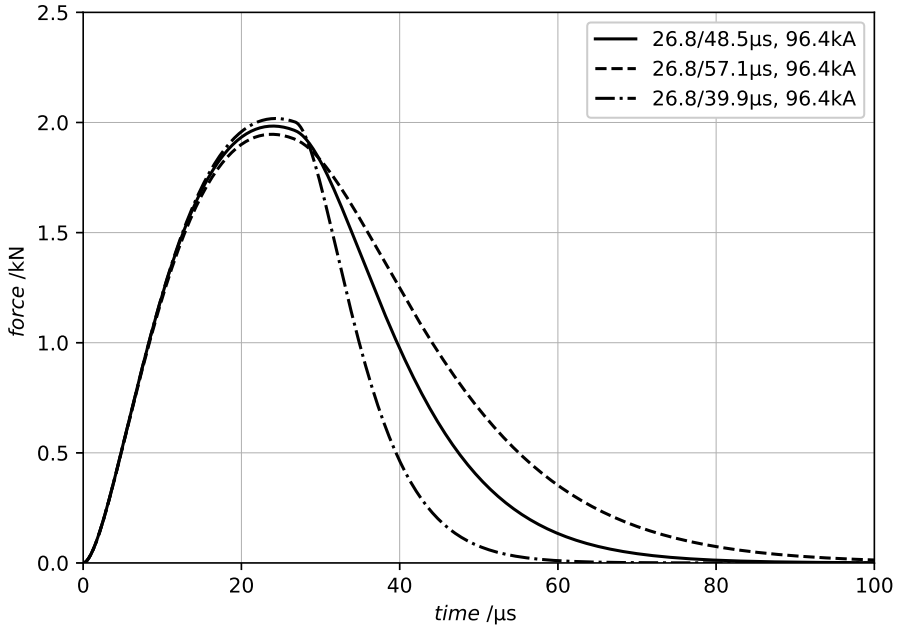


Figure 7.36: Force magnitude caused by magnetic forces as a function of time for for waveform alternatives to assess action integral influence for ECF 73

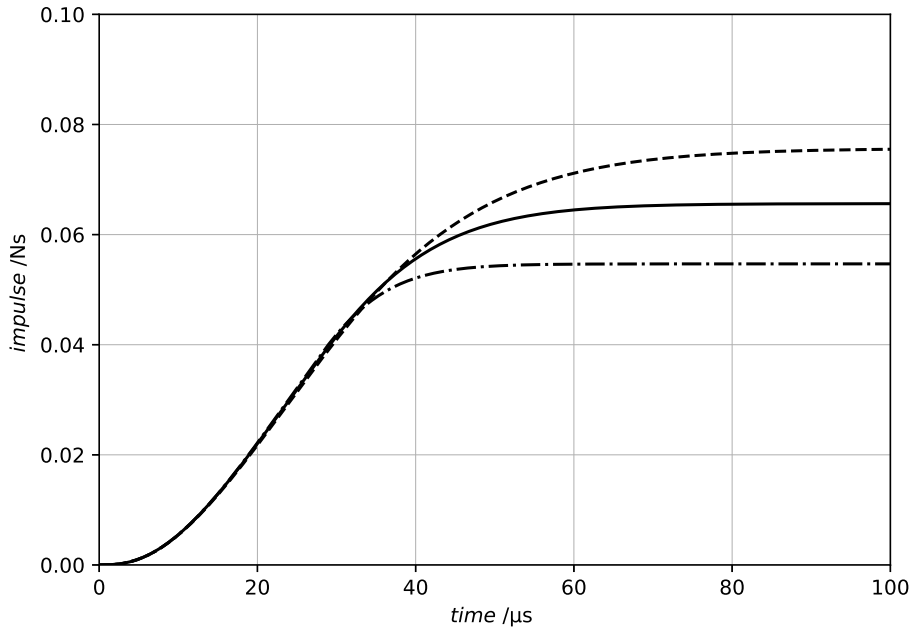
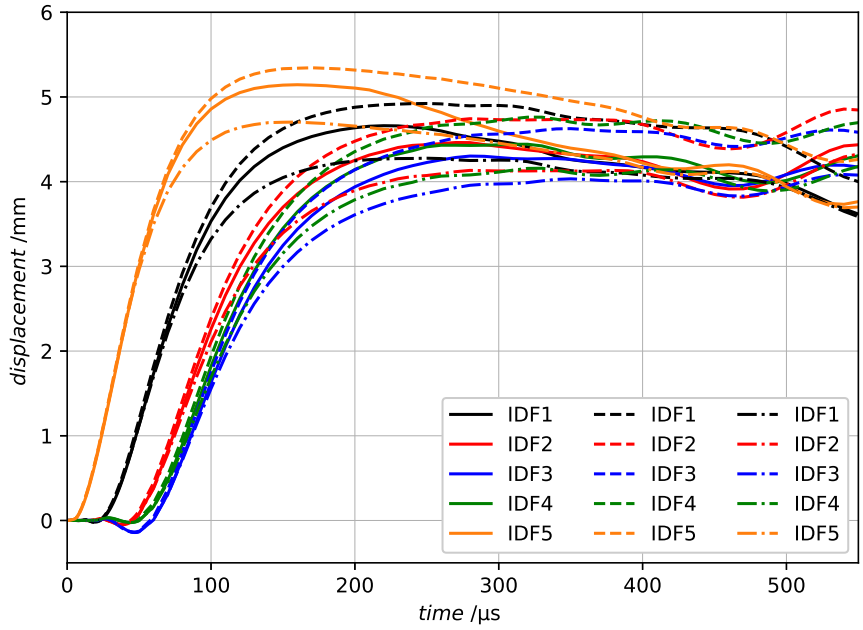


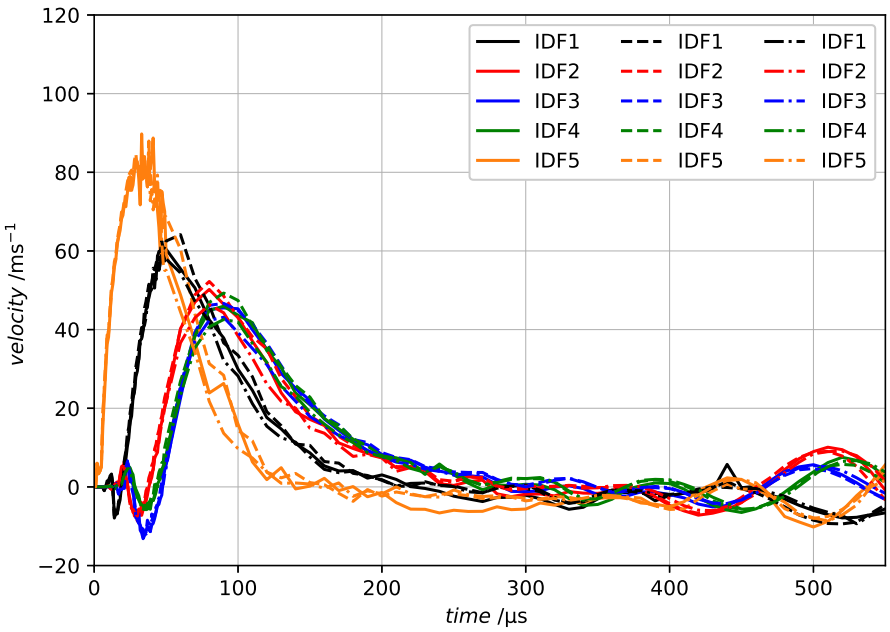
Figure 7.37: Impulse magnitude caused by magnetic forces as a function of time for waveform alternatives to assess action integral influence for ECF 73

7.4.1.5 Finite element predictions

The evaluation of the displacement and velocity of the five points already considered in the previously validated models and in the peak current influence studies are also performed, see Figure 7.38.



(a) Displacement



(b) Velocity

Figure 7.38: Finite element predictions for waveform alternatives to assess action integral influence, where solid lines represents the waveform 26.8/48.5 µs, 96.4 kA, dashed lines the waveform 26.8/57.1 µs, 96.4 kA and dashed dotted lines the waveform 26.8/39.9 µs, 96.4 kA for ECF 73

7.4.1.6 Damage maps

Following the previous analyses, an illustrative evaluation of the damage induced is shown. For each layer of the laminate, the damage variables in the longitudinal direction (d_1), Table 7.18, transverse direction (d_2), Table 7.19, shear (d_6), Table 7.20, and delamination (d), Table 7.21.

Table 7.18: Damage map assessment for damage variable in the longitudinal direction (d_1) for waveform alternatives to assess action integral influence for ECF 73

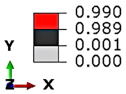
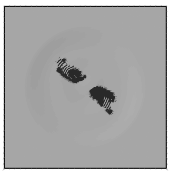
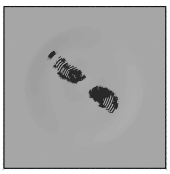
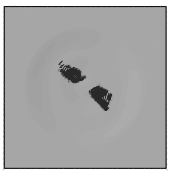
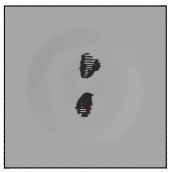
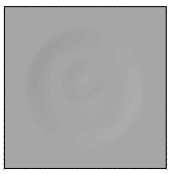
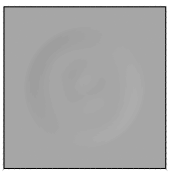
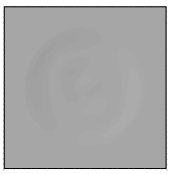
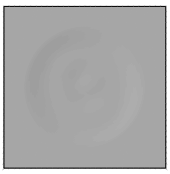
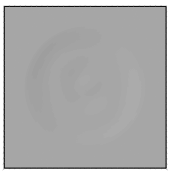
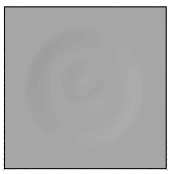
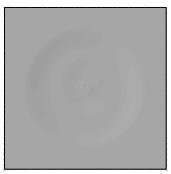
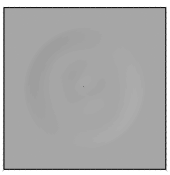
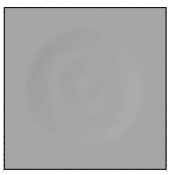
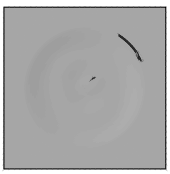
	26.8/48.5 µs, 96.4 kA	26.8/57.1 µs, 96.4 kA	26.8/39.9 µs, 96.4 kA
Layer 8			
Layer 7			
Layer 6			
Layer 4 and 5			
Layer 3			
Layer 2			
Layer 1			

Table 7.19: Damage map assessment for damage variable in the transverse direction (d_2) for waveform alternatives to assess action integral influence for ECF 73

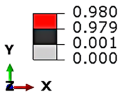
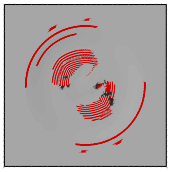
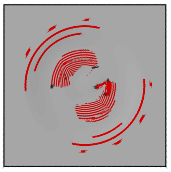
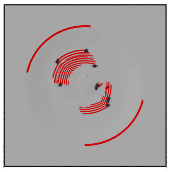
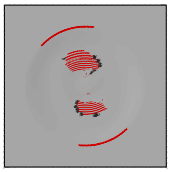
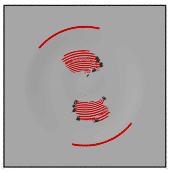
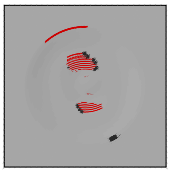
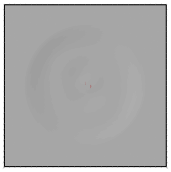
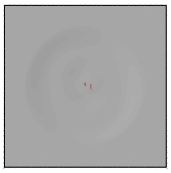
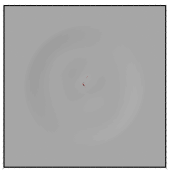
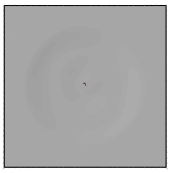
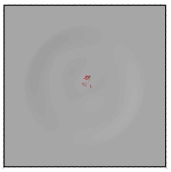
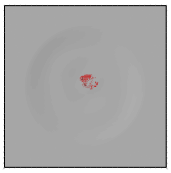
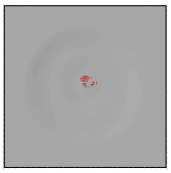
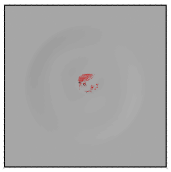
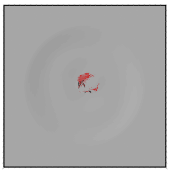
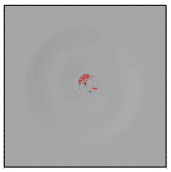
	26.8/48.5 µs, 96.4 kA	26.8/57.1 µs, 96.4 kA	26.8/39.9 µs, 96.4 kA
Layer 8			
Layer 7			
Layer 6			
Layer 4 and 5			
Layer 3			
Layer 2			
Layer 1			

Table 7.20: Damage map assessment for shear damage variable (d_6) for waveform alternatives to assess action integral influence for ECF 73

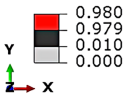
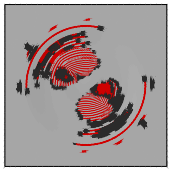
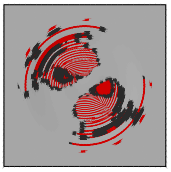
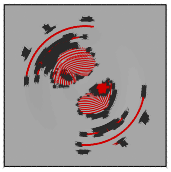
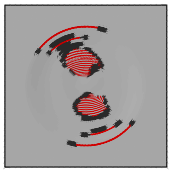
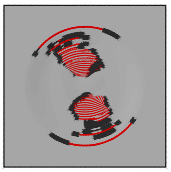
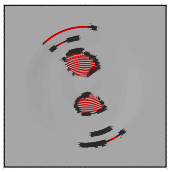
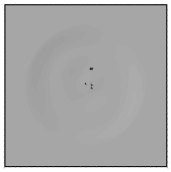
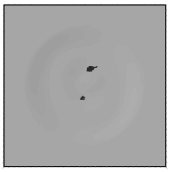
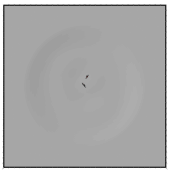
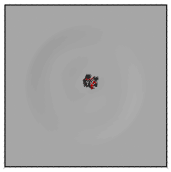
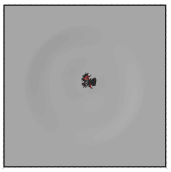
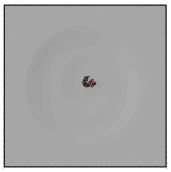
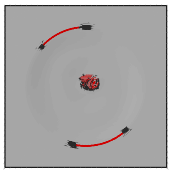
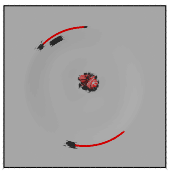
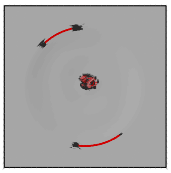
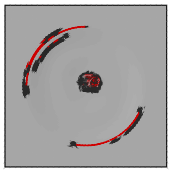
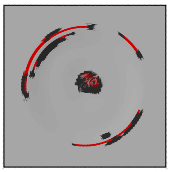
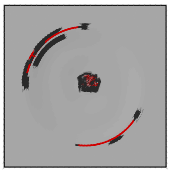
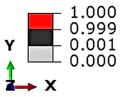
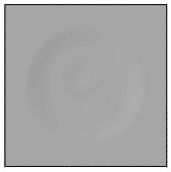
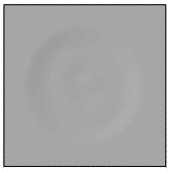
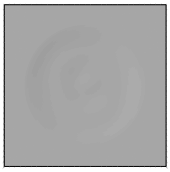
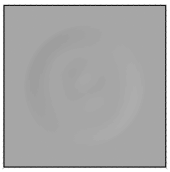
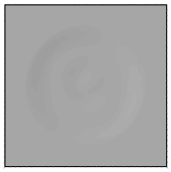
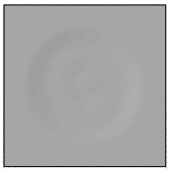
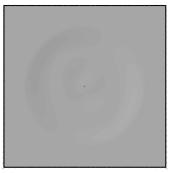
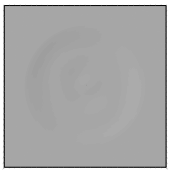
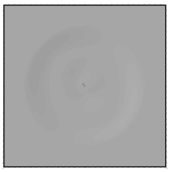
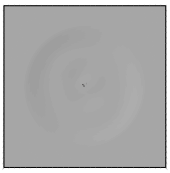
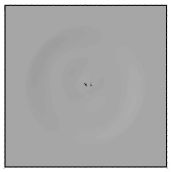
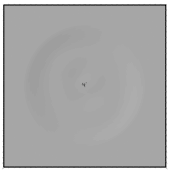
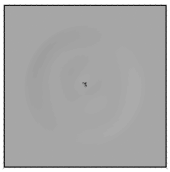
	26.8/48.5 µs, 96.4 kA	26.8/57.1 µs, 96.4 kA	26.8/39.9 µs, 96.4 kA
Layer 8			
Layer 7			
Layer 6			
Layer 4 and 5			
Layer 3			
Layer 2			
Layer 1			

Table 7.21: Damage map assessment for delamination (d) for waveform alternatives to assess action integral influence for ECF 73

	26.8/48.5 µs, 96.4 kA	26.8/57.1 µs, 96.4 kA	26.8/39.9 µs, 96.4 kA
Layer 8			
Layer 7			
Layer 6			
Layer 4 and 5			
Layer 3			
Layer 2			
Layer 1			

7.4.2 Expanded copper foil 195

7.4.2.1 Root radius

Carried out the simulations of the waveform alternatives to assess action integral influence for the ECF 195, the fitted root radii as a function of time are plotted in Figure 7.39 and Table 7.22 presents the respective parameters.

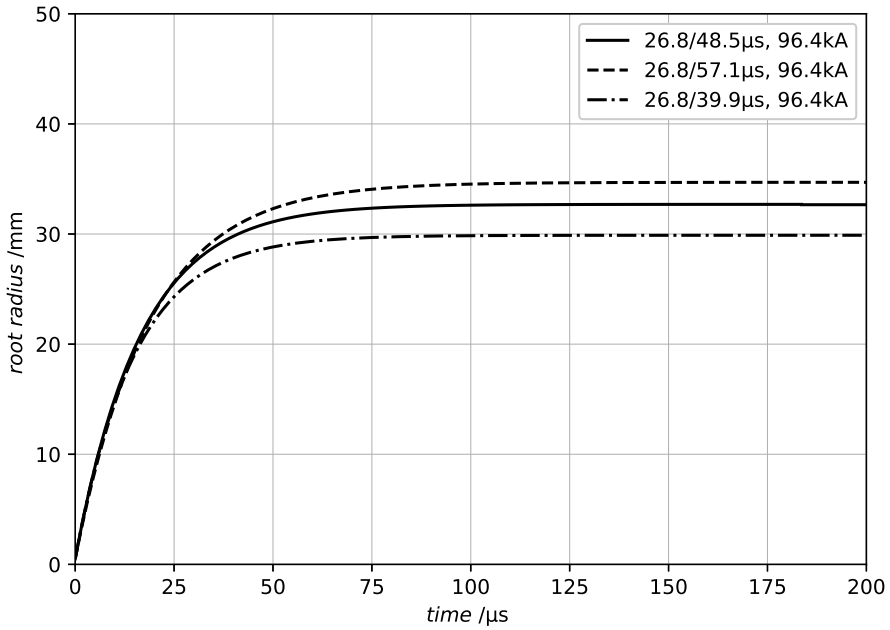


Figure 7.39: Root radius for waveform alternatives to assess action integral influence for ECF 195

Table 7.22: Root radius parameters for waveform alternatives to assess action integral influence for ECF 195

	a /mm	α /μs^{-1}	β /μs^{-1}	R_{R_0} /(mm)
26.8/57.1 µs, 96.4 kA	34.21	-1.86×10^{-6}	−0.053 13	0.5
26.8/39.9 µs, 96.4 kA	29.39	-5.21×10^{-7}	−0.066 43	0.5

Table 7.23: Root radius parameters for waveform alternatives to assess action integral influence for ECF 195

	t_s /μs	c /mm
26.8/57.1 µs, 96.4 kA	193.65	34.70
26.8/39.9 µs, 96.4 kA	176.59	29.89

7.4.2.2 Near-surface explosion

For the near-surface explosion of the lightning protection layer contribution the pressure, force and impulse magnitude are presented in Figure 7.40, Figure 7.41 and Figure 7.42, respectively.

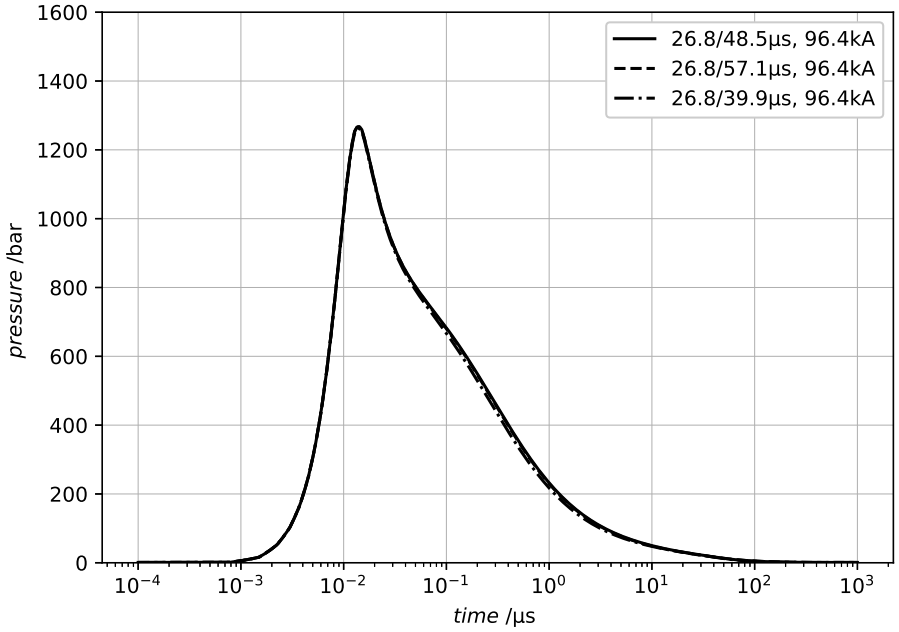


Figure 7.40: Overpressure caused by explosion of lightning protection layers as a function of time for waveform alternatives to assess action integral influence for ECF 195

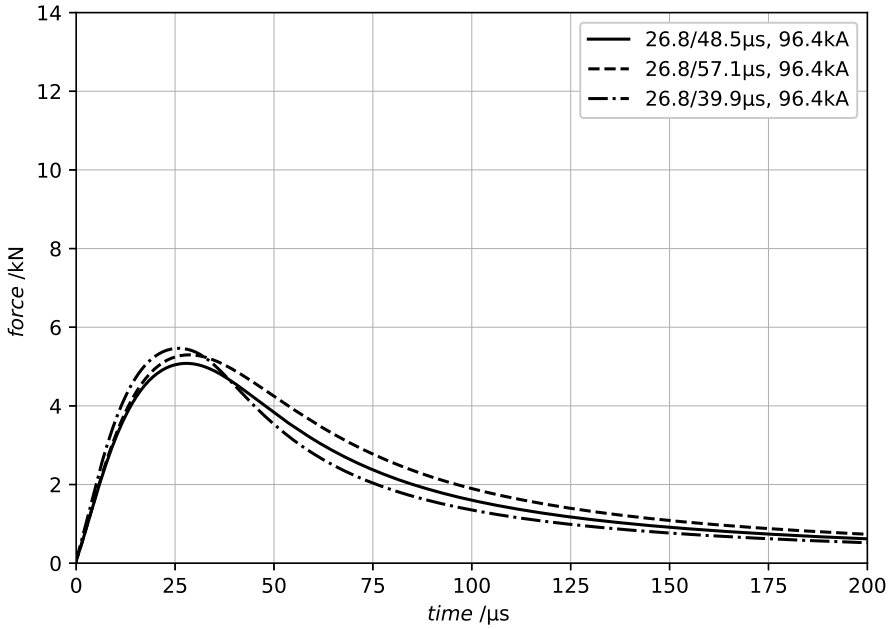


Figure 7.41: Force magnitude caused by explosion of lightning protection layers as a function of time for waveform alternatives to assess action integral influence for ECF 195

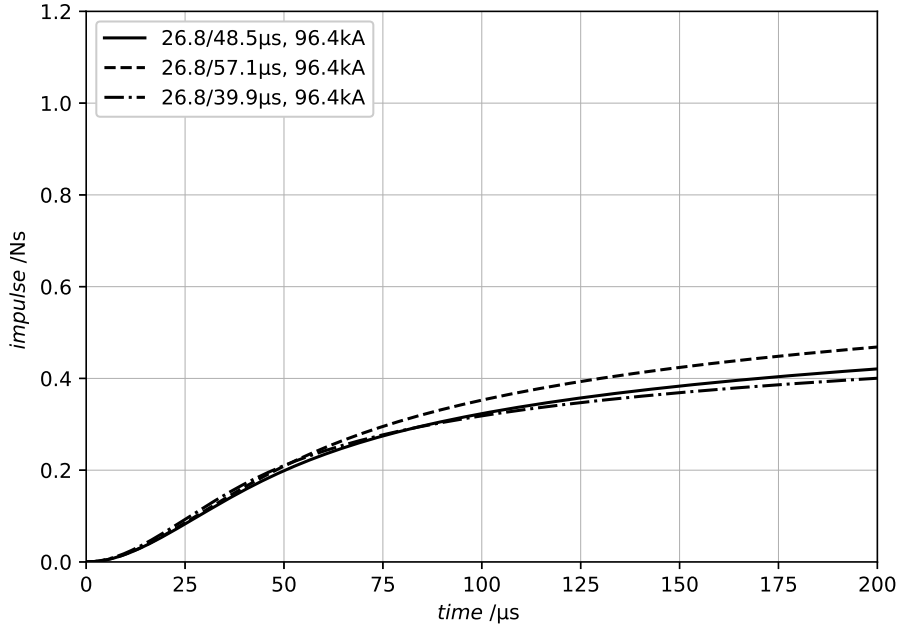


Figure 7.42: Impulse magnitude caused by explosion of lightning protection layers as a function of time for waveform alternatives to assess action integral influence for ECF 195

7.4.2.3 Supersonic plasma expansion

The parameters of the strong shock wave approximation are present in Table 7.24.

Table 7.24: Cylindrical shock wave parameters for waveform alternatives to assess action integral influence for ECF 195

	α_s /mm $\mu s^{-1/2}$	α /bar μs	β /bar μs^{-1}
26.8/41 µs, 106.04 kA	8.8040	98.5016	392.2952
26.8/58.6 µs, 86.76 kA	8.8040	98.5016	392.2952

Figure 7.43 represents the computed shock radius for the reference and waveforms in study, and Figure 7.44, Figure 7.45 and Figure 7.46 shown the pressure, force and impulse magnitudes generated by the supersonic plasma expansion, respectively.

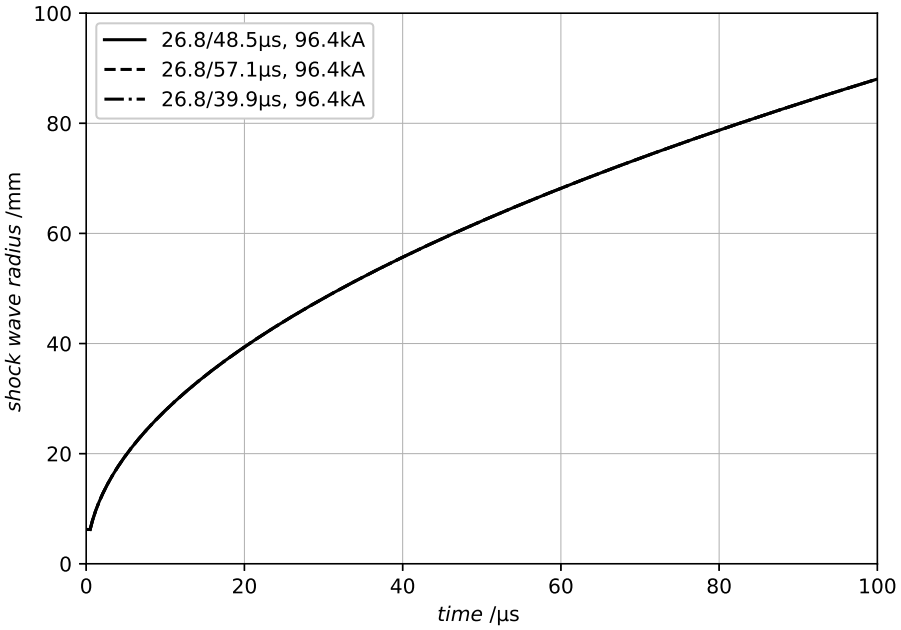


Figure 7.43: Computed shock radius for waveform alternatives to assess action integral influence for ECF 195

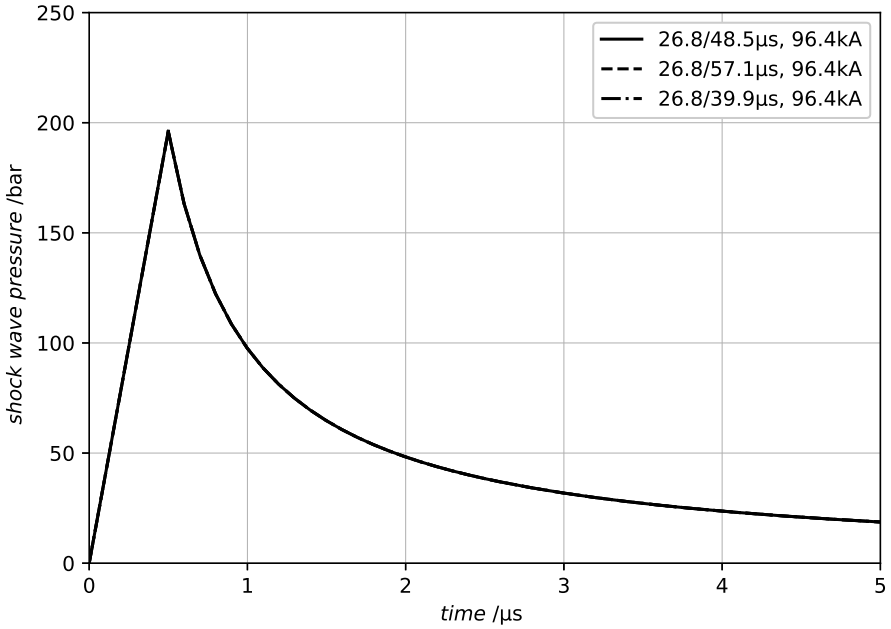


Figure 7.44: Mean cylindrical shock wave pressure as a function of time due to supersonic plasma expansion for waveform alternatives to assess action integral influence for ECF 195

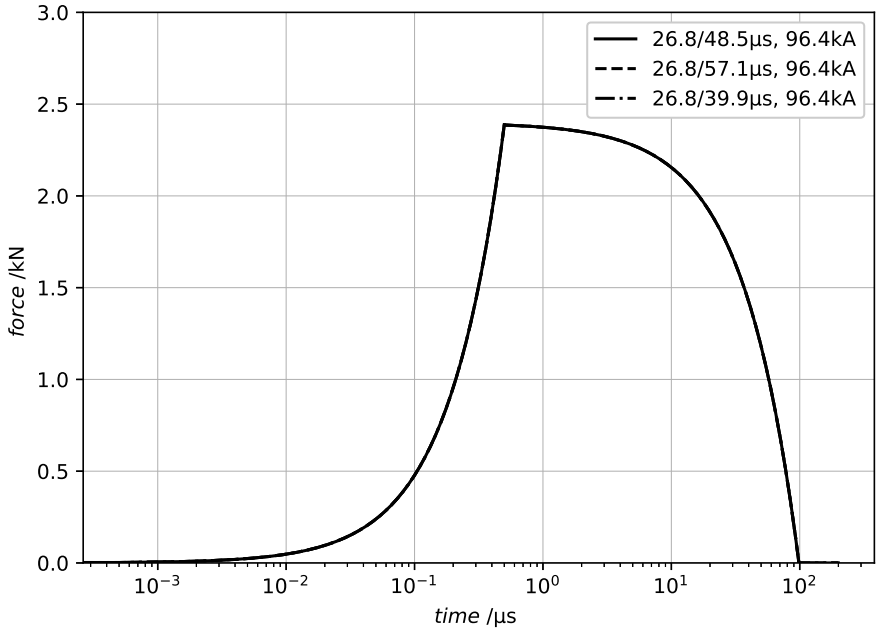


Figure 7.45: Force magnitude caused by supersonic plasma expansion as a function of time for waveform alternatives to assess action integral influence for ECF 195

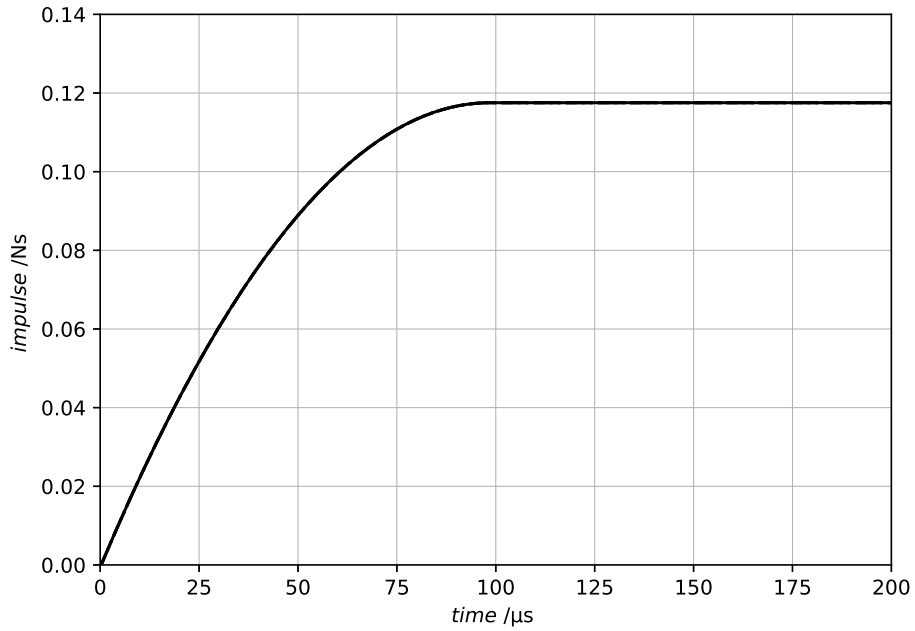


Figure 7.46: Impulse magnitude caused by supersonic plasma expansion as a function of time for waveform alternatives to assess action integral influence for ECF 195

7.4.2.4 Magnetic forces

To a complete analysis, pressure, force and impulse magnitudes generated by the magnetic forces contribution are presented in Figure 7.47, Figure 7.48 and Figure 7.49, respectively.

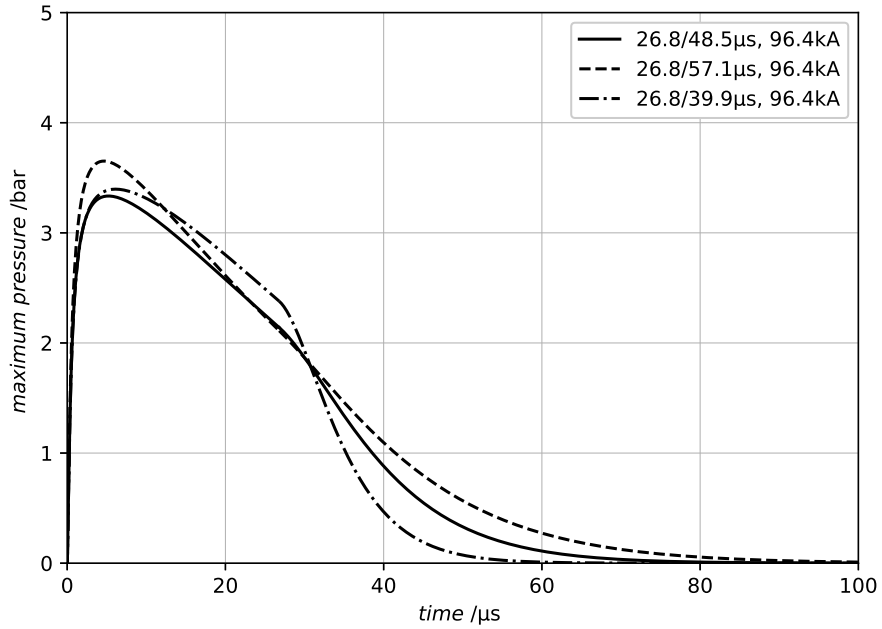


Figure 7.47: Maximum magnetic pressure evolution with time for waveform alternatives to assess action integral influence for ECF 195

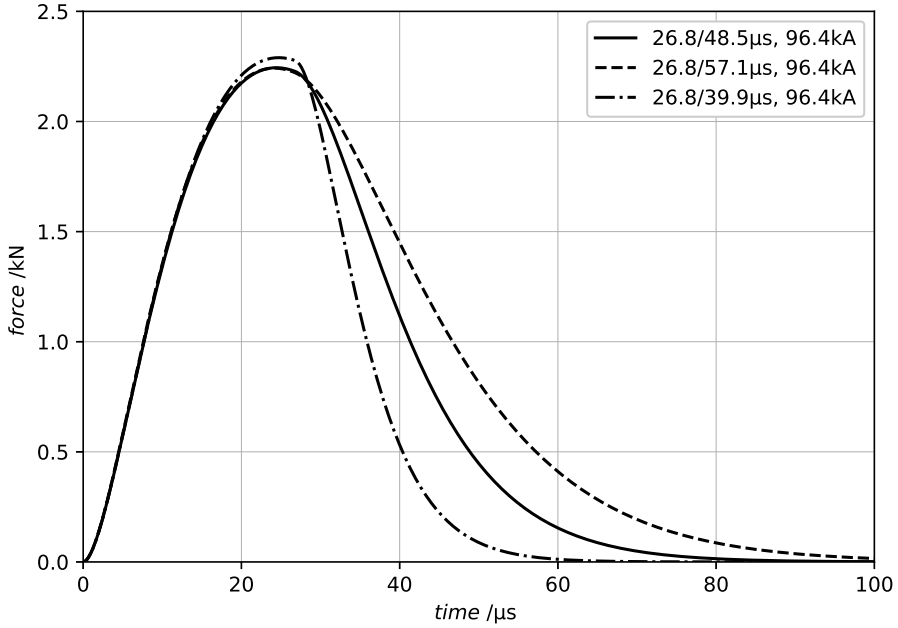


Figure 7.48: Force magnitude caused by magnetic forces as a function of time for for waveform alternatives to assess action integral influence for ECF 195

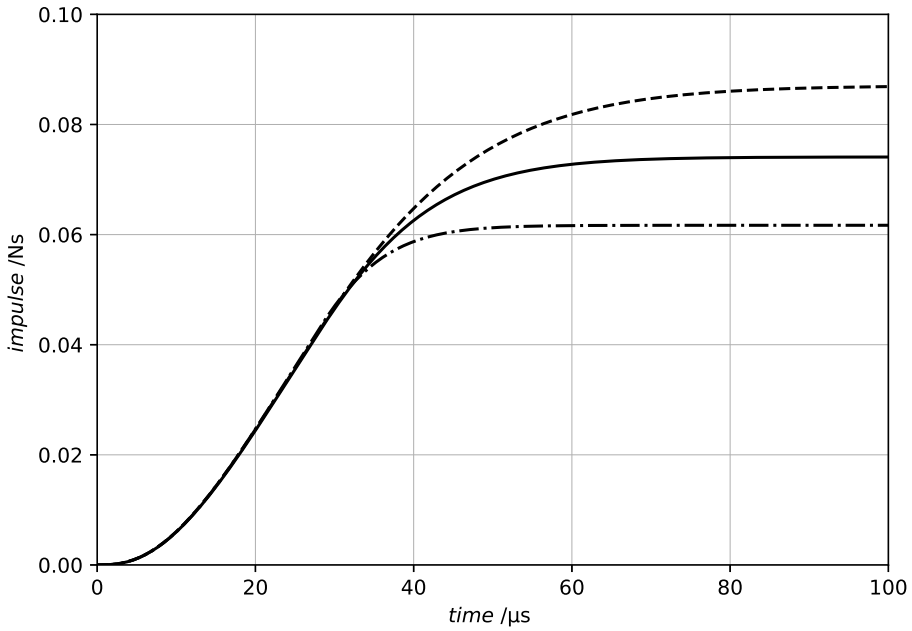
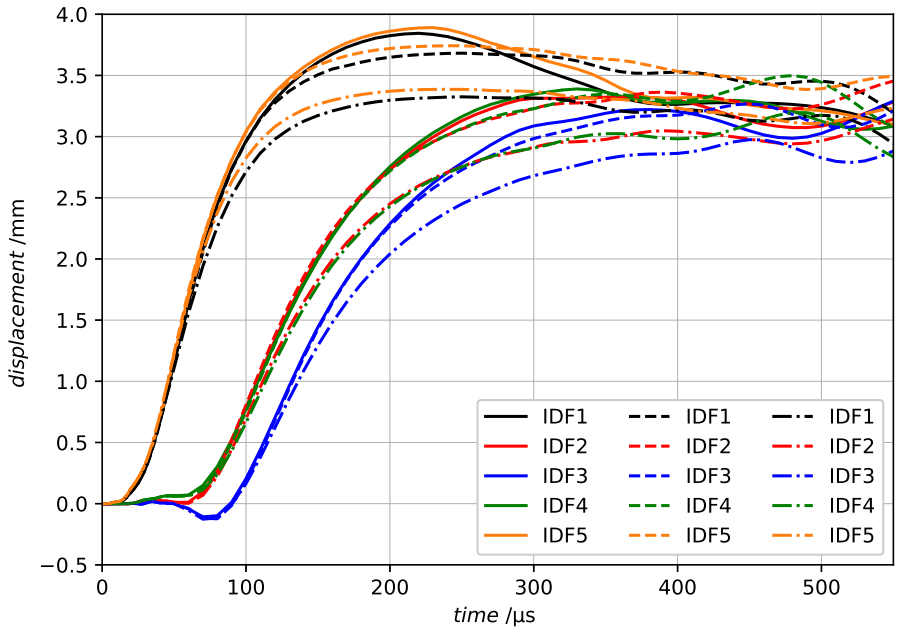


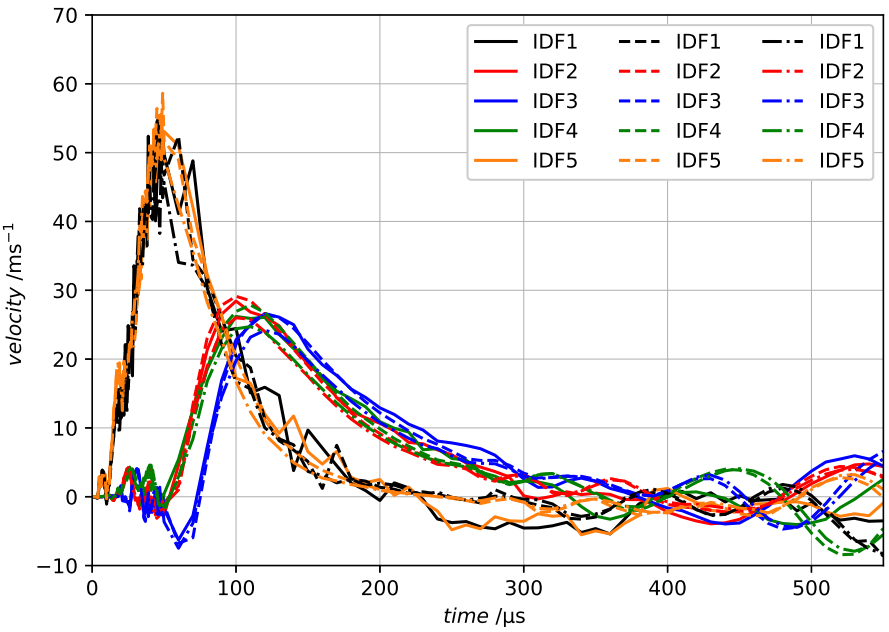
Figure 7.49: Impulse magnitude caused by magnetic forces as a function of time for waveform alternatives to assess action integral influence for ECF 195

7.4.2.5 Finite element predictions

The evaluation of the displacement and velocity of the five points already considered in the previously validated models, in the peak current influence studies and in the action integral influence study for ECF 73 are also performed for ECF 195, see Figure 7.50.



(a) Displacement



(b) Velocity

Figure 7.50: Finite element predictions for waveform alternatives to assess action integral influence, where solid lines represents the waveform 26.8/48.5 µs, 96.4 kA, dashed lines the waveform 26.8/57.1 µs, 96.4 kA and dashed dotted lines the waveform 26.8/39.9 µs, 96.4 kA for ECF 195

7.4.2.6 Damage maps

The damage map assessment was also performed for ECF 195. For each layer of the laminate, the damage variables in the longitudinal direction (d_1), Table 7.25, transverse direction (d_2), Table 7.26, shear (d_6), Table 7.27, and delamination (d), Table 7.28.

Table 7.25: Damage map assessment for damage variable in the longitudinal direction (d_1) for waveform alternatives to assess action integral influence for ECF 195

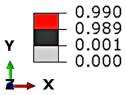
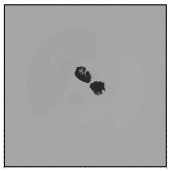
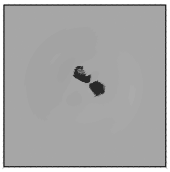
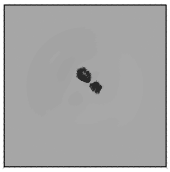
	26.8/48.5 µs, 96.4 kA	26.8/57.1 µs, 96.4 kA	26.8/39.9 µs, 96.4 kA
Layer 8			
Layer 7			
Layer 6			
Layer 4 and 5			
Layer 3			
Layer 2			
Layer 1			

Table 7.26: Damage map assessment for damage variable in the transverse direction (d_2) for waveform alternatives to assess action integral influence for ECF 195

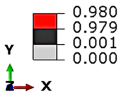
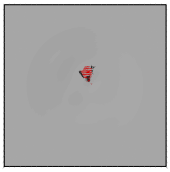
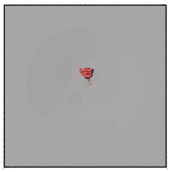
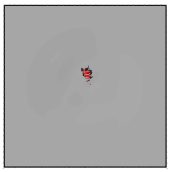
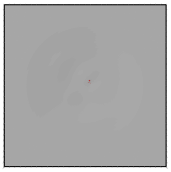
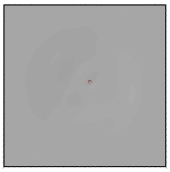
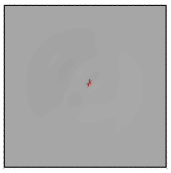
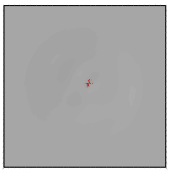
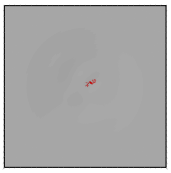
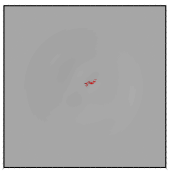
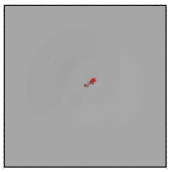
	26.8/48.5 µs, 96.4 kA	26.8/57.1 µs, 96.4 kA	26.8/39.9 µs, 96.4 kA
Layer 8			
Layer 7			
Layer 6			
Layer 4 and 5			
Layer 3			
Layer 2			
Layer 1			

Table 7.27: Damage map assessment for shear damage variable (d_6) for waveform alternatives to assess action integral influence for ECF 195

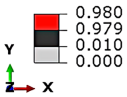
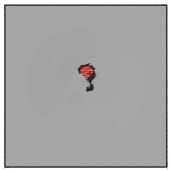
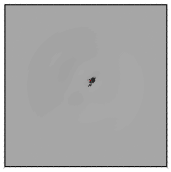
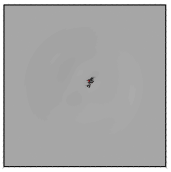
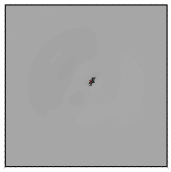
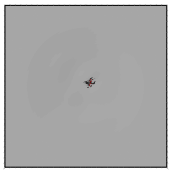
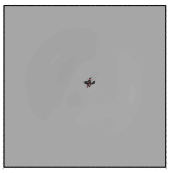
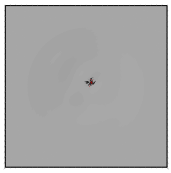
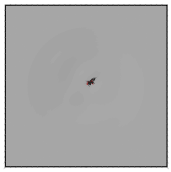
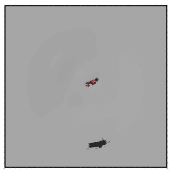
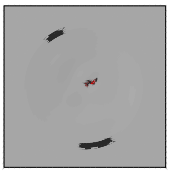
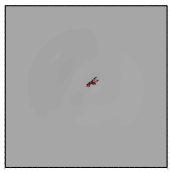
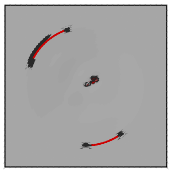
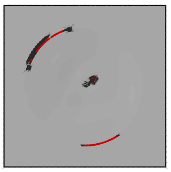
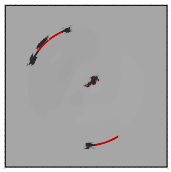
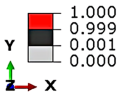
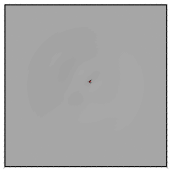
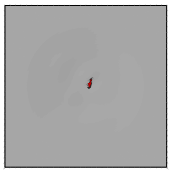
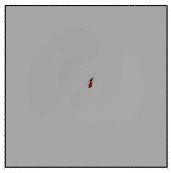
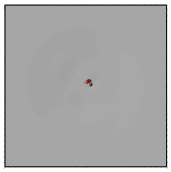
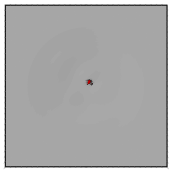
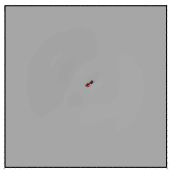
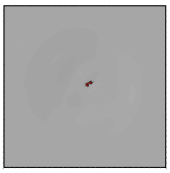
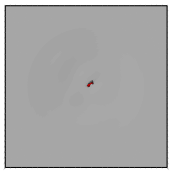
	26.8/48.5 µs, 96.4 kA	26.8/57.1 µs, 96.4 kA	26.8/39.9 µs, 96.4 kA
Layer 8			
Layer 7			
Layer 6			
Layer 4 and 5			
Layer 3			
Layer 2			
Layer 1			

Table 7.28: Damage map assessment for delamination (d) for waveform alternatives to assess action integral influence for ECF 195

	26.8/48.5 µs, 96.4 kA	26.8/57.1 µs, 96.4 kA	26.8/39.9 µs, 96.4 kA
Layer 8			
Layer 7			
Layer 6			
Layer 4 and 5			
Layer 3			
Layer 2			
Layer 1			

7.5 Discussion and conclusions

This parametric study presented a total of eight new numerical simulations, considering four alternative waveforms for each lightning strike protection layer analysed in previous chapters. This assessment not only reproduced the trends observed by Hirano et al. [24], but also provides useful guidance regarding the two major trends addressed here:

Influence of peak current
It is notorious the impact of ± 10% variation on the peak current in the damage generated. A simple way to perceive the origin of this impact is the graphical visualization of the pressure, force and impulse magnitude over time induced onto the surface of the composite panel. It is clear that the waveform with the maximum peak current, 106.04 kA, produces more damage. Contrarily, the waveform that presents the lower value of peak current, 86.76 kA, leads to smaller damaged areas.

Influence of action integral
Analogously, the waveform representing higher action integral induces more damage to the structure. This is attributed to two main reasons: (i) waveforms with higher action integral lead to larger root radii, and (ii) once the action integral represents the ability of the current to deposit energy on a resistive object, higher values of action integral increase the potential of vaporization of the surface, originating a bigger explosion and, consequently, more damage.

Part V

Case study

Chapter 8

SAE ARP 5412 recommended lightning current waveform: sensitivity analysis

Contents

8.1 Introduction
8.2 Mechanical loads
8.3 Waveform 1.42/44.3 µs, 96.4 kA
8.4 Waveform 3.18/34.5 µs, 100 kA
8.5 Waveform 4/34 µs, 110 kA
8.6 Waveform 5/23.6 µs, 110 kA
8.7 Waveform 6/51 µs, 90 kA
8.8 Waveform 7/35 µs, 90 kA
8.9 Damage maps
8.10 Discussion
8.11 Conclusion

Objectives

The purpose of this chapter is to explore the effect of the tolerances on the peak amplitude and time dependent parameters of the standardised current waveform of the Aerospace Recommended Practice, ARP 5412 [14], established by SAE (Society of Automotive Engineers). This part of the work intends to support the aeronautical industry providing quantitative information about the sensitivity of the mechanical response of composite laminates to the range of lightning current parameters defined by the relevant standardisation authorities, supplementing the theoretical study performed in Chapter 7. Based on analytical models, several hypotheses of waveforms verified by the normative document are presented in detail. Furthermore, a new equation for root radius evaluation is proposed.

8.1 Introduction

The normative documentation provided by SAE (Society of Automotive Engineers) establish some acceptable intervals of the lightning parameters of the current waveforms derived to represent the lightning environment. This report is internationally considered as the sole standard concerning the lightning threat. This threat is defined using data of lightning to the ground [5].

Since the most severe mechanical damage at and around the lightning attachment area of protected and unprotected airframe composite parts occurs during the transient A or D current components, and using as a reference a transient D current waveform with a time to peak of 26.8 µs, a decay time of 48.5 µs, and a peak current of 96.4 kA used by Lepetit et al. in the experimental tests [19], a detailed examination of six waveforms are presented.

The suggested waveforms, presented below, are establish using an optimization algorithm to determine the constants A, α and β in Equation 8.1. The algorithm is based in the python library *scipy.optimize.curve_fit* [90].

$$I(t) = A\, I_0\, (e^{-\alpha t} - e^{-\beta t}) \tag{8.1}$$

where I_0 represents the peak current of the waveform.

The six waveforms and their characterization are:

1.42/44.3 µs, 96.4 kA

This waveform consist of an identical waveform to the reference waveform 26/48.5 µs, 96.4 kA in terms of peak current and action integral. Karch et al. [43] proposed a modified double exponential equation to describe accurately enough the measured current waveforms tested by Lepetit et al. [19], however for the present analysis required a standard equation to describe the lightning transient current waveform D according to the normative documentation [14] (see Equation 3.1).

3.18/34.5 µs, 100 kA

This waveform is given in the Aerospace Recommend Practice [14] provided by SAE as the nominal waveform for a transient D current component, i.e., a peak intensity of 100 kA and an action integral of 0.25×10^6 A^2s.

4/34 µs, 110 kA

This waveform represents the maximum value allowed of peak current and action integral, which means a numerical value of 110 kA for peak current and $0.3 \times 10^6 A^2s$ for action integral.

5/23.6 µs, 110 kA

In opposition, keeping the maximum value of peak current, this waveform presents the minimum admissible value of action integral, $0.2 \times 10^6 A^2s$.

6/51 µs, 90 kA

This waveform represents the minimum value allowed of peak current and the maximum action integral, which means a numerical value of 90 kA for peak current and $0.3 \times 10^6 \mathrm{A}^2\mathrm{s}$ for action integral.

7/35 µs, 90 kA

Finally, this waveform represents the two minimum values admissible, i.e., 90 kA for peak current and $0.2 \times 10^6 \mathrm{A}^2\mathrm{s}$ for action integral,

8.2 Mechanical loads

The equations used to compute the pressure distributions for the six suggested transient D current waveforms are previously described in chapter 3. However, during the investigation it was noted that the fitting of the root radius equation not accurately describe the root radius expansion calculations using the finite volume degradation approach. Therefore, a further research could lead to a new proposed equation:

$$R_R(t) = R_{R_0} + c\,\left(1 - e^{\beta t^{\alpha}}\right) \tag{8.2}$$

Regardless the fact that this equation gives a better fitting on the calculations by finite volume method, some others benefits can be recognize. This new proposed root radius equation is defined by only one mathematical statement and not a branch equation as Equation 3.5, decreasing the computational effort and simply the implementation. Note that when $t \to \infty$, which means $e^{\beta t^{\alpha}} \to 0$, the constant value of root radius are given by $R_{r0}+c$. Also, the initial arc root radius is assured, thus when $t = 0$ imply $c\,\left(1 - e^{\beta t^{\alpha}}\right) = 0$. The validation of this equation is presented in Figure 8.1.

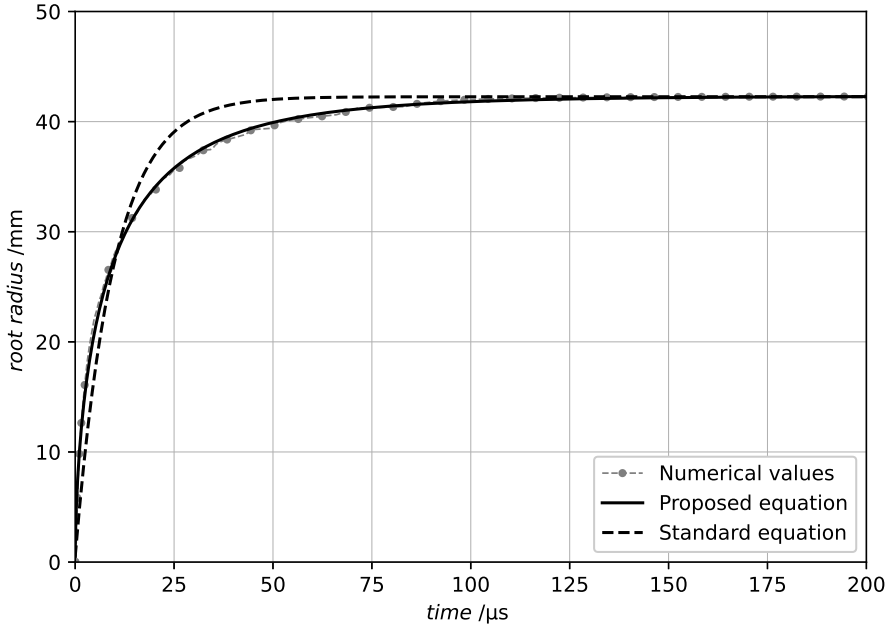


Figure 8.1: Root radius fitting comparison between new proposed equation and standard equation

In the following sections a detailed examination of each waveform implemented in the numerical reference model with the expanded copper foil 73 as lightning protection layer is described.

In this chapter, the equations of shock position as a function of time and the strong shock wave approximation of supersonic plasma expansion contribution are simplified by Equation 8.3 and Equation 8.4, respectively.

$$R(t) \cong \begin{cases} \alpha_s \sqrt{0.5} & , t < 0.5\ \mu\text{s} \\ \alpha_s \sqrt{t} & , t \geq 0.5\ \mu\text{s} \end{cases} \tag{8.3}$$

$$p(t) \cong \begin{cases} \beta \cdot t & , t < 0.5\ \mu\text{s} \\ \alpha/t - 1 & , t \geq 0.5\ \mu\text{s} \\ 0 & t > 100\ \mu\text{s} \end{cases} \tag{8.4}$$

8.3 Waveform 1.42/44.3 µs, 96.4 kA

The waveform 1.42/44.3 µs, 96.4 kA and the corresponding mechanical loads and mechanical deformation predictions are shown in Figure 8.2 to Figure 8.14 and from Table 8.1 to Table 8.3.

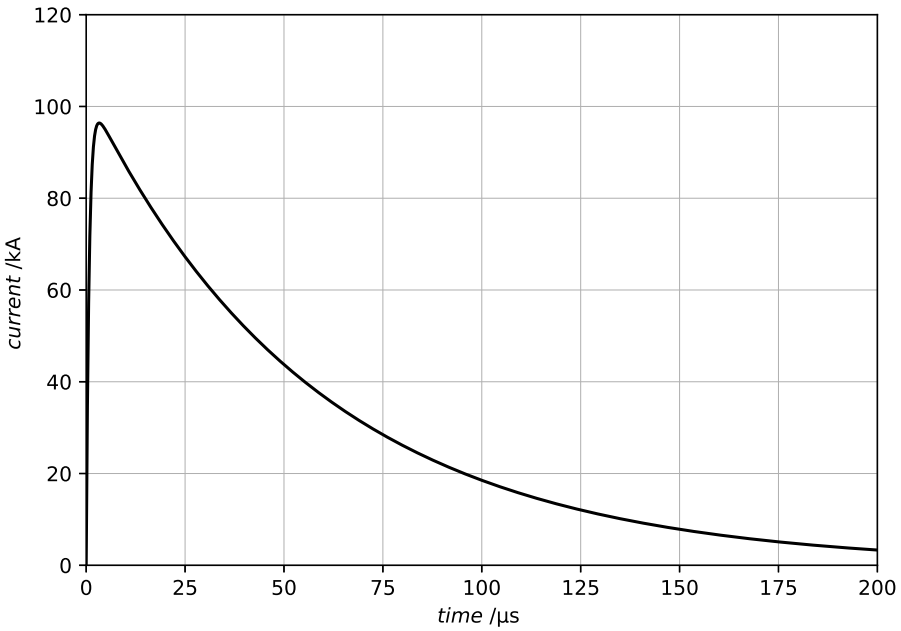


Figure 8.2: Double exponential for the waveform 1.42/44.3 µs, 96.4 kA

Table 8.1: Waveform parameters for the waveform 1.42/44.3 µs, 96.4 kA

a /s^{-1}	b /s^{-1}	A /-	I_{max} /kA
1.719×10^4	1.340×10^6	1.072	96.4

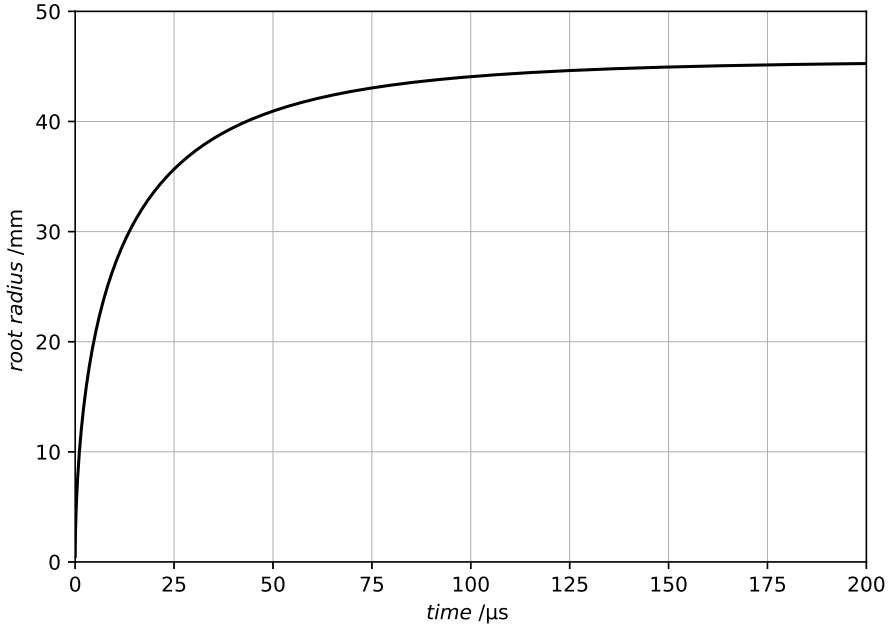


Figure 8.3: Root radius for the waveform 1.42/44.3 µs, 96.4 kA

Table 8.2: Root radius parameters for the waveform 1.42/44.3 µs, 96.4 kA

	c /mm	α /mm	β /mm	R_{R_0} /mm
ECF 73	45.02	0.5884	−0.2287	0.5

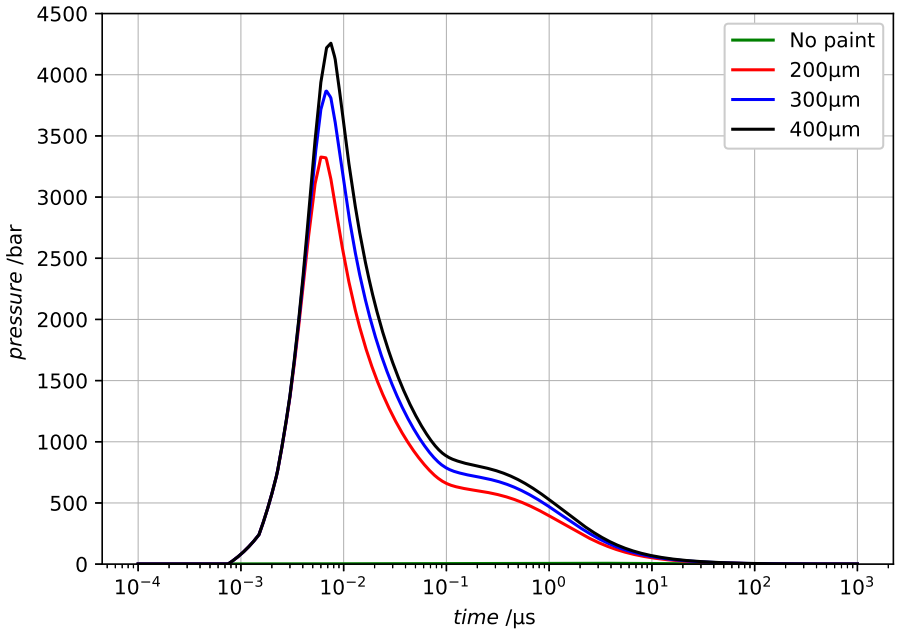


Figure 8.4: Pressure magnitude due to surface explosion for the waveform 1.42/44.3 µs, 96.4 kA

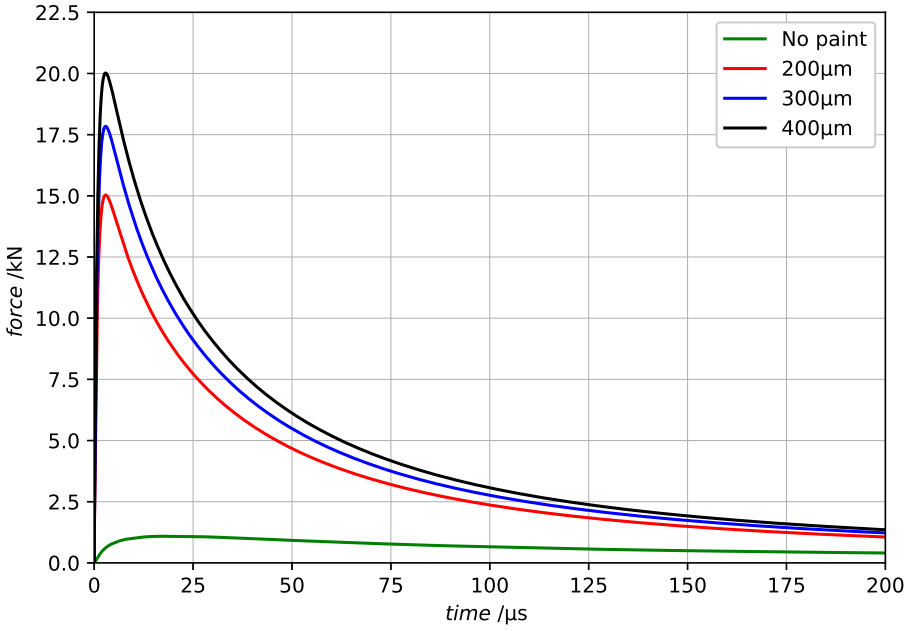


Figure 8.5: Force magnitude due to surface explosion for the waveform 1.42/44.3 µs, 96.4 kA

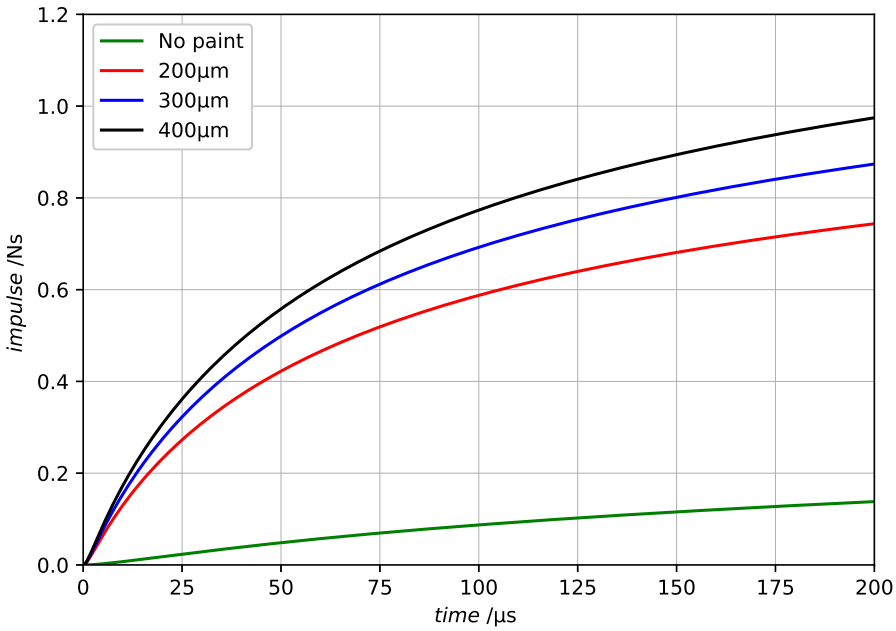


Figure 8.6: Impulse magnitude due to surface explosion for the waveform 1.42/44.3 µs, 96.4 kA

Table 8.3: Cylindrical shock wave parameters for the waveform 1.42/44.3 µs, 96.4 kA

α_s /mm $\mu s^{-1/2}$	α /bar μs	β /bar μs^{-1}
8.804 00	98.5016	392.2952

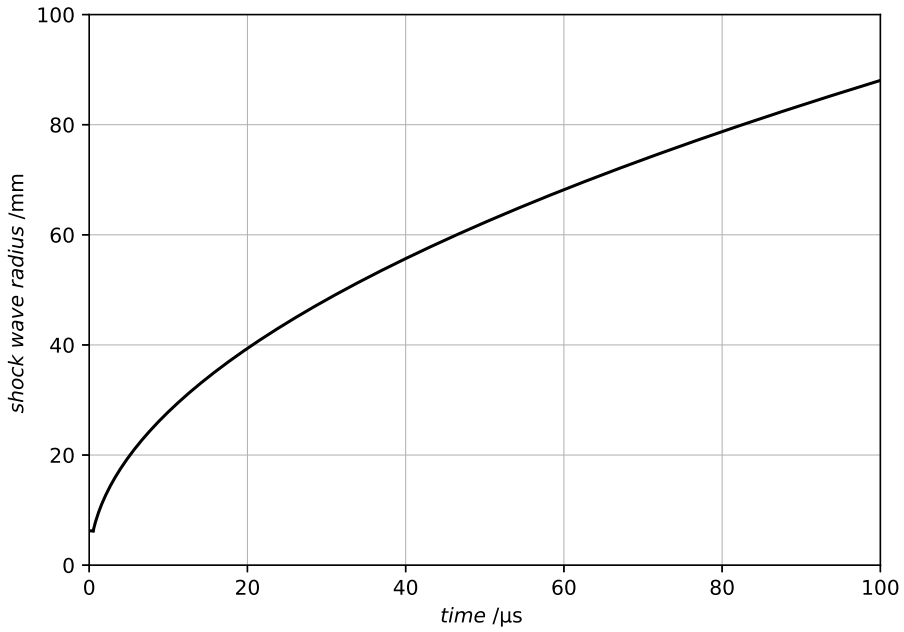


Figure 8.7: Shock radius for the waveform 1.42/44.3 µs, 96.4 kA

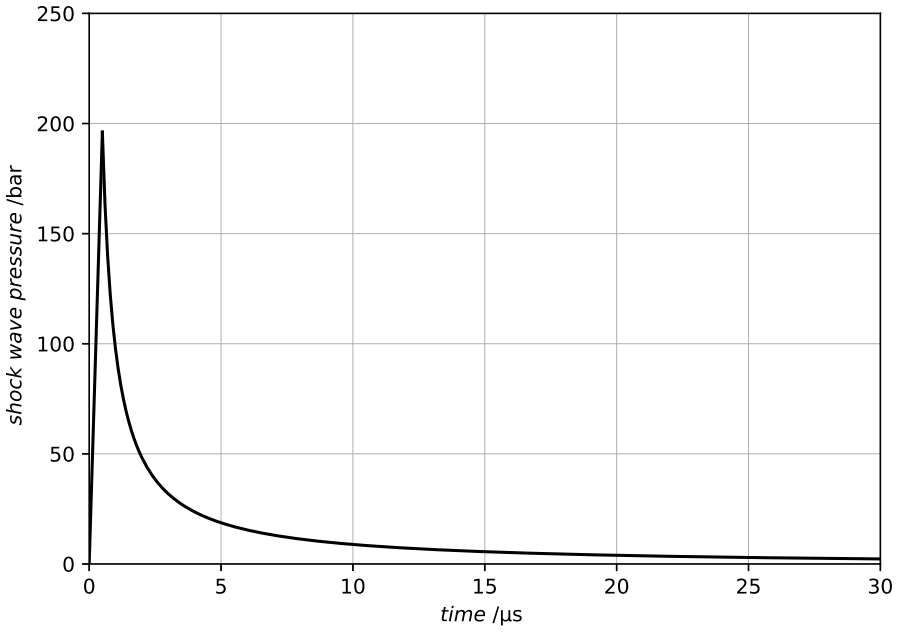


Figure 8.8: Mean shock wave pressure magnitude due to supersonic expansion for the waveform 1.42/44.3 µs, 96.4 kA

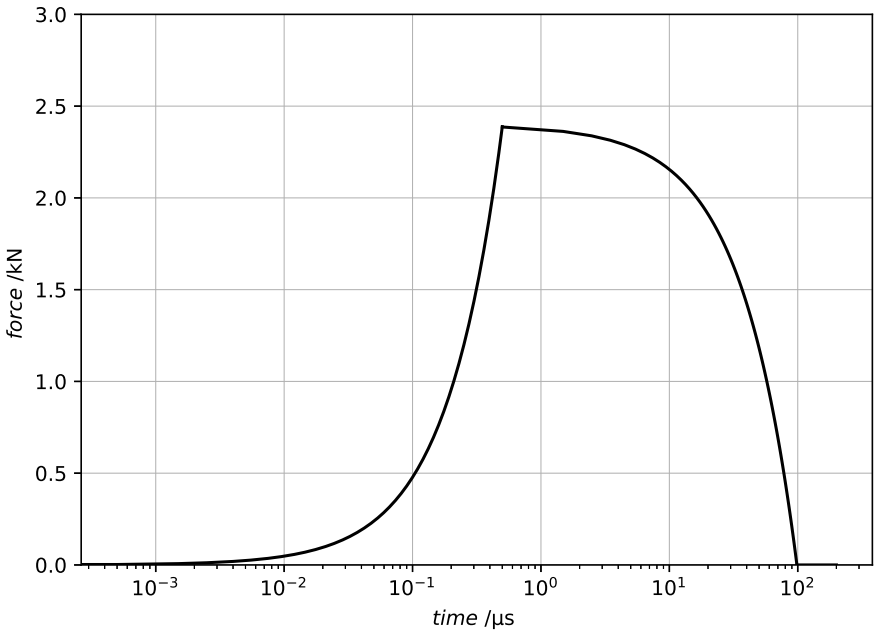


Figure 8.9: Force due to supersonic expansion for the waveform 1.42/44.3 µs, 96.4 kA

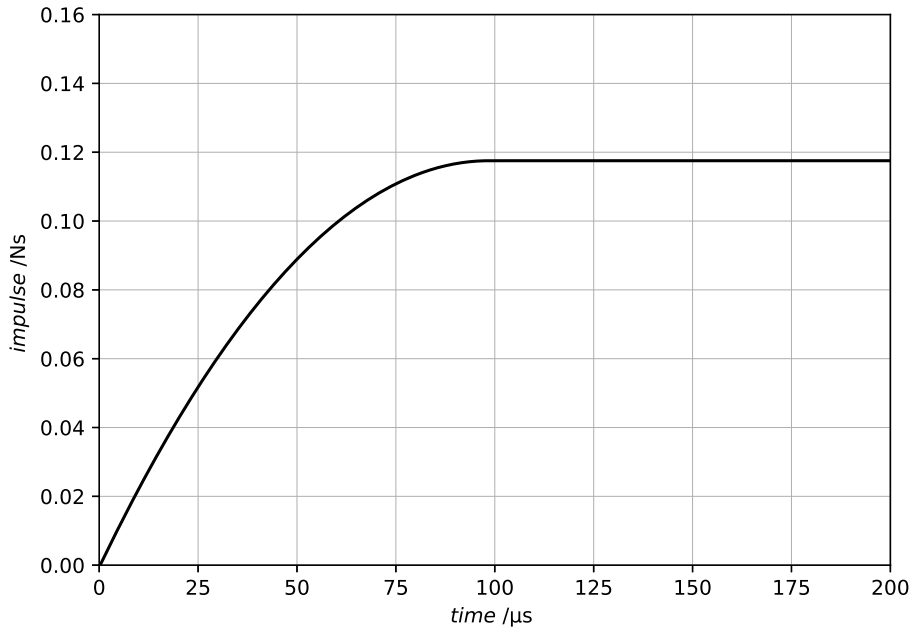


Figure 8.10: Impulse magnitude due to supersonic expansion for the waveform 1.42/44.3 µs, 96.4 kA

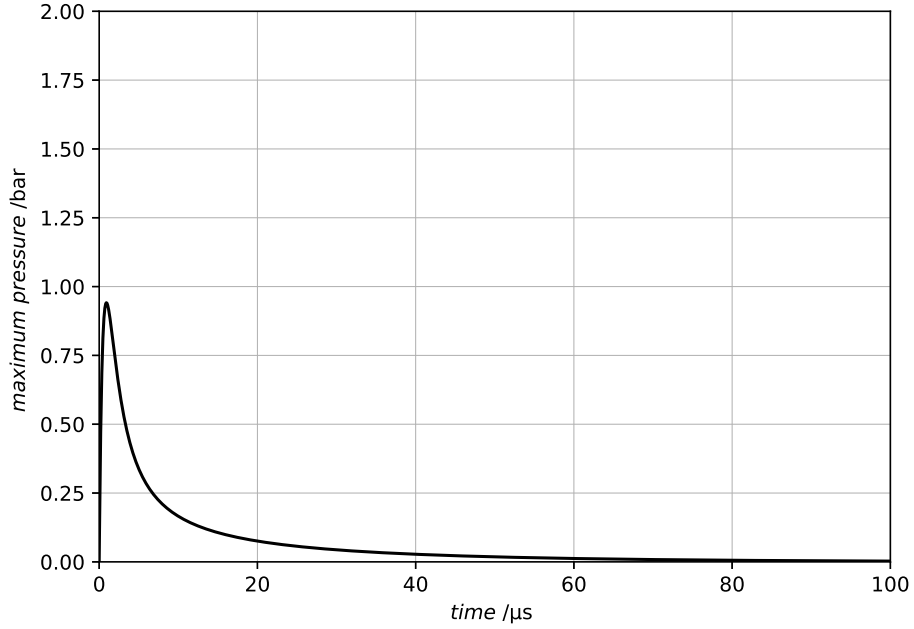


Figure 8.11: Pressure magnitude due to magnetic forces for the waveform 1.42/44.3 µs, 96.4 kA

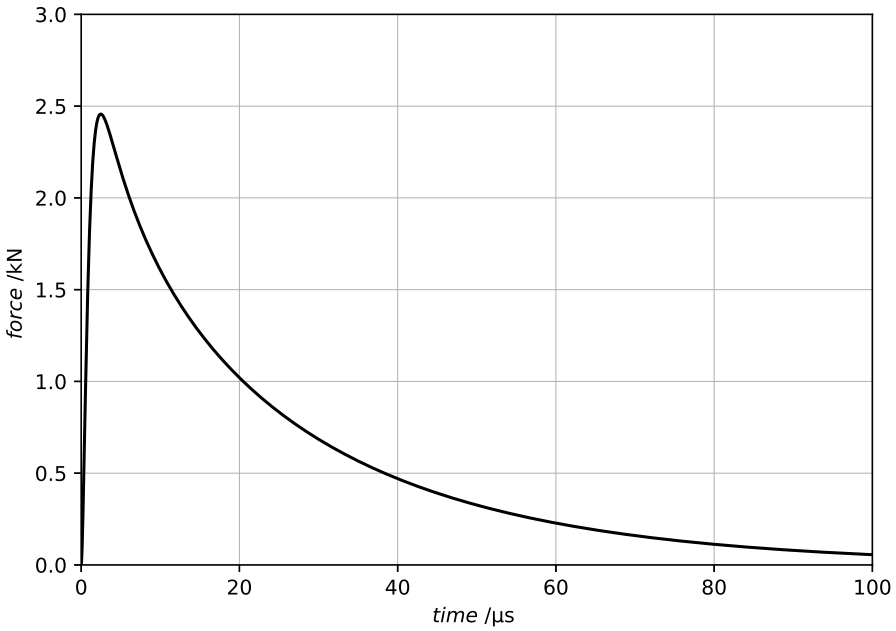


Figure 8.12: Force due to magnetic forces for the waveform 1.42/44.3 µs, 96.4 kA

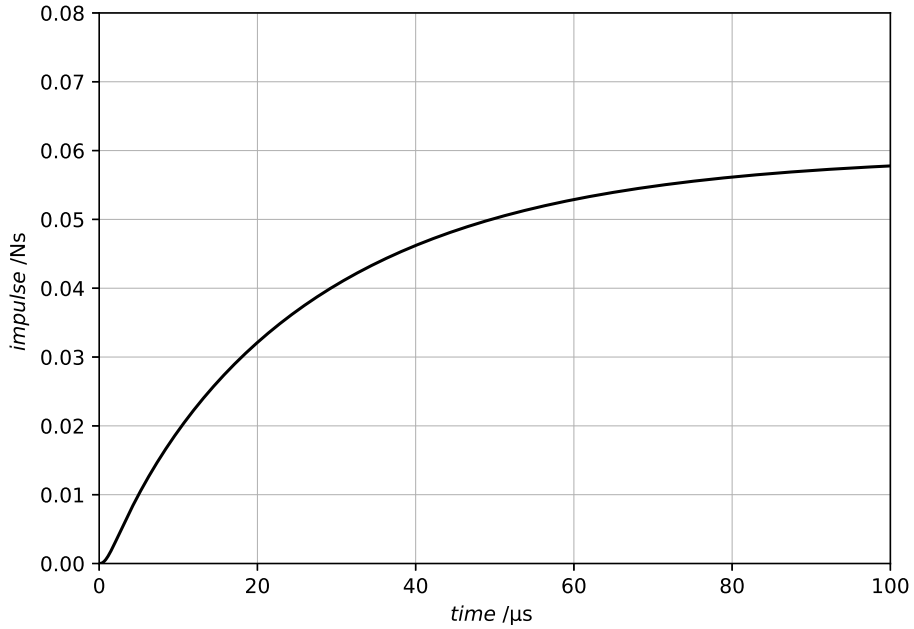
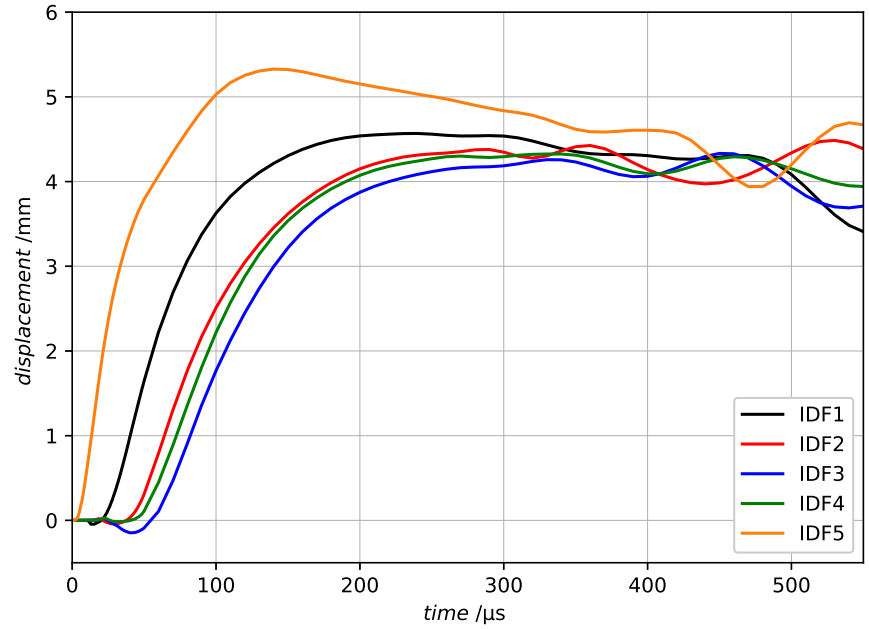
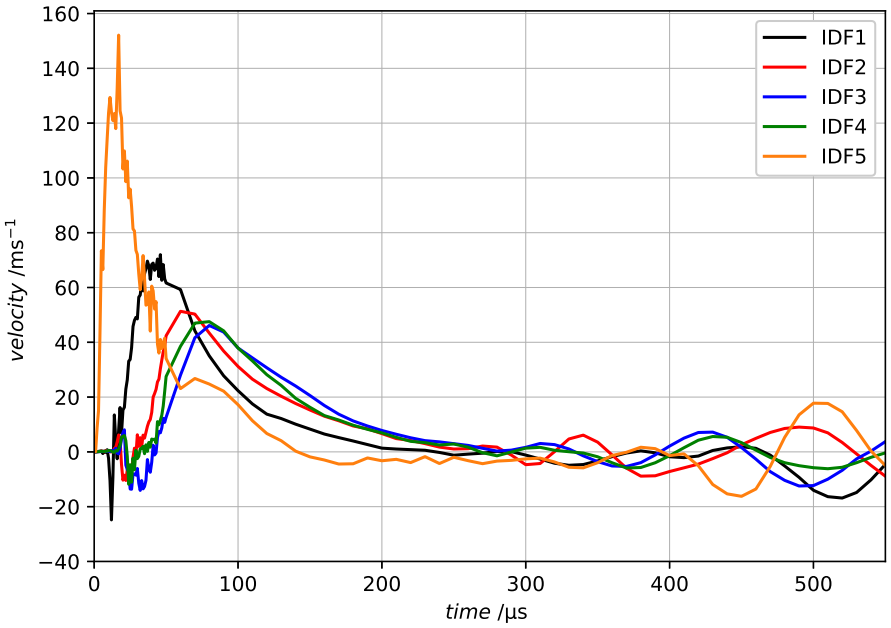


Figure 8.13: Impulse magnitude due to magnetic forces for the waveform 1.42/44.3 µs, 96.4 kA



(a) Displacement



(b) Velocity

Figure 8.14: Finite element predictions for the waveform 1.42/44.3 µs, 96.4 kA

8.4 Waveform 3.18/34.5 µs, 100 kA

The waveform 3.18/34.5 µs, 100 kA and the corresponding mechanical loads and mechanical deformation predictions are shown in Figure 8.15 to Figure 8.27 and from Table 8.4 to Table 8.6.

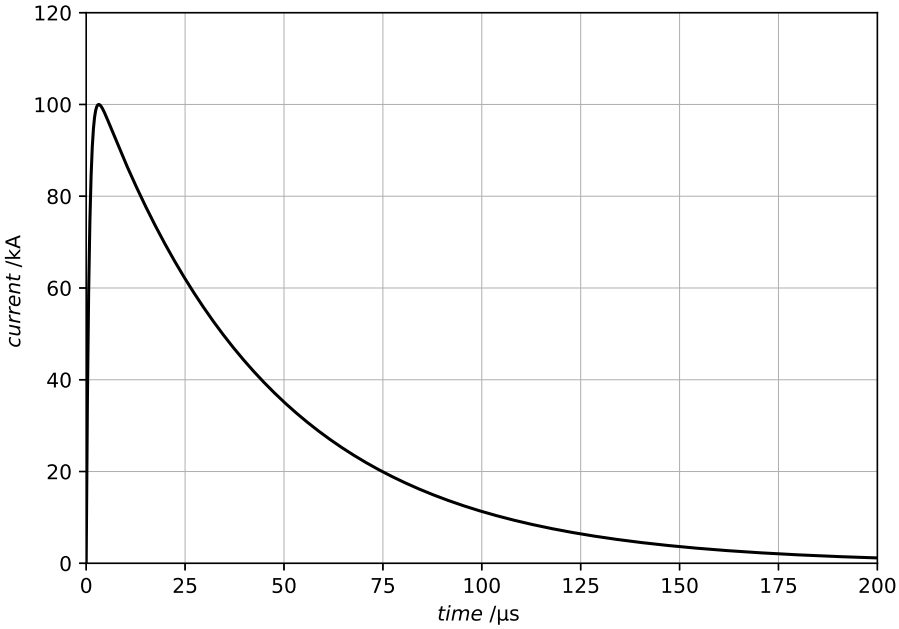


Figure 8.15: Double exponential for 3.18/34.5 µs, 100 kA

Table 8.4: Waveform parameters for 3.18/34.5 µs, 100 kA

a /s^{-1}	b /s^{-1}	A /-	I_{max} /kA
22708	1294530	1.094	100

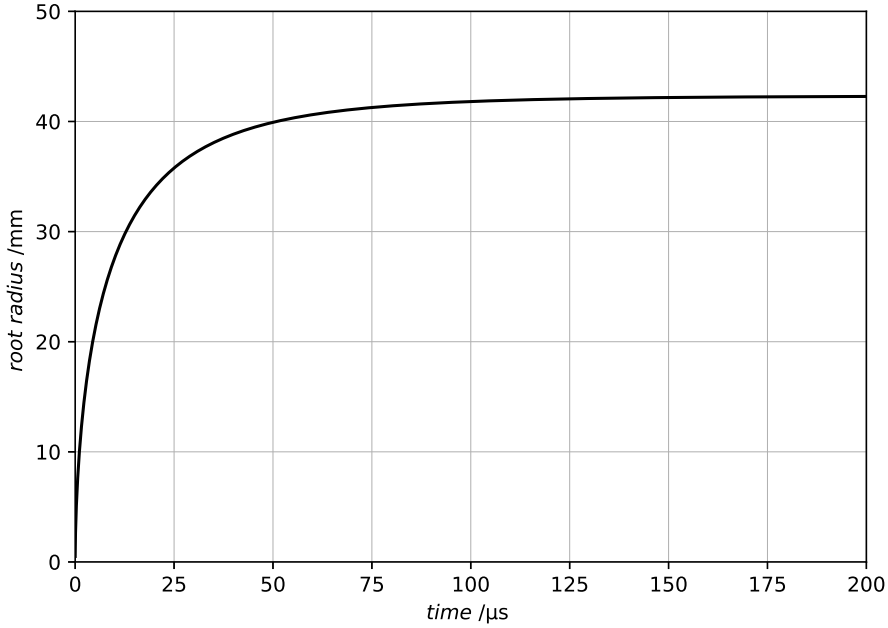


Figure 8.16: Root radius for 3.18/34.5 µs, 100 kA

Table 8.5: Root radius parameters for 3.18/34.5 µs, 100 kA

	c /mm	α /mm	β /mm	R_{R_0} /mm
ECF 73	41.82	0.6249	−0.2481	0.5

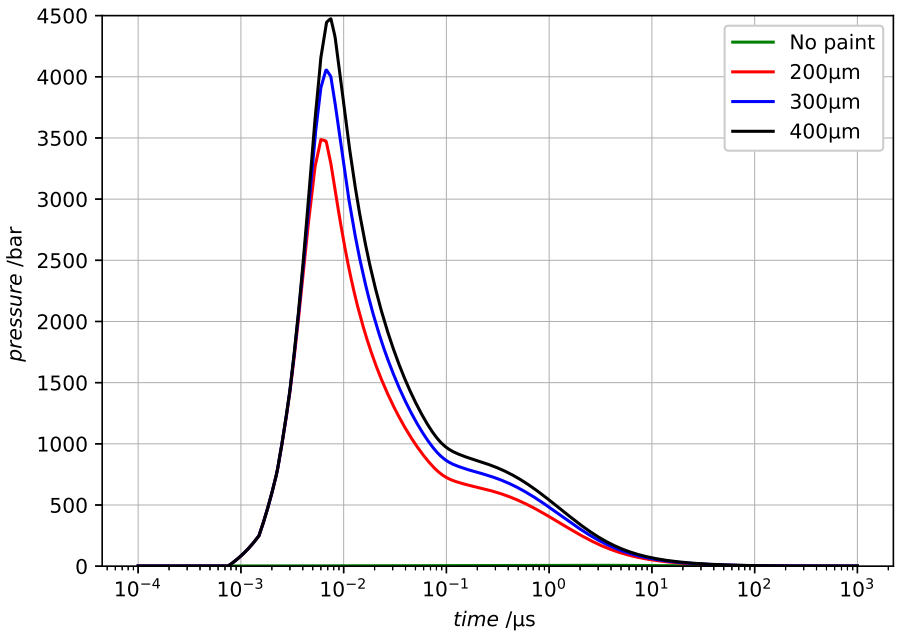


Figure 8.17: Overpressure caused by explosion of lightning protection layers as a function of time for 3.18/34.5 µs, 100 kA

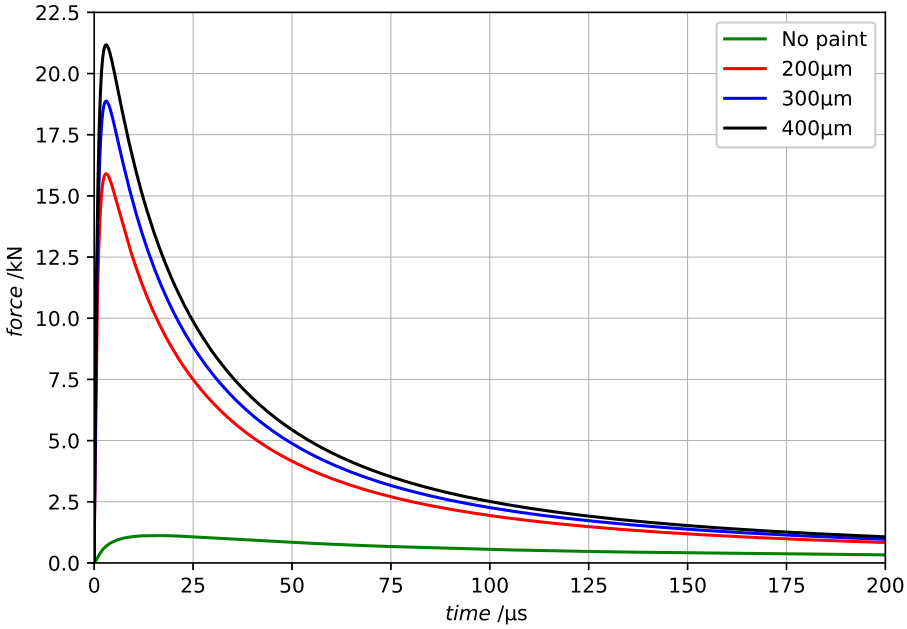


Figure 8.18: Force magnitude caused by explosion of lightning protection layers as a function of time for 3.18/34.5 µs, 100 kA

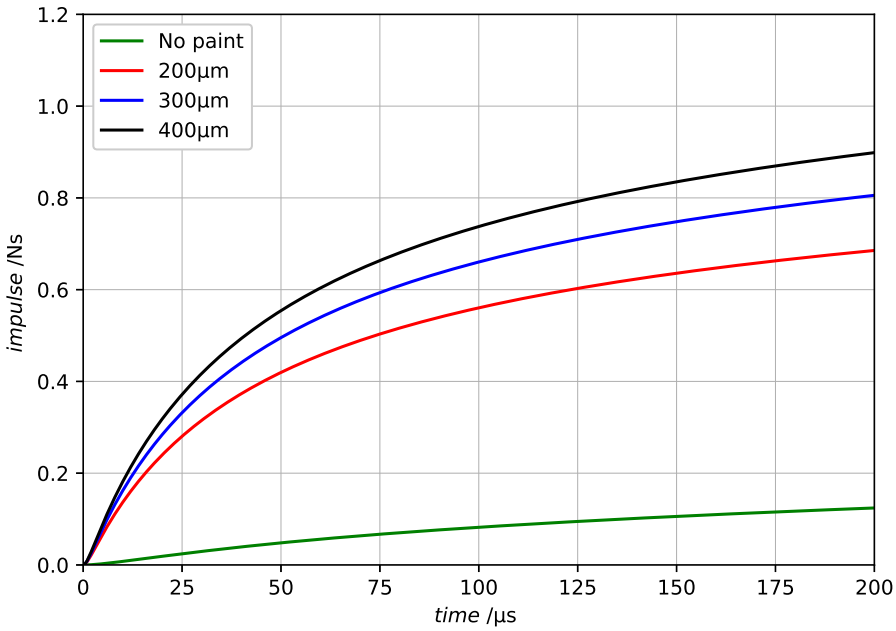


Figure 8.19: Impulse magnitude caused by explosion of lightning protection layers as a function of time for 3.18/34.5 µs, 100 kA

Table 8.6: Cylindrical shock wave parameters for 3.18/34.5 µs, 100 kA

α_s /mm $\mu s^{-1/2}$	α /bar μs	β /bar μs^{-1}
8.9054	100.7848	401.4348

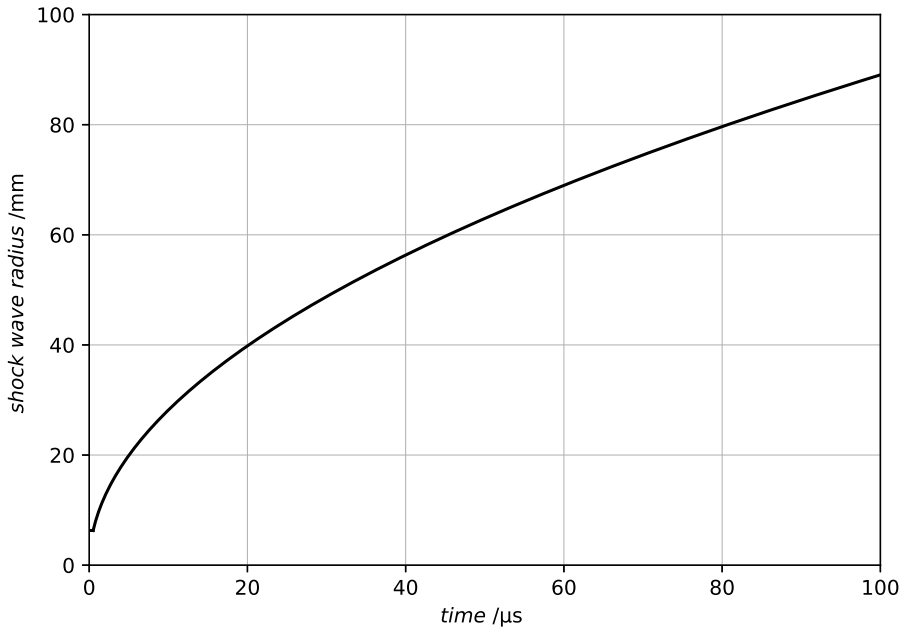


Figure 8.20: Computed shock radius for 3.18/34.5 µs, 100 kA

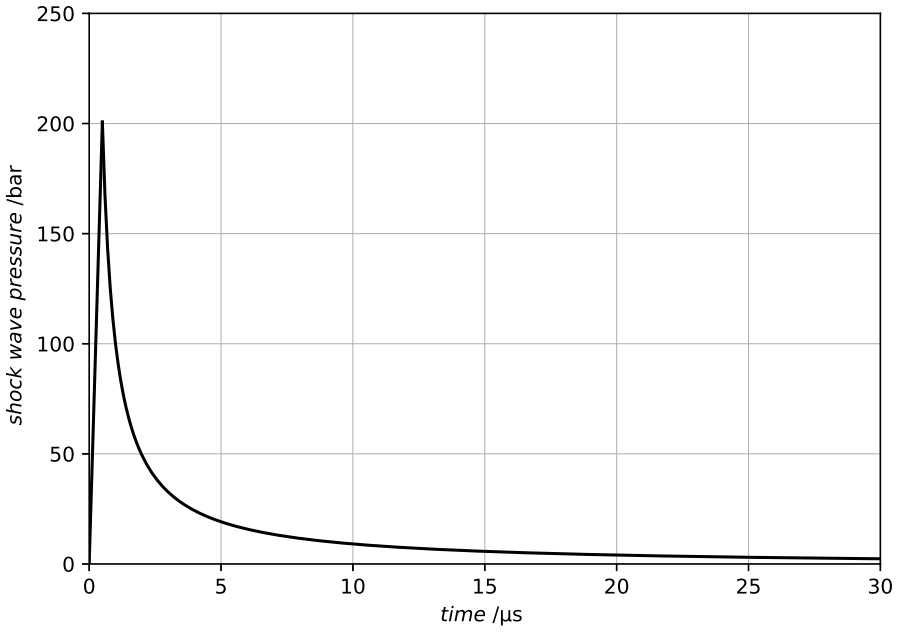


Figure 8.21: Mean cylindrical shock wave pressure as a function of time due to supersonic plasma expansion for 3.18/34.5 µs, 100 kA

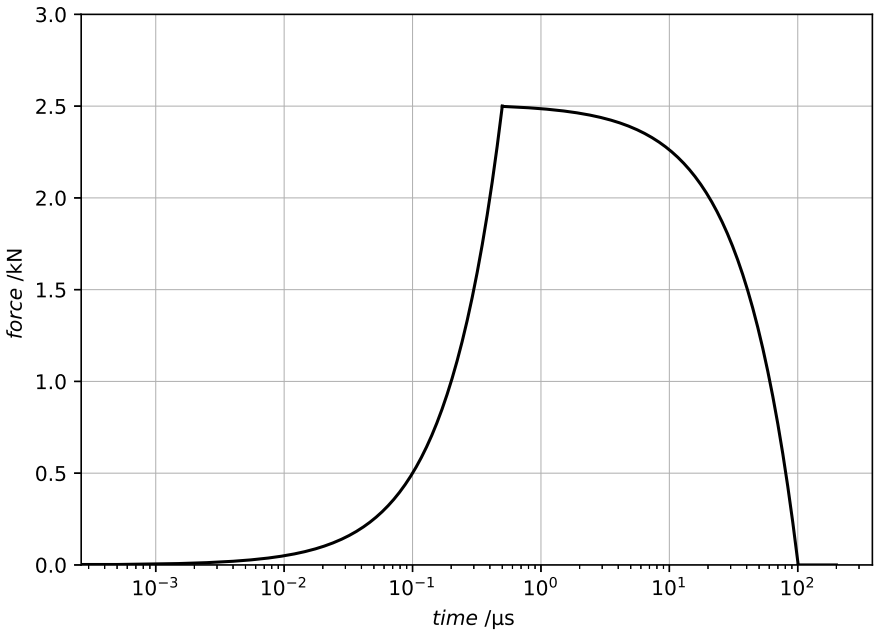


Figure 8.22: Force magnitude caused by supersonic plasma expansion as a function of time for 3.18/34.5 µs, 100 kA

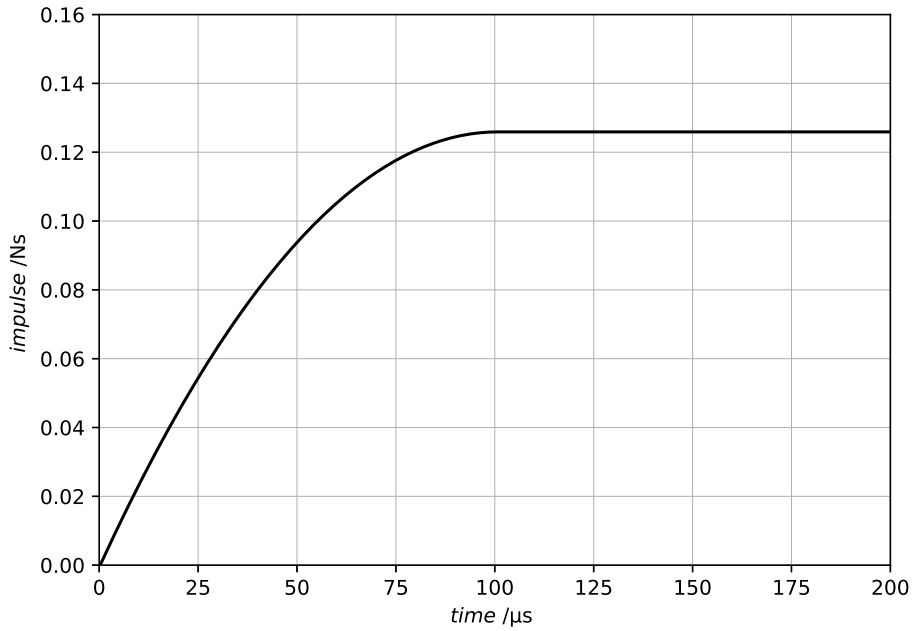


Figure 8.23: Impulse magnitude caused by supersonic plasma expansion as a function of time for 3.18/34.5 µs, 100 kA

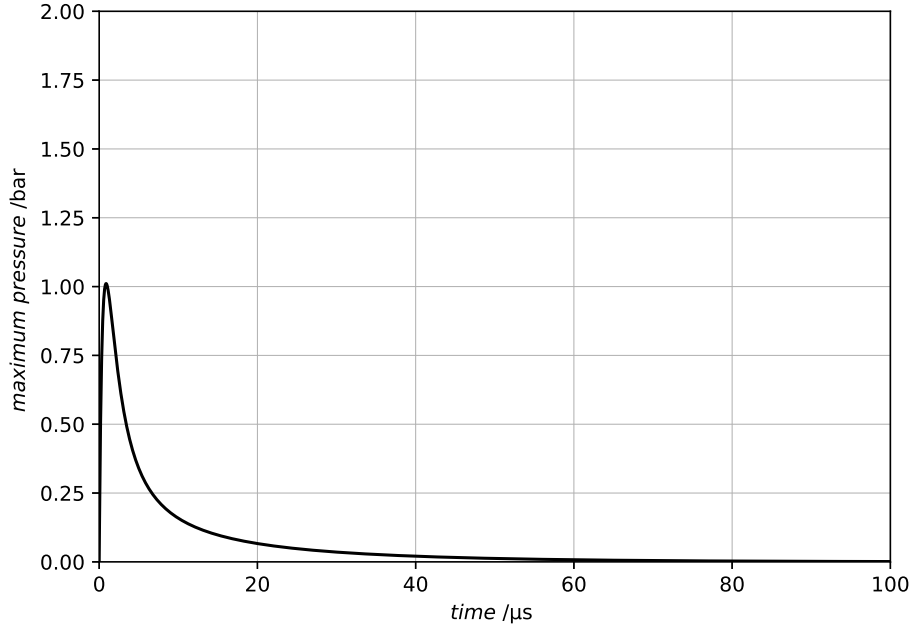


Figure 8.24: Maximum magnetic pressure evolution with time for 3.18/34.5 µs, 100 kA

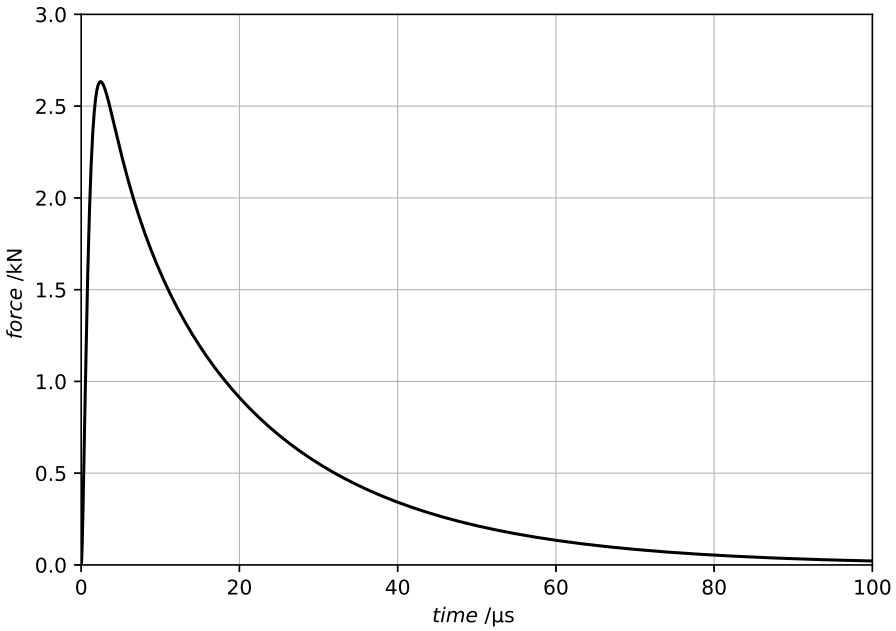


Figure 8.25: Force magnitude caused by magnetic forces as a function of time for 3.18/34.5 µs, 100 kA

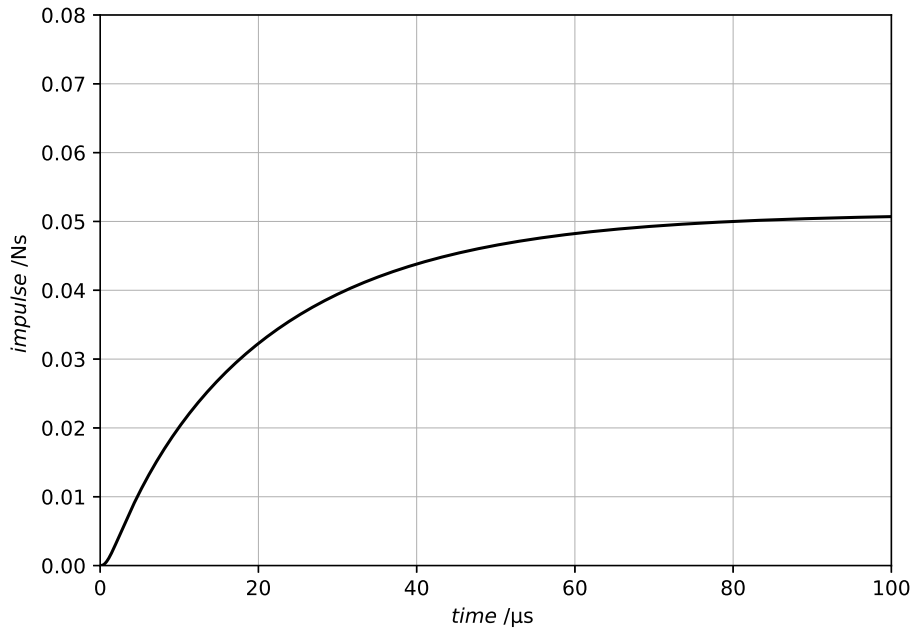
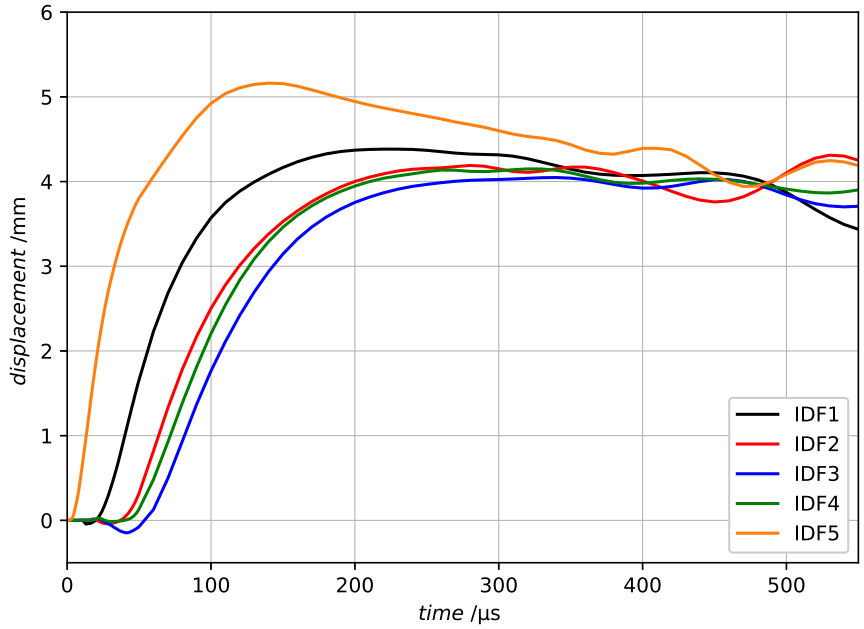
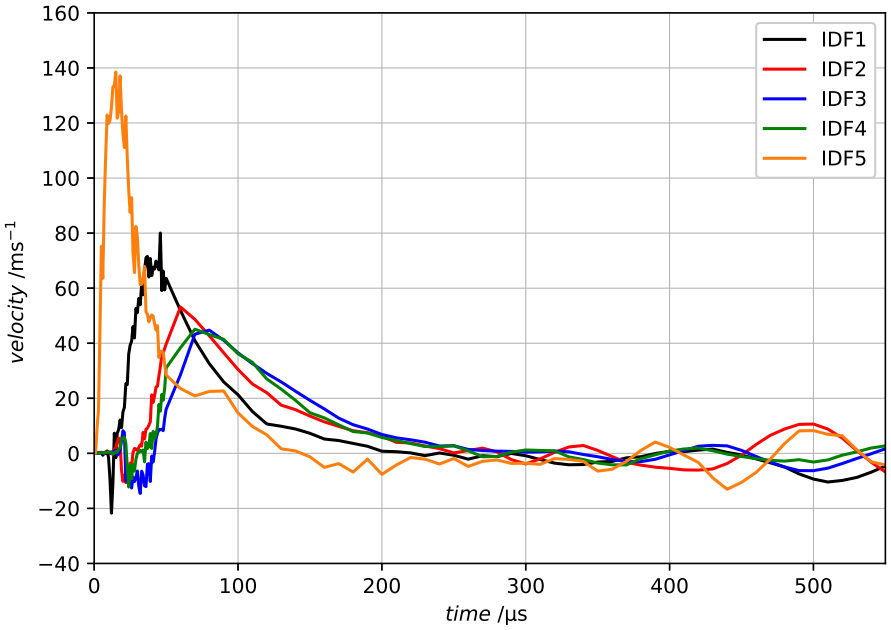


Figure 8.26: Impulse magnitude caused by magnetic forces as a function of time for 3.18/34.5 µs, 100 kA



(a) Displacement



(b) Velocity

Figure 8.27: Finite element predictions for 3.18/34.5 µs, 100 kA

8.5 Waveform 4/34 µs, 110 kA

The waveform 4/34 µs, 110 kA and the corresponding mechanical loads and mechanical deformation predictions are shown in Figure 8.28 to Figure 8.40 and from Table 8.7 to Table 8.9.

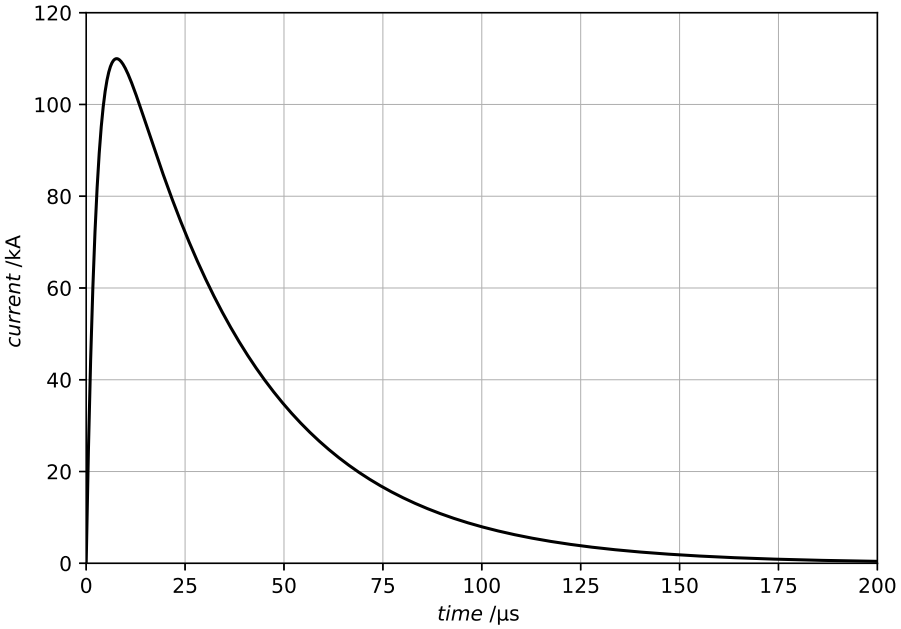


Figure 8.28: Double exponential for 4/34 µs, 110 kA

Table 8.7: Waveform parameters for 4/34 µs, 110 kA

a /s^{-1}	b /s^{-1}	A /-	I_{max} /kA
2.940×10^4	3.520×10^5	1.368	110

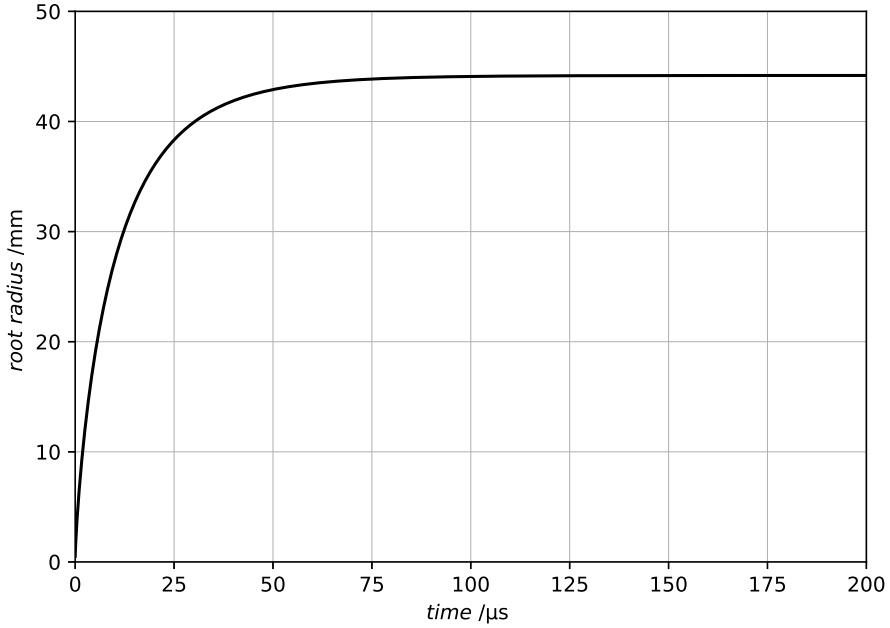


Figure 8.29: Root radius for 4/34 µs, 110 kA

Table 8.8: Root radius parameters for 4/34 µs, 110 kA

	c /mm	α /mm	β /mm	R_{R_0} /mm
ECF 73	43.68	0.8117	−0.1474	0.5

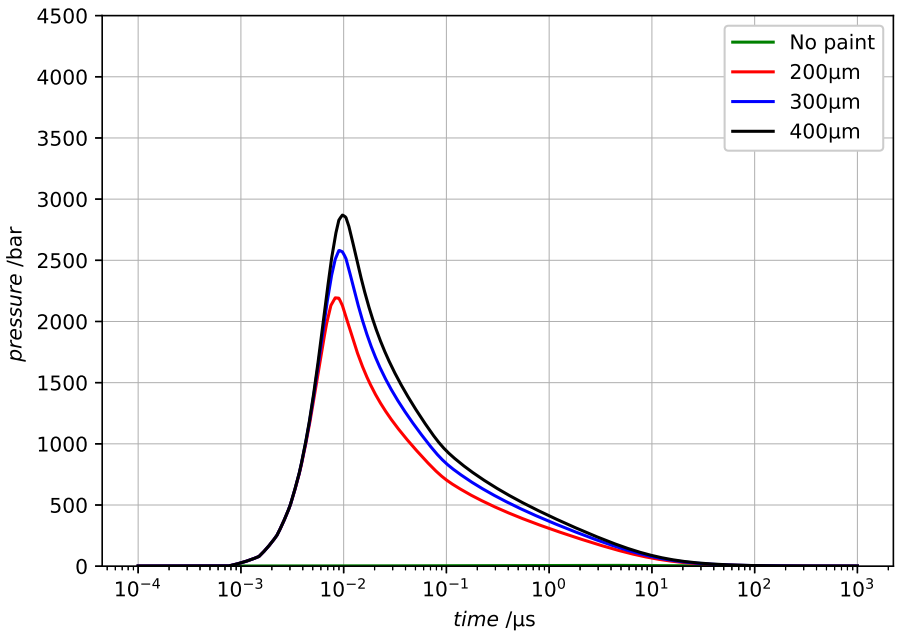


Figure 8.30: Overpressure caused by explosion of lightning protection layers as a function of time for 4/34 µs, 110 kA

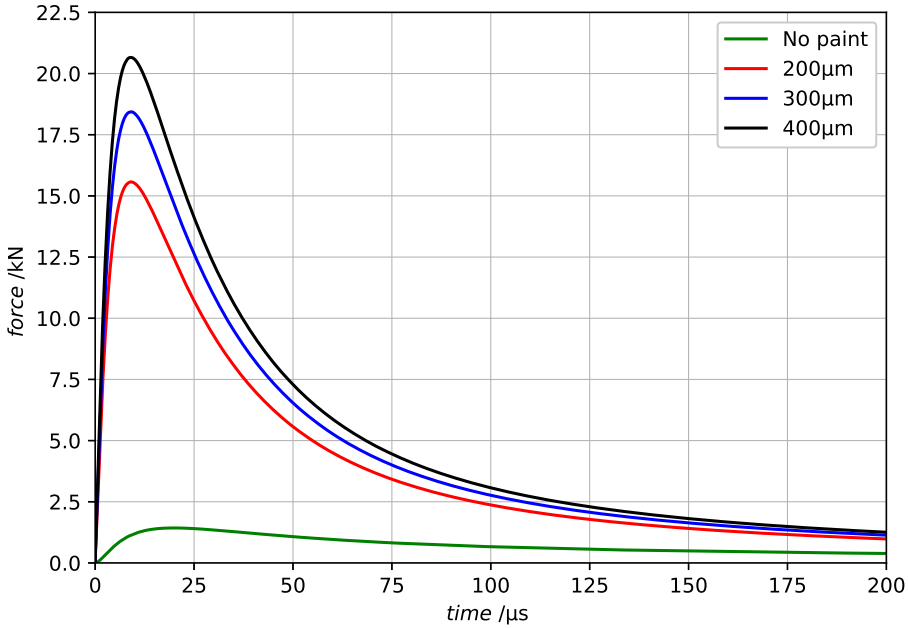


Figure 8.31: Force magnitude caused by explosion of lightning protection layers as a function of time for 4/34 µs, 110 kA

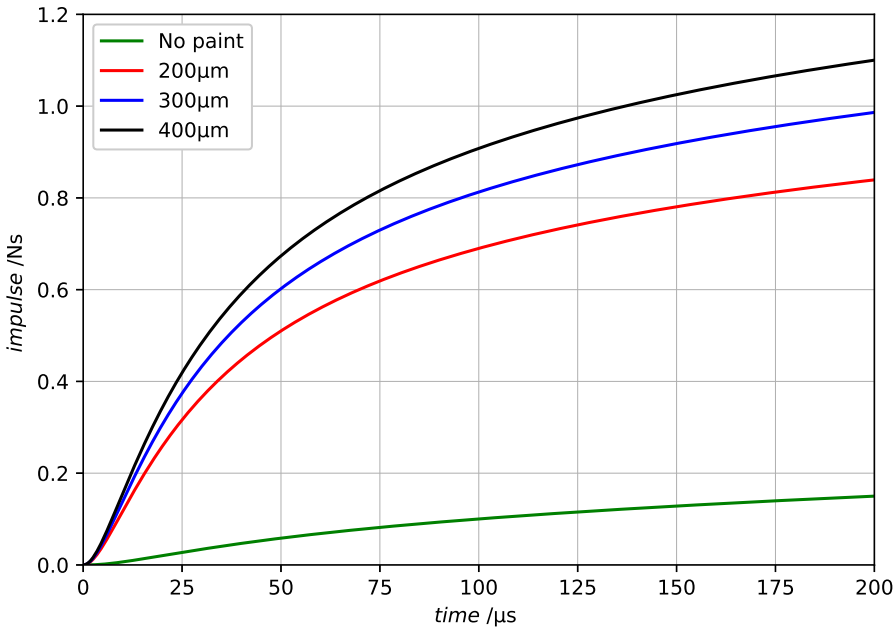


Figure 8.32: Impulse magnitude caused by explosion of lightning protection layers as a function of time for 4/34 µs, 110 kA

Table 8.9: Cylindrical shock wave parameters for 4/34 µs, 110 kA

α_s /mm $\mu s^{-1/2}$	α /bar μs	β /bar μs^{-1}
9.175	106.9709	426.1972

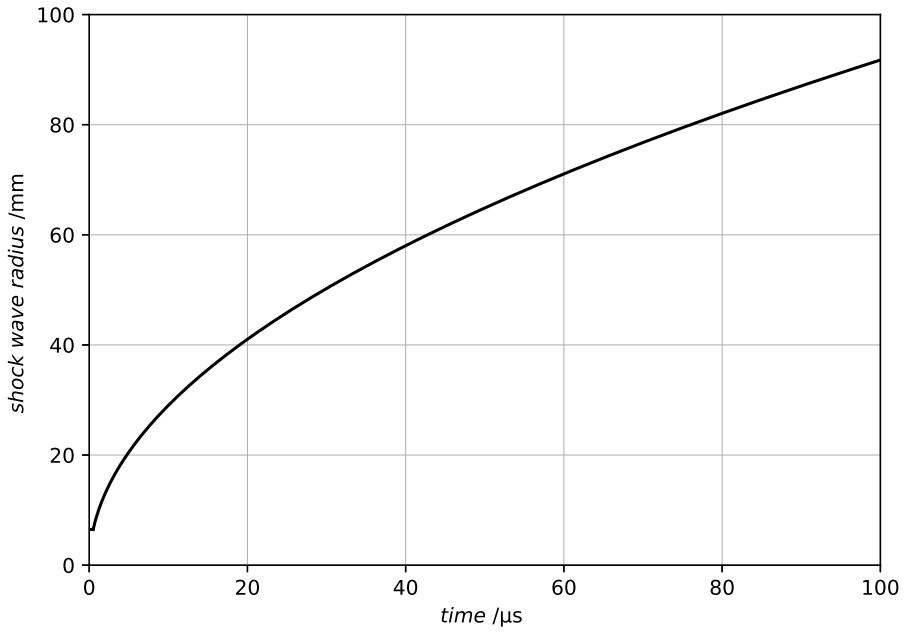


Figure 8.33: Computed shock radius for 4/34 µs, 110 kA

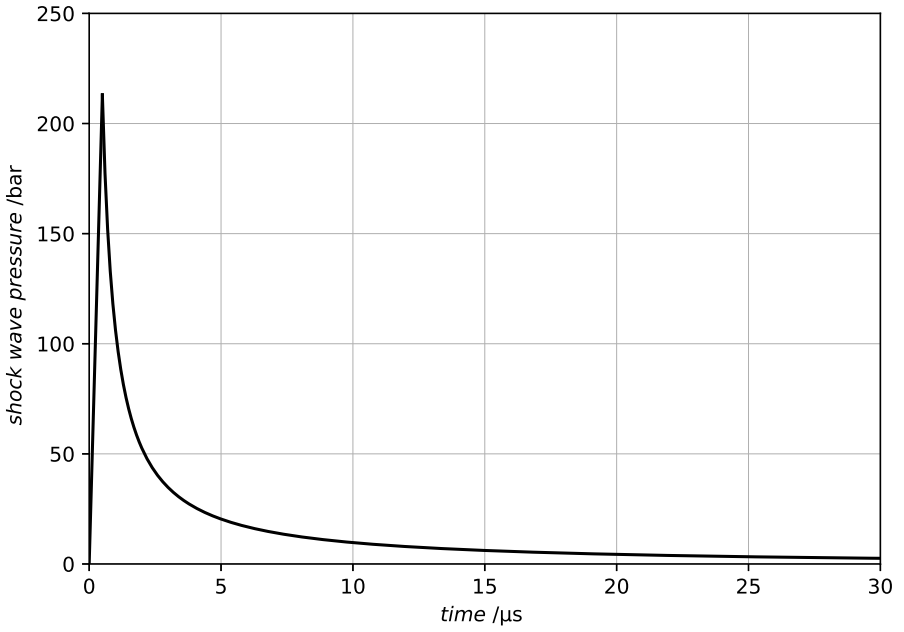


Figure 8.34: Mean cylindrical shock wave pressure as a function of time due to supersonic plasma expansion for 4/34 µs, 110 kA

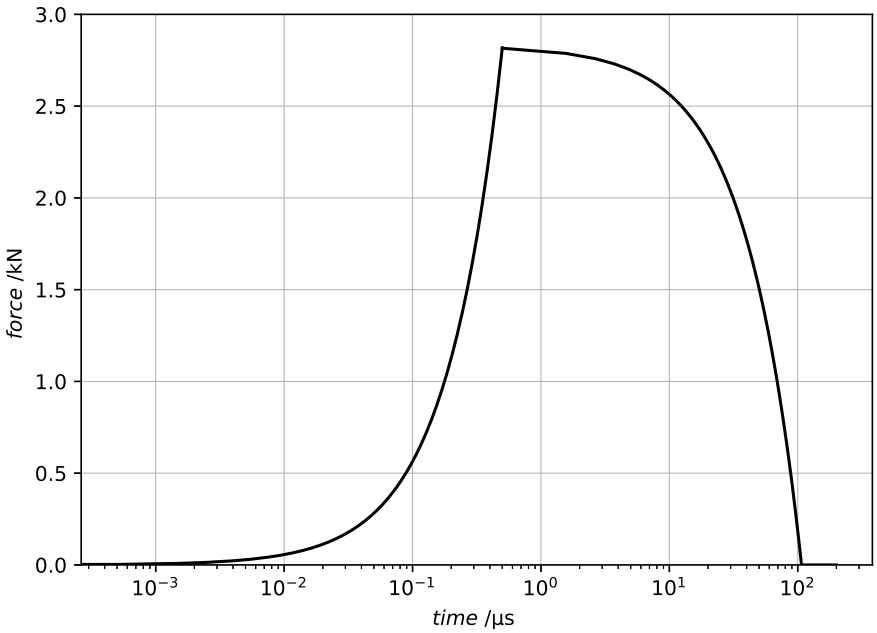


Figure 8.35: Force magnitude caused by supersonic plasma expansion as a function of time for 4/34 µs, 110 kA

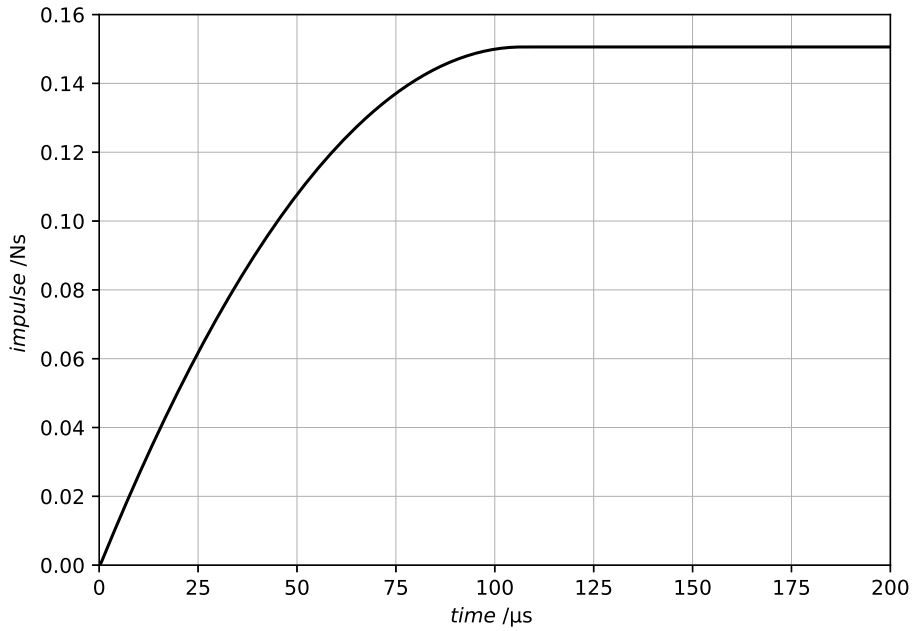


Figure 8.36: Impulse magnitude caused by supersonic plasma expansion as a function of time for 4/34 µs, 110 kA

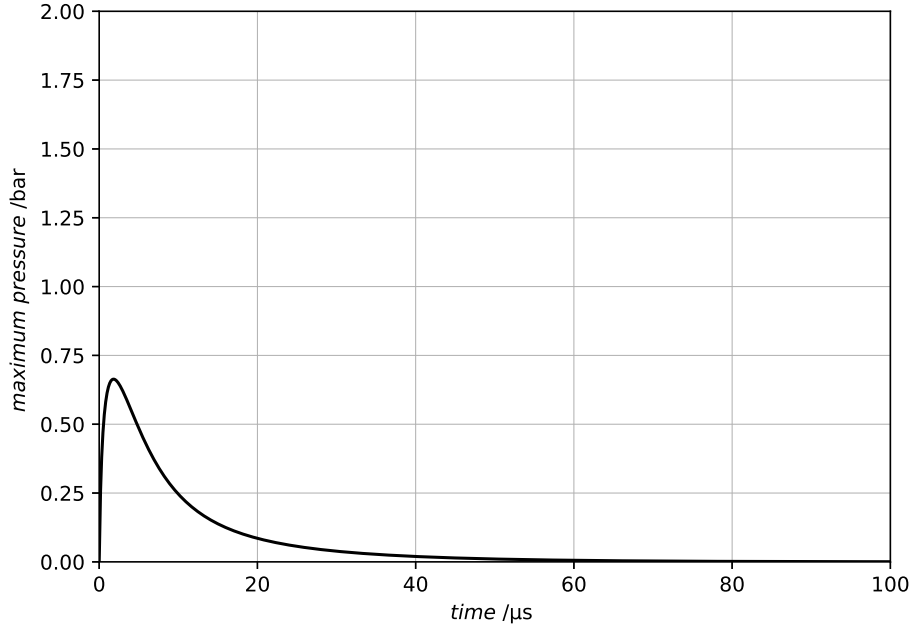


Figure 8.37: Maximum magnetic pressure evolution with time for 4/34 µs, 110 kA

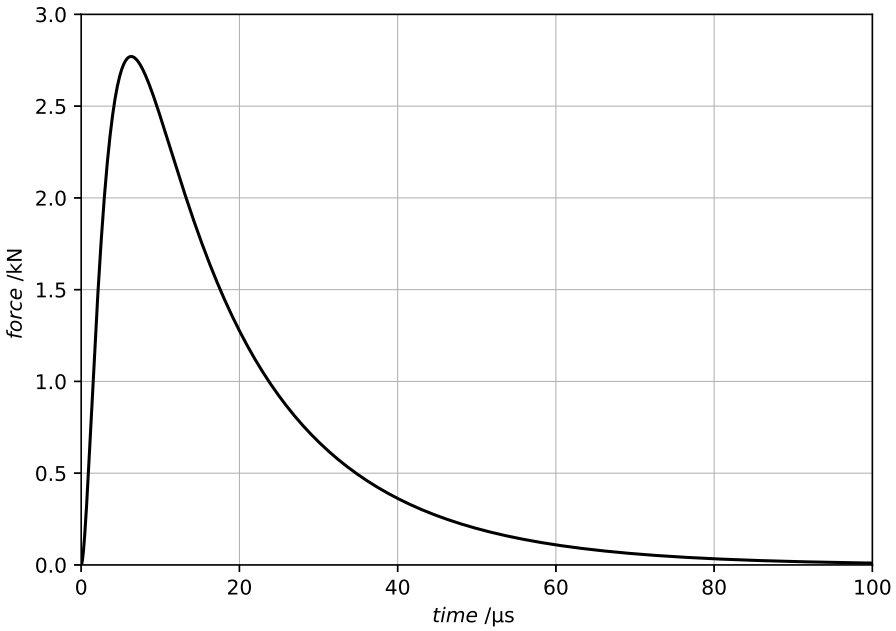


Figure 8.38: Force magnitude caused by magnetic forces as a function of time for 4/34 µs, 110 kA

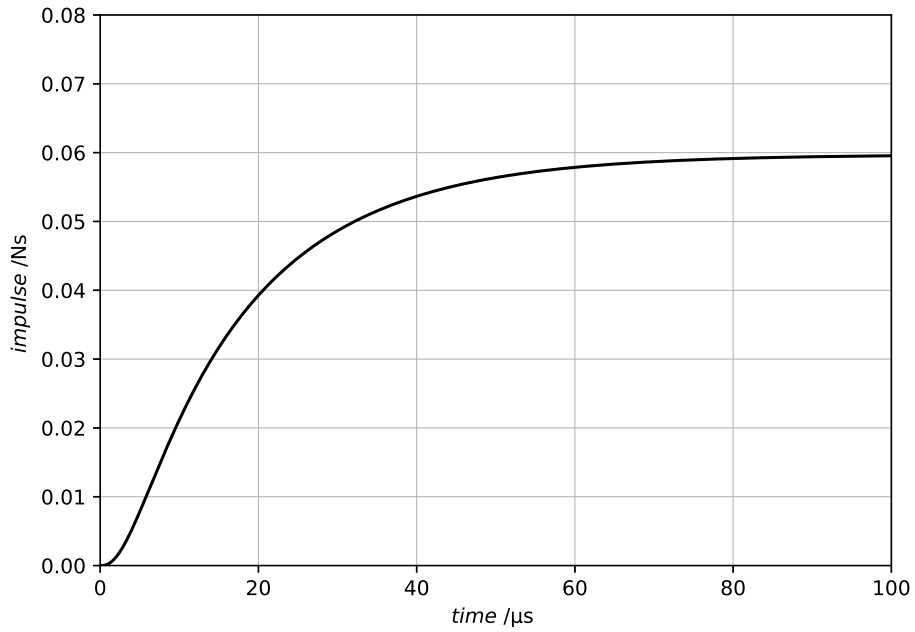
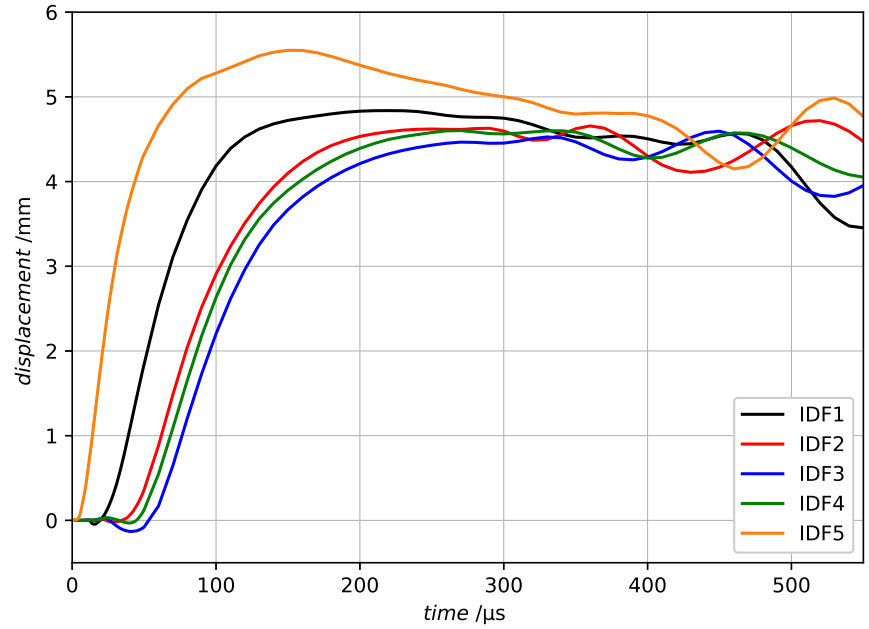
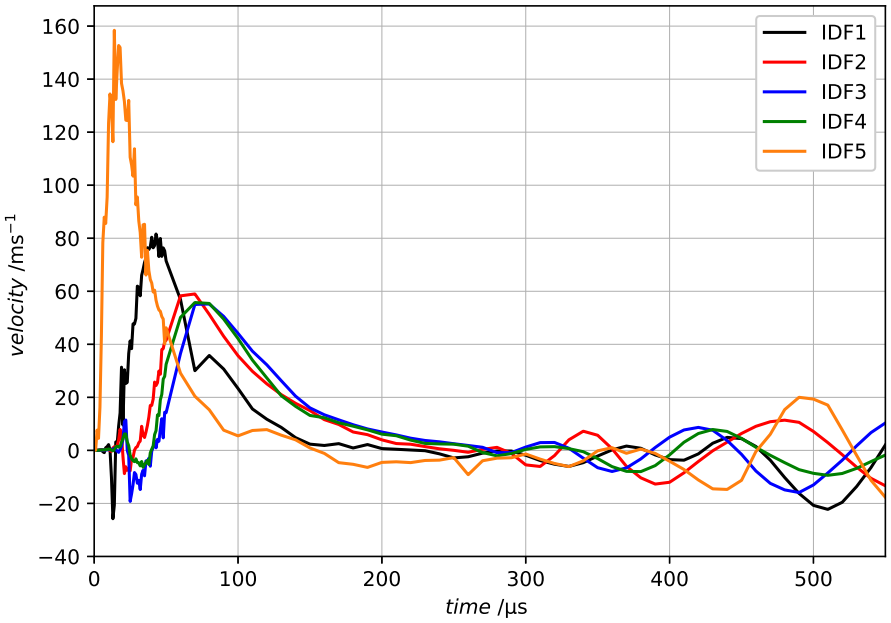


Figure 8.39: Impulse magnitude caused by magnetic forces as a function of time for 4/34 µs, 110 kA



(a) Displacement



(b) Velocity

Figure 8.40: Finite element predictions for 4/34 µs, 110 kA

8.6 Waveform 5/23.6 µs, 110 kA

The waveform 5/23.6 µs, 110 kA and the corresponding mechanical loads and mechanical deformation predictions are shown in Figure 8.41 to Figure 8.53 and from Table 8.10 to Table 8.12.

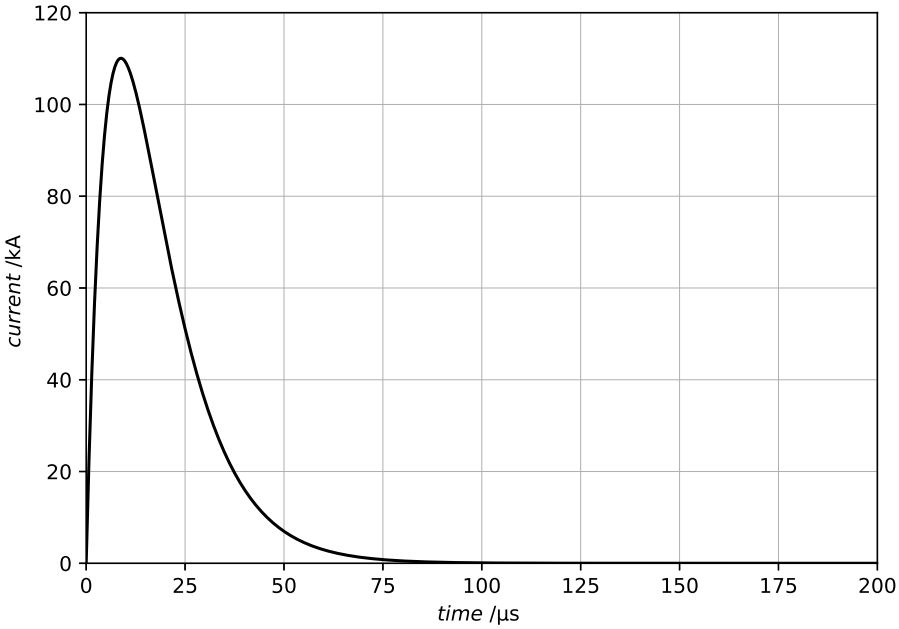


Figure 8.41: Double exponential for 5/23.6 µs, 110 kA

Table 8.10: Waveform parameters for 5/23.6 µs, 110 kA

a /s^{-1}	b /s^{-1}	A /-	I_{max} /kA
8.909×10^4	1.424×10^5	5.853	110

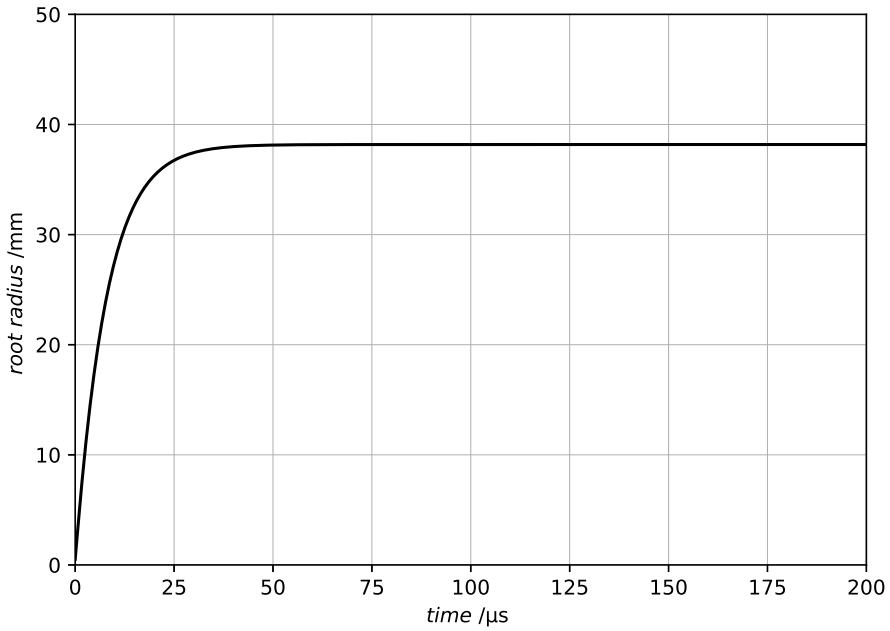


Figure 8.42: Root radius for 5/23.6 µs, 110 kA

Table 8.11: Root radius parameters for 5/23.6 µs, 110 kA

	c /mm	α /mm	β /mm	R_{R_0} /mm
ECF 73	37.68	1.03	−0.1186	0.5

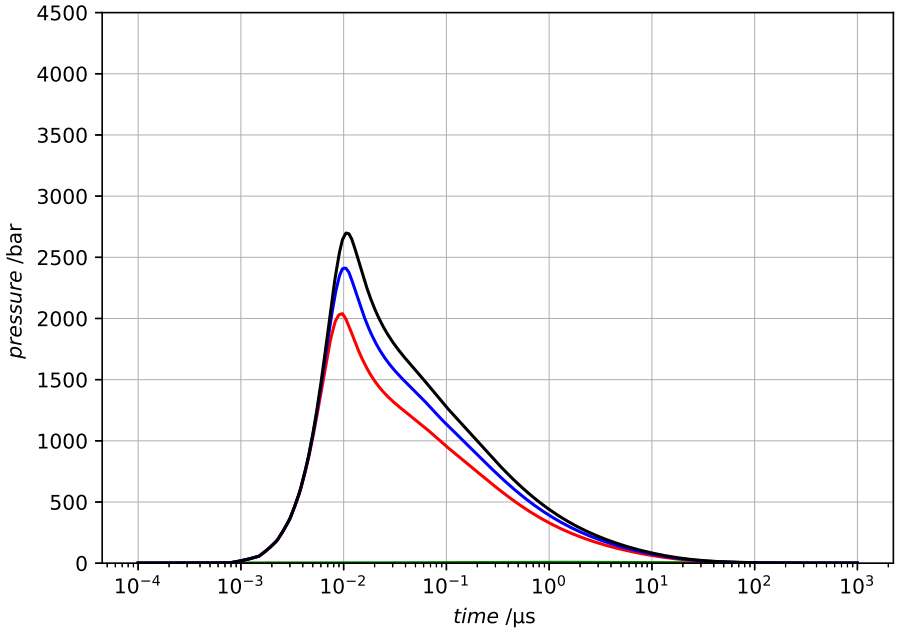


Figure 8.43: Overpressure caused by explosion of lightning protection layers as a function of time for 5/23.6 µs, 110 kA

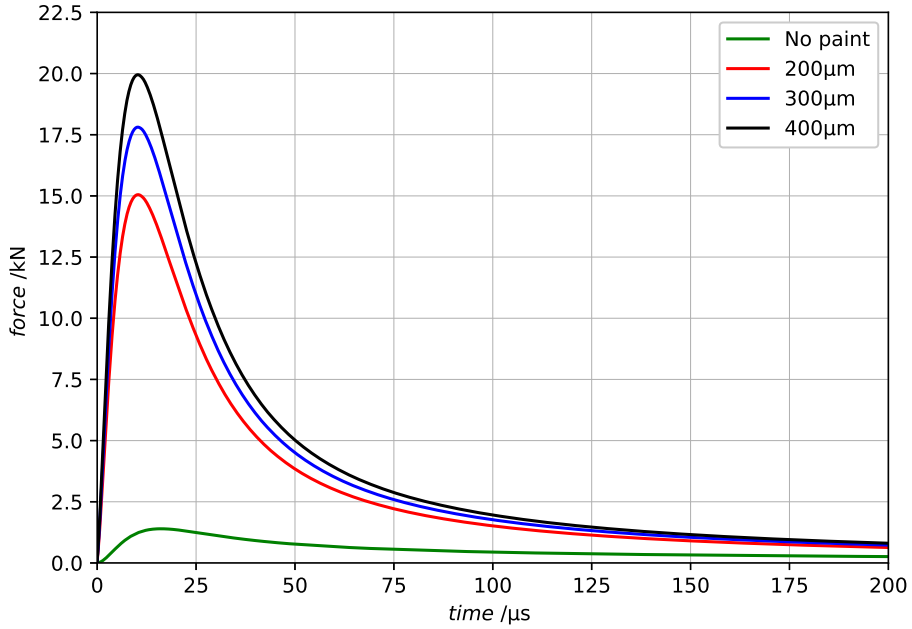


Figure 8.44: Force magnitude caused by explosion of lightning protection layers as a function of time for 5/23.6 µs, 110 kA

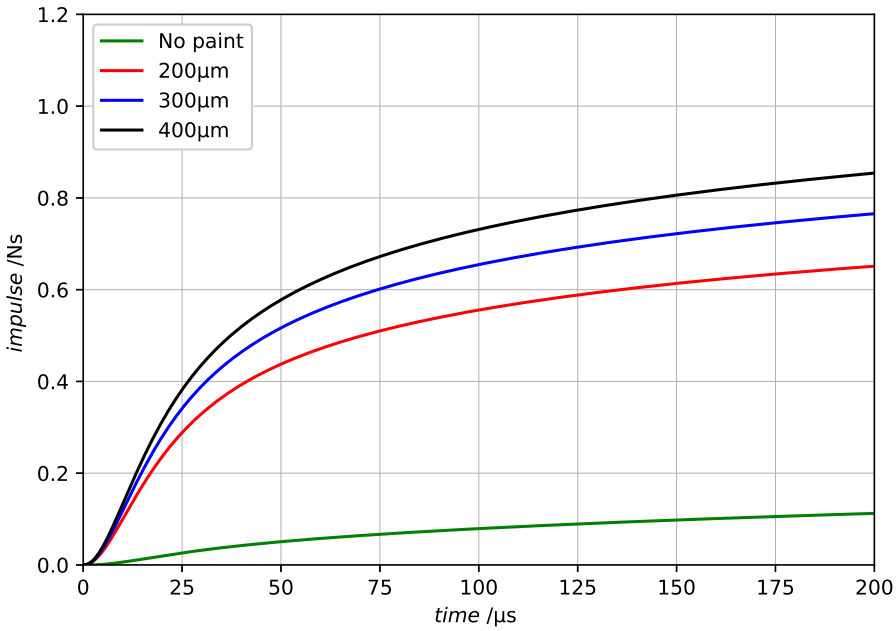


Figure 8.45: Impulse magnitude caused by explosion of lightning protection layers as a function of time for 5/23.6 µs, 110 kA

Table 8.12: Cylindrical shock wave parameters for 5/23.6 µs, 110 kA

α_s /mm $\mu s^{-1/2}$	α /bar μs	β /bar μs^{-1}
9.1746	106.9709	426.1972

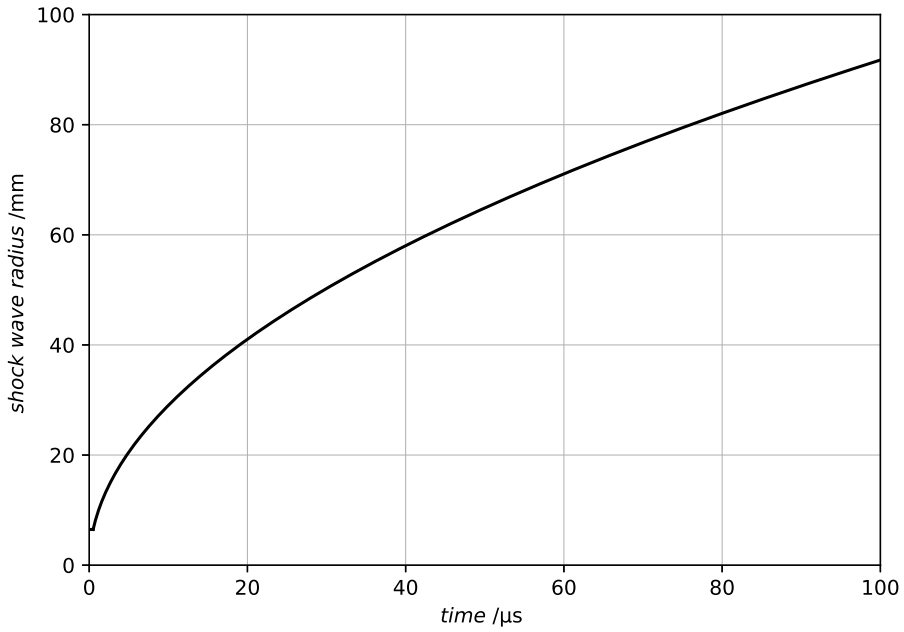


Figure 8.46: Computed shock radius for 5/23.6 µs, 110 kA

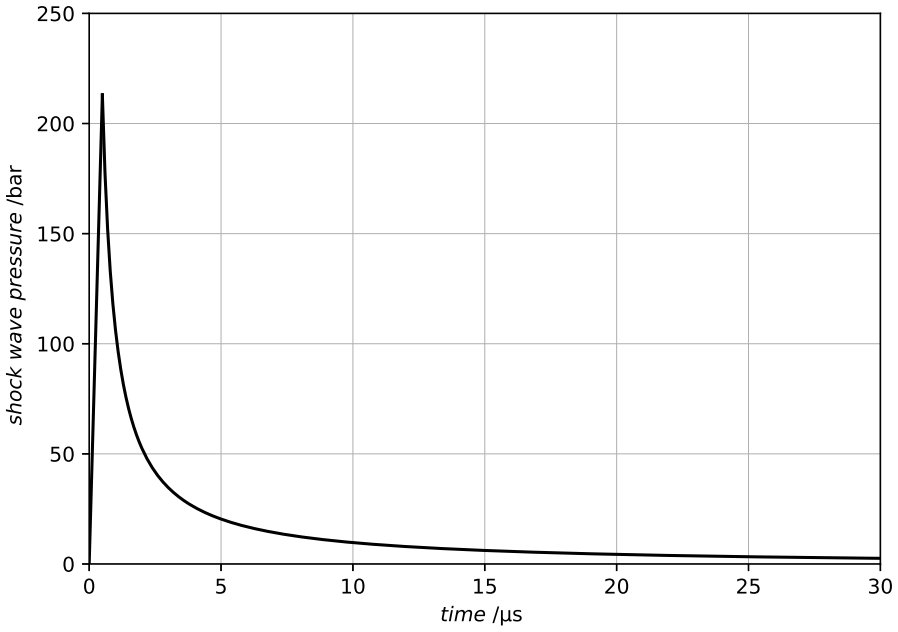


Figure 8.47: Mean cylindrical shock wave pressure as a function of time due to supersonic plasma expansion for 5/23.6 µs, 110 kA

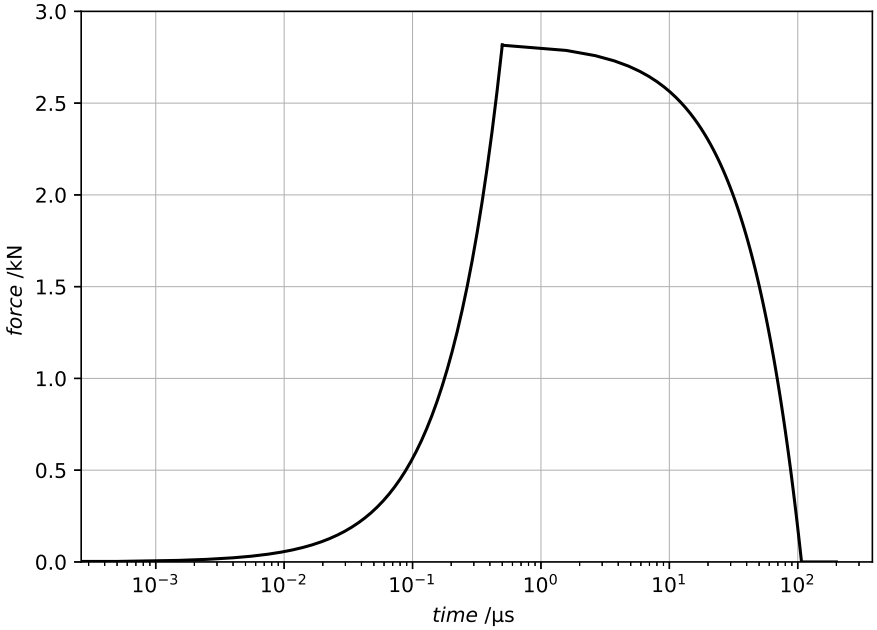


Figure 8.48: Force magnitude caused by supersonic plasma expansion as a function of time for 5/23.6 µs, 110 kA

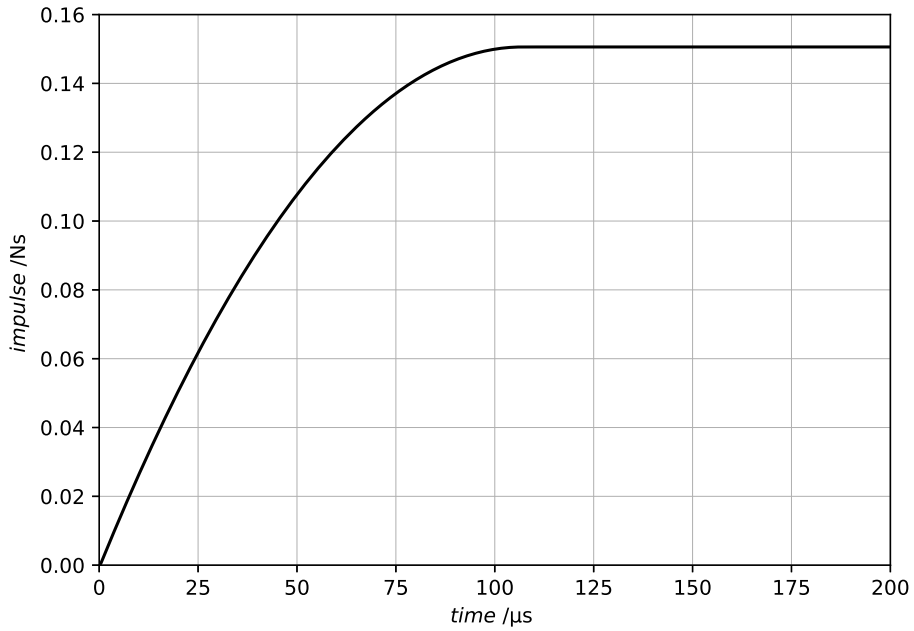


Figure 8.49: Impulse magnitude caused by supersonic plasma expansion as a function of time for 5/23.6 µs, 110 kA

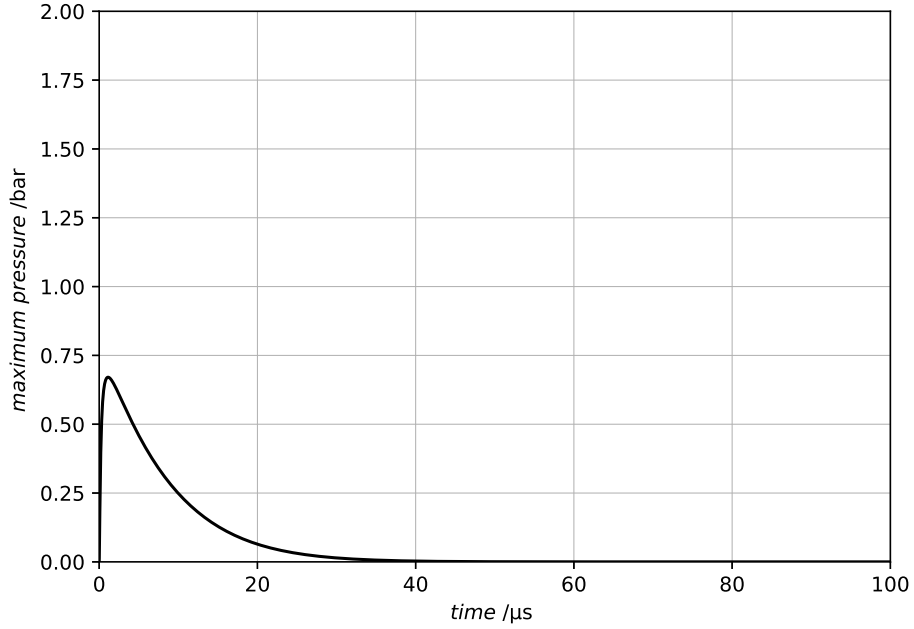


Figure 8.50: Maximum magnetic pressure evolution with time for 5/23.6 µs, 110 kA

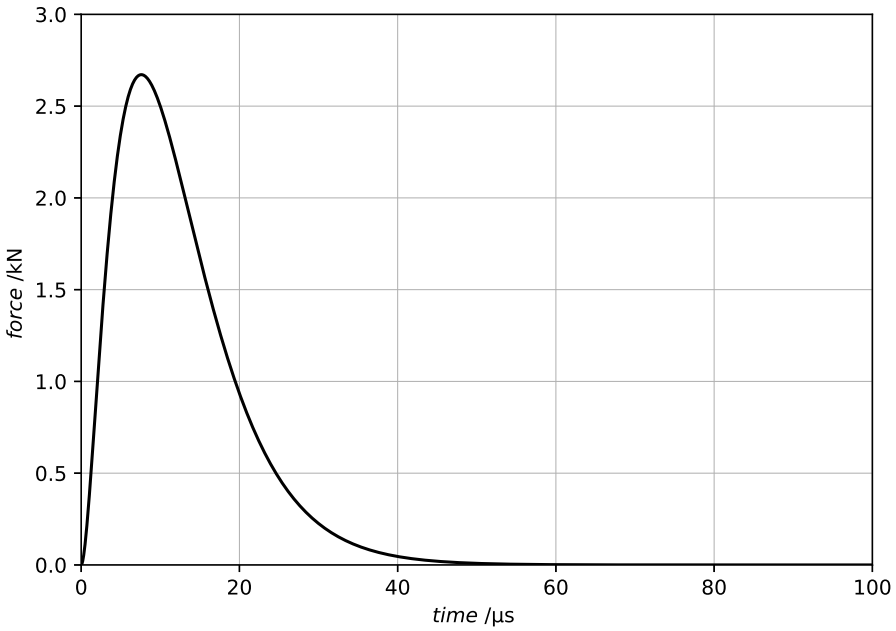


Figure 8.51: Force magnitude caused by magnetic forces as a function of time for 5/23.6 µs, 110 kA

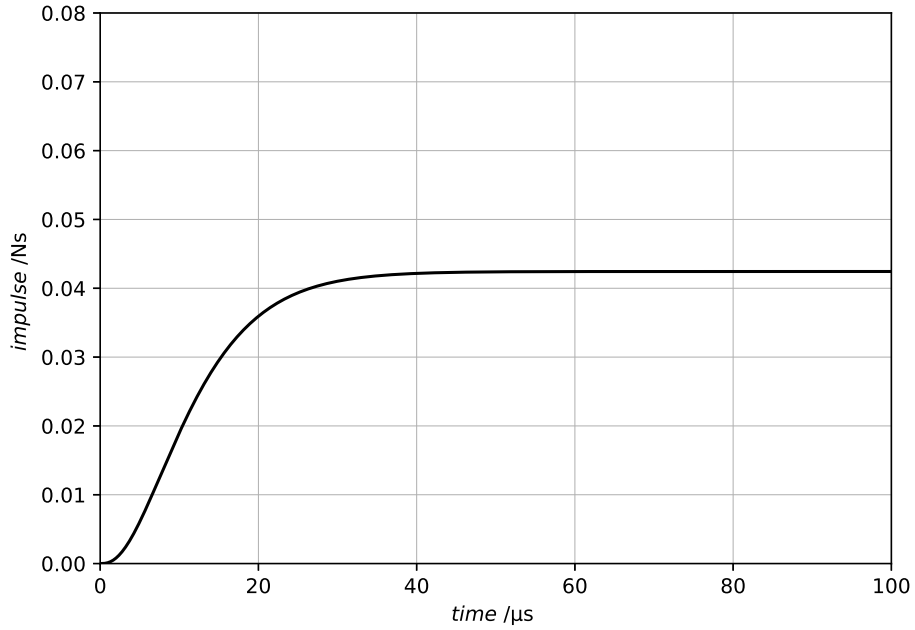
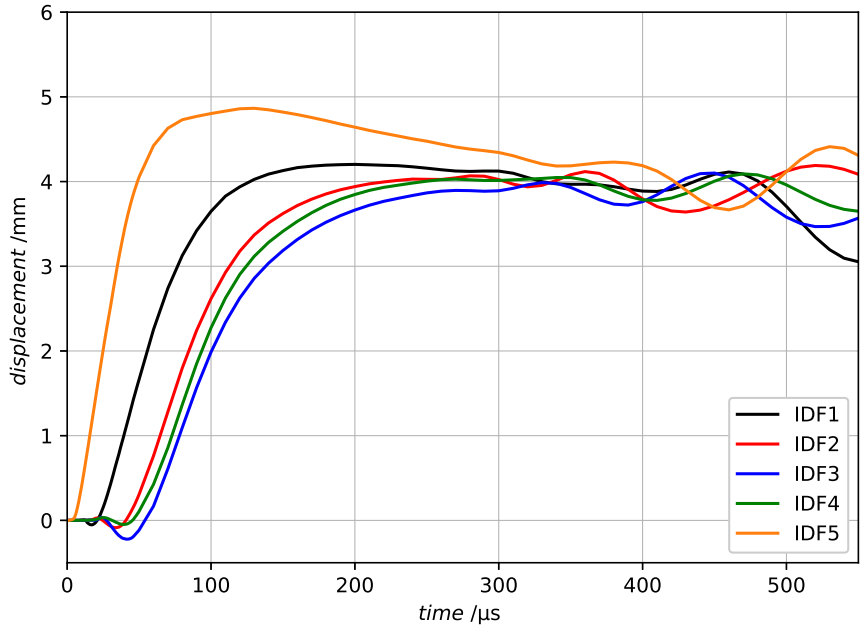
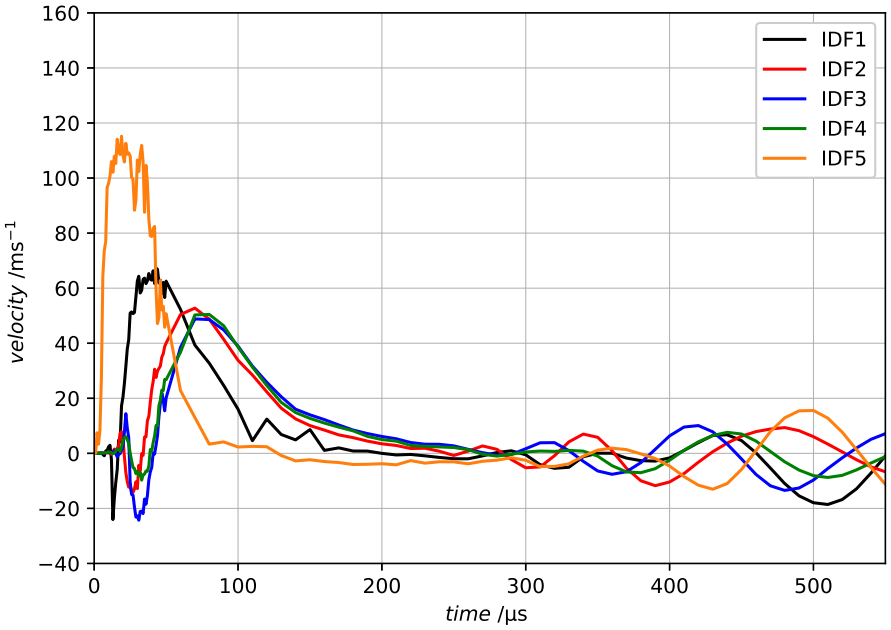


Figure 8.52: Impulse magnitude caused by magnetic forces as a function of time for 5/23.6 µs, 110 kA



(a) Displacement



(b) Velocity

Figure 8.53: Finite element predictions for 5/23.6 µs, 110 kA

8.7 Waveform 6/51 µs, 90 kA

The waveform 6/51 µs, 90 kA and the corresponding mechanical loads and mechanical deformation predictions are shown in Figure 8.54 to Figure 8.66 and from Table 8.13 to Table 8.15.

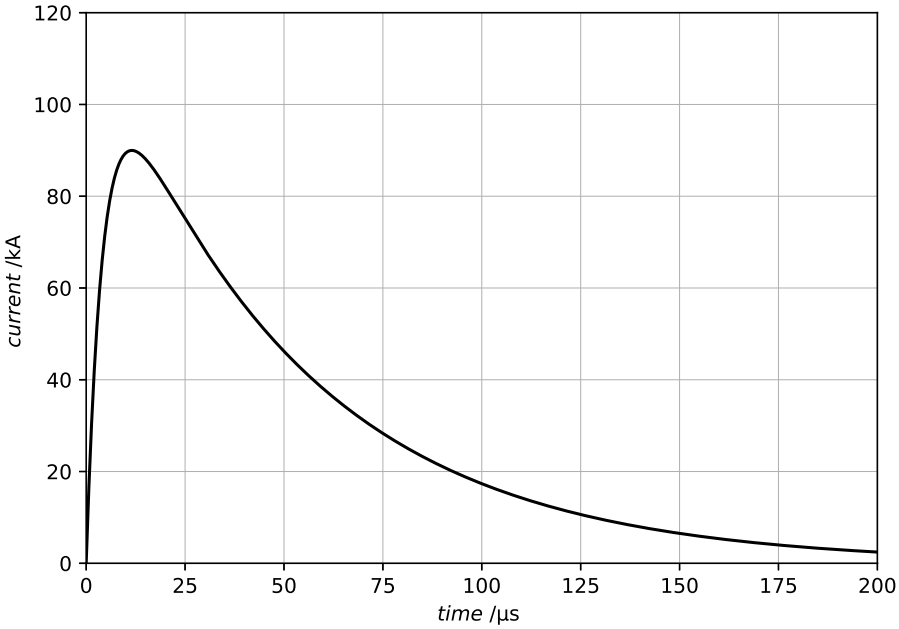


Figure 8.54: Double exponential for 6/51 µs, 90 kA

Table 8.13: Waveform parameters for 6/51 µs, 90 kA

a /s^{-1}	b /s^{-1}	A /-	I_{max} /kA
1.960×10^4	2.346×10^5	1.368	90

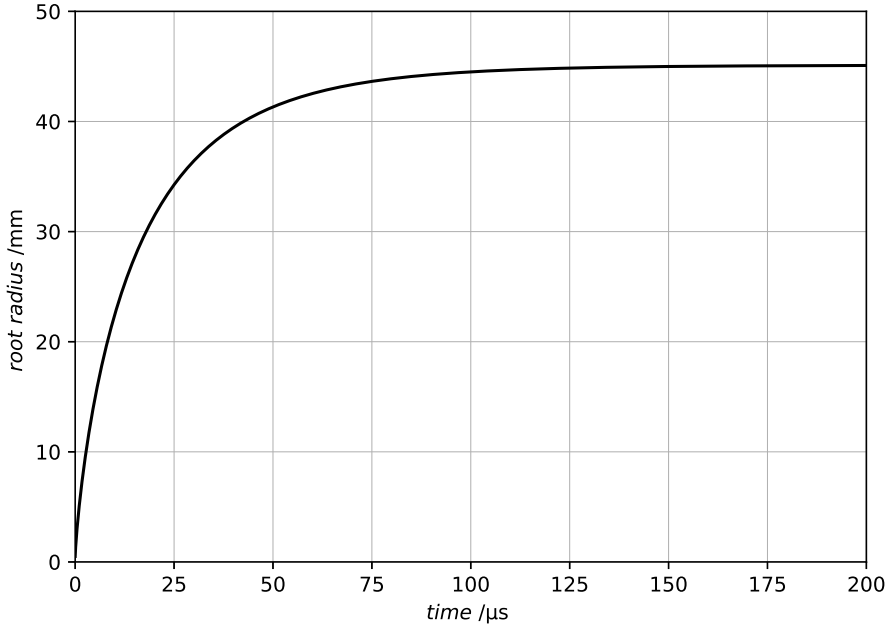


Figure 8.55: Root radius for 6/51 µs, 90 kA

Table 8.14: Root radius parameters for 6/51 µs, 90 kA

	c /mm	α /mm	β /mm	R_{R_0} /mm
ECF 73	44.61	0.8027	−0.1067	0.5

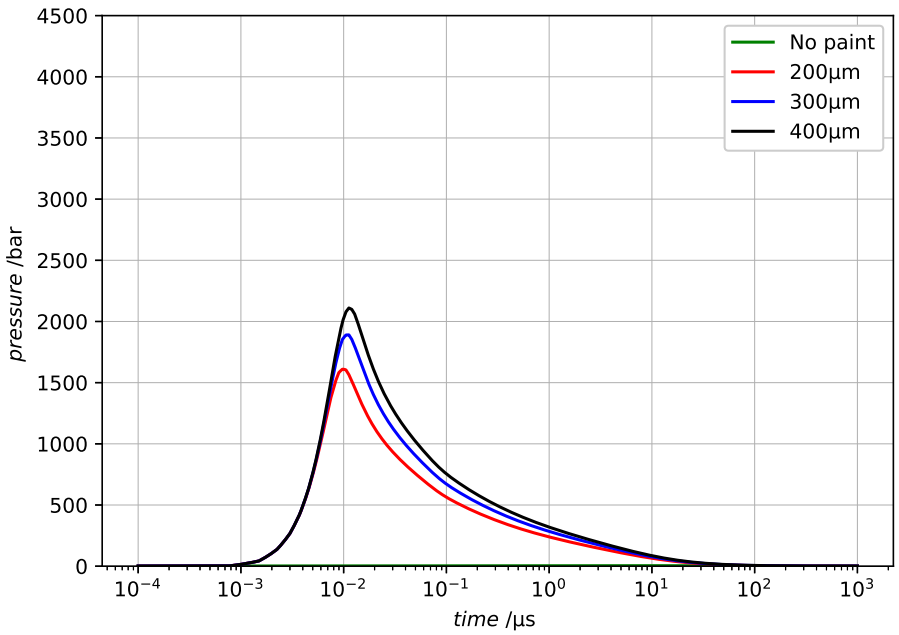


Figure 8.56: Overpressure caused by explosion of lightning protection layers as a function of time for 6/51 µs, 90 kA

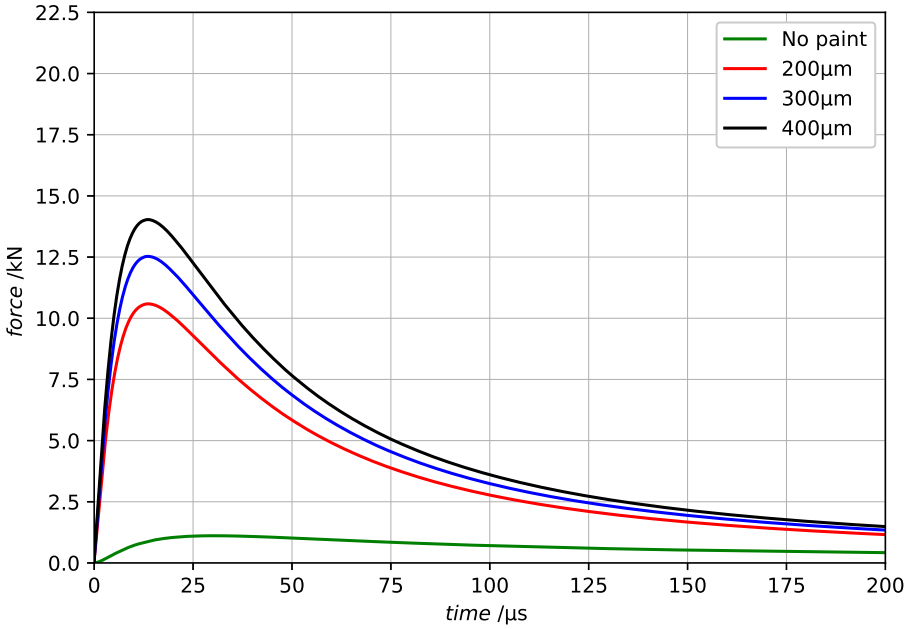


Figure 8.57: Force magnitude caused by explosion of lightning protection layers as a function of time for 6/51 µs, 90 kA

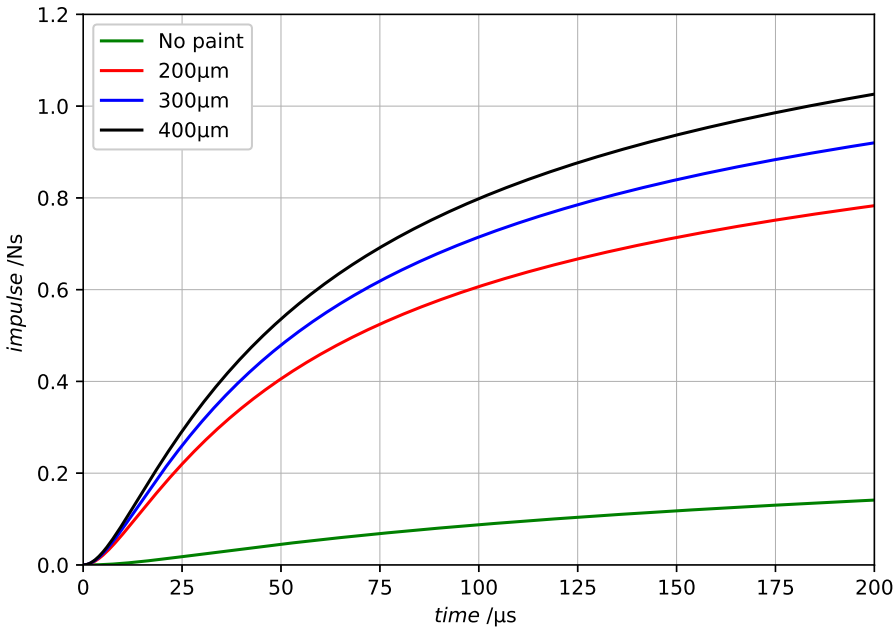


Figure 8.58: Impulse magnitude caused by explosion of lightning protection layers as a function of time for 6/51 µs, 90 kA

Table 8.15: Cylindrical shock wave parameters for 6/51 µs, 90 kA

α_s /mm $\mu s^{-1/2}$	α /bar μs	β /bar μs^{-1}
8.6170	94.3619	375.7242

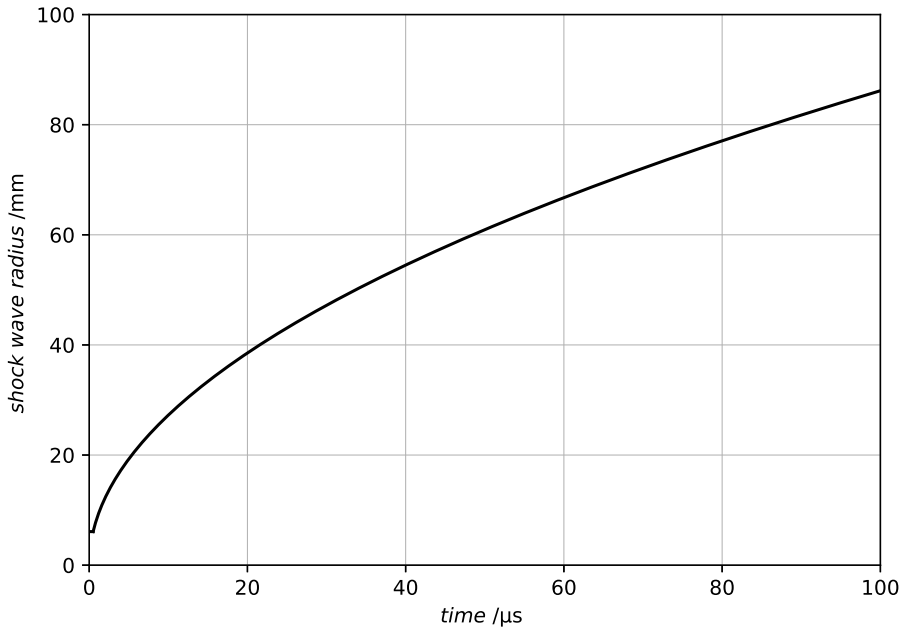


Figure 8.59: Computed shock radius for 6/51 µs, 90 kA

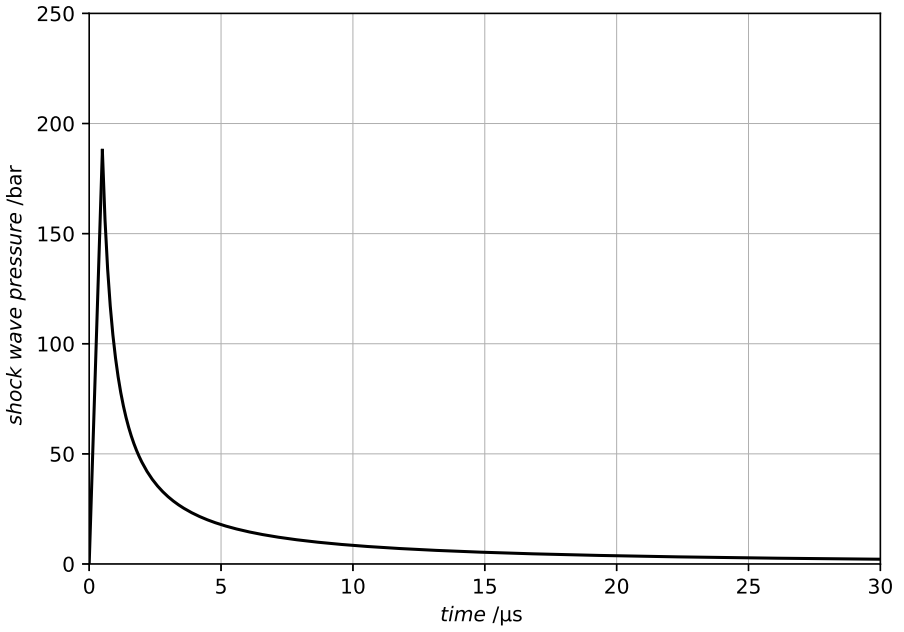


Figure 8.60: Mean cylindrical shock wave pressure as a function of time due to supersonic plasma expansion for 6/51 µs, 90 kA

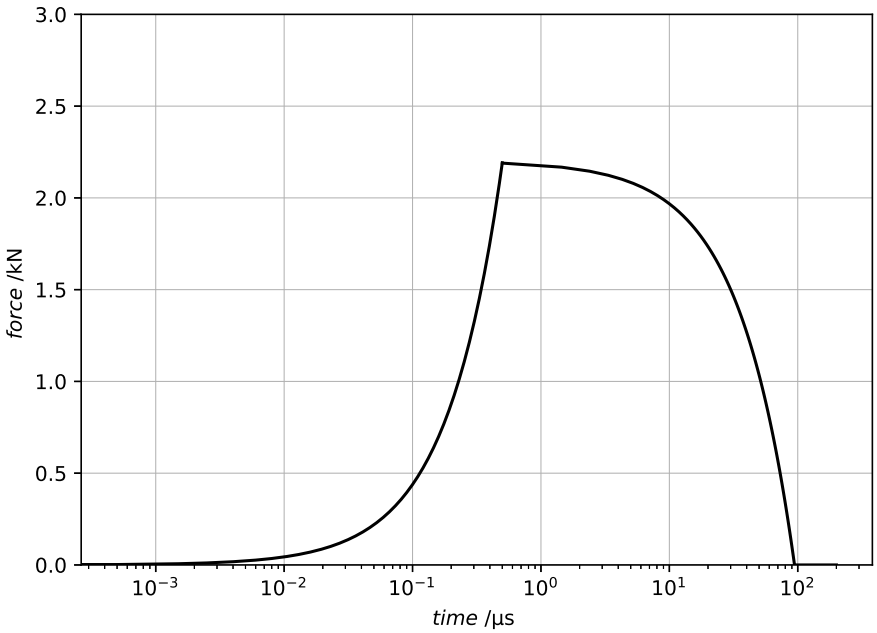


Figure 8.61: Force magnitude caused by supersonic plasma expansion as a function of time for 6/51 µs, 90 kA

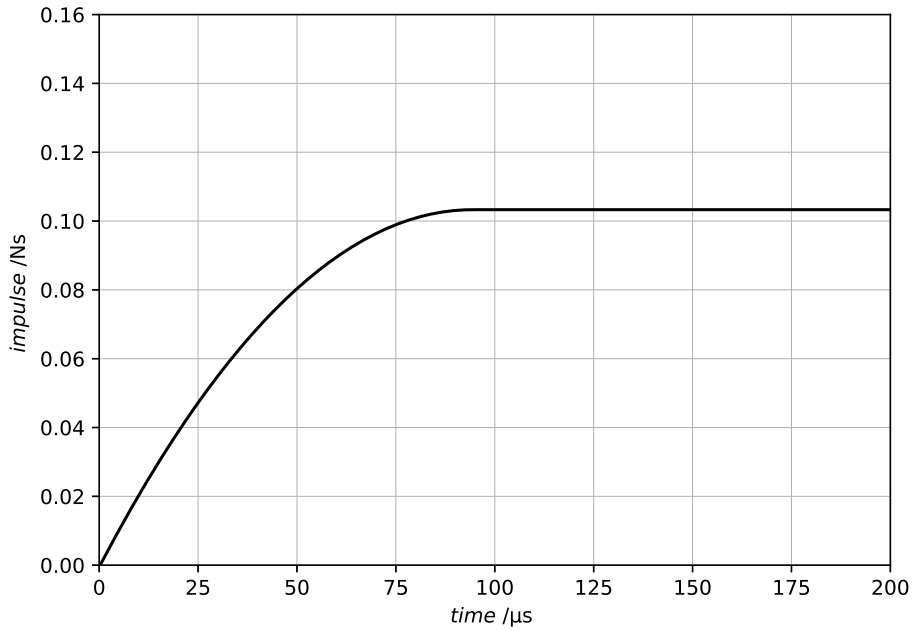


Figure 8.62: Impulse magnitude caused by supersonic plasma expansion as a function of time for 6/51 µs, 90 kA

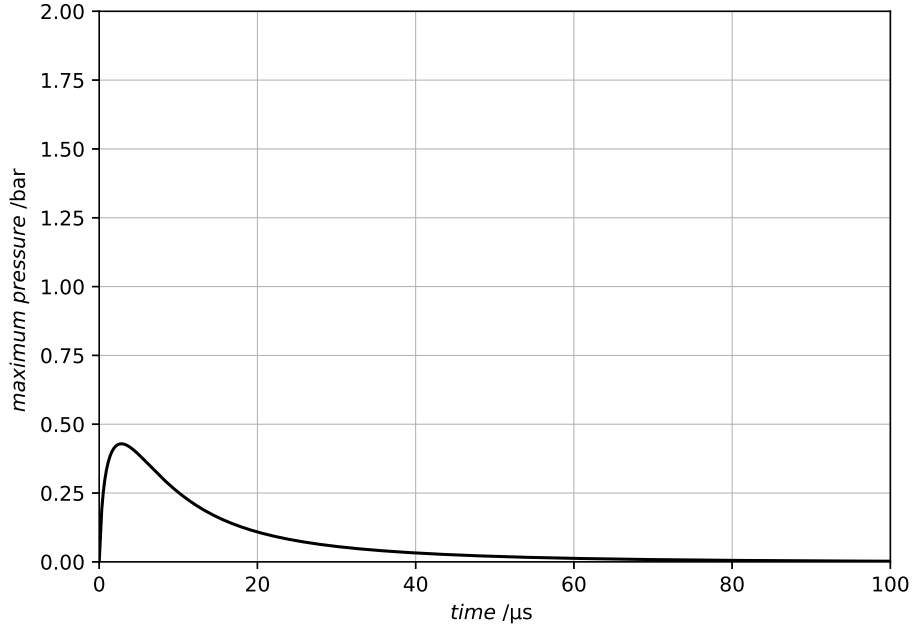


Figure 8.63: Maximum magnetic pressure evolution with time for 6/51 µs, 90 kA

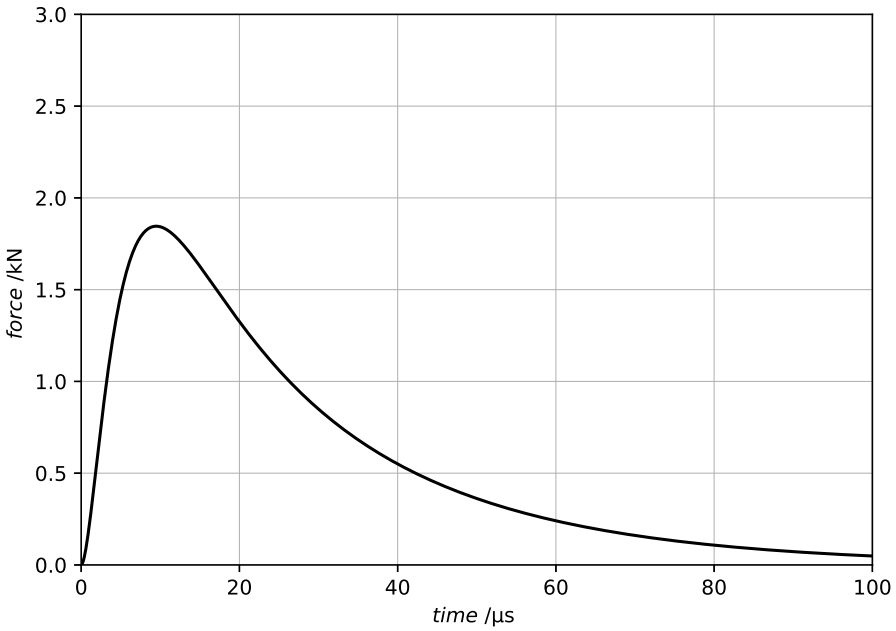


Figure 8.64: Force magnitude caused by magnetic forces as a function of time for 6/51 µs, 90 kA

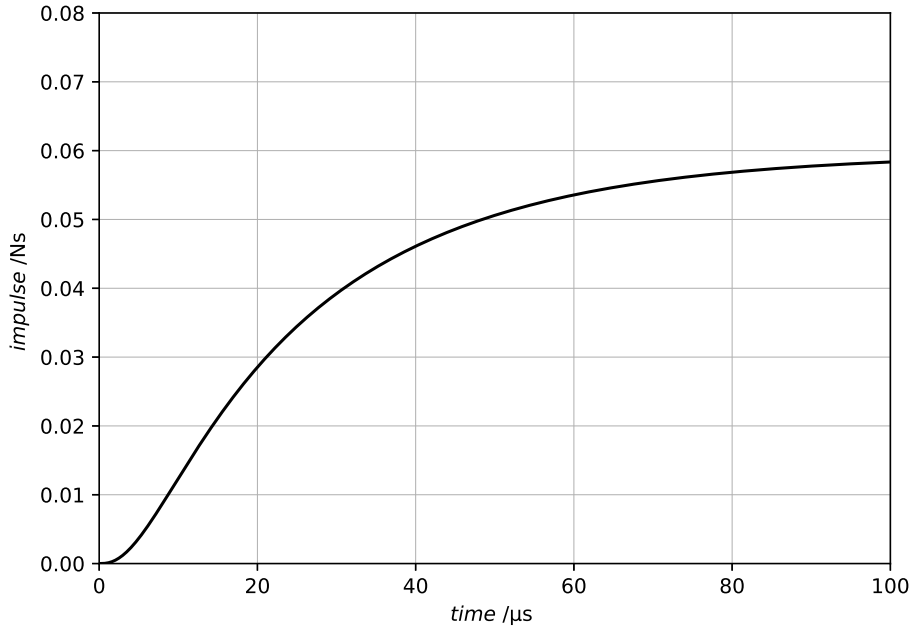
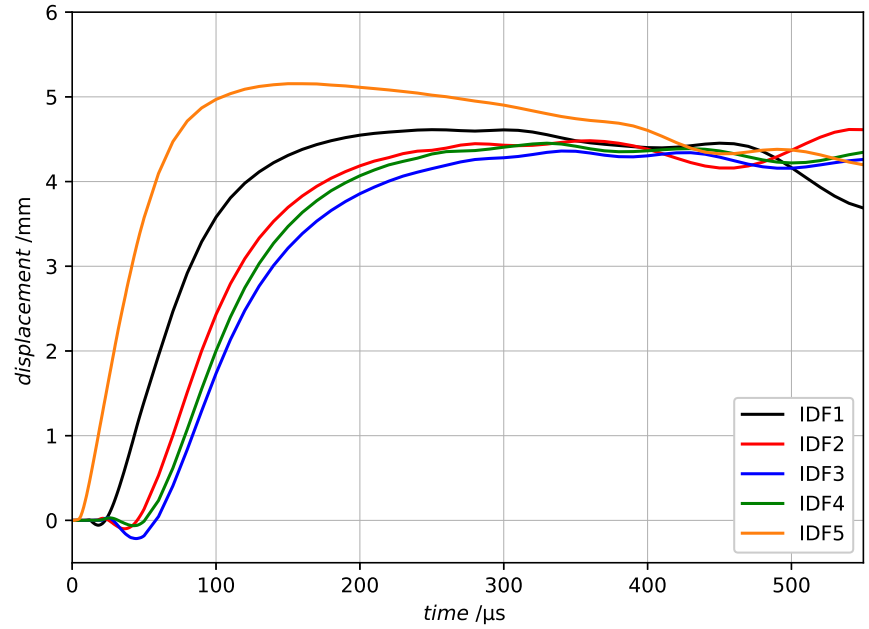
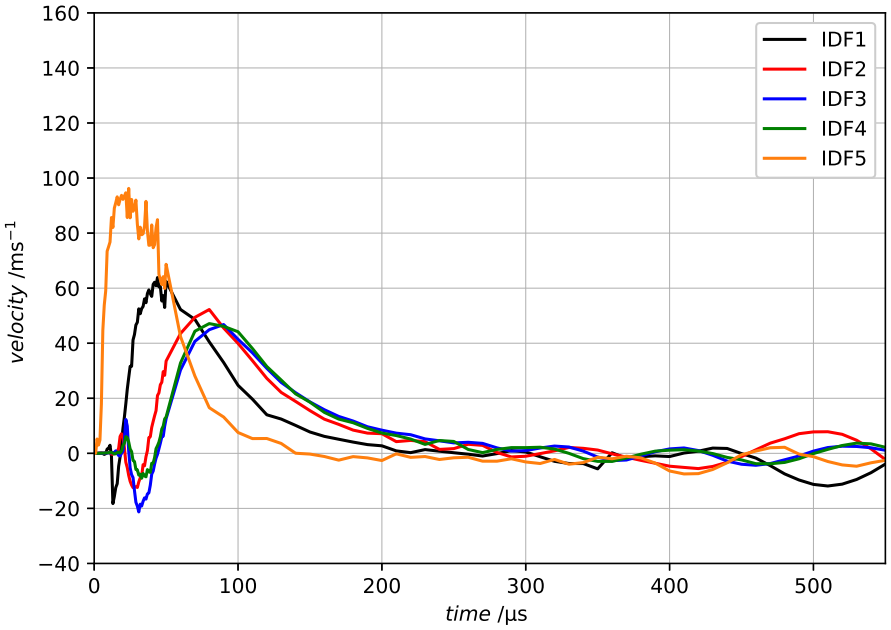


Figure 8.65: Impulse magnitude caused by magnetic forces as a function of time for 6/51 µs, 90 kA



(a) Displacement



(b) Velocity

Figure 8.66: Finite element predictions for 6/51 µs, 90 kA

8.8 Waveform 7/35 µs, 90 kA

The waveform 7/35 µs, 90 kA and the corresponding mechanical loads and mechanical deformation predictions are shown in Figure 8.67 to Figure 8.79 and from Table 8.16 to Table 8.18.

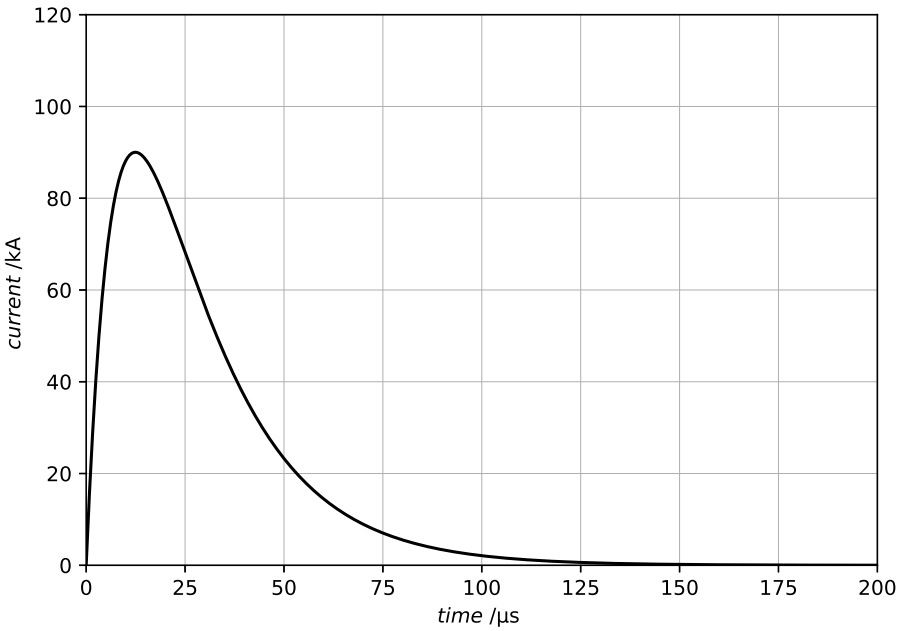


Figure 8.67: Double exponential for 7/35 µs, 90 kA

Table 8.16: Waveform parameters for 7/35 µs, 90 kA

a /s^{-1}	b /s^{-1}	A /-	I_{max} /kA
4.87×10^4	1.24×10^5	3.025	90

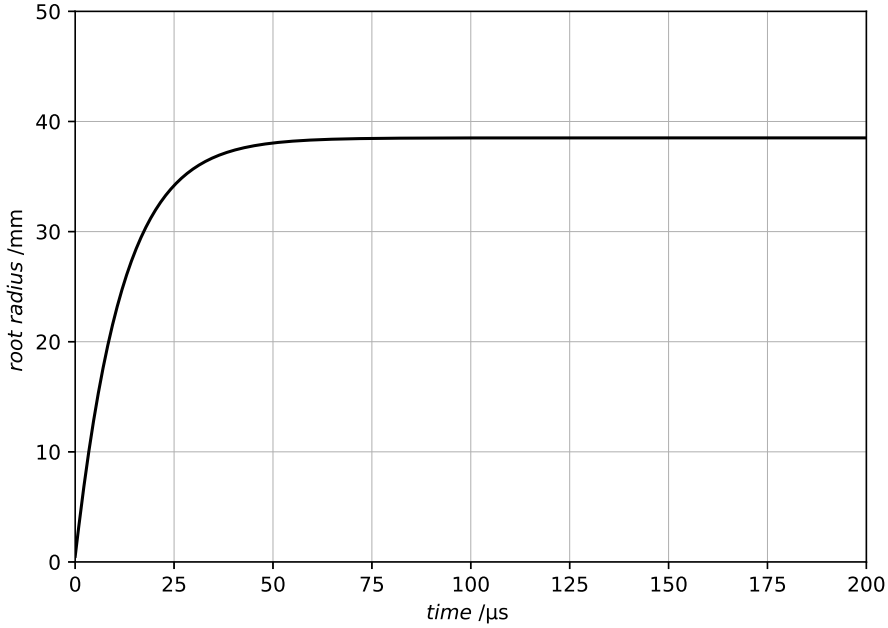


Figure 8.68: Root radius for 7/35 µs, 90 kA

Table 8.17: Root radius parameters for 7/35 µs, 90 kA

	c /mm	α /mm	β /mm	R_{R_0} /mm
ECF 73	38.01	1.0190	−0.0818	0.5

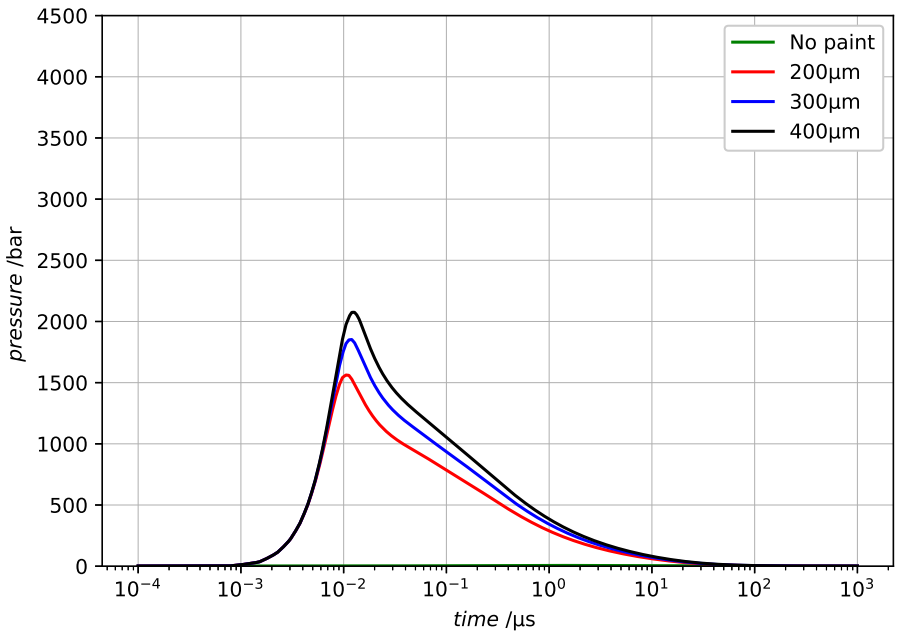


Figure 8.69: Overpressure caused by explosion of lightning protection layers as a function of time for 7/35 µs, 90 kA

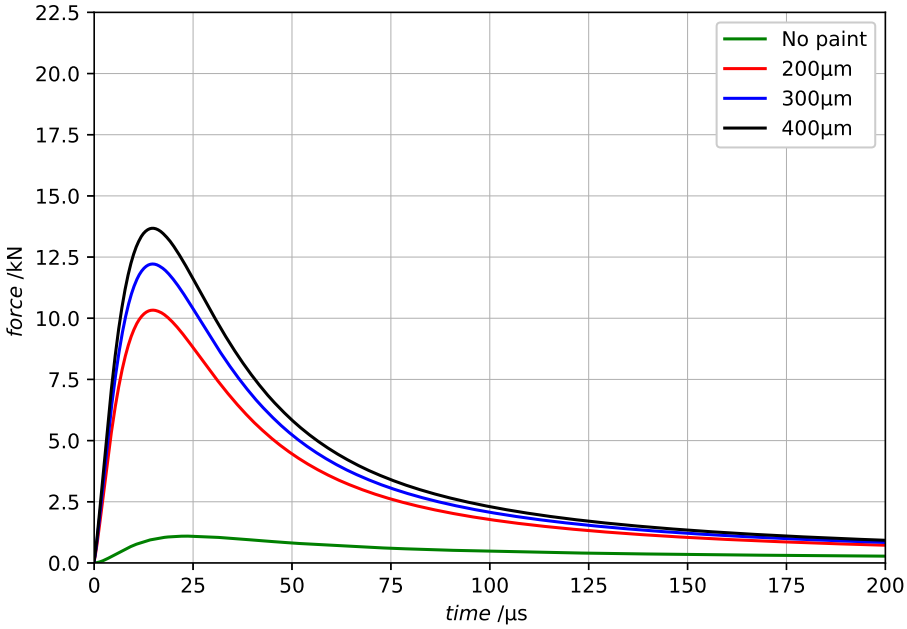


Figure 8.70: Force magnitude caused by explosion of lightning protection layers as a function of time for 7/35 µs, 90 kA

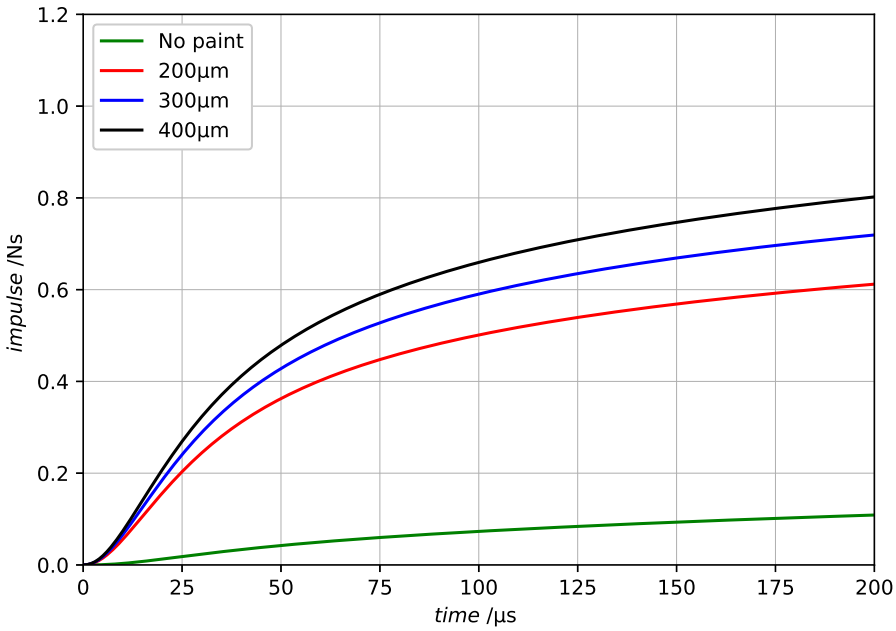


Figure 8.71: Impulse magnitude caused by explosion of lightning protection layers as a function of time for 7/35 µs, 90 kA

Table 8.18: Cylindrical shock wave parameters for 7/35 µs, 90 kA

α_s /mm $\mu s^{-1/2}$	α /bar μs	β /bar μs^{-1}
8.6170	94.3619	375.7242

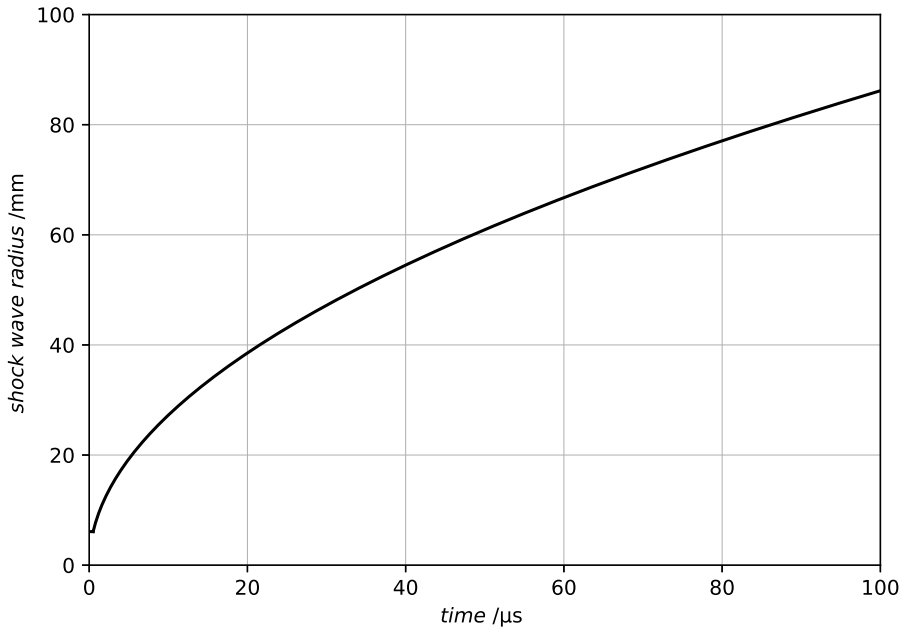


Figure 8.72: Computed shock radius for 7/35 µs, 90 kA

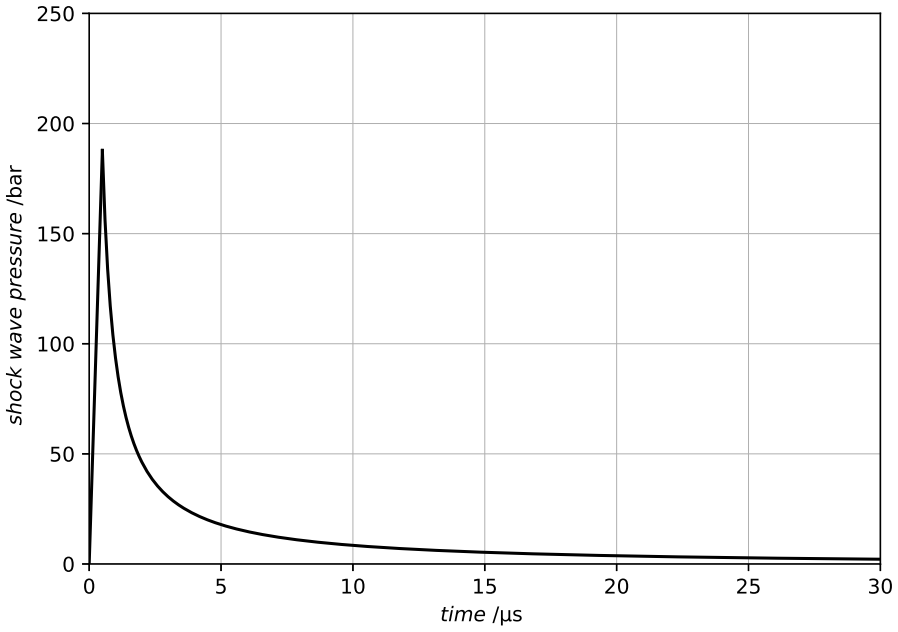


Figure 8.73: Mean cylindrical shock wave pressure as a function of time due to supersonic plasma expansion for 7/35 µs, 90 kA

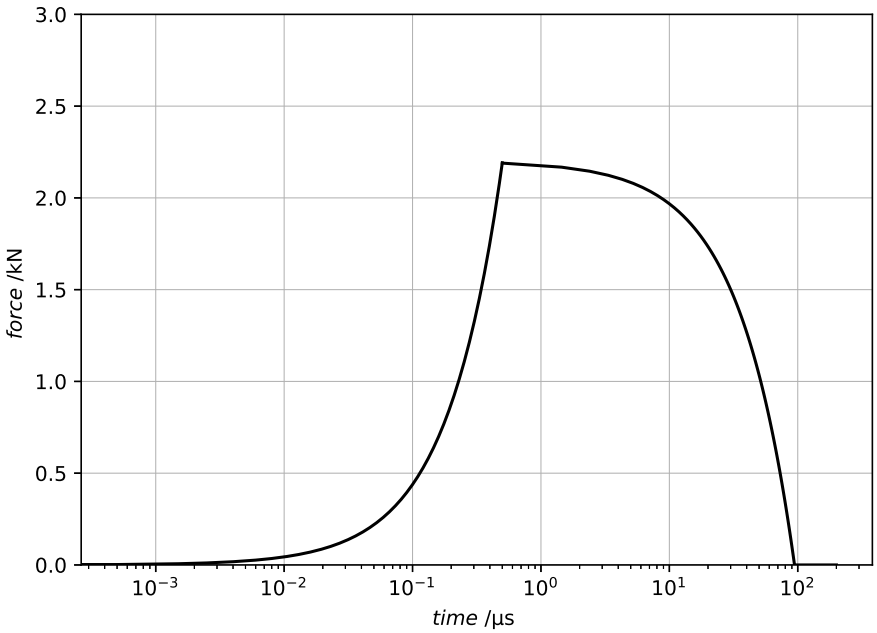


Figure 8.74: Force magnitude caused by supersonic plasma expansion as a function of time for 7/35 µs, 90 kA

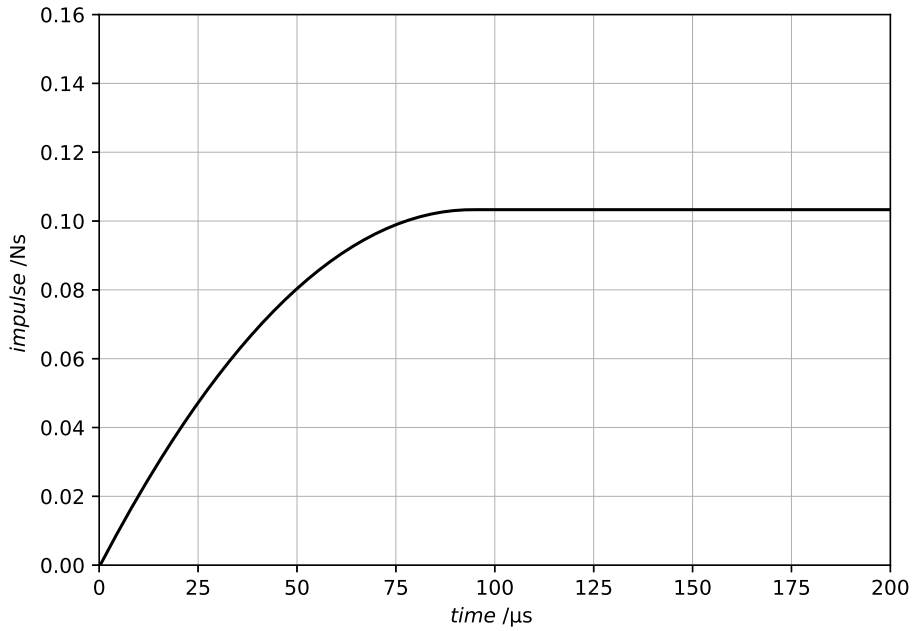


Figure 8.75: Impulse magnitude caused by supersonic plasma expansion as a function of time for 7/35 µs, 90 kA

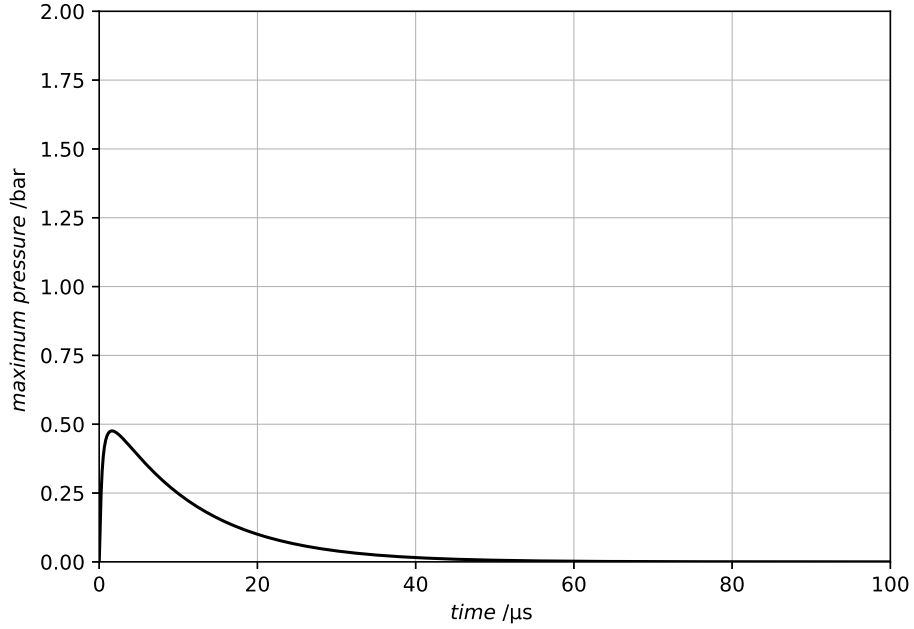


Figure 8.76: Maximum magnetic pressure evolution with time for 7/35 µs, 90 kA

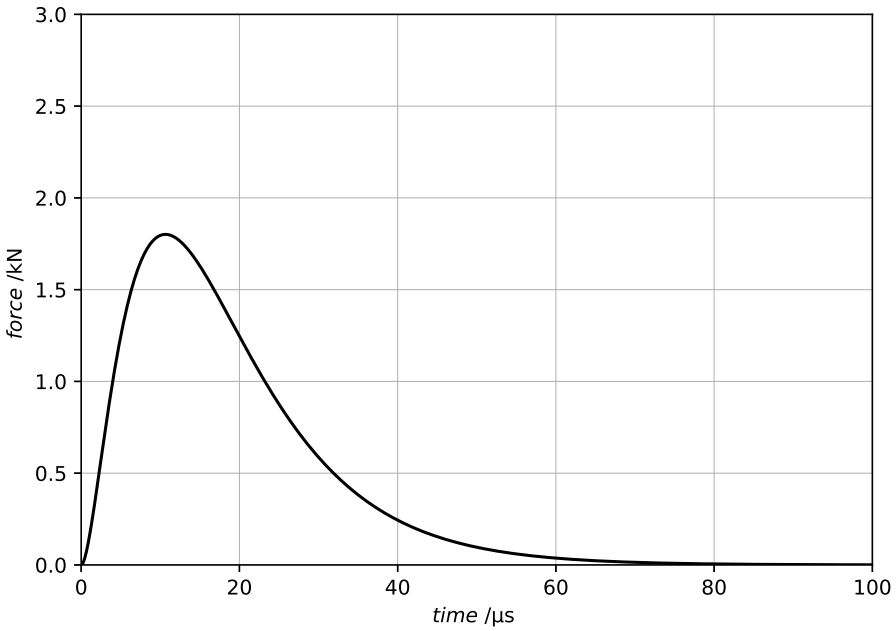


Figure 8.77: Force magnitude caused by magnetic forces as a function of time for 7/35 µs, 90 kA

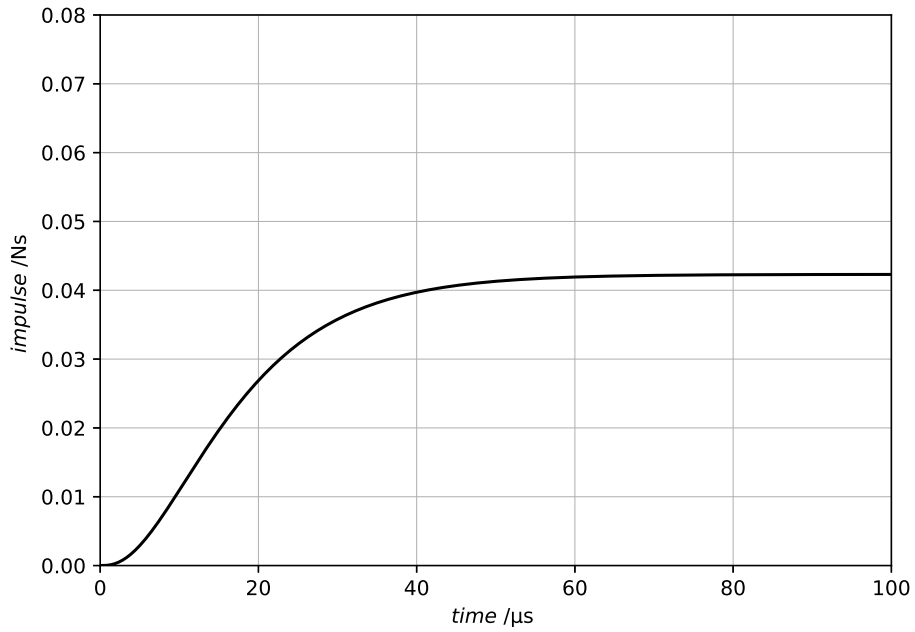
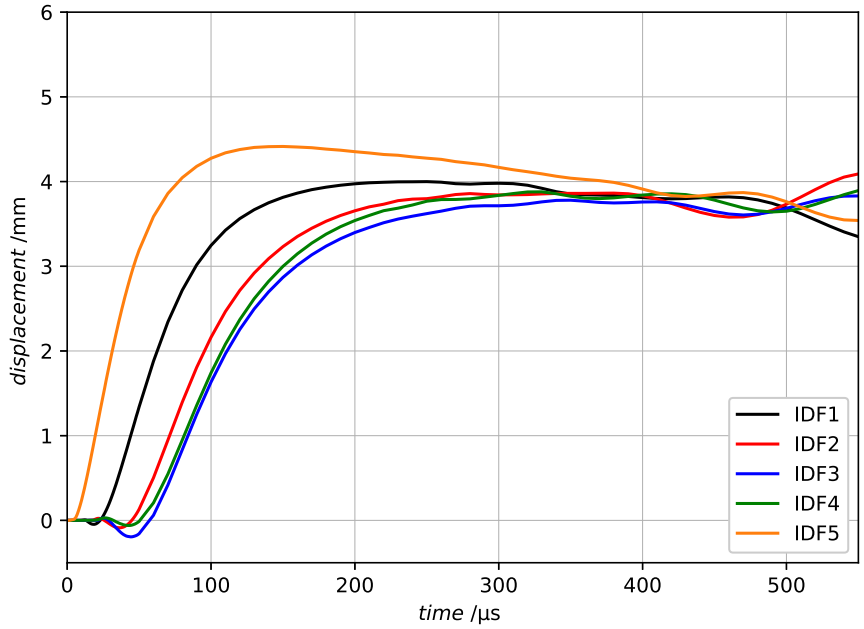
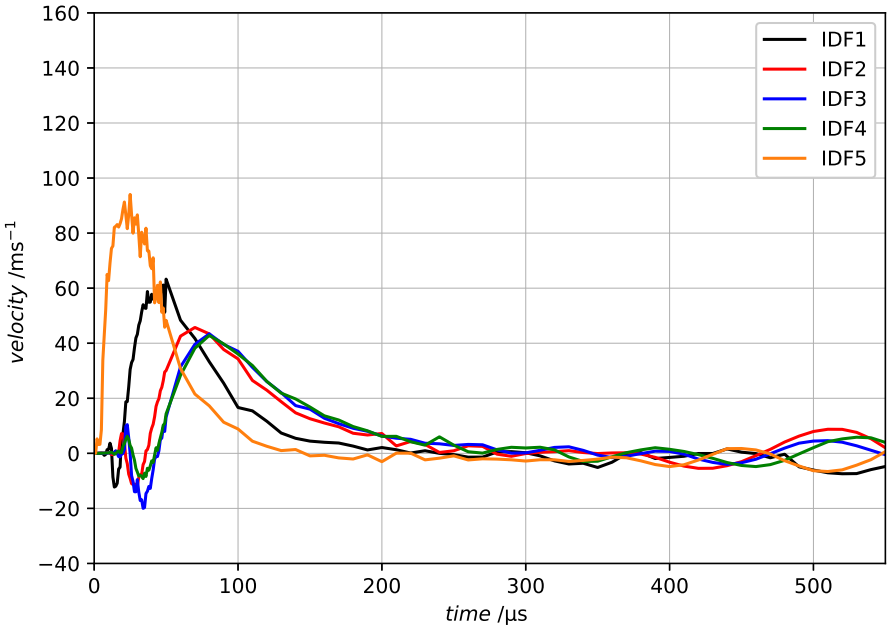


Figure 8.78: Impulse magnitude caused by magnetic forces as a function of time for 7/35 µs, 90 kA



(a) Displacement



(b) Velocity

Figure 8.79: Finite element predictions for 7/35 µs, 90 kA

8.9 Damage maps

Similarly to the analyses in previous chapters, a damage map assessment considering the damage variables in the longitudinal direction (d_1), transverse direction (d_2), shear (d_6) and delamination (d) is presented in Table 8.19 to Table 8.22. Note that for each damage variable, three different tables are presented, considering the following division of the waveforms, where (1) reflects the effect of the waveform shape, (2) the effect of action integral for maximum peak current, and (3) the effect of action integral for minimum peak current:

1. 26.8/48.5 µs, 96.4 kA
   1.42/44.3 µs, 96.4 kA
   3.18/34.5 µs, 100 kA

2. 26.8/48.5 µs, 96.4 kA
   4/34.3 µs, 110 kA
   5/23.6 µs, 110 kA

3. 26.8/48.5 µs, 96.4 kA
   6/51 µs, 90 kA
   7/35 µs, 90 kA

Table 8.19: Longitudinal damage induced by alternative waveforms within the range specified by the SAE ARP 5412 standard

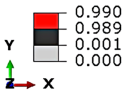
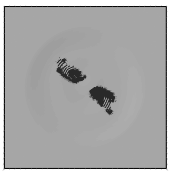
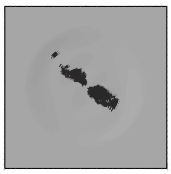
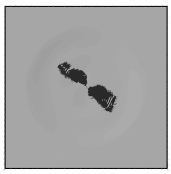
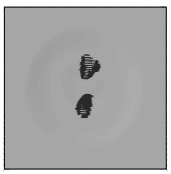
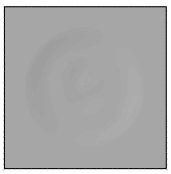
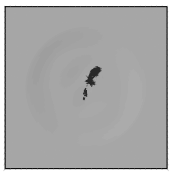
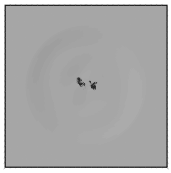
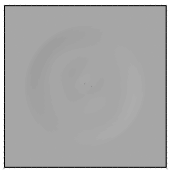
	26.8/48.5 µs, 96.4 kA	1.42/44.3 µs, 96.4 kA	3.18/34.5 µs, 100 kA
Layer 8			
Layer 7			
Layer 6			
Layer 4 and 5			
Layer 3			
Layer 2			
Layer 1			

Table 8.19: Longitudinal damage induced by alternative waveforms within the range specified by the SAE ARP 5412 standard

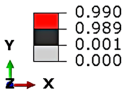
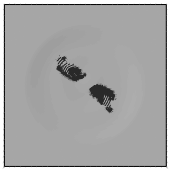
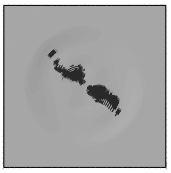
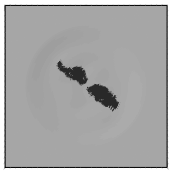
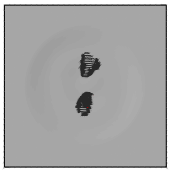
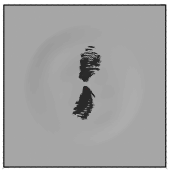
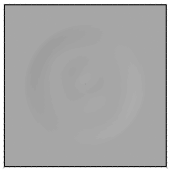
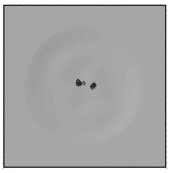
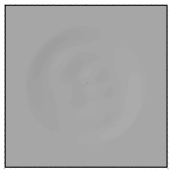
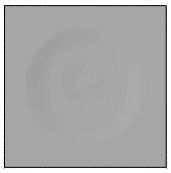
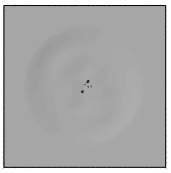
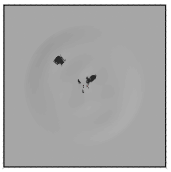
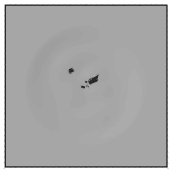
	26.8/48.5 µs, 96.4 kA	4/34.3 µs, 110 kA	5/23.6 µs, 110 kA
Layer 8			
Layer 7			
Layer 6			
Layer 4 and 5			
Layer 3			
Layer 2			
Layer 1			

Table 8.19: Longitudinal damage induced by alternative waveforms within the range specified by the SAE ARP 5412 standard

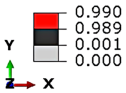
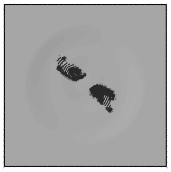
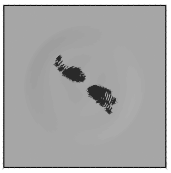
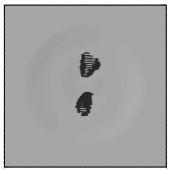
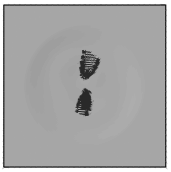
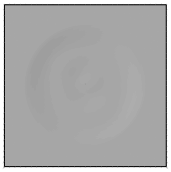
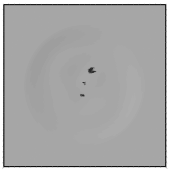
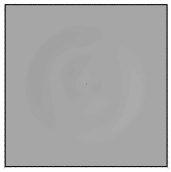
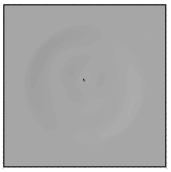
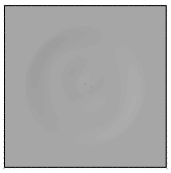
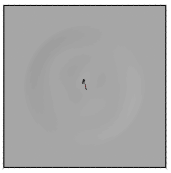
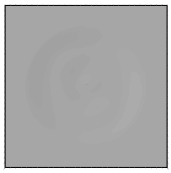
	26.8/48.5 µs, 96.4 kA	6/51 µs, 90 kA	7/35 µs, 90 kA
Layer 8			
Layer 7			
Layer 6			
Layer 4 and 5			
Layer 3			
Layer 2			
Layer 1			

Table 8.20: Transverse damage induced by alternative waveforms within the range specified by the SAE ARP 5412 standard

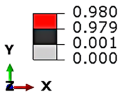
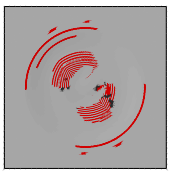
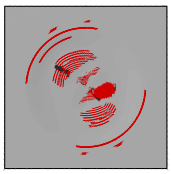
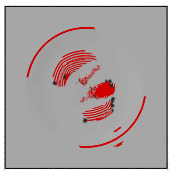
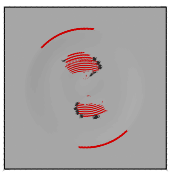
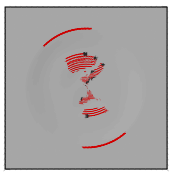
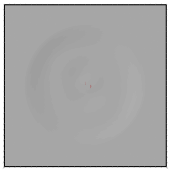
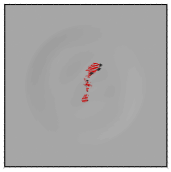
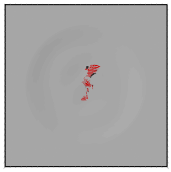
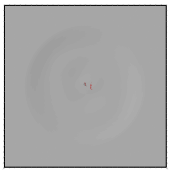
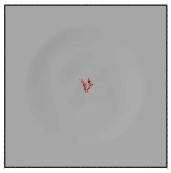
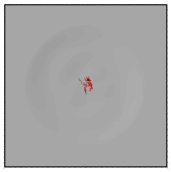
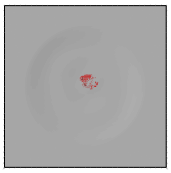
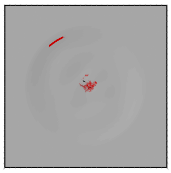
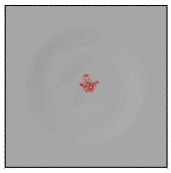
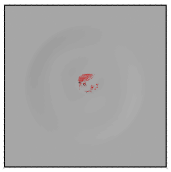
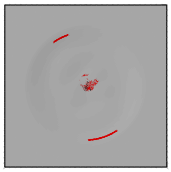
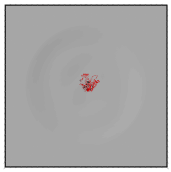
	26.8/48.5 µs, 96.4 kA	1.42/44.3 µs, 96.4 kA	3.18/34.5 µs, 100 kA
Layer 8			
Layer 7			
Layer 6			
Layer 4 and 5			
Layer 3			
Layer 2			
Layer 1			

Table 8.20: Transverse damage induced by alternative waveforms within the range specified by the SAE ARP 5412 standard

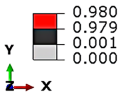
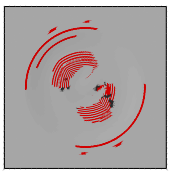
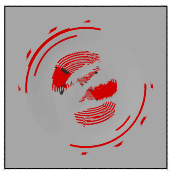
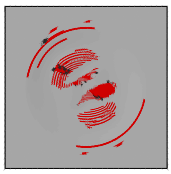
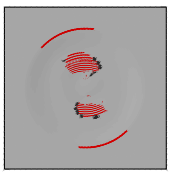
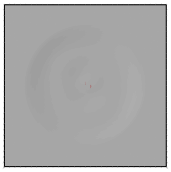
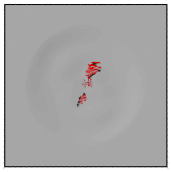
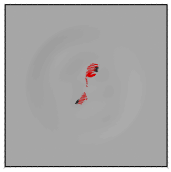
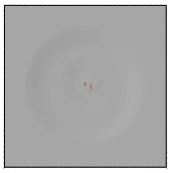
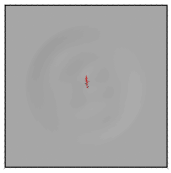
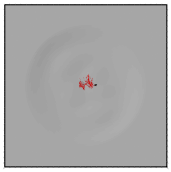
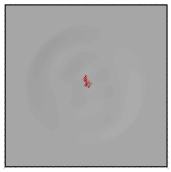
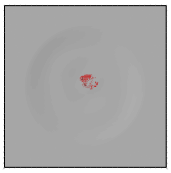
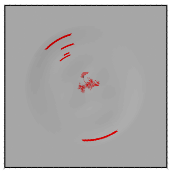
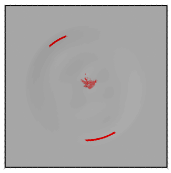
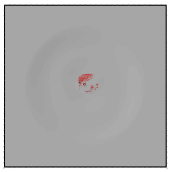
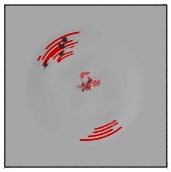
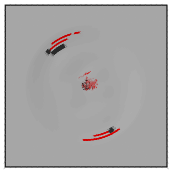
	26.8/48.5 µs, 96.4 kA	4/34.3 µs, 110 kA	5/23.6 µs, 110 kA
Layer 8			
Layer 7			
Layer 6			
Layer 4 and 5			
Layer 3			
Layer 2			
Layer 1			

Table 8.20: Transverse damage induced by alternative waveforms within the range specified by the SAE ARP 5412 standard

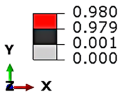
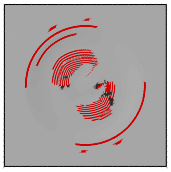
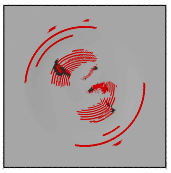
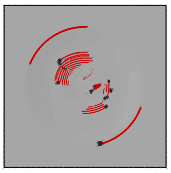
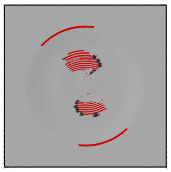
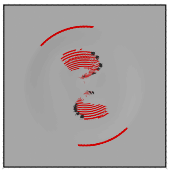
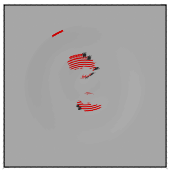
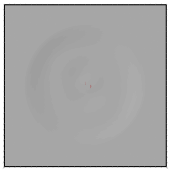
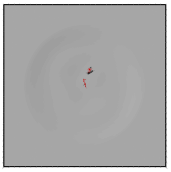
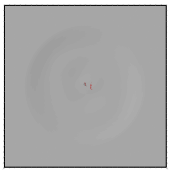
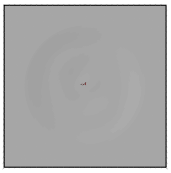
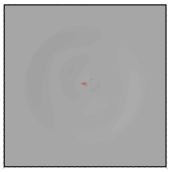
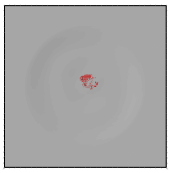
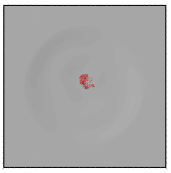
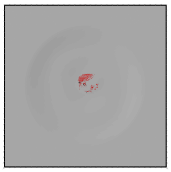
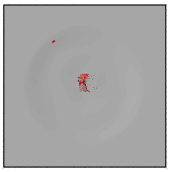
	26.8/48.5 µs, 96.4 kA	6/51 µs, 90 kA	7/35 µs, 90 kA
Layer 8			
Layer 7			
Layer 6			
Layer 4 and 5			
Layer 3			
Layer 2			
Layer 1			

Table 8.21: Shear damage induced by alternative waveforms within the range specified by the SAE ARP 5412 standard

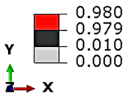
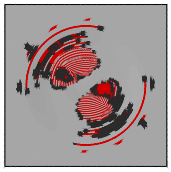
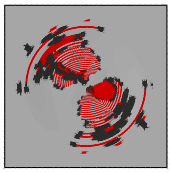
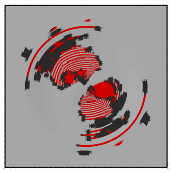
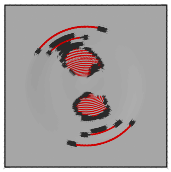
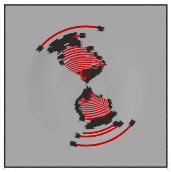
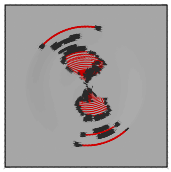
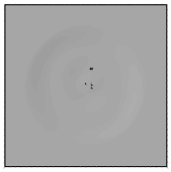
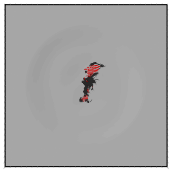
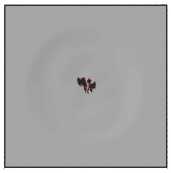
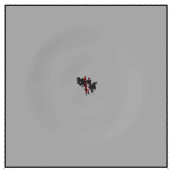
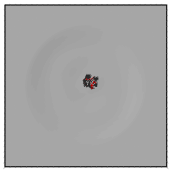
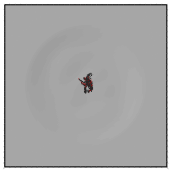
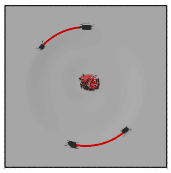
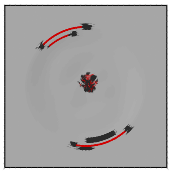
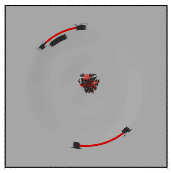
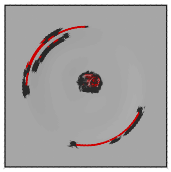
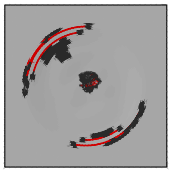
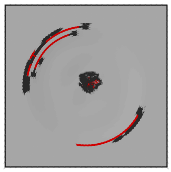
	26.8/48.5 µs, 96.4 kA	1.42/44.3 µs, 96.4 kA	3.18/34.5 µs, 100 kA
Layer 8			
Layer 7			
Layer 6			
Layer 4 and 5			
Layer 3			
Layer 2			
Layer 1			

Table 8.21: Shear damage induced by alternative waveforms within the range specified by the SAE ARP 5412 standard

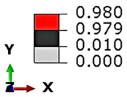
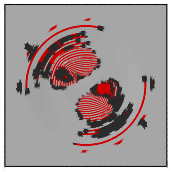
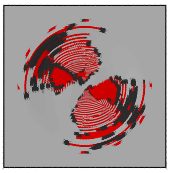
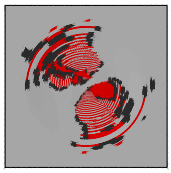
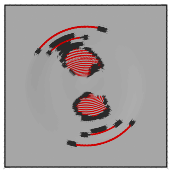
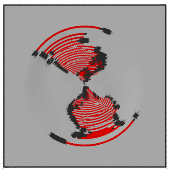
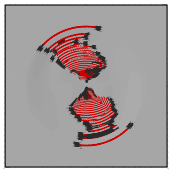
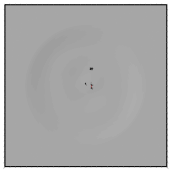
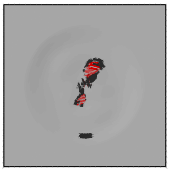
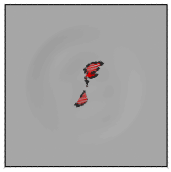
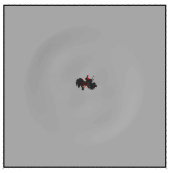
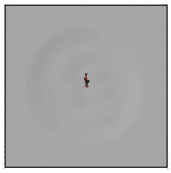
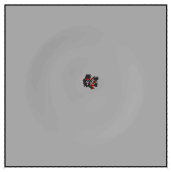
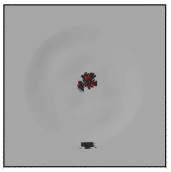
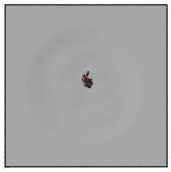
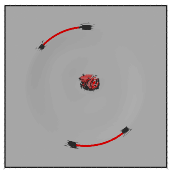
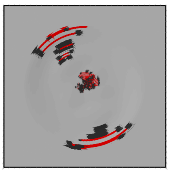
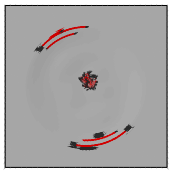
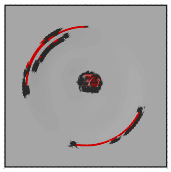
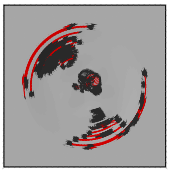
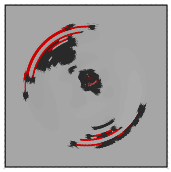
	26.8/48.5 µs, 96.4 kA	4/34.3 µs, 110 kA	5/23.6 µs, 110 kA
Layer 8			
Layer 7			
Layer 6			
Layer 4 and 5			
Layer 3			
Layer 2			
Layer 1			

Table 8.21: Shear damage induced by alternative waveforms within the range specified by the SAE ARP 5412 standard

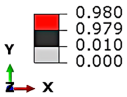
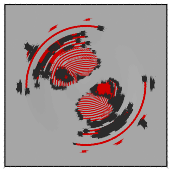
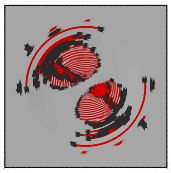
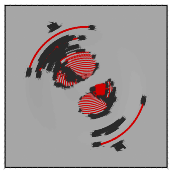
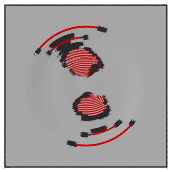
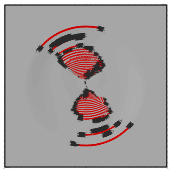
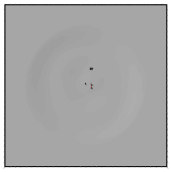
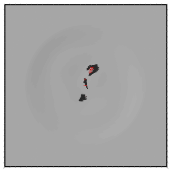
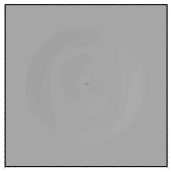
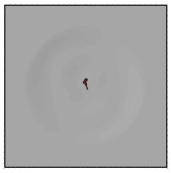
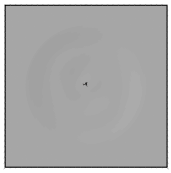
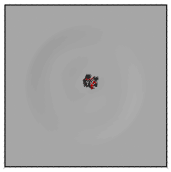
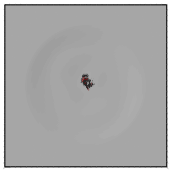
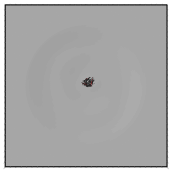
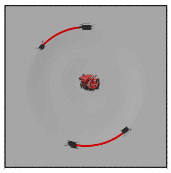
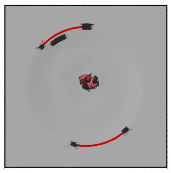
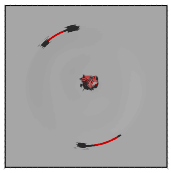
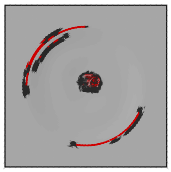
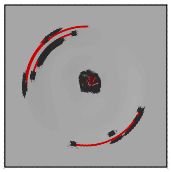
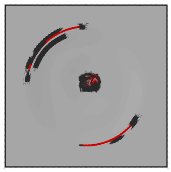
	26.8/48.5 µs, 96.4 kA	6/51 µs, 90 kA	7/35 µs, 90 kA
Layer 8			
Layer 7			
Layer 6			
Layer 4 and 5			
Layer 3			
Layer 2			
Layer 1			

Table 8.22: Delamination induced by alternative waveforms within the range specified by the SAE ARP 5412 standard

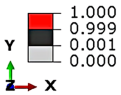
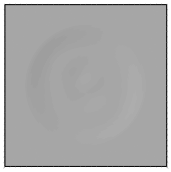
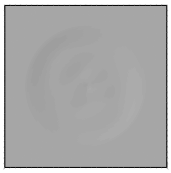
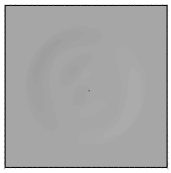
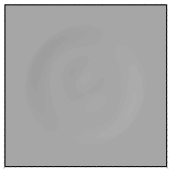
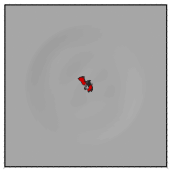
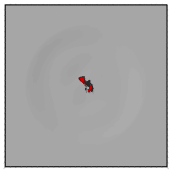
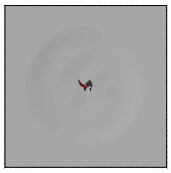
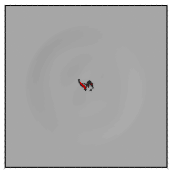
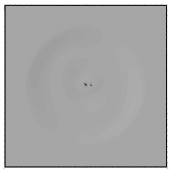
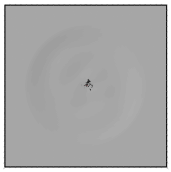
	26.8/48.5 µs, 96.4 kA	1.42/44.3 µs, 96.4 kA	3.18/34.5 µs, 100 kA
Layer 8			
Layer 7			
Layer 6			
Layer 4 and 5			
Layer 3			
Layer 2			
Layer 1			

Table 8.22: Delamination damage induced by alternative waveforms within the range specified by the SAE ARP 5412 standard

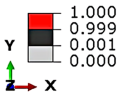
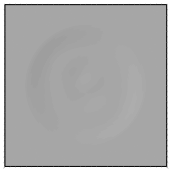
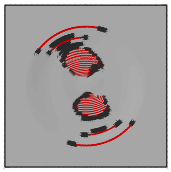
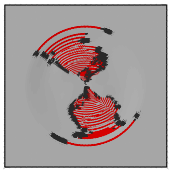
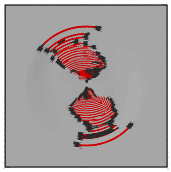
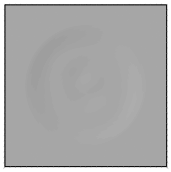
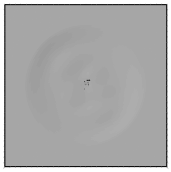
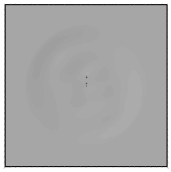
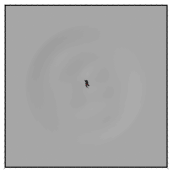
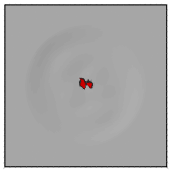
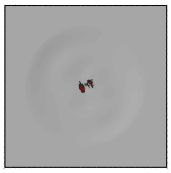
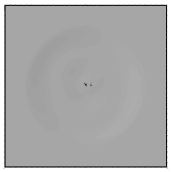
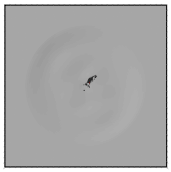
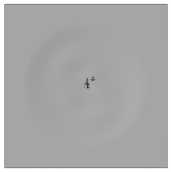
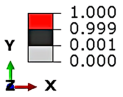
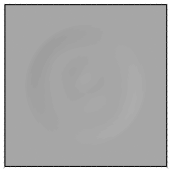
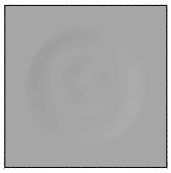
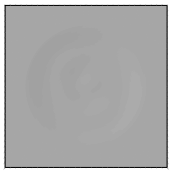
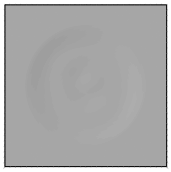
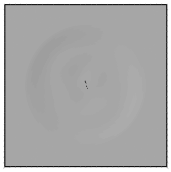
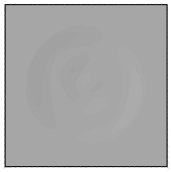
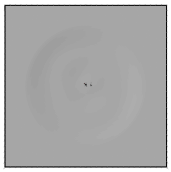
	26.8/48.5 µs, 96.4 kA	4/34.3 µs, 110 kA	5/23.6 µs, 110 kA
Layer 8			
Layer 7			
Layer 6			
Layer 4 and 5			
Layer 3			
Layer 2			
Layer 1			

Table 8.22: Delamination damage induced by alternative waveforms within the range specified by the SAE ARP 5412 standard

	26.8/48.5 µs, 96.4 kA	6/51 µs, 90 kA	7/35 µs, 90 kA
Layer 8			
Layer 7			
Layer 6			
Layer 4 and 5			
Layer 3			
Layer 2			
Layer 1			

8.10 Discussion

An important aspect to be noticed is that all the waveforms have a small time to peak ($t_1 \leq 7$), creating some divergences with the cases previously studied using a time to peak with a factor three times higher. Comparing the reference waveform 26/48.5 µs, 96.4 kA with the waveform 1.42/44.3 µs, 96.4 kA which have identical values of peak current and action integral, but distinct values of pressure magnitude, leading to different damage extent. Also the shape of the pressure caused by the explosion of the lightning protection layers show a more accentuated curve compared to cases with longer time to peak.

Considering the waveform 3.18/34.5 µs, 100 kA, which has the nominal values of peak current and action integral proposed by the ARP 5412 standard, it is possible to understand the average damage induced by a lightning strike. This is fundamental to help aircraft manufacturers and engineers for the design of structures susceptible of lightning strikes without causing significant structural damage that jeopardizes the physical integrity of the structure and service life.

Focusing in the waveforms with the maximum and minimum values of peak current and action integral, the trends already observed in Chapter 7 are confirmed. Correlating the waveforms based on the action integral values, it is possible to perceive the impact on the extent of damage. However, it is clear that the peak current is the most influencing lightning parameter on damage induced by lightning strikes.

8.11 Conclusion

This assessment provides an extensive analysis of the normative documentation, leading to the understanding of the divergences of the test domains. According to this evaluation, no several damage will be created by these deviations.

Complementary, this part of the study helps to understand the discrepancies imposed due to the distinct values of time to peak (t_1). Thus, not only the lightning parameters have impact on the damage produced, but the shape of the waveform alone could lead to different results.

Part VI

Conclusions and future work

Chapter 9

Conclusions and future work

The work presented in this thesis aimed at improving the understanding of the impact of lightning strike events on protected carbon-fibre reinforced composite plates. This chapter presents the main conclusions of the work carried out, and enumerates the topics that should be subject of future analysis and further development.

9.1 Conclusions

As the aeronautical industry moves towards hybrid experimental/numerical design and certification processes, the development of reliable models that accurately predict the main effects of lightning strikes in the context of damage tolerance criteria becomes crucial. Some aspects related to the impact induced by lightning strikes were numerically assessed. While models in the literature, either thermal-electrical or thermal-mechanical, have been validated solely in terms of the size and shape of the lightning-induced damage detected visually from the surface of the coupons or obtained by non-destructive inspection techniques (e.g., C-scan) the predictions of the mechanical response obtained with the model proposed in this work is validated against direct measurements of the out-of-plane velocity and displacement of coupons.

The following major conclusions can be drawn from this work

Strong shock wave approximation validation The strong shock wave approximation introduced to characterize the mechanical load generated by the rapid temperature rise of the lightning plasma channel was validated.
Three different EOS were implemented in a CFD simulation to determine the overpressure generated, and the finite element calculations compared with those using the analytical strong shock wave approximation, with equivalent predictions of the mechanical response and induced damage.

Paint thickness effect The effect of the thickness of the paint layer was evident. Thicker paint lead to more damage.

Waveform lightning parameters effect The influence of the lightning parameters, in particular peak current and action integral, was assessed. It is shown that higher values of peak current and action integral generated more damage.

Test domain of ARP 5412
An extensive and detailed study was carried out to explore the test domain recommended by the normative documentation used in the aeronautical industry. Some discrepancies were noted between the acceptable range of values of the peak current and action integral, however the safety of aerospace structures it is not questionable.

9.2 Future Work

In spite of the increasing number of publications exploring the lightning strike phenomenon, either focus in experimental data or numerical simulations, aircraft certification requires further investigations. With the aeronautical industry moving towards hybrid experimental/ numerical design and certification processes, the development of reliable models to predict the direct effects of lightning strikes demands, on one hand, developments in terms of capability and complexity of numerical models, and, on the other hand, a larger amount of open experimental data suitable for validation of these models.

Despite the advances presented in this study some considerations of future work include:

Sensitivity study of model parameters: Examples of these parameters are the initial arc root radius R_{R_0}, which has an expected acceptable range between 0.5 mm and 1 mm [20].
Another parameter is the parameter k introduced in the spatial distribution of the expanding plasma pressure (Equation 3.6), used to limit the pressure distribution mainly to the arc root area $\pi R_R(t)^2$.

Constitutive model: The most common composite structure for aircraft is carbon fibre reinforced plastics (CFRP) with epoxy matrix, i.e., a thermoset composite. However, in recent years researchers have been trying to increase the use of the thermoplastic composites in primary structures [91]. Thus, in order to develop the model proposed and cooperate with the industry, thermoplastic constitutive models can be employed. The use of numerical simulations can also support the progress in these composite materials.

Finite element model: In a real strike scenario, lightning will enter at a point and exit at a remote point, producing conditions where the current flows towards the exit point via the path of least resistance. Therefore, two clamped opposing edges (or a single clamped edge) may better represent the true physics for lightning strike interaction with aircraft composite panels for a real-world application [38]. This leads to the question that experimental boundary conditions in a laboratory cannot necessarily represent those in a real aircraft, so a study of different boundary conditions and their impact on the predictions of damage induced by lightning strikes can be performed.

Every small steps concerning the development of reliable models to predict damage by lightning strikes are crucial to the use of numerical simulations in aircraft certification. The ultimate step would be the development of a thermo-electro-mechanical coupled model.

References

[1] B. Farahmand, *Virtual testing and predictive modeling.* USA: TASS – Americas, a subsidiary of TASS Inc., 2009.

[2] A. Arteiro, "Technology development and structural mechanics of composites built of spread tow thin-ply technology," Master's thesis, University of Porto, 2012.

[3] I. Lapczyk and J. A. Hurtado, "Progressive damage modeling in fiber-reinforced materials," *Compos. Part A Appl. Sci. Manuf.*, vol. 38, no. 11, pp. 2333–2341, 2007.

[4] F. Soulas, C. Espinosa, F. Lachaud, S. Guinard, B. Lepetit, and I. Revel, "Equivalent impact set-up for lightning strike damage on composite coupons," *ICCM Int. Conf. Compos. Mater.*, vol. 2015-July, no. July, 2015.

[5] EUROCAE, "Technical Work Programme," 2022.

[6] V. Rakov and M. Uman, *Lightning: Physics and Effects.* Cambridge University Press, 2007.

[7] V. Cooray, *An introduction to lightning.* 2015.

[8] R. Martins, *Experimental and theoretical studies of lightning arcs and their interaction with aeronautical materials.* PhD thesis, Université Paris-Saclay,, 2016.

[9] R. D. Jones, C. and G. Odam, "Probabilities of catastrophe in lightning hazard assessments," tech. rep., 2001.

[10] F. Lago, "Lightning in aeronautics," *J. Phys. Conf. Ser.*, vol. 550, no. 1, 2014.

[11] F. A. Administration, "Federal Aviation Administration , DOT ARDS : TRANSPORT CATEGORY Subpart A — General," *Main*, no. 1, pp. 650–735, 2009.

[12] EASA, "CS-25 Certification Specifications and Acceptable Means of Compliance for Large Aeroplanes," no. November, 2011.

[13] J. L. Ludovic Noels, "Aircraft structures–certification," tech. rep., 2016.

[14] S. of Automotive Engineers, "ARP5412: Aircraft Lightning Environment and Related Test Waveforms," *Society*, vol. 7323, 2013.

[15] P. Feraboli and M. Miller, "Damage resistance and tolerance of carbon/epoxy composite coupons subjected to simulated lightning strike," *Compos. Part A Appl. Sci. Manuf.*, vol. 40, no. 6-7, pp. 954–967, 2009.

[16] F. Soulas, "Développement d'un modèle mécanique pour la prédiction des dommages de panneaux composites aéronautiques soumis à un choc foudre," 2016.

[17] G. Sweers, B. Birch, and J. Gokcen, "Lightning Strikes: Protection, Inspection and Repair," *Aero Q.*, vol. 4, no. 28, pp. 18–28, 2012.

[18] F. Nobis, "Modelling of lightning-induced damage in composite materials," Master's thesis, TU Dresden, 2017.

[19] B. Lepetit, C. Escure, S. Guinard, I. Revel, and G. Peres, "Thermo-mechanical effects induced by lightning on carbon fiber composite materials," *Int. Conf. Light. Static Electr.*, pp. 1–8, 2011.

[20] J. S. K. D. C. Karch, R. Honke, "Contributions of lightning current pulses to mechanical damage of cfrp structures," 2015.

[21] L. Chemartin, P. Lalande, B. Peyrou, A. Chazottes, P. Elias, C. Delalondre, B. Cheron, and F. Lago, "Direct Effects of Lightning on Aircraft Structure: Analysis of the Thermal, Electrical and Mechanical Constraints," *J. Aerosp. Lab*, no. 5, pp. 1–15, 2012.

[22] P. Aguilera, C. Lair, F. Issac, B. Michielsen, M. Hélier, and M. Darces, "Indirect effects of lightning on aircraft engine," *IET Semin. Dig.*, vol. 2015, no. 11, pp. 1–27, 2015.

[23] R. B. Neufeld, "Lightning direct effects on anisotropic materials from electro-thermal simulation," *IET Semin. Dig.*, vol. 2015, no. 11, pp. 1–5, 2015.

[24] Y. Hirano, S. Katsumata, Y. Iwahori, and A. Todoroki, "Artificial lightning testing on graphite/epoxy composite laminate," *Compos. Part A Appl. Sci. Manuf.*, vol. 41, no. 10, pp. 1461–1470, 2010.

[25] B. Lepetit, F. Soulas, S. Guinard, I. Revel, and G. Peres, "Analysis of composite panel damages due to a lightning strike: mechanical effects.," *Int. Conf. Light. Static Electr.*, pp. 1–8, 2013.

[26] A. Bigand and Y. Duval, "Quantification of the mechanical impact of lightning strike protection explosion confined by thick paint," pp. 1–7, 2017.

[27] P. K. Bollavaram, "Lightning strike protection and eletromagnetic interference shielding for composite structures using metallic submicrofilm and nanofilm," Master's thesis, School of Wichita State University, 2016.

[28] S. Kamiyama, Y. Hirano, T. Okada, and T. Ogasawara, "Lightning strike damage behavior of carbon fiber reinforced epoxy, bismaleimide, and polyetheretherketone composites," *Compos. Sci. Technol.*, vol. 161, no. April, pp. 107–114, 2018.

[29] C. Karch, M. Schreiner, R. Honke, and J. Wolfrum, "Shock waves from a lightning discharge," *34th Int. Conf. Light. Prot. ICLP 2018*, no. 1, 2018.

[30] Y. Li, R. Li, L. Lu, and X. Huang, "Experimental study of damage characteristics of carbon woven fabric/epoxy laminates subjected to lightning strike," *Compos. Part A Appl. Sci. Manuf.*, vol. 79, pp. 164–175, 2015.

[31] N. Hosokawa, T. Ooto, S. Kubo, M. Anzai, A. Yoshiya, and A. Nakagoshi, "Lightning strike protection for composite laminates by pitch-based carbon fiber skin," 2013.

[32] H. Kawakami, *Lightning strike induced damage mechanisms of carbon ber composites*. PhD thesis, University of Washington;, 2011.

[33] S. Yamashita, T. Sonehara, J. Takahashi, K. Kawabe, and T. Murakami, "Effect of thin-ply on damage behaviour of continuous and discontinuous carbon fibre reinforced thermoplastics subjected to simulated lightning strike," *Composites Part A: Applied Science and Manufacturing*, vol. 95, pp. 132–140, 2017.

[34] I. Y. S. K. W. T. H. Y. Mamizu H, Kuraishi A, "Lightning damage evaluation of composite laminates using direct measurements," *International Conference on Lightning and Static Electricity (ICOLSE 2017).*, pp. 175–191, 2017.

[35] Y. Li, R. Li, L. Huang, K. Wang, and X. Huang, "Effect of hygrothermal aging on the damage characteristics of carbon woven fabric/epoxy laminates subjected to simulated lightning strike," *Materials and Design*, vol. 99, 03 2016.

[36] G. V. D. Y. C. F. Murillo R, Flourens F, "Lightning strike protection of carbon composite skin. kinetic and signature of the damage.," *International Conference on Lightning and Static Electricity (ICOLSE 2017)*, 2017.

[37] A. Bigand, C. Espinosa, and J. M. Bauchire, "Equivalent mechanical load model methodology to simulate lightning strike impact on protected and painted composite structure," *Compos. Struct.*, vol. 280, no. September 2021, p. 114886, 2022.

[38] S. L. J. Millen and A. Murphy, "Modelling and analysis of simulated lightning strike tests : A review," *Compos. Struct.*, vol. 274, no. July, p. 114347, 2021.

[39] Y. Wang, "Multiphysics analysis of lightning strike damage in laminated carbon/glass fiber reinforced polymer matrix composite materials: A review of problem formulation and computational modeling," *Composites: Part A*, 2017.

[40] T. Ogasawara, Y. Hirano, and A. Yoshimura, "Coupled thermal–electrical analysis for carbon fiber/epoxy composites exposed to simulated lightning current," *Composites Part A: Applied Science and Manufacturing*, vol. 41, no. 8, pp. 973–981, 2010.

[41] P. Foster, G. Abdelal, and A. Murphy, "Understanding how arc attachment behaviour in fl uences the prediction of composite specimen thermal loading during an arti fi cial lightning strike test," *Compos. Struct.*, vol. 192, no. March, pp. 671–683, 2018.

[42] P. Foster, G. Abdelal, and A. Murphy, "Modelling of mechanical failure due to constrained thermal expansion at the lightning arc attachment point in carbon fibre epoxy composite material," *Engineering Failure Analysis*, vol. 94, pp. 364–378, 2018.

[43] C. Karch, A. Arteiro, and P. P. Camanho, "Modelling mechanical lightning loads in carbon fibre-reinforced polymers," *Int. J. Solids Struct.*, vol. 162, pp. 217–243, 2019.

[44] J. Sun, Y. Li, X. Tian, Y. Duan, X. Yao, and B. Wang, "Experimental and numerical analysis of damage mechanisms for carbon fiber-reinforced polymer composites subjected to lightning strikes," *Eng. Fail. Anal.*, vol. 118, no. September, p. 104894, 2020.

[45] S. L. J. Millen and A. Murphy, "Coupled Thermal-Mechanical Progressive Damage Model with Strain and Heating Rate Effects for Lightning Strike Damage Assessment," pp. 1437–1459, 2019.

[46] Q. Dong, G. Wan, L. Ping, Y. Guo, X. Yi, and Y. Jia, "Coupled thermal-mechanical damage model of laminated carbon fiber/resin composite subjected to lightning strike," *Composite Structures*, vol. 206, pp. 185–193, 2018.

[47] C. Karch and W. Wulbrand, "Thermo-Mechanical Damage of Protected Cfrp Structures," *Int. Conf. Light. Static Electr. USA*, no. October, 2013.

[48] F. Moupfouma, "Aircraft structure paint thickness and lightning swept stroke damages," *SAE International Journal of Aerospace*, vol. 6, pp. 392–398, 07 2013.

[49] A. Bigand, "Damage assessment on aircraft composite structure due to lightning constraints," 2020.

[50] I. The MathWorks, *Curve Fitting Toolbox*. Natick, Massachusetts, United State, 2020.

[51] R. Landfried, T. Leblanc, R. Andlauer, and P. Teste, "Surface temperature measurement of a copper anode submitted to a non-stationary electric arc in air. contribution to the assessment of the power balance," *European Physical Journal Applied Physics*, vol. 56, pp. 30801–, 12 2011.

[52] S. Haigh, "Impulse effects during simulated lightning attachments to lightweight composite panels," in *International Conference on Lightning and Static Electricity, Paris*, 2007.

[53] R. Fabbro, J. Fournier, P. Ballard, D. Devaux, and J. Virmont, "Physical study of laser-produced plasma in confined geometry," *J. Appl. Phys.*, vol. 68, no. 2, pp. 775–784, 1990.

[54] HILL RD, "Channel heating in return- stroke lightning," *J Geophys Res*, vol. 76, no. 3, pp. 637–645, 1971.

[55] Shao-Chi Lin, "Cylindrical Shock Waves Produced by Instantaneous Energy Release," *Applied physics*, 1954.

[56] A. H. Paxton, R. L. Gardner, and L. Baker, "Lightning return stroke. A numerical calculation of the optical radiation," *Phys. Fluids*, vol. 29, no. 8, p. 2736, 1986.

[57] C. Karch and W. Wulbrand, "Lightning direct effects–magnetic forces," *EADS IW Report, CTO/IW-SE-2010-067*, 2010.

[58] C. Furtado, G. Catalanotti, A. Arteiro, P. J. Gray, B. L. Wardle, and P. P. Camanho, "Simulation of failure in laminated polymer composites: Building-block validation," *Compos. Struct.*, vol. 226, p. 111168, 2019.

[59] P. Maimí, P. P. Camanho, J. A. Mayugo, and C. G. Dávila, "A continuum damage model for composite laminates: Part I - Constitutive model," *Mech. Mater.*, vol. 39, no. 10, pp. 897–908, 2007.

[60] P. Maimí, P. P. Camanho, J. A. Mayugo, and C. G. Dávila, "A continuum damage model for composite laminates: Part II - Computational implementation and validation," *Mech. Mater.*, vol. 39, no. 10, pp. 909–919, 2007.

[61] P. P. Camanho, C. G. Dávila, S. T. Pinho, L. Iannucci, and P. Robinson, "Prediction of in situ strengths and matrix cracking in composites under transverse tension and in-plane shear," *Composites Part A: Applied Science and Manufacturing*, vol. 37, no. 2, pp. 165–176, 2006. CompTest 2004.

[62] Abaqus, *ABAQUS/Standard User's Manual, Version 6.14*. United States: Dassault Systèmes Simulia Corp, 2014.

[63] P. Camanho, A. Arteiro, A. Melro, G. Catalanotti, and M. Vogler, "Three-dimensional invariant-based failure criteria for fibre-reinforced composites," *International Journal of Solids and Structures*, vol. 55, pp. 92–107, 2015.

[64] Z. Bažant and B. Oh, "Crack band theory for fracture of concrete," *Materiaux et constructions*, vol. 16, pp. 155–177, May 1983.

[65] P. Maimí, *Modelización constitutiva y computacional del daño y la fractura de materiales compuestos*. PhD thesis, Universitat de Girona, Catalunya, Spain, 2007.

[66] C. G. Dá, P. P. Camanho, and C. A. Rose, "Failure criteria for FRP laminates," *J. Compos. Mater.*, vol. 39, no. 4, pp. 323–345, 2005.

[67] P. Moran, X. Liu, and C. Shih, "Kink band formation and band broadening in fiber composites under compressive loading," *Acta Metallurgica et Materialia*, vol. 43, no. 8, pp. 2943–2958, 1995.

[68] M. Benzeggagh and M. Kenane, "Measurement of mixed-mode delamination fracture toughness of unidirectional glass/epoxy composites with mixed-mode bending apparatus," *Composites Science and Technology*, vol. 56, no. 4, pp. 439–449, 1996.

[69] A. Turon, P. Camanho, J. Costa, and J. Renart, "Accurate simulation of delamination growth under mixed-mode loading using cohesive elements: Definition of interlaminar strengths and elastic stiffness," *Composite Structures*, vol. 92, no. 8, pp. 1857–1864, 2010.

[70] "blastFoam: A solver for compressible multi-fluid flow with application to high-explosive detonation," 2019.

[71] C. Greenshields, *OpenFOAM v10 User Guide*. London, UK: The OpenFOAM Foundation, 2022.

[72] C. K. Robert Honke, "Shock waves from a lightning discharge," *International Conference on Lightning and Static Electricity (ICOLSE 2022)*, 2022.

[73] E. F. Toro, M. Spruce, and W. Speares, "Restoration of the contact surface in the HLL-Riemann solver," *Shock Waves*, vol. 4, no. 1, pp. 25–34, 1994.

[74] E. F. Toro, *Riemann Solvers and Numerical Methods for Fluid Dynamics*. 2009.

[75] M. Plooster, "Shock Waves from Line Sources ," *Shock*, no. NCAR-TN-37, p. 80, 1968.

[76] L. R. Doan and G. H. Nickel, "A subroutine for the equation of state of air," 1963.

[77] M. N. Plooster, "Shock waves from line sources. Numerical solutions and experimental measurements," *Phys. Fluids*, vol. 13, no. 11, pp. 2665–2675, 1970.

[78] M. N. Plooster, "Numerical model of the return stroke of the lightning discharge," *Phys. Fluids*, vol. 14, no. 10, pp. 2124–2133, 1971.

[79] F. F. Tristant F, "Lightning direct effects degradation of composite material depending on paint thickness.," in *Proceedings of ICOLSE 2017*, 2017.

[80] AIRBUS, "Aims 04-04-014 - airbus industrie material specification - external paint system: Primer+intermediate coat+top coat material specification.,"

[81] "Paints and varnishes — cross-cut test," standard, International Organization for Standardization, 2020.

[82] "Paints and varnishes – rapid-deformation (impact resistance) tests – part 1: Falling-weight test, large-area indenter," standard, International Organization for Standardization, 2011.

[83] "Paints and varnishes – determination of scratch resistance – part 1: Constant-loading method," standard, International Organization for Standardization, 2019.

[84] "Paints and varnishes — bend test (cylindrical mandrel)," standard, International Organization for Standardization, 2011.

[85] Y. Guo, Y. Xu, Q. Wang, Q. Dong, X. Yi, and Y. Jia, "Enhanced lightning strike protection of carbon fiber composites using expanded foils with anisotropic electrical conductivity," *Compos. Part A Appl. Sci. Manuf.*, vol. 117, no. 17923, pp. 211–218, 2019.

[86] V. Kumar, T. Yokozeki, C. Karch, A. A. Hassen, C. J. Hershey, S. Kim, J. M. Lindahl, A. Barnes, Y. K. Bandari, and V. Kunc, "Factors affecting direct lightning strike damage to fiber reinforced composites: A review," *Compos. Part B Eng.*, vol. 183, pp. 1–47, 2020.

[87] G. V. D. Y. C. F. Murillo R, Flourens F, "Lightning strike protection of carbon composite skin. kinetic and signature of the damage.," *International Conference on Lightning and Static Electricity.*, 2005.

[88] F. Lago, "Measurements by stereo correlation of the deflexion of panels submitted to lightning pulse currents," *International Conference on Lightning and Static Electricity (ICOLSE 2011)*, 2011.

[89] C. Espinosa, T. Montel, J. Montes Pons, F. Lachaud, and F. Soulas, "A numerical study of the pressure applied on CFRP panels during a lightning strike using a coupled electro-thermal-mechanical model," in *ICOLSE 2017 International Conference on Lightning and Static Electricity, 13-15 sept. 2017, Nagoya (J)*, 2017.

[90] G. Van Rossum and F. L. Drake Jr, *Python reference manual*. Centrum voor Wiskunde en Informatica Amsterdam, 1995.

[91] N. H. R. S. K. M. M. B. U. V. M. H. M. T. S. K. A. A. H. V. K. Vipin Kumar, Pritesh S. Yeole, "Internal arcing and lightning strike damage in short carbon fiber reinforced thermoplastic composites," 2020.

[92] C. Karch, A. Arteiro, F. Nobis, Y. Duval, and J. Wolfrum, "Modelling and Simulation of Lightning- Induced Damage of CFRP Structures Modelling and Simulation of Lightning-Induced Damage of CFRP Structures," *2017 Int. Conf. Light. Static Electr.*, no. September, pp. 1–8, 2017.

[93] HILL RD, "Channel heating in return- stroke lightning," *J Geophys Res*, vol. 76, no. 3, pp. 637–645, 1971.

[94] S. Kamiyama, Y. Hirano, T. Okada, and T. Ogasawara, "Lightning strike damage behavior of carbon fiber reinforced epoxy, bismaleimide, and polyetheretherketone composites," *Compos. Sci. Technol.*, vol. 161, no. April, pp. 107–114, 2018.

[95] Barker L.M., "Laser interferometry in shock- wave research," *ASME, New Mex. Sec Univ New Mex. Proc 11th Annu Symp Exp Mech, Albuquerque, NMex*, pp. 121–133, 1971.

[96] P. Aguilera, C. Lair, F. Issac, B. Michielsen, M. Hélier, and M. Darces, "Indirect effects of lightning on aircraft engine," *IET Semin. Dig.*, vol. 2015, no. 11, pp. 1–27, 2015.

[97] V. Buljak and G. Ranzi, *Constitutive Modeling of Engineering Materials: Theory, Computer Implementation, and Parameter Identification.* 2021.

[98] G. Goyer and M. N. Plooster, "Shock wave from lightning discharge," 1968.

[99] D. Morgan, C. J. Hardwick, S. J. Haigh, and a. J. Meakins, "The Interaction of Lightning with Aircraft and the Challenges of Lightning Testing," *J. Aerosp. Lab*, no. 5, pp. 1–10, 2012.

[100] C. Karch, "Micromechanical Analysis of Thermal Expansion Coefficients," *Model. Numer. Simul. Mater. Sci.*, vol. 04, no. 03, pp. 104–118, 2014.

[101] S. S. A. Kumar, "Incorporation of graphene thin films into the carbon fiber reinforced composite via 3d composite concept against the lightning strikes on composite aircraft," *Dep. Mech. Eng.*, vol. Master of, no. December, p. 146, 2011.

[102] B. Alemour, H. N. Lim, M. H. Yaacob, O. Badran, and M. Roshdi Hassan, "Improving the electrical conductivity of carbon fiber reinforced epoxy composite using reduced graphene oxide," *Mater. Res. Express*, vol. 6, no. 6, 2019.

[103] S. Das and T. Yokozeki, "A brief review of modified conductive carbon/glass fibre reinforced composites for structural applications: Lightning strike protection, electromagnetic shielding, and strain sensing," *Compos. Part C Open Access*, vol. 5, no. May, p. 100162, 2021.

[104] G. Gardiner, "Lightning strike protection for composite structures," *High-Performance Compos.*, vol. 14, no. 4, pp. 44–50, 2006.

[105] J. Gou, Y. Tang, F. Liang, Z. Zhao, D. Firsich, and J. Fielding, "Carbon nanofiber paper for lightning strike protection of composite materials," *Compos. Part B Eng.*, vol. 41, no. 2, pp. 192–198, 2010.

[106] Y. Hirano, T. Yokozeki, Y. Ishida, T. Goto, T. Takahashi, D. Qian, S. Ito, T. Ogasawara, and M. Ishibashi, "Lightning damage suppression in a carbon fiber-reinforced polymer with a polyaniline-based conductive thermoset matrix," *Compos. Sci. Technol.*, vol. 127, pp. 1–7, 2016.

[107] K. Jagannadham, "Electrical conductivity of copper–graphene composite films synthesized by electrochemical deposition with exfoliated graphene platelets," *J. Vac. Sci. Technol. B, Nanotechnol. Microelectron. Mater. Process. Meas. Phenom.*, vol. 30, no. 3, p. 03D109, 2012.

[108] F. Wang, Y. Wu, W. Huang, Y. Li, and Z. Li, "Thermal-damage suppression of composite material by anti-lightning NCF/CIPCF film," *Compos. Sci. Technol.*, vol. 227, no. May, p. 109604, 2022.

[109] B. Zhang, V. R. Patlolla, D. Chiao, D. K. Kalla, H. Misak, and R. Asmatulu, "Galvanic corrosion of Al/Cu meshes with carbon fibers and graphene and ITO-based nanocomposite coatings as alternative approaches for lightning strikes," *Int. J. Adv. Manuf. Technol.*, vol. 67, no. 5-8, pp. 1317–1323, 2013.

[110] H. Zhu, K. Fu, B. Yang, and Y. Li, "Nickel-coated nylon sandwich film for combination of lightning strike protection and electromagnetic interference shielding of CFRP composite," *Compos. Sci. Technol.*, vol. 207, no. August 2020, p. 108675, 2021.

[111] O. Vryonis, T. Andritsch, A. S. Vaughan, and P. L. Lewin, "Improved lightning protection of carbon fiber reinforced polymer wind turbine blades: Epoxy/graphene oxide nanocomposites," *Annu. Rep. - Conf. Electr. Insul. Dielectr. Phenomena, CEIDP*, vol. 2016-December, pp. 635–638, 2016.

[112] M. Khalil, N. Abuelfoutouh, G. Abdelal, and A. Murphy, "Numerical Simulation of Lightning Strike Direct Effects on Aircraft Skin Composite Laminate," *World Acad. Sci. Eng. Technol. Int. J. Archit. Environ. Eng*, vol. 12, no. 2, pp. 160–173, 2018.

[113] J. Morgan, "Thermal Simulation and Testing of Expanded Metal Foils Used for Lightning Protection of Composite Aircraft Structures," *SAE Int. J. Aerosp.*, vol. 6, no. 2, pp. 371–377, 2013.

[114] R. E. Orville, J. H. Helsdon, and W. H. Evans, "Quantitative analysis of a lightning return stroke for diameter and luminosity changes as a function of space and time," *J. Geophys. Res.*, vol. 79, no. 27, pp. 4059–4067, 1974.

[115] T. Sonehara, H. Kusano, N. Tokuoka, and Y. Hirano, "Visualization of lightning impulse current discharge on CFRP laminate," *2014 Int. Conf. Light. Prot. ICLP 2014*, vol. 4, pp. 835–839, 2014.

[116] J. Sun, X. Yao, X. Tian, J. Chen, and Y. Wu, "Damage Characteristics of CFRP Laminates Subjected to Multiple Lightning Current Strike," *Appl. Compos. Mater.*, vol. 26, no. 3, pp. 745–762, 2019.

[117] D. Alonso, "Numerical modelling of damage induced by lightning strike events in composite plates," Master's thesis, University of Porto, 2019.

[118] M. Ilyas, *Damage modeling of carbon epoxy laminated composites submitted to impact loading*. PhD thesis, Institut Supérieur de l'Aéronautique et de l'Espace, 2010.

[119] "Plastics — determination of tensile properties — part 1: General principles," standard, International Organization for Standardization, 2012.

[120] Z. Q. Liu, Z. F. Yue, F. S. Wang, and Y. Y. Ji, "Combining Analysis of Coupled Electrical-Thermal and BLOW-OFF Impulse Effects on Composite laminate Induced by Lightning Strike," *Appl. Compos. Mater.*, vol. 22, no. 2, pp. 189–207, 2015.

[121] O. O. Ochoa and J. N. Reddy, *Finite Element Analysis of Composite Laminates*, pp. 37–109. Dordrecht: Springer Netherlands, 1992.

[122] H. Huang, G. S. Springer, and R. M. Christensen, "Predicting Failure in Composite Laminates Using Dissipated Energy," *J. Compos. Mater.*, vol. 37, no. 23, pp. 2073–2099, 2003.

[123] A. C. Orifici, I. Herszberg, and R. S. Thomson, "Review of methodologies for composite material modelling incorporating failure," *Compos. Struct.*, vol. 86, no. 1-3, pp. 194–210, 2008.

[124] V. Buljak and G. Ranzi, "Calibration of constitutive models," *Const. Model. Eng. Mater.*, pp. 43–53, 2021.